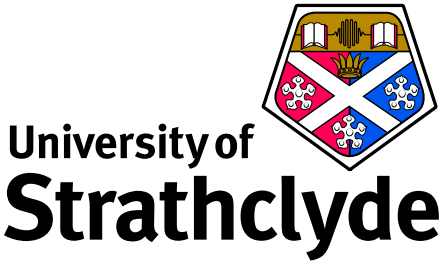

Unsteady Flows of Thin Films

Yazariah Mohd Yatim

Department of Mathematics and Statistics

University of Strathclyde

Glasgow, UK

July 2010

This thesis is submitted to the University of Strathclyde for the degree of Doctor of Philosophy in the Faculty of Science.

This thesis is the result of the author's original research. It has been composed by the author and has not been previously submitted for examination which has led to the award of a degree.

Signed: Date:

Dedicated to my husband and my parents

for their endless love, continuous prayers and encouragement.

Acknowledgements

بسم الله الرحمن الرحيم

In the name of Allah, Most Beneficent, Most Merciful

First and foremost, thank you Allah for giving me strength and endurance. The completion of this thesis is indebted to a great many people. In particular, I would like to express my heartfelt gratitude and appreciation to both of my supervisors, Dr Brian Duffy and Prof. Stephen Wilson for their invaluable knowledge, generous advice, ideas and encouragement throughout my studies. My sincere thanks to Prof. Nigel Mottram, Dr Andrew Davidson and Franck Kalala Mutombo for their guidance in the numerical work. I am deeply indebted to my dearest husband, Khairul Azman Hasran for his continuous support and endless patience through thick and thin, to my beloved parents, Mohd Yatim Zakaria, Azizah Jusoh, Hasran Tahir and Salimah Surif for their love and prayers, as well as to my siblings and in-laws for always putting smiles on my face. I am really grateful to the Ministry of Higher Education, Malaysia and University of Science, Malaysia for their financial support via an Academic Staff Training Fellowship. Last but not least, thank you to all my friends (Julie, Meetu, Fuaada, Maymona and other postgraduate students) and to the staff of Department of Mathematics and Statistics for all the help, friendship and for sharing their time and thoughts with me. *Terima kasih!*

"***By time. Indeed, mankind is in loss.***
Except for those who have believed and done righteous deeds,
and advised each other to truth and advised each other to patience."
Al-Quran (103) : 1−3

Abstract

The lubrication approximation is used to analyse a variety of unsteady three-dimensional flows of thin films on an inclined plane. Specifically, flows of slender non-uniform rivulets and flows around slender dry patches are considered, the flow in each case being driven by gravity or a constant shear stress at the free surface. First, we consider gravity-driven flow of rivulets of Newtonian fluid. Two distinct physically realisable similarity solutions are obtained, corresponding to rivulets whose cross-sectional profiles are "single-humped" and "double-humped", respectively. Each solution represents both a sessile rivulet that narrows and thins with distance down the plane but widens and thickens with time, and a pendent rivulet that widens and thickens with distance down the plane but narrows and thins with time. To investigate the stability of these similarity solutions, we examine numerically the evolution of small superposed perturbations; the numerical results suggest that the solutions for sessile rivulets are stable whereas those for pendent rivulets are unstable. We then extend the work to obtain similarity solutions for gravity-driven flow of rivulets of a non-Newtonian power-law fluid; in particular, we analyse the effects of strongly shear-thinning and strongly shear-thickening behaviour on the solutions. We then consider surface-shear-stress-driven flow of a power-law fluid, for which we show that there is not only a physically realisable similarity solution for a rivulet but also an analogous similarity solution for flow around a dry patch (unlike the case of gravity-driven flow). Lastly, we obtain a different kind of similarity solution, namely a travelling-wave solution for both gravity-driven flow and surface-shear-stress-driven flow around a dry patch. In each case the dry patch has a parabolic shape, and travels down the plane at constant speed; also the thickness of the fluid film increases monotonically away from the dry patch.

Contents

Chapter 1

Introduction

1.1 Thin-Film Flow

Thin-film flows occur in many situations, including in geophysical, biological and industrial contexts. Owing to their great practical importance, there is a considerable scientific literature on thin-film flows.

For instance, in geophysical applications, the slenderness of various mud and lava flows has been exploited to develop thin-film theories to describe them. These types of flow have been investigated theoretically and experimentally by several authors, such as Coussot and Proust [21] and Wilson and Burgess [106] for mud flow, and Balmforth et al. [6] and Osiptsov [71] for lava flow. Thin-film theories also help in understanding the spreading of oil on the sea (Hoult [40]) and the flow of ice sheets (Morland and Johnson [64]).

In industrial contexts, thin-film flows occur in, for example, coating and lubricating processes, inkjet printing, painting, textile dyeing, spray forming and flow in heat exchangers, as well as in the manufacture of solar cells. In the coating process known as lithography, a topography template is pressed into a thin layer of fluid on a substrate, the intention being that the impressed fluid should, in general, replicate the structure of the template; hence it is crucial to understand the evolution of the thin fluid layer after the template is removed. Colburn et al. [19]

Figure 1.1: Ice accretion on an aircraft wing. Picture courtesy of Aviation Education Multimedia Library.

applied a thin-film approximation to obtain an effective approach for fluid delivery for dispensing low viscosity imprint solutions in such a lithography technique. Another example is ice accretion, which occurs when a layer of ice builds up on solid objects that are exposed to freezing precipitation, supercooled fog or cloud droplets (as shown in Figure 1.1). Its occurrence on aircraft wings is one of the major causes of aircraft accidents, and has been the subject of intense study for a long time (see, for example, Myers et al. [68]).

In biological contexts, thin-film flows occur in various places throughout the human body, such as in the cornea of the eye, in the ureter, in lubrication layers in joints (for example, in knees) and in mucus films lining airways. For example, Braun and Fitt [17] used a thin-film theory to model the drainage of the precorneal tear film in human eyes once the eyelid has opened after a blink. This thin tear film is important in lubricating and protecting the cornea. Thin-film theories have also been used in describing the function of the human ureter and predicting its shape (see, for example, Lykoudis and Roos [54]).

Since thin-film theories have been applied to a wide range of problems, from large scale natural phenomena (such as the spreading of lava in a volcanic eruption) to small and complex flows (such as in the manufacture of transistors and electronic

circuits), one may ask what exactly is meant by the term "thin". It is important to understand that thin here does not necessarily mean "small" in everyday terms. A more precise definition is that a thin film is one whose typical thickness, H, is much smaller than its typical length, L, that is, its non-dimensional aspect ratio is small: $\delta = H/L \ll 1$, and the flow is predominantly in the direction in which the film has the longer length scale. The flow may have either (stationary or moving) prescribed boundaries or unknown free surfaces, and may be driven by forces such as gravity, surface shear stress, rotation, surface tension and surface-tension gradients, as well as a variety of thermal effects.

In general, the flow of an incompressible fluid is governed by the balance of linear momentum (Newton's second law)

$$\rho \frac{\mathrm{D}\mathbf{u}}{\mathrm{D}t} = \rho \mathbf{f} + \nabla \cdot \boldsymbol{\sigma}, \tag{1.1}$$

and the incompressibility condition

$$\nabla \cdot \mathbf{u} = 0, \tag{1.2}$$

where ρ is the fluid density, $\mathbf{f} = \mathbf{f}(\mathbf{x}, t)$ is the body force (per unit volume), $\mathbf{u} = \mathbf{u}(\mathbf{x}, t)$ is the fluid velocity, $\mathbf{x}$ is the spatial position, t is time, ∇ is the usual vector differential gradient operator, $\dfrac{\mathrm{D}}{\mathrm{D}t} = \dfrac{\partial}{\partial t} + \mathbf{u} \cdot \nabla$ is the usual convective derivative, and $\boldsymbol{\sigma}$ is the stress tensor (which for many materials, is a symmetric tensor, as may be shown by consideration of angular momentum).

A Newtonian fluid (discussed further in Section 1.2) is one whose constitutive equation is given by

$$\boldsymbol{\sigma} = -p\mathbf{I} + \boldsymbol{\sigma}', \qquad \boldsymbol{\sigma}' = 2\mu\mathbf{e}, \tag{1.3}$$

where p is the fluid pressure, $\mathbf{I}$ is the identity tensor, $\boldsymbol{\sigma}'$ is the extra stress tensor, μ is the fluid viscosity and $\mathbf{e}$ is the rate-of-deformation tensor, given by

$$\mathbf{e} = \frac{1}{2}\left[(\nabla \mathbf{u}) + (\nabla \mathbf{u})^T\right]. \tag{1.4}$$

With (1.3) and (1.4), equation (1.1) yields the well-known Navier–Stokes equation

$$\rho \frac{\mathrm{D}\mathbf{u}}{\mathrm{D}t} = \rho \mathbf{f} - \nabla p + \mu \nabla^2 \mathbf{u}. \tag{1.5}$$

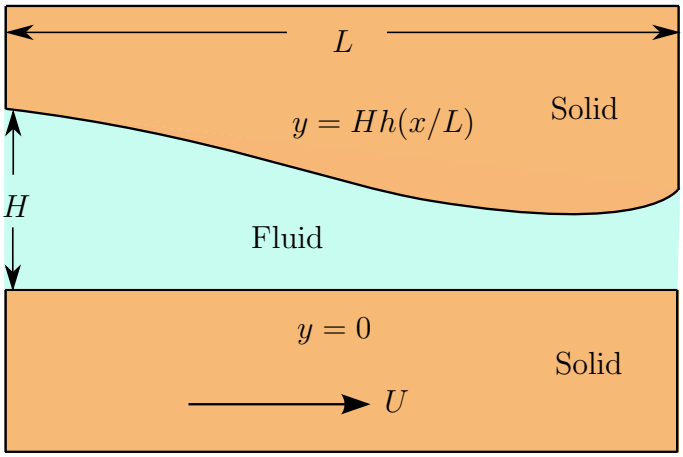

Figure 1.2: Sketch of the slider-bearing problem.

In general, equations (1.2) and (1.5) must be solved numerically; however, when the film is thin, we may simplify these equations considerably via a "thin-film" or "lubrication" approximation based on the smallness of the aspect ratio δ defined above. The simplest way to present this idea is to consider the well-known steady, two-dimensional slider-bearing problem from classical lubrication theory, in which one rigid surface slides over another plane rigid surface to which it is nearly parallel, lubricated by a thin film of fluid in between. A sketch of such a bearing is shown in Figure 1.2, where L is the length of the bearing and H is the maximum gap of the bearing. The lower planar surface $y = 0$ moves in the x direction with a constant velocity U while the upper non-planar surface $y = Hh(x/L)$ is stationary.

First, we re-scale and non-dimensionalise the problem in the natural way by writing

$$\begin{gathered} t = \frac{L}{U}t^*, \quad x = Lx^*, \quad y = Hy^*, \\ u = Uu^*, \quad v = \frac{UH}{L}v^*, \quad p - p_\mathrm{a} = \mu\frac{UL}{H^2}p^*, \end{gathered} \tag{1.6}$$

where p_a denotes the ambient pressure. With the star superscript dropped for clarity, equation (1.2) and equation (1.5) (with $\mathbf{f} = \mathbf{0}$) in the x and y directions become

$$\frac{\partial u}{\partial x} + \frac{\partial v}{\partial y} = 0, \tag{1.7}$$

$$Re\,\delta^2\left(\frac{\partial u}{\partial t}+u\frac{\partial u}{\partial x}+v\frac{\partial u}{\partial y}\right)=-\frac{\partial p}{\partial x}+\left(\delta\frac{\partial^2 u}{\partial x^2}+\frac{\partial^2 u}{\partial y^2}\right), \tag{1.8}$$

$$Re\,\delta^4\left(\frac{\partial v}{\partial t}+u\frac{\partial v}{\partial x}+v\frac{\partial v}{\partial y}\right)=-\frac{\partial p}{\partial y}+\delta^2\left(\delta^2\frac{\partial^2 u}{\partial x^2}+\frac{\partial^2 u}{\partial y^2}\right), \tag{1.9}$$

respectively, where $Re=\rho UL/\mu$ denotes the Reynolds number. At leading order in the thin-film limit $\delta\to 0$, equations (1.7)–(1.9) become

$$\frac{\partial u}{\partial x}+\frac{\partial v}{\partial y}=0, \tag{1.10}$$

$$0=-\frac{\partial p}{\partial x}+\frac{\partial^2 u}{\partial y^2}, \tag{1.11}$$

$$0=-\frac{\partial p}{\partial y}, \tag{1.12}$$

respectively, to be solved subject to the non-dimensional boundary conditions

$$u=1,\quad v=0\quad\text{at}\quad y=0,\quad u=0,\quad v=0\quad\text{at}\quad y=h. \tag{1.13}$$

Equations (1.10)–(1.12) demonstrate how the mathematical problem for the flow has been simplified dramatically by means of a thin-film approximation based on the assumptions that both the aspect ratio $\delta\ll 1$ and the reduced Reynolds number $Re\,\delta^2=\dfrac{\rho UL}{\mu}\delta^2\ll 1$ are small. Note that the Reynolds number Re need not be small, provided only that $Re\,\delta^2\ll 1$. Equations (1.11) and (1.12) may be solved subject to (1.13) to give

$$p=p(x),\quad u=\frac{1}{2}\frac{\mathrm{d}p}{\mathrm{d}x}y\,(y-h)+1-\frac{y}{h}. \tag{1.14}$$

Then, integrating equation (1.10) from $y=0$ to h and using boundary conditions (1.13) for v yields

$$\frac{1}{6}\frac{\mathrm{d}}{\mathrm{d}x}\left(\frac{\mathrm{d}p}{\mathrm{d}x}h^3\right)=\frac{\mathrm{d}h}{\mathrm{d}x}. \tag{1.15}$$

This is called the Reynolds equation, from which p may be determined if the form of $h(x)$ is prescribed and the values of p at the ends $x=0,1$ of the bearing are known. Integrating equation (1.15) twice and assuming that $p=0$ at $x=0,1$ we obtain

$$p(x)=6\int_0^x\frac{h(\bar{x})-h_0}{h^3(\bar{x})}\,\mathrm{d}\bar{x}, \tag{1.16}$$

where h_0 is a constant, determined by $\int_0^1 \frac{h(\bar{x}) - h_0}{h^3(\bar{x})}\,\mathrm{d}\bar{x} = 0$. The slider bearing involves prescribed rigid boundaries, but the thinness of, for example, thin films bounded by free surfaces or by deformable solid may be exploited in an analogous fashion.

The simplicity of the equations arising in thin-film theory has allowed analytical and numerical progress to be made on a wide range of thin-film flow problems. Thin-film theories and their development have been reviewed by several authors, for example, by Oron et al. [70], by O'Brien and Schwartz [69], by Colinet et al. [20], and recently by Craster and Matar [22].

1.2 Newtonian and Non-Newtonian Fluids

Fluids may be categorised very broadly into Newtonian and non-Newtonian fluids. In many types of flow, the behaviour of a fluid can be understood in terms of the relationship between two fundamental quantities, namely the shear stress and the local shear rate. This may be illustrated by reference to the steady simple shearing flow shown in Figure 1.3, in which a fluid is located between two parallel plates of area A. The upper plate moves with velocity V due to the action of a shearing force F as shown, whereas the lower plate is stationary; this creates a shearing friction which shears the fluid. The ratio of the force F to the surface area over which it is applied, A, is the shear stress, τ (that is, $\tau = F/A$), whereas the ratio of the difference in velocity between the two plates to the distance between them, h, is the shear rate, γ (that is, $\gamma = V/h$). The ratio of shear stress to shear rate is the fluid viscosity, μ, which describes the resistance of fluid to flow (a measure of internal friction) and is one of the most important material properties in rheology[1].

A Newtonian fluid, named after Sir Isaac Newton, is a fluid for which the shear stress at any point is proportional to the shear rate at that point, i.e. the viscosity

[1]Rheology, which comes from the Greek word *rheo* (whose root meaning is "to flow"), is the study of the deformation and flow of matter.

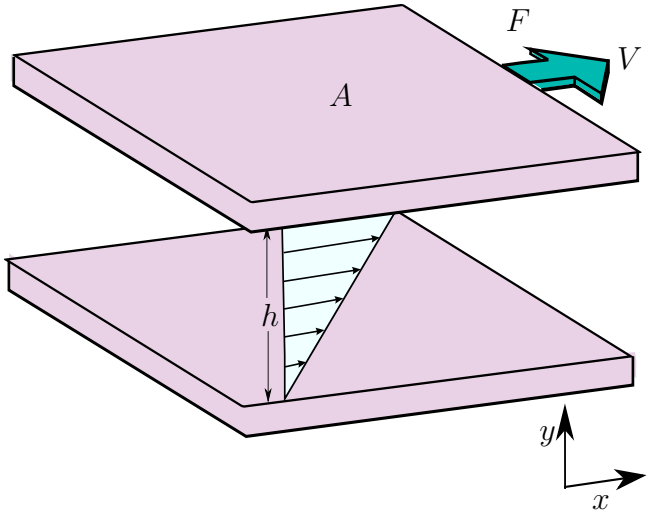

Figure 1.3: Sketch of simple shearing flow.

of the fluid is independent of shear rate. Water and air are common examples of fluids that can be well modelled as Newtonian fluids over a wide range of physical conditions. The equation of motion for a Newtonian fluid is the Navier–Stokes equation (1.5).

Generally, a fluid showing any deviation from the simple Newtonian behaviour (i.e. stress proportional to shear rate) is called a non-Newtonian fluid; such fluids are extensively studied in rheology. Some common examples of non-Newtonian fluids are ketchup, paint and quicksand. Non-Newtonian fluids are of great interest because they have many applications in our daily life, in nature and in industry, and can exhibit complex behaviour. For instance, since the viscosity of ketchup depends on its shear rate, the quickest way to pour the ketchup is by shaking it first to reduce its viscosity. However, to escape quicksand it is best to reduce the stress by trying to move slowly. Some occurrences of non-Newtonian fluid behaviour in nature and industrial situations have been described by Ferguson and Kemblowski [28], Chhabra and Richardson [18] and Tanner [102].

The simplest type of non-Newtonian fluid model is the so-called generalised Newtonian model, in which the viscosity μ is a known function of the local shear

rate γ, i.e. $\mu = \mu(\gamma)$, where γ is defined by

$$\gamma = \left(2\,\mathrm{tr}(\mathbf{e}^2)\right)^{\frac{1}{2}}. \tag{1.17}$$

The constitutive equation of a generalised Newtonian fluid is given by

$$\boldsymbol{\sigma}' = 2\mu(\gamma)\mathbf{e}. \tag{1.18}$$

The simplest generalised Newtonian model is the power-law fluid, which can be useful in describing non-Newtonian behaviour of many materials over restricted ranges of values of γ. For a power-law fluid the viscosity is given by

$$\mu = k\gamma^{N-1}, \tag{1.19}$$

where k and $N > 0$ are material constants. The constant k is a measure of the consistency of the fluid (the larger the value of k the more viscous the fluid) and the power-law index N is a measure of the non-Newtonian behaviour. With equations (1.4) and (1.18), equation (1.1) becomes

$$\rho\frac{\mathrm{D}\mathbf{u}}{\mathrm{D}t} = \rho\mathbf{f} - \nabla p + \mu\nabla^2\mathbf{u} + (\nabla\mu)\cdot\left[(\nabla\mathbf{u}) + (\nabla\mathbf{u})^T\right]. \tag{1.20}$$

A power-law fluid may be either shear-thinning (a pseudoplastic fluid, like ketchup) when $N < 1$, or shear-thickening (a dilatant fluid, like quicksand) when $N > 1$; the case $N = 1$ corresponds to a Newtonian fluid. For a shear-thinning fluid, the viscosity decreases with increasing rate of shear, whereas for a shear-thickening fluid, the viscosity increases with increasing rate of shear. Barnes et al. [9] give examples of materials that exhibit power-law behaviour, such as toothpaste and skin cream (which are shear-thinning) and anti-misting solution in jet fuel (which is shear-thickening). Hamrock [34] and Szeri [99] describe the use of power-law fluids in modelling non-Newtonian lubricants in geometries with rigid boundaries.

An improvement to the power-law model is the Carreau model, for which the viscosity function is given by

$$\frac{\mu - \mu_\infty}{\mu_0 - \mu_\infty} = \left[1 + (k\gamma)^2\right]^{\frac{N-1}{2}}, \tag{1.21}$$

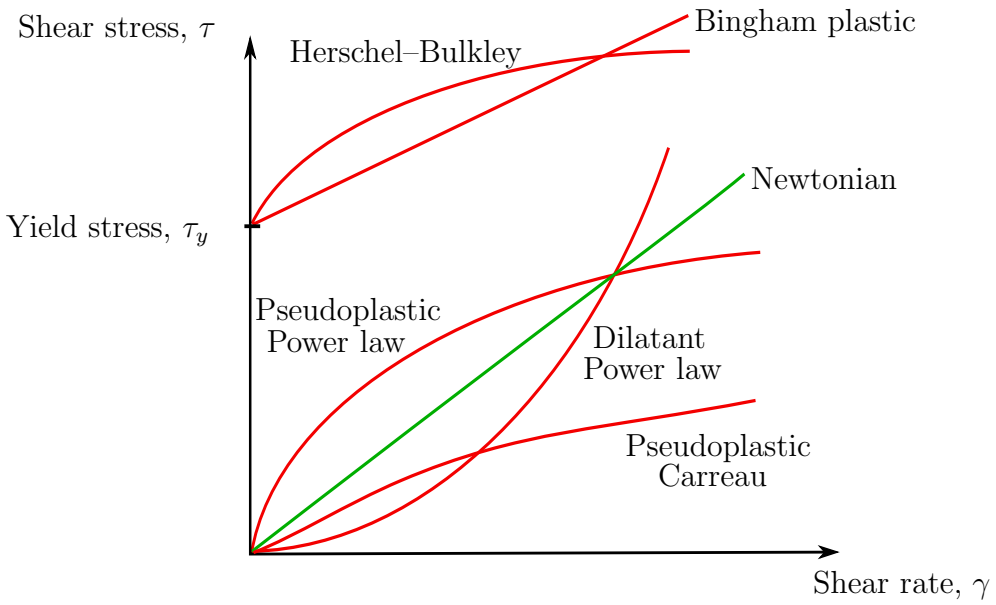

Figure 1.4: Sketch of the relationships between shear stress, τ, and shear rate, γ, for Newtonian and certain generalised Newtonian fluids in simple shearing flows.

where μ_0 and μ_∞ are material constants, and $0 < N \leq 1$. This model essentially reduces to the power-law model at moderate values of shear rate, but predicts a finite viscosity μ_0 at zero shear rate and a constant viscosity μ_∞ at infinite shear rate. Myers [67] gives comparisons between predictions of the power-law model and the Carreau model in thin-film flow on an inclined plane and in flow in a channel.

Other popular types of generalised Newtonian model are the Bingham and Herschel–Bulkley models for viscoplastic fluids. In these two models there is a critical value of the shear stress, τ_y (known as the yield stress) which has to be exceeded before the fluid will start to flow, and below which it behaves like a solid. When the stress exceeds the yield stress a Bingham plastic material behaves like a Newtonian fluid with shear stress $\tau - \tau_y$, whereas a Herschel–Bulkley material exhibits non-Newtonian pseudoplastic behaviour with shear stress $\tau - \tau_y$. These two models have been used to describe mud and slurries, as well as lava. Figure 1.4 summarises the relationships between shear stress and shear rate for Newtonian

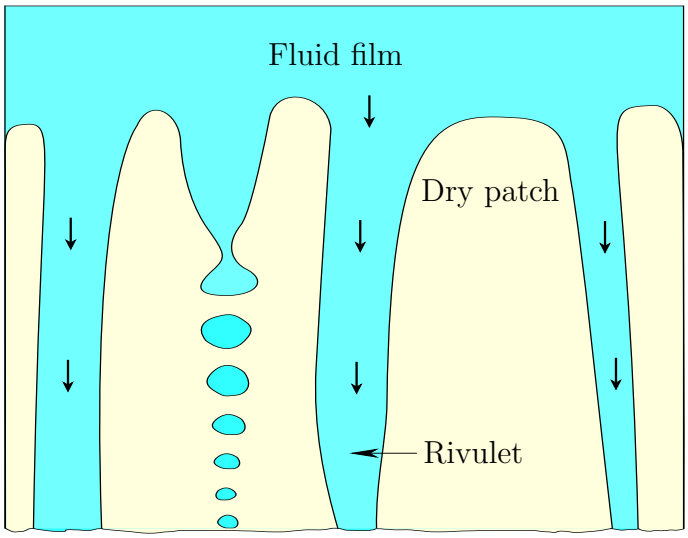

Figure 1.5: Sketch of possible flows when a thin film of fluid drains under gravity down an inclined plane, including rivulets, dry patches and droplets.

and certain generalised non-Newtonian fluids (dilatant power law, pseudoplastic power law, pseudoplastic Carreau, Bingham plastic and Herschel–Bulkley).

It is worth noting that there are many other types of non-Newtonian fluid, including viscoelastic materials and time-dependent thixotropic and rheopectic materials (for which the viscosities depend on the duration of shear stress). However, in this thesis we utilise only the power-law model for our work concerning a non-Newtonian fluid.

1.3 Review of Previous Literature

Figure 1.5 shows a sketch of possible flows when a thin film of fluid drains under gravity down an inclined plane, including rivulets, dry patches and droplets. In this thesis, we shall focus our attention on various unsteady three-dimensional similarity solutions for flows of thin rivulets and for flows of thin films around dry patches on an inclined plane for both Newtonian and non-Newtonian power-law fluids. We shall consider the flow to be driven either by gravity or by a constant

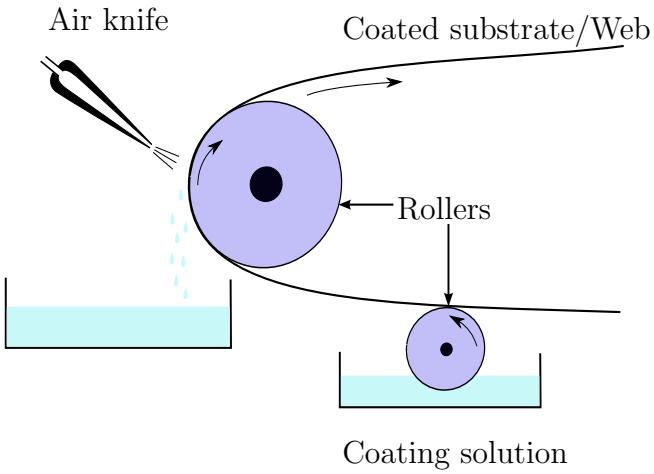

Figure 1.6: Sketch of a simple air-knife coating process.

shear stress at the free surface. In this subsection, we will review some of the previous work that is relevant to our studies, and present some key ideas required for our analysis.

1.3.1 Thin-film flow driven by an external force

A thin-film flow can be driven by various external forces such as gravity, surface shear stress and imposed pressure differences. Some technologically significant examples are the icing of aircraft wings (mentioned in Section 1.1), and the so-called "air-knife" coating process where a strong jet of air is used to remove excess fluid from a coated substrate. A sketch of such a simple air-knife coating process is shown in Figure 1.6. One simple everyday occurrence is rainwater running down a window of a house or of a moving car (see Figure 1.7).

Several of these flows involve rivulets driven by gravitational effects. Generally, a rivulet is a narrow stream of fluid (sometimes also called a "trickle") that flows on a substrate and shares a curved free surface with the surrounding atmosphere. Rivulets have contact angles at the three-phase contact lines between the fluid, the substrate and the surrounding atmosphere. The motion of rainwater on the windscreen of a fast moving vehicle provides an everyday example of a rivulet

(a)  (b) 

Figure 1.7: Examples of (a) drops of rainwater on a window, and (b) rivulets of rainwater on a moving car window. Pictures courtesy of Prof. S. K. Wilson.

flow driven by both gravity and external forces (including both pressure and shear stress) due to the motion of the air. In industrial applications, rivulets may occur in, for example, condensers and heat exchangers. Due to the many practical occurrences of rivulet flow, there is considerable previous literature on both steady and unsteady flows of rivulets and thin films.

(a) Steady flows of rivulets

The study of steady three-dimensional gravity-driven flow of a slender non-uniform rivulet of a Newtonian fluid down an inclined plane was pioneered by Smith [92], who considered steady flow of a symmetric rivulet driven by gravity g when surface-tension effects are negligible. On the solid substrate $z = 0$ the fluid velocity is zero (no-slip and no-penetration conditions), while on the free surface the usual normal and tangential stress balances and the kinematic condition apply, and there is a symmetry condition at the middle of the rivulet at $y = 0$. The free surface is denoted by $z = h(x, y)$, where the x and y axes are in the downstream and cross-stream directions, respectively and the z axis is normal to the inclined plane $z = 0$. The partial differential equation (which will be derived carefully in Chapter 2) satisfied by h is

$$\cos\alpha \left(h^3 h_y\right)_y - \sin\alpha \left(h^3\right)_x = 0, \tag{1.22}$$

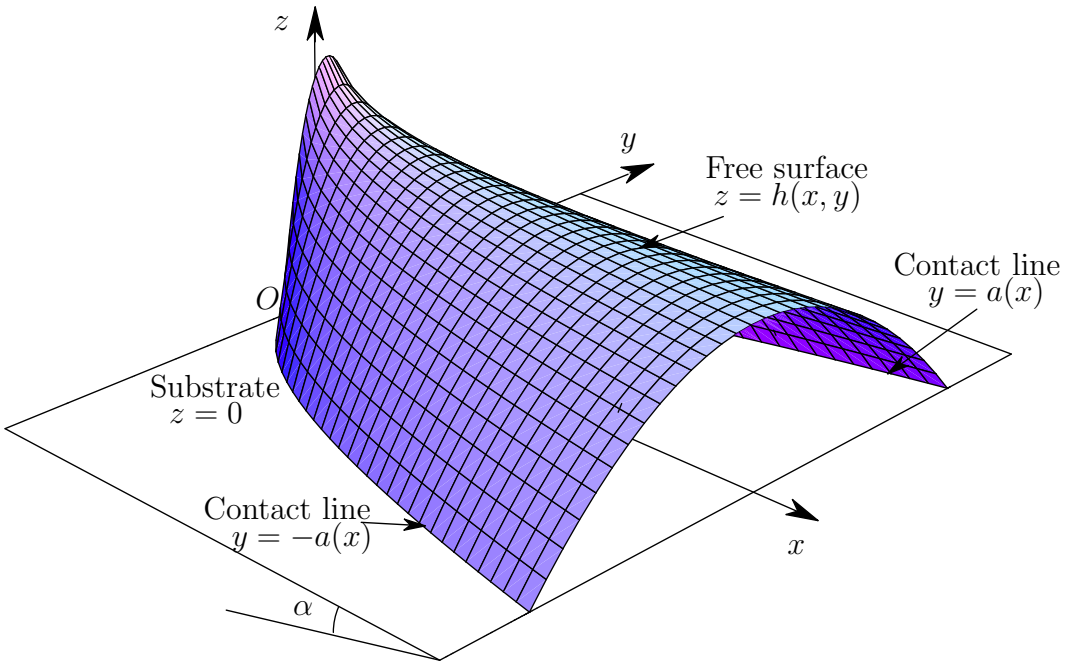

Figure 1.8: Smith's [92] steady rivulet solution.

where α is the angle of inclination of the plane to the horizontal. The volume flux of fluid down the plane is given by

$$Q = \frac{\rho g \sin\alpha}{3\mu} \int_{-a}^{a} h^3 \, \mathrm{d}y, \tag{1.23}$$

where $a = a(x)$ is the semi-width of the rivulet. Smith [92] obtained the unique similarity solution

$$h = h_m \left(1 - \frac{y^2}{a^2}\right), \quad a = (cx)^{\frac{3}{7}}, \tag{1.24}$$

where the maximum middle height of the rivulet $h_m = h(x, 0)$ and the constant c are given by

$$h_m = \frac{3c \tan\alpha}{14\,(cx)^{\frac{1}{7}}}, \quad c = \frac{7\cot\alpha}{3} \left(\frac{105\mu\bar{Q}}{4\rho g \sin\alpha}\right)^{\frac{1}{3}}, \tag{1.25}$$

where $\bar{Q} > 0$ is the prescribed constant value of Q. A typical plot of Smith's [92] rivulet solution is shown in Figure 1.8. His similarity solution predicts that the rivulet has a parabolic transverse profile with a single global maximum $h = h_m$ at $y = 0$, and that it widens according to $x^{3/7}$ and thins according to $x^{-1/7}$. This

solution may be interpreted as both a sessile rivulet (on the upper side of the plane) and a pendent rivulet (on the lower side of the plane). For $\cos\alpha > 0$ (so that $c > 0$) the solution represents a widening and shallowing sessile rivulet in $x > 0$, while for $\cos\alpha < 0$ (so that $c < 0$) it represents a narrowing and deepening pendent rivulet in $x < 0$. Smith's [92] similarity solution was found to be in good agreement with his own physical experiments, and subsequently with numerical solutions of the unsteady thin-film equations at large distances from the source obtained by Schwartz and Michaelides [89] and by Lister [52], and by Higuera [36] in the case when the slope of the inclined plane is small ($\alpha \ll 1$). Numerical solution obtained by Schwartz and Michaelides [89] will be discussed in detail in Chapter 3.

Several papers have been written in the spirit of Smith's [92]. Most notably, Duffy and Moffatt [24] generalised Smith's [92] similarity solution to include surface-tension effects. When surface-tension effects dominate those of gravity in the transverse direction the partial differential equation for h becomes

$$\sigma\left(h^3 h_{yyy}\right)_y + \rho g \sin\alpha \left(h^3\right)_x = 0, \tag{1.26}$$

where σ denotes the coefficient of surface tension. The volume flux of fluid down the plane is still given by equation (1.23). Duffy and Moffatt [24] obtained a one-parameter family of solutions parameterised by $G_0 \geq 0$ which may be written in the form

$$h = h_m\left(1 - \frac{y^2}{a^2}\right)\left(G_0 - \frac{Sy^2}{24a^2}\right), \quad a = (cx)^{\frac{3}{13}}, \tag{1.27}$$

where

$$h_m = \frac{3|c|\rho g\sin\alpha}{13\sigma\,(cx)^{\frac{1}{13}}}, \quad |c| = \frac{13\sigma}{3\rho g\sin\alpha}\left(\frac{3\mu\bar{Q}}{I\rho g\sin\alpha}\right)^{\frac{1}{3}}, \tag{1.28}$$

$S = \mathrm{sgn}(c)$ and the function $I = I(G_0)$ is given by

$$I = \int_{-1}^{1}\left[\left(1-\eta^2\right)\left(G_0 - \frac{S\eta^2}{24}\right)\right]^3 \mathrm{d}\eta = \frac{32}{35}G_0^3 - \frac{4S}{315}G_0^2 + \frac{1}{6930}G_0 - \frac{S}{1297296}. \tag{1.29}$$

Duffy and Moffatt's [24] similarity solution predicts that the rivulet widens according to $x^{3/13}$ and thins according to $x^{-1/13}$. For $S = 1$ (so that $c > 0$) this solution represents a widening and shallowing rivulet in $x > 0$, while for $S = -1$ (so that $c < 0$) it represents a narrowing and deepening rivulet in $x < 0$.

Also based on the work of Smith [92] is the paper by Wilson[2] and Burgess [106], who generalised it to the case of a non-Newtonian power-law fluid, with power-law index N. They obtained a similarity solution that predicts that the rivulet widens according to $x^{(2N+1)/(5N+2)}$ and thins according to $x^{-N/(5N+2)}$, and found that since the exponent of x does not change greatly as N is varied, the profile of the rivulet is rather insensitive to the value of N.

Wilson et al. [110] considered steady rivulet flow on an inclined plane driven by either gravity or a constant shear stress at the free surface of the fluid. In general, they found that the solutions for a shear-stress-driven rivulet are qualitatively similar to those for a gravity-driven rivulet. Wilson et al. [110] considered both Newtonian and power-law fluids. In particular, for gravity-driven flow, they recovered the solutions of Wilson and Burgess [106], while for shear-stress-driven flow, they found that the rivulet widens according to $x^{1/3}$ and thins according to $x^{-1/6}$. Note that for shear-stress-driven flow the exponent of x is independent of N.

All the works described above concern similarity solutions, but other types of solution for steady rivulet flow have been obtained. For example, Towell and Rothfeld [104], who studied steady unidirectional flow of a rivulet flowing down an inclined plane in the presence of significant surface-tension effects, calculated the profile of the rivulet numerically and found excellent agreement with their own experimental results. Subsequently, Allen and Biggin [5] and Duffy and Moffatt [23] used the lubrication approximation to obtain an asymptotic solution in the case when the transverse profile of the rivulet is thin. Duffy and Moffatt [23]

[2]Note that the first author of this work is S. D. R. Wilson, who should not be confused with S. K. Wilson, who is one of the supervisors of the present work.

also interpreted their results as describing the locally unidirectional flow down a plane of slowly varying slope in the longitudinal direction, and in particular, used them to describe the flow in the azimuthal direction round a large horizontal circular cylinder. Bentwich et al. [12] considered a wider range of contact angle of the rivulet and obtained numerical results for the flow on an inclined plane and a vertical plane. Wilson and Duffy [108] and Sullivan et al. [98] studied steady unidirectional flow of a symmetric rivulet of a non-perfectly wetting fluid on a vertical plane and of a perfectly wetting fluid on an inclined plane, respectively, subject to a constant longitudinal shear stress at its free surface; they showed that there are five possible types of cross-sectional flow pattern, and investigated the quasi-steady stability of the rivulet, as well as determining conditions for it to be energetically favourable to split into sub-rivulets.

More generally, there has been work on other thin-film flows subject to surface forces and pressure gradients due to an air flow. For example, King et al. [45] studied steady periodic surface waves on an infinite sheet of fluid on an inclined plane whose draining due to gravity is resisted by the pressure and shear forces associated with an upward stream of air flowing over its free surface. Their model is based on lubrication theory and thin-airfoil theory, and they assumed that the surface shear stress is constant but that the pressure gradient is influenced by the shape of the free surface of the film. They deduced that steady waves are possible only for a restricted range of values of mass flux, those of largest (finite) flux being sinusoidal, and those of smallest (non-zero) flux being solitary waves. Using a similar approach King and Tuck [44] considered the corresponding problem for a steady two-dimensional ridge of fluid of finite width on an inclined plane. They found numerically that a steady solution is possible only if the slope is below a critical value, but that below this value there are either one or two possible solutions.

(b) Unsteady flows of rivulets and thin films

In two-dimensional gravity-driven spreading on a horizontal plane the free-surface profile $h(x,t)$ is governed by the second-order nonlinear diffusion equation

$$h_t + \left(h^n\, h_x\right)_x = 0, \tag{1.30}$$

with $n = 3$ for a Newtonian fluid. Note that equation (1.30) is known as the second-order porous medium equation, and it has been studied extensively in various contexts, for example, in ground water filtration (Barenblatt [8]), in the diffusion of dopants in semiconductors (King [46]), and in the propagation of heat in an isotropic medium (Pert [80]).

Pioneering work on unsteady diffusion was performed by Zel'dovich and Kompaneets [116] and subsequently by Pattle [75] who obtained a similarity solution describing diffusion of a substance (of concentration h) from an instantaneous point source at the origin in one, two and three dimensions when the diffusivity is proportional to h^n for some exponent n. It was found that the diameter of the region of diffusing substance varies according to $t^{1/(sn+2)}$, and that the concentration at the origin varies according to $t^{-s/(sn+2)}$, where $s = 1$, 2 or 3 for planar, axisymmetric and spherically symmetric geometries, respectively.

By adopting Pattle's [75] analysis in the case $n = 3$, Smith[3] [93] described the gravity-driven spreading of a sessile thin film of a constant volume of fluid over a horizontal plane in two and three dimensions (corresponding to Pattle's [75] solution with $s = 1$ and $s = 2$, respectively). It was found that the fluid spreads according to $t^{1/5}$ in two dimensions and according to $t^{1/8}$ in three dimensions; in both cases, the slopes of the free surface at the (moving) contact lines (i.e. the contact angles) are infinite.

Wilson and Burgess [106] noted a formal analogy between their steady three-

[3]Note that the author of this work is S. H. Smith, who should not be confused with P. C. Smith, who obtained the steady similarity solution for a rivulet described in the previous subsection.

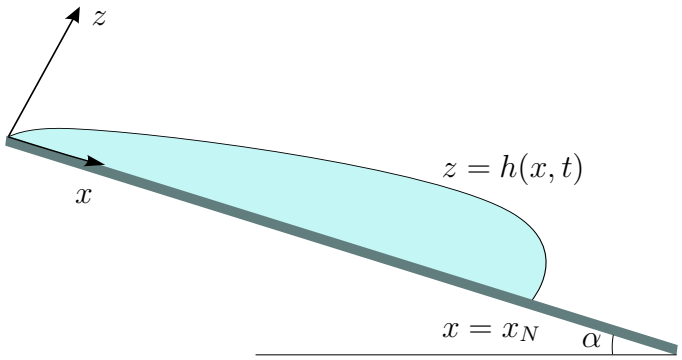

Figure 1.9: Sketch of the geometry of two-dimensional unsteady flow down an inclined plane studied by Huppert [41].

dimensional rivulet problem and an unsteady two-dimensional nonlinear diffusion problem, specifically equation (1.30) (with the time variable t replaced by a space variable), and Perazzo and Gratton [79] used this analogy to obtain solutions to a variety of free-surface thin-film flow problems, and, in particular, to recover the similarity solution of Wilson and Burgess [106] from the known solutions of the diffusion problem given by Zel'dovich and Kompaneets [116] and Pattle [75].

An extension of the Pattle's [75] and Smith's [93] problems was studied by Huppert [42] (see also Huppert [43]) who obtained similarity solutions describing two-dimensional and axisymmetric gravity-driven spreading of a thin film of a Newtonian fluid emanating from a time-dependent source on a horizontal plane. Huppert [41] also studied two-dimensional unsteady flow of a thin film of a Newtonian fluid down an inclined plane as sketched in Figure 1.9. In this case h satisfies the governing equation

$$h_t + \frac{\rho g \sin\alpha}{3\mu}\left(h^3\right)_x = 0. \tag{1.31}$$

In particular, he obtained the simple similarity solution

$$h = \left(\frac{\mu}{\rho g \sin\alpha}\right)^{\frac{1}{2}}\left(\frac{x}{t}\right)^{\frac{1}{2}}, \tag{1.32}$$

which is valid at long times and predicts that the height of the free surface varies with x and t according to $x^{1/2}$ and $t^{-1/2}$. By truncating this solution appropriately,

Huppert [41] found that the "nose" (i.e. the front) of the flow $x = x_N(t)$ is given by

$$x_N = \left(\frac{9A^2\rho g \sin\alpha}{4\mu}\right)^{\frac{1}{3}} t^{\frac{1}{3}}, \tag{1.33}$$

where $A = \int_0^{x_N} h(x,t)\,\mathrm{d}x$ is the (prescribed) area of the film, showing that the length of a fixed volume of fluid varies according to $t^{1/3}$. His similarity solution is in remarkably good agreement with his own physical experiments. Huppert [41] pointed out that surface-tension effects would become significant in the vicinity of the front of the film, and subsequently Moriarty et al. [63] constructed an appropriate uniformly valid composite solution to describe this, which they found to be in good agreement with their numerical solutions to the unsteady thin-film equations.

Lister [52] obtained similarity solutions describing unsteady flow of a Newtonian fluid down an inclined plane from a point source and a line source for short times and long times which were found to be in good agreement with his own numerical and experimental results. Recently, Takagi and Huppert [100] obtained similarity solutions representing unsteady flow of a finite volume of a Newtonian fluid along horizontal and inclined channels with semi-circular and V-shaped boundaries, and showed that these solutions are in good agreement with their own experimental results. Subsequently, Takagi and Huppert [101] investigated unsteady flow of a Newtonian fluid inside slowly varying channels and fractures with the fluid volume increasing with time; in the case of a constant flux, their similarity solutions are again in good agreement with their experimental results.

Gorodtsov [30] obtained similarity solutions describing unsteady two-dimensional and axisymmetric gravity-driven spreading of a power-law fluid on a horizontal plane, generalising the earlier solutions for a Newtonian fluid given by Smith [93] (for the case when the volume of fluid is constant) and Huppert [42] (for the case when the volume changes according to some power of t). These solutions were rediscovered independently by Pascal [72] (in the two-dimensional constant-volume

case), Pascal [73] (in the axisymmetric constant-volume case), and Gratton et al. [31]. Gorodtsov [30] also obtained a similarity solution describing spreading of a power-law fluid on a horizontal plane with vertical side-wall boundaries, and Gratton et al. [31] obtained a variety of waiting-time and travelling-wave solutions for thin-film flows of a power-law fluid on a horizontal plane.

Perazzo and Gratton [77] found a similarity solution describing unsteady two-dimensional gravity-driven flow of a power-law fluid down an inclined plane which predicts that the height of the free surface varies according to $(x/t)^{N/(N+1)}$, generalizing the result given by Huppert [41] for the Newtonian case $N = 1$. Perazzo and Gratton [77, 78] also obtained families of travelling-wave solutions for thin-film flows of a power-law fluid on an inclined plane. For instance, Perazzo and Gratton [77] found three families of solution, namely downslope travelling waves with a front and downslope travelling waves without a front for the case $c > 0$, as well as upslope travelling waves for the case $c < 0$, where c is the travelling-wave speed. Figure 1.10 shows the profile of the travelling wave for these three families of solutions with power-law index $N = 0.9$, 1 and 1.1.

The fourth-order nonlinear diffusion equation

$$h_t + \left(h^n\, h_{xxx}\right)_x = 0, \tag{1.34}$$

with $n > 0$ has also been the subject of extensive investigations. Equation (1.34) has several physical interpretations; for example, in the case $n = 3$, it represents surface-tension-driven flow of a thin film of a Newtonian fluid. Smyth and Hill [94] obtained exact waiting-time solutions for all n except for $n = 2$ and $n = 4$, and an exact closed-form similarity solution for $n = 0$ and $n = 1$. Smyth and Hill's [94] similarity solution for $n = 1$ was proved to be linearly stable by Bernoff and Witelski [13]. Witelski [111] obtained exact closed-form similarity solutions of (1.34) and presented some examples of spreading and contracting solutions for a range of values of n including $n = 3$. Equation (1.34) was also studied by King [47], who generalized it to two degenerate fourth-order parabolic equations,

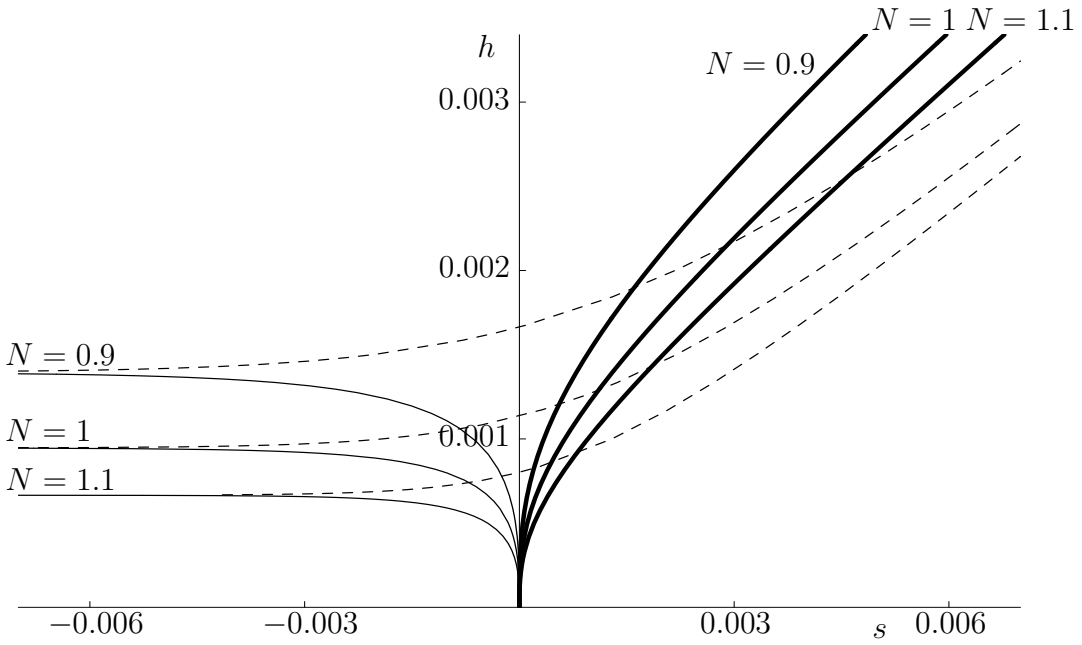

Figure 1.10: Plot of the profile of the film h as a function of the travelling-wave variable $s = x - ct$ for power-law index $N = 0.9$, 1 and 1.1 obtained by Perazzo and Gratton [77]; the thin lines represent downslope travelling waves with a front, the dashed lined represent downslope travelling waves without a front, and the thick lines represent downslope travelling waves.

one of which is relevant to surface-tension-driven flow of a power-law fluid. Betelu and Fontelos [15] obtained a travelling-wave solution and a similarity solution describing two-dimensional spreading of a power-law fluid with $N < 1$ (shear-thinning fluid) driven by surface tension. Subsequently, Betelu and Fontelos [16] used the same approach to investigate the spreading of a circular drop of a shear-thinning fluid. An extensive review of surface-tension-driven flows of a thin film and their applications has been written by Myers [66].

In the case of unsteady flow driven by surface shear, Eames et al. [25] used a similar approach to that of Lister [52] to obtain similarity solutions describing the effect of a constant surface shear stress due to the flow of an overlying fluid on a spreading viscous gravity current emanating from a point or line source in a horizontal channel; they found that their analytical and numerical solutions are

in good agreement with their own experimental results for the cases of a constant volume and a constant flux of fluid released from a point source. Pascal [74] studied the two-dimensional spreading of a fixed volume of a power-law fluid over a slightly denser ambient layer of Newtonian fluid subject to gravity and a constant shear stress at the free surface. He obtained numerical solutions for both single-layer and two-layer models, and an analytical solution for a single-layer model. He found that this problem can be treated as a single-layer model only in the case when the ambient layer is relatively deep.

There have also been many studies of unsteady flows subject to surface forces and pressure gradients due to an external air flow. For example, McKinley et al. [59] studied the spreading of a ridge of fluid and of a droplet on a horizontal plane subject to a non-uniform pressure associated with a jet of air blowing normally onto it, and subsequently McKinley and Wilson [57, 58] investigated the linear stability of the ridge and droplet, respectively.

1.3.2 Flows around dry patches

A dry patch can occur in a fluid film for many reasons, including there being insufficient fluid to wet the substrate, a high temperature of the substrate which causes the fluid to dry out, the presence of air bubbles within the film, inhomogeneities in the substrate, or the presence of surfactant in the fluid. A common example of dry patch formation is when a thin film of fluid runs down an inclined plane, forming fingers (rivulets) with dry patches in-between, as sketched in Figure 1.11. This problem is of considerable practical interest, especially in industrial contexts such as in heat exchangers and coating processes. In a heat-transfer device, the presence of dry patches must generally be avoided because it may reduce the efficiency or may result in overheating or corrosion of the dry area in the device. In coating processes the formation of dry patches is also clearly undesirable, and therefore it is crucial to understand when a layer of fluid will leave a hole on the substrate and whether the holes that exist will persist or will close up during the

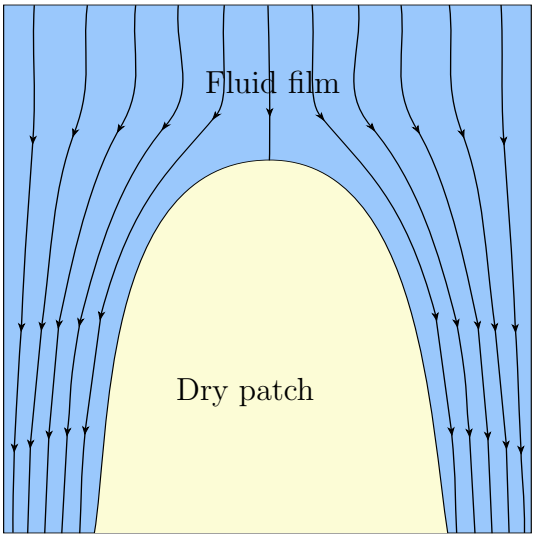

Figure 1.11: Sketch of the flow around a dry patch in a flowing film.

coating process.

Dry patches or holes can occur within a stationary film or a flowing film. A pioneering study of a dry patch in a stationary film was performed both theoretically and experimentally by Taylor and Michael [103]. They considered an infinite film of fluid on a horizontal plane under the influence of surface tension and gravity effects. They found a unique axisymmetric equilibrium hole configuration provided that the film is sufficiently thin. By considering the energy of this equilibrium configuration they showed that these holes are unstable, and obtained a criterion for when holes would open and when they would close; specifically they found that a hole would close if its radius is smaller than the unstable equilibrium hole, but would open if it is larger. Moriarty and Schwartz [62] analysed numerically the unsteady dynamics of an axisymmetric hole in a thin fluid film in a bounded geometry, including the motion of the contact line. In particular, they found that in this case there are two equilibrium hole configurations, a smaller unstable one and a larger stable one. They also found that the criterion given by Taylor and Michael [103] holds except for holes with radius slightly larger than the unstable equilibrium hole which can either close or open. Subsequently, Wilson and

Duffy [107] studied equilibrium holes in the asymptotic limit when the radius of the hole is small. López et al. [53] performed a three-dimensional linear stability analysis on the axisymmetric equilibrium solutions obtained by Moriarty and Schwartz [62]. They found that larger holes are stable to axisymmetric perturbations, whereas smaller ones are unstable, but that all solutions are unstable to asymmetric perturbations.

One of the first studies of a dry patch in a flowing film draining vertically under gravity and surface shear stress was performed by Hartley and Murgatroyd [35]. They obtained two different criteria, namely a force-balance criterion (based on the balance between surface-tension and inertia forces at the stagnation point at the apex of a dry patch) and a minimum total-energy-flow criterion (including kinetic and surface energy) which they used to predict the critical film thickness and the maximum flow rates of fluid for the dry patch to persist. Subsequently, Murgatroyd [65] included the effects of surface shear stress and form drag in this analysis. Murgatroyd's [65] theoretical prediction has been validated experimentally and numerically using computational fluid dynamics (CFD) simulation by Penn et al. [76].

Hobler [37] used a minimum total energy criterion similar to that of Hartley and Murgatroyd [35] and included the effect of contact angle to calculate when it is energetically favourable for a film on a vertical substrate to break up into rivulets. Ponter et al. [84] derived corresponding conditions for a dry patch to persist in a film flowing down a vertical plane in the presence of mass transfer, and showed that their theoretical prediction is in good agreement with their own experiments. In their experiment, they noticed the formation of a "collar" of fluid near the contact line at the apex of the dry patch, which is absent in the theory of Hartley and Murgatroyd [35]. Wilson [105] developed a more sophisticated model to incorporate the presence of this collar/ridge, and he concluded that the surface tension and contact angle play an important role in collar formation in a dry patch. Subsequently, Bankoff [7] compared the total energy flow in a uniform thin

film of fluid and in a periodic array of rivulets (of the same size) draining down a vertical wall to determine when the fluid film will break up into rivulets. He assumed that rivulets will occur when the two configurations have the same total energy flow. Mikielewicz and Moszynski [60] adopted the approach of Hobler [37] and Bankoff [7], but accounted for the dry areas between the rivulets. They also pointed out the algebraic error in Bankoff's [7] analysis which yields an unphysical result when corrected. Later, Mikielewicz and Moszynski [61] improved their earlier analysis by using conformal mapping technique to determine the exact form of velocity distributions in rivulets driven by a prescribed uniform longitudinal surface shear stress and by gravity, and used these in an improved energy analysis. El-Genk and Saber [26] determined the velocity distribution within a rivulet numerically to predict the break-up of a thin film into rivulets based on the minimum total energy flow. Later, Saber and El-Genk [87] extended their work to investigate the break-up of thin film flowing down or climbing up a vertical or inclined surface subject to a prescribed non-uniform longitudinal surface shear stress. The solutions from both of their works are in good agreement with experimental results.

Wilson et al. [109] obtained two steady similarity solutions for a flow around a non-uniform slender dry patch in a thin film draining under gravity on an inclined plane, namely one for the case of weak surface tension and one for the case of strong surface tension. In the case of weak surface-tension effects, so that the flow is purely driven by gravity, the free surface profile h satisfies equation (1.22), and the average volume flux around the dry patch down is given by

$$Q = \frac{\rho g \sin\alpha}{3\mu} \lim_{y\to\infty} y^{-1} \int_{a(x)}^{y} h(x,y)^3 \,\mathrm{d}y = \frac{\rho g \sin\alpha}{3\mu} h_\infty^3, \tag{1.35}$$

where $a = a(x)$ is the semi-width of the dry patch and h_∞ is the uniform height of the film far from the contact line. Wilson et al.'s [109] similarity solution takes the form

$$h = \frac{c\tan\alpha}{2} G(\eta), \quad \eta = \frac{y}{(cx)^{\frac{1}{2}}}, \tag{1.36}$$

where the function $G = G(\eta)$ satisfies the second-order ordinary differential equa-

tion

$$\left(G^3G'\right)' + \eta\left(G^3\right)' = 0, \tag{1.37}$$

subject to the boundary conditions

$$G(1) = 0, \qquad \lim_{\eta\to\infty} G(\eta) = G_\infty, \tag{1.38}$$

where the constant G_∞ satisfies

$$Q = \frac{\rho g \sin\alpha}{3\mu}\left(\frac{c\tan\alpha G_\infty}{2}\right)^3. \tag{1.39}$$

The exact solution of (1.37) is not available, but asymptotic analysis reveals that near the contact line $\eta = 1$ the relevant solution satisfies

$$G = K(\eta-1)^{\frac{1}{4}} - \frac{4}{7}(\eta-1) + \frac{48}{245K}(\eta-1)^{\frac{7}{4}} + o(\eta-1)^{\frac{7}{4}} \tag{1.40}$$

as $\eta \to 1$, where the constant $K > 0$ is not determined locally, showing that the lubrication approximation fails near the contact line; at leading order in the limit $G_\infty \to 0$ it is found that $K = \sqrt{2}G_\infty^{3/4}$, and that

$$G \sim G_\infty + L\eta^{-1}\exp\left(-\frac{3\eta^2}{2G_\infty}\right) \tag{1.41}$$

as $\eta \to \infty$, where the constant L is not determined locally, showing that G approaches G_∞ monotonically. There is a unique solution for G for all values of G_∞. The solution predicts that the dry patch has a parabolic shape and that the transverse profile of the free surface has a monotonically increasing shape. For $\cos\alpha > 0$ (so that $c > 0$) this solution represents a widening sessile dry patch in $x > 0$, whereas for $\cos\alpha < 0$ (so that $c < 0$) it represents a narrowing pendent dry patch in $x < 0$. Figure 1.12 shows a typical plot of a solution for $\cos\alpha > 0$. An existence theory for solutions of Wilson et al.'s [109] mathematical problem was provided by Agarwal and O'Regan [4].

In the case when surface-tension effects dominates the flow, the free surface profile h satisfies equation (1.26), and the average volume flux around the dry

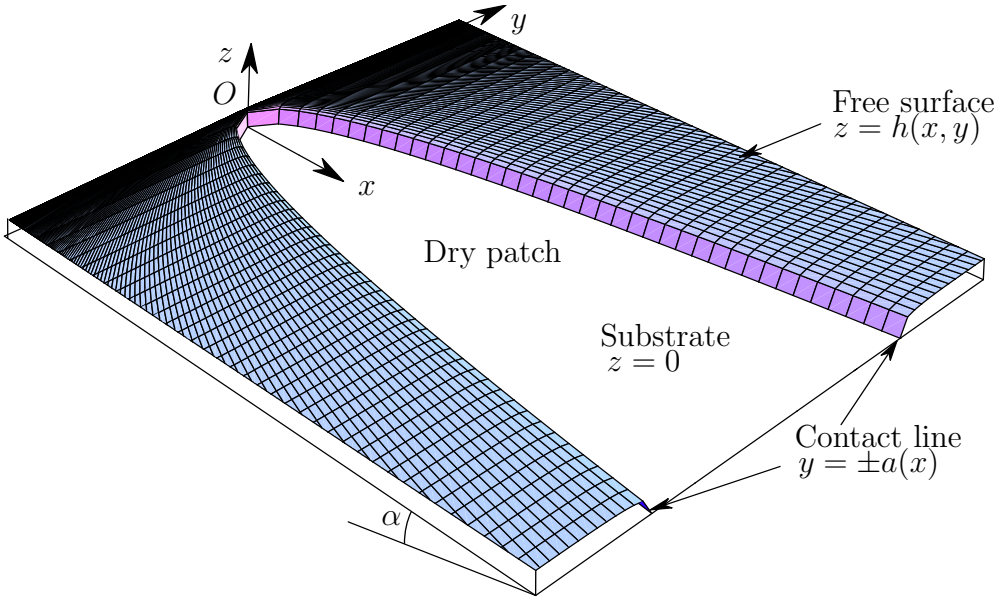

Figure 1.12: Wilson et al.'s [109] steady dry patch solution.

patch is again given by equation (1.35). In this case, Wilson et al.'s [109] similarity solution takes the form

$$h = \frac{c\rho g \sin\alpha}{4\sigma} G(\eta), \quad \eta = \frac{y}{(cx)^{\frac{1}{4}}}, \tag{1.42}$$

where the function $G = G(\eta)$ satisfies the fouth-order ordinary differential equation

$$\left(G^3 G'''\right)' + \eta \left(G^3\right)' = 0, \tag{1.43}$$

subject to the boundary conditions (1.38), where the constant G_∞ satisfies

$$Q = \frac{\rho g \sin\alpha}{3\mu} \left(\frac{c\rho g \sin\alpha G_\infty}{4\sigma}\right)^3. \tag{1.44}$$

The exact solution of (1.43) is not available, but asymptotic analysis reveals that the relevant solution satisfies

$$G = K(\eta - 1)^{\frac{3}{4}} + \frac{64}{429}(\eta - 1)^3 + \frac{192}{6851}(\eta - 1)^4 + o(\eta - 1)^4 \tag{1.45}$$

as $\eta \to 1$, where the constant $K > 0$ is not determined locally, showing that the lubrication approximation again fails near the contact line $\eta = 1$, and that

$$G \sim G_\infty + L\eta^{-\frac{2}{3}} \exp\left[-\frac{3}{8}\left(\frac{3}{G_\infty}\right)^{\frac{1}{3}} \eta^{\frac{4}{3}}\right] \cos\left[\frac{3\sqrt{3}}{8}\left(\frac{3}{G_\infty}\right)^{\frac{1}{3}} \eta^{\frac{4}{3}} + \psi\right] \tag{1.46}$$

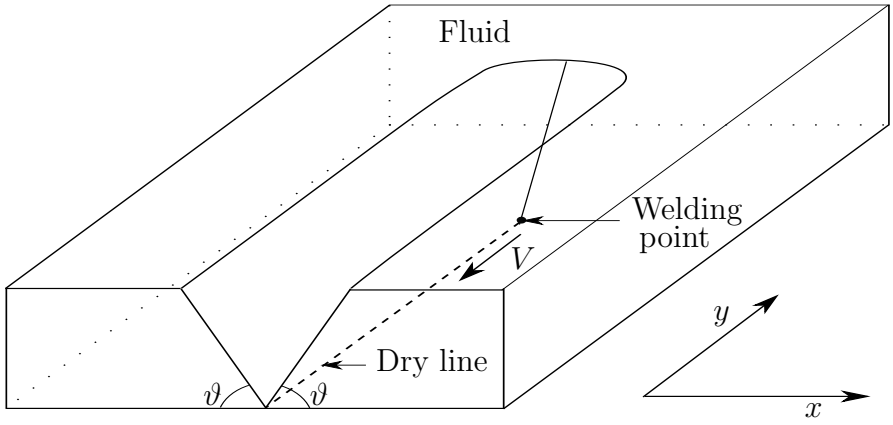

Figure 1.13: Sketch of Betelu and Diez's [14] problem. The welding point advances at velocity V.

as $\eta \to \infty$, where the constant L and the phase shift ψ are not determined locally, showing that G approaches G_∞ in an oscillatory manner. There is a one-parameter family of solutions (parameterised by ψ) for G for $G_\infty \geq G_{\infty c}$ (where $G_{\infty c} \simeq 2.4$). The solution predicts that the dry patch has a quartic shape and that the transverse profile of the free surface has an oscillatory shape with a characteristic "capillary ridge" near the contact line.

Betelu and Diez [14] examined the evolution of two contact lines of a fluid (with contact angle ϑ) that meet to form a dry line. This dry line is gradually "welded" at a point (a "welding point") that moves at constant velocity V along the contact line, so that eventually the dry line will vanish. A sketch of their problem is shown in Figure 1.13. They obtained a similarity solution that shows that the velocity in the region behind the advancing welding point is larger than that ahead of it, and that the slope behind the welding point is smaller than the contact angle of the fluid.

The shapes and stability of dry patches in a flowing film on a partially wetting inclined plane were studied both theoretically and experimentally by Podgorski et al. [81]. They observed the presence of a collar of the fluid at the apex of the dry patch, and derived a simple model to describe the flow which is similar to the model

proposed by Wilson [105]. Their model is based on a balance between surface-tension forces and the weight of the collar of fluid. Podgorski et al. [81] found that the dry patch becomes narrower with increasing flow rate and increasing inclination angle, and they determined the critical flow rate below which the dry patch will persist but above which it will be swept away. Their theoretical prediction is in satisfactory agreement with their own experimental results. A similar experiment was subsequently conducted by Podgorski et al. [83] for a flow with a larger contact angle. An improved model was studied by Sébilleau et al. [91] which includes contact line curvature, hydrostatic pressure in the fluid film and inertial effects. Their solution is in good agreement with experimental results of Podgorski et al. [81] and their own experimental results. Rio et al. [85] and Rio and Limat [86] studied the shape of a dry patch experimentally using a laser sheet. Rio and Limat [86] investigated the effect of increasing and decreasing the flow rate; in particular, they discovered that the contact angle distribution is uniform along the contact line for an increasing flow rate, whereas the situation is more complicated for a decreasing flow rate. They also obtained the minimum and maximum flow rates for the dry patch to persist. Some of their experimental results are shown in Figure 1.14, which shows that the dry patch becomes narrower as the flow rate increases and becomes wider as the flow rate decreases.

1.3.3 Other driving mechanisms

The works mentioned so far are mainly concerned with steady and unsteady flow of a thin film that is driven either by gravity, by shear-stress or by surface-tension effects. However, fluid flow can be driven by other forces such as Marangoni effects or other thermal effects. Here, we briefly discuss some examples of these types of flow which are relevant to the work presented in this thesis.

There are many studies of flow driven by gradients of surface tension induced by surface-temperature gradients (i.e. the well-known Marangoni effect). Surface-shear-driven flows of this type were considered by, for example, Fanton et al. [27],

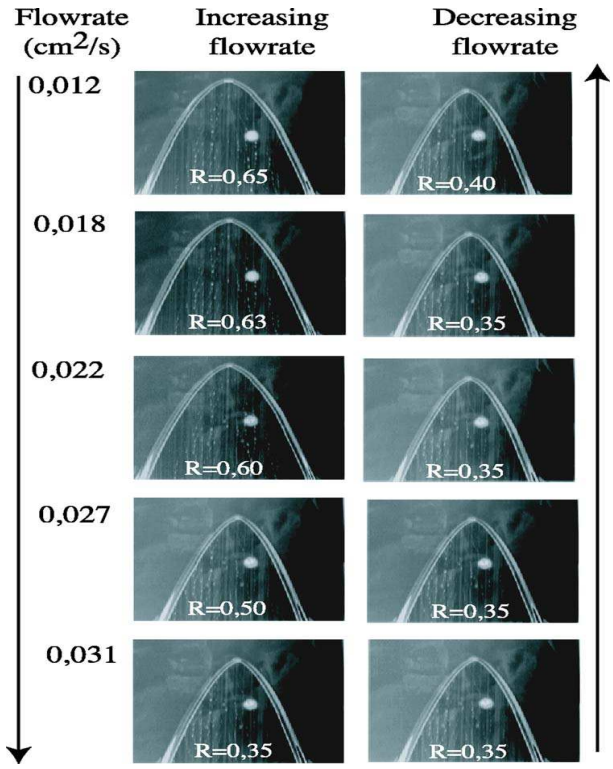

Figure 1.14: The evolution of the shape of dry patches with increasing and decreasing flow rate obtained experimentally by Rio and Limat [86]. R is the radius of the contact line curvature at the apex of a dry patch. Reprinted with permission from Rio and Limat [86]. Copyright 2006, American Institute of Physics.

who studied the climbing of a film on a vertical or tilted wall theoretically and experimentally, and predicted the thickness and shape of the film, and Schwartz [88], who obtained the thickness of a film of a fluid being withdrawn from a bath onto a vertical plane theoretically and found good agreement with the experimental results of Fanton et al. [27]. Recently, Gatapova and Kabov [29] considered effects of both air flow and a temperature gradient in their studies of flow in an inclined rectangular microchannel sheared by gas flow with a local heater at the bottom of the channel. As well as a surface temperature gradient, surfactants are known to lower the surface tension of a fluid, and this effect can induce gradients in surface tension in flow. Some studies of fluid with insoluble surfactant on an

inclined plane have been performed by Levy et al. [50], and recently by Manukian and Schecter [55].

Thin-film flows on an inclined plane that is either heated or cooled relative to the surrounding atmosphere have been considered by Holland et al. [39] for a rivulet flow, and by Holland et al. [38] for a flow around a dry patch. They obtained steady similarity solutions for a flow driven by thermocapillarity, gravity or a constant surface shear stress.

1.3.4 Sliding drop on an inclined plane

Similarity solutions have also been used successfully for describing the shape of a drop sliding down an inclined plane.

Podgorski et al. [82] showed that a drop running down a partially wetted inclined plane can develop various shapes, with the formation of a corner, or a cusp, or with smaller drops being shed (known as "pearling") with increasing velocity (by an increase in the inclination angle). The evolution of the drop shape from a rounded drop to the pearling drops with increasing velocity is shown in Figure 1.15. In their experiments Podgorski et al. [82] found that the transition between different shapes depends on the capillary number, $Ca = \mu U/\sigma$ (where U is the velocity of the drop), and is independent of the size of the drop. They also measured the angle between the contact line and the direction of motion at the trailing edge of the drop, θ (shown in Figure 1.16). Podgorski et al. [82] argued that in the corner region, the effective capillary number is $Ca \sin\theta$ and that the contact line adapts to keep the velocity in the direction of its normal constant; together these imply the scaling $\sin\theta \propto 1/Ca$.

Following on from Podgorski et al.'s [82] experiments, there have been several theoretical studies of similarity solutions for drops which are steady in a frame moving with the drop. Ben Amar et al. [10, 11] predicted the shape of the corner by assuming that it has a "saddle-point" structure, based on a balance of gravity and surface-tension forces. On the other hand, Stone et al. [97] obtained a simi-

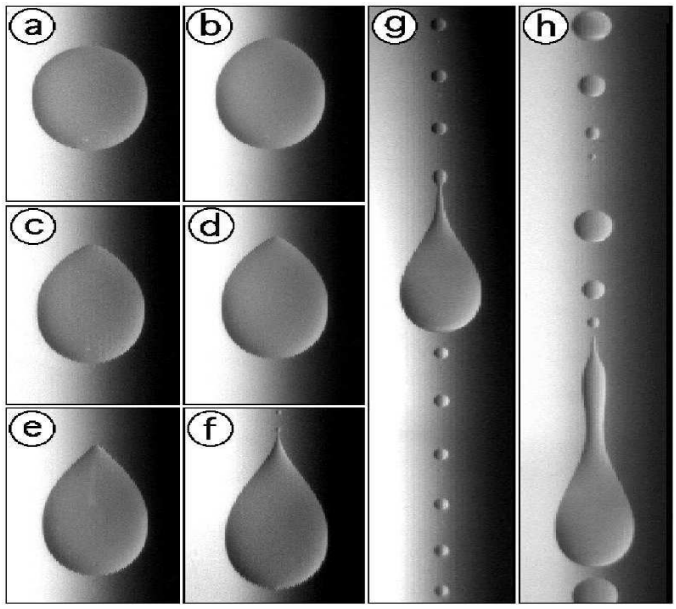

Figure 1.15: Transition of a sliding drop on an inclined plane with increasing velocity obtained experimentally by Podgorski et al. [82]: (a) and (b) rounded drop with circle and oval shape, respectively, (c)-(e) formation of a corner, (f) corner becomes sharper and forms a cusp which releases small drop, (g) pearling drop releasing smaller drops of constant size at a constant rate, and (h) pearling drop releasing periodic series of smaller drop. Reprinted with permission from Podgorski et al. [82], Phys. Rev. Lett., 87, 036102-2, 2001. Copyright 2001 by the American Physical Society.

larity solution to describe the shape of the corner based on a balance of viscous and surface-tension forces, in which case the corner has a conical structure. Subsequently a three-dimensional similarity solution of this problem was obtained by Limat and Stone [51]. Limat and Stone [51] also confirmed the scaling used by Podgorski et al. [82] (that the relevant capillary number is $Ca \sin\theta$ rather than Ca) and showed that the contact angle ω is nonzero at the threshold and is uniquely related to θ, which is different from the assumption of Podgorski et al. [82] that ω vanishes at the threshold. More detailed studies and further experiments on this problem have been performed by Le Grand et al. [49]. They presented results

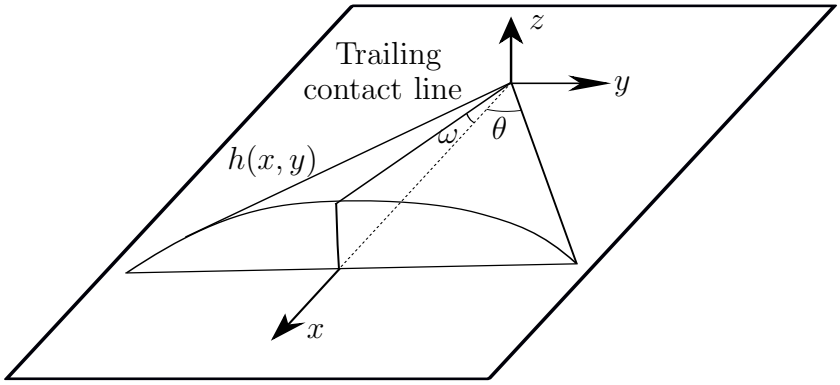

Figure 1.16: Geometry of the trailing edge of a sliding drop.

that are in agreement with those of Stone et al. [97] and Limat and Stone [51] in describing the structure of the corner, and other results that are in agreement with those of Ben Amar et al. [10] in the cusp regime. Snoeijer et al. [96] investigated the self-similar velocity fields that occur within the corner, and performed experiments using particle image velocimetry (PIV) measurements at the rear of sliding drops to verify the model. They also addressed the effect of contact line curvature at the corner. Subsequently, Snoeijer et al. [95] accounted for the formation of a slender rivulet from the sliding drop both theoretically and experimentally. They predicted the opening angle at the tip of the drop, the velocity of the drop and the width of the rivulet, all of which are in good agreement with their experimental results.

Schwartz et al. [90] obtained numerical solutions which predict the motion of a drop sliding on a perfectly homogeneous vertical wall using a finite-difference method. Their theory was based on a disjoining-pressure model that assumes that there is a thin precursor layer of fluid on the substrate. Their computed solutions capture the evolution of sliding drops and show similar shapes to those in the experiments of Podgorski et al. [82]. However, the computed drop breaks up into an almost chaotic pattern which is quite different from the carefully controlled experiment of Podgorski et al. [82] where the drop breaks up into a periodic pattern. Recently, Koh et al. [48] performed numerical studies to simulate the motion of

a sliding drop on an inclined plane using a multigrid method, and reported good agreement with the experiments of Podgorski et al. [82] and Le Grand et al. [49]. They also noted that both the thickness of the precursor layer and refinement of the numerical grid play important roles in the accuracy of the solutions.

1.4 Outline of Thesis

The aim of this thesis is to analyse unsteady three-dimensional flows of thin slender non-uniform rivulets and flows of thin films around slender dry patches on an inclined plane. We shall consider both gravity-driven and constant surface-shear-stress-driven flows of both Newtonian and non-Newtonian power-law fluids, and obtain two fundamentally different types of similarity solution.

In Chapter 2 we consider the unsteady flow of a gravity-driven rivulet of a Newtonian fluid on an inclined plane. We obtain a similarity solution of the appropriate governing equations which we analyse numerically and asymptotically in appropriate asymptotic limits.

In Chapter 3 we analyse the stability of the similarity solutions obtained in Chapter 2 numerically using the finite element package COMSOL Multiphysics. In order to validate our numerical procedures we seek to recover previously known similarity solutions obtained by Smith [92], Duffy and Moffatt [24], Smith [93] and Huppert [42]. By doing this, we also obtained new numerical results that verify Duffy and Moffatt's [24] similarity solutions.

In Chapter 4 we use the general approach of our work on rivulets of a Newtonian fluid in Chapter 2 to obtain similarity solutions describing unsteady gravity-driven draining of a rivulet of a non-Newtonian power-law fluid.

In Chapter 5 we extend our work of Chapter 2 and 4 to consider similarity solutions for unsteady shear-stress-driven flow. Both Newtonian and non-Newtonian power-law fluids are studied. Unlike the analysis of gravity-driven flow in Chapter 2 and Chapter 4 in which corresponding solutions for flow around dry patches

are found to be impossible, for shear-stress-driven flow, solutions corresponding to dry patches are obtained and analysed. We also present comparison between the solutions for shear-stress-driven rivulets and the solutions for gravity-driven rivulets obtained in Chapter 2 and Chapter 4.

In Chapter 6 we consider a completely different kind of similarity solution, namely travelling-wave solutions for flows around dry patches. Here, we consider both gravity-driven and shear-stress-driven flows of a Newtonian fluid draining on an inclined plane, obtaining similarity solutions for dry patches for both types of flow. However, it is found that there are no corresponding travelling-wave solutions for rivulets.

Finally, in Chapter 7 we summarize the key ideas and highlight the main findings of the thesis and include some suggestions for possible further work.

1.5 Presentations and Publications

Various aspects of the work discussed in Chapters 2 and 3 were presented at the British Applied Mathematics Colloquium in Manchester in 2008, the Edinburgh Mathematical Society Postgraduate Students' Meeting in Edzell, Scotland in 2008, the University of Strathclyde Research Day in 2008, the European Consortium for Mathematics in Industry (ECMI) Conference in London in 2008, the European Postgraduate Fluid Dynamics Conference in Keele in 2008, the 7th EUROMECH Fluid Mechanics Conference in Manchester in 2008, and the EUROMECH Colloquium 497 in Edinburgh in 2009. A short account of the work presented in Chapters 2 and 3 has been published in the Proceedings of European Consortium for Mathematics in Industry (ECMI) Conference 2008 (Yatim et al. [115]), and a full version has been accepted for publication in the Quarterly Journal of Mechanics and Applied Mathematics (Yatim et al. [113]).

The work in Chapter 4 and some of Chapter 5 was presented at the British Applied Mathematics Colloquium in Nottingham in 2009, the 22nd Scottish Fluid

Mechanics Meeting in Oban, Scotland in 2009, and the European Coating Symposium in Karlsruhe, Germany in 2009. The work presented in Chapter 4 has been published in the Journal of Non-Newtonian Fluid Mechanics (Yatim et al. [114]) and the work presented in Chapter 5 has been submitted to the Journal of Engineering Mathematics (Yatim et al. [112]).

Recently, the work in Chapter 6 has been presented at the British Applied Mathematics Colloquium in Edinburgh in 2010, the European Consortium for Mathematics in Industry (ECMI) Conference in Wuppertal, Germany in July 2010, and the 8th Euromech Fluid Mechanics Conference (EFMC8) in Bad Reichenhall, Germany in September 2010. A full account of the work in Chapter 6 is currently in preparation for submission.

Chapter 2

Unsteady Gravity-Driven Rivulets of a Newtonian Fluid

In this chapter we investigate unsteady three-dimensional gravity-driven flows of thin slender non-uniform rivulets of a Newtonian fluid on an inclined plane using the lubrication approximation.

2.1 Problem Formulation

Consider the unsteady flow of a thin rivulet of Newtonian fluid with constant density ρ, surface tension σ and viscosity μ driven by gravity g down a planar substrate inclined at an angle α ($0 < \alpha < \pi$) to the horizontal. When $0 < \alpha < \pi/2$ the fluid is on the upper side of the inclined plane (a sessile rivulet), and when $\pi/2 < \alpha < \pi$ it is on the lower side of the inclined plane (a pendent rivulet).

Cartesian coordinates $Oxyz$ with the x axis down the line of greatest slope and the z axis normal to the substrate are adopted, with the substrate at $z = 0$. We denote the free surface profile of the rivulet by $z = h(x, y, t)$, where t denotes time. We restrict our attention to flows that are symmetric about $y = 0$ (i.e. to solutions for which h is even in y) with (unknown) semi-width $a = a(x, t)$, so that $h = 0$ at the contact lines $y = \pm a$. The geometry of the problem is sketched in Figure 2.1.

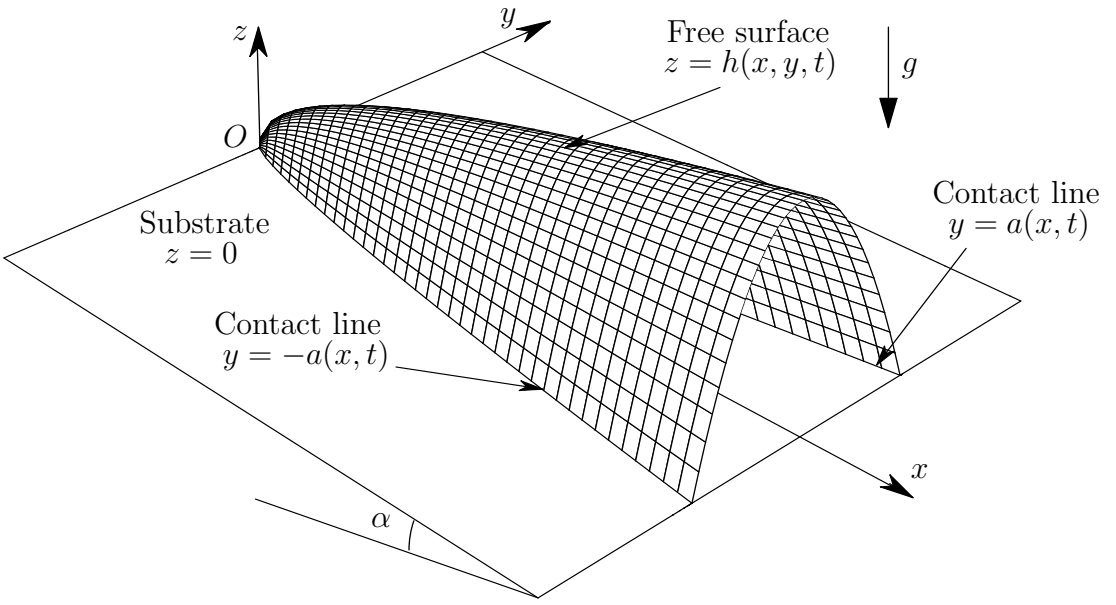

Figure 2.1: Sketch of the geometry of the problem.

With the familiar lubrication approximation, the velocity (u, v, w), pressure p and the height h satisfy the governing equations

$$u_x + v_y + w_z = 0, \tag{2.1}$$

$$\mu u_{zz} - p_x + \rho g \sin\alpha = 0, \tag{2.2}$$

$$\mu v_{zz} - p_y = 0, \tag{2.3}$$

$$-p_z - \rho g \cos\alpha = 0, \tag{2.4}$$

subject to the boundary conditions of no slip and no penetration on the substrate $z = 0$:

$$u = v = w = 0, \tag{2.5}$$

and balances of normal and tangential stress on the free surface $z = h$:

$$p = p_{\mathrm{a}} - \sigma\nabla^2 h, \quad u_z = v_z = 0, \tag{2.6}$$

where p_{a} denotes atmospheric pressure, together with the kinematic condition on $z = h$, which may be written in the form

$$h_t + \bar{u}_x + \bar{v}_y = 0, \tag{2.7}$$

where the local fluxes $\bar{u} = \bar{u}(x, y, t)$ and $\bar{v} = \bar{v}(x, y, t)$ are defined by

$$\bar{u} = \int_0^h u \, \mathrm{d}z, \quad \bar{v} = \int_0^h v \, \mathrm{d}z, \tag{2.8}$$

and the zero-mass-flux condition at the contact lines $y = \pm a(x, t)$:

$$\bar{v} = \pm a_x \bar{u}. \tag{2.9}$$

Integrating equations (2.2)–(2.4) subject to boundary conditions (2.5) and (2.6) yields

$$p = p_\mathrm{a} + \rho g \cos\alpha \, (h - z) - \sigma \nabla^2 h, \tag{2.10}$$

$$u = \frac{(\rho g \sin\alpha - p_x)}{2\mu} \, (2h - z) \, z, \tag{2.11}$$

$$v = -\frac{p_y}{2\mu} \, (2h - z) \, z. \tag{2.12}$$

Substituting (2.11) and (2.12) into (2.8) gives

$$\bar{u} = \frac{\rho g \sin\alpha - p_x}{3\mu} h^3, \quad \bar{v} = -\frac{p_y}{3\mu} h^3, \tag{2.13}$$

and hence the kinematic condition (2.7) yields the governing partial differential equation for h, namely

$$3\mu h_t = \nabla \cdot \left[h^3 \nabla \left(\rho g \cos\alpha h - \sigma \nabla^2 h \right) \right] - \rho g \sin\alpha \left[h^3 \right]_x . \tag{2.14}$$

We will consider the case in which the rivulet is slender, i.e. it varies much more slowly in the longitudinal (x) direction than in the transverse (y) direction; correspondingly, the term p_x in (2.2), (2.11) and (2.13) may be neglected in comparison with $\rho g \sin\alpha$ (see later in this section), and hence (2.14) simplifies to

$$3\mu h_t = \left[h^3 \left(\rho g \cos\alpha h - \sigma h_{yy} \right)_y \right]_y - \rho g \sin\alpha \left[h^3 \right]_x . \tag{2.15}$$

In general, it is not possible to obtain similarity solutions of equation (2.15) when all four terms appear simultaneously; however, just as Smith [92] and Duffy and Moffatt [24] found in their corresponding analyses of steady rivulet flow, it is possible to make progress in the cases when surface-tension effects are either much

weaker or much stronger than gravity effects in the transverse direction. In this thesis, we will consider the case of weak surface-tension effects only, in which case equation (2.15) becomes

$$3\mu h_t = \rho g \cos\alpha \left[h^3 h_y\right]_y - \rho g \sin\alpha \left[h^3\right]_x . \tag{2.16}$$

From (2.13) we have $\bar{u} = 0$ at $y = \pm a$, so the zero-mass-flux condition (2.9) at the contact lines reduces to $\bar{v} = 0$ at $y = \pm a$; thus we have the contact-line conditions

$$h = 0 \quad \text{at} \quad y = \pm a, \qquad h^3 h_y \to 0 \quad \text{as} \quad y \to \pm a. \tag{2.17}$$

We seek an unsteady similarity solution of equation (2.16) in the form

$$h = h_0 |x|^m |t|^n H(\eta), \qquad y = y_0 |x|^r |t|^s \eta, \tag{2.18}$$

where the exponents m, n, r and s, the positive (dimensional) constants h_0 and y_0, and the function $H = H(\eta)$ are to be determined. Here, H and η are defined to be dimensionless, and $H \geq 0$. With (2.18), the terms in (2.16) balance provided that

$$m = \frac{1}{2}, \qquad n = -\frac{1}{2}, \qquad r = \frac{3}{4}, \qquad s = -\frac{1}{4}, \tag{2.19}$$

and if we choose

$$h_0 = \left(\frac{\mu}{\rho g \sin\alpha}\right)^{\frac{1}{2}}, \qquad y_0 = \left(\frac{4\mu \cos^2\alpha}{9\rho g \sin^3\alpha}\right)^{\frac{1}{4}} \tag{2.20}$$

then the solution (2.18) takes the form

$$h = \left(\frac{\mu|x|}{\rho g \sin\alpha\, |t|}\right)^{\frac{1}{2}} H(\eta), \qquad y = \left(\frac{4\mu \cos^2\alpha\, |x|^3}{9\rho g \sin^3\alpha\, |t|}\right)^{\frac{1}{4}} \eta, \tag{2.21}$$

and (2.16) reduces to the second order ordinary differential equation

$$S_t \left[\frac{1}{2}\eta H' - H\right] = S_g \left[H^3 H'\right]' + S_x \left[\frac{1}{2}\eta \left(H^3\right)' - H^3\right] \tag{2.22}$$

for H, where a dash denotes differentiation with respect to η, and we have introduced the notation $S_t = \text{sgn}(t) = \pm 1$, $S_g = \text{sgn}(\cos\alpha) = \pm 1$ and $S_x = \text{sgn}(x) =$

± 1. The cases $S_t = 1$ and $S_t = -1$ correspond to time running from 0 to ∞ and from $-\infty$ to 0, respectively; also $S_g = 1$ and $S_g = -1$ correspond to the sessile and pendent cases, respectively, and $S_x = 1$ and $S_x = -1$ correspond to the fluid being in $x > 0$ and $x < 0$, respectively.

For a symmetric rivulet, regular at $y = 0$, appropriate boundary conditions are

$$H = H_0, \quad H' = 0 \qquad \text{at} \qquad \eta = 0, \tag{2.23}$$

where the parameter $H_0 \geq 0$ is to be determined. The (unknown) position where $H = 0$ is denoted $\eta = \eta_0$ (corresponding to the contact-line position $y = a$), so that from (2.17)

$$H = 0 \quad \text{at} \quad \eta = \eta_0, \qquad H^3 H' \to 0 \quad \text{as} \quad \eta \to \eta_0. \tag{2.24}$$

The middle height of the rivulet, $h_{\mathrm{m}} = h(x, 0, t)$, and the semi-width of the rivulet vary with x and t according to

$$h_{\mathrm{m}} = \left(\frac{\mu |x|}{\rho g \sin\alpha \, |t|} \right)^{\frac{1}{2}} H_0, \qquad a = \left(\frac{4\mu \cos^2\alpha \, |x|^3}{9\rho g \sin^3\alpha \, |t|} \right)^{\frac{1}{4}} \eta_0, \tag{2.25}$$

predicting that at any time t the rivulet widens or narrows according to $|x|^{3/4}$ and thickens or thins according to $|x|^{1/2}$, and that at any station x it widens or narrows according to $|t|^{-1/4}$ and thickens or thins according to $|t|^{-1/2}$. Also (2.25) shows that the rivulet has a nose (at which $h = 0$ and $a = 0$) that remains stationary at O for all t.

The cross-sectional area of the rivulet (2.21) at any station x, denoted by A, is given by

$$A = 2 \int_0^a h \, \mathrm{d}y = \left(\frac{4\mu^3 \cos^2\alpha \, |x|^5}{9\rho^3 g^3 \sin^5\alpha \, |t|^3} \right)^{\frac{1}{4}} I_1, \tag{2.26}$$

and the volume flux of fluid draining in the longitudinal direction, denoted by Q, is given by

$$Q = 2 \int_0^a \bar{u} \, \mathrm{d}y = \frac{2\rho g \sin\alpha}{3\mu} \int_0^a h^3 \, \mathrm{d}y = \frac{1}{3} \left(\frac{4\mu^3 \cos^2\alpha \, |x|^9}{9\rho^3 g^3 \sin^5\alpha \, |t|^7} \right)^{\frac{1}{4}} I_3, \tag{2.27}$$

where the I_n are constants defined by

$$I_n = 2\int_0^{\eta_0} H^n \,\mathrm{d}\eta. \tag{2.28}$$

Conditions for the rivulet to be thin and slender are that the length scales in the x, y and z directions (namely $|x|$, a and h_m, respectively) satisfy $h_\mathrm{m} \ll a \ll |x|$, which in turn requires that

$$\frac{|xt|\rho g\cos^2\alpha}{\mu\sin\alpha} \gg 1, \quad \frac{|xt|\rho g\sin^3\alpha}{\mu\cos^2\alpha} \gg 1, \tag{2.29}$$

showing that $|xt|$ must be sufficiently large (and that α cannot be close to 0, $\pi/2$ or π). In addition, conditions for the neglect of the down-slope pressure gradient p_x and of surface-tension effects are

$$|h_x| \ll 1, \quad \frac{\rho g x^2}{\sigma} \gg 1, \tag{2.30}$$

respectively. In principle, all these restrictions are achieved at sufficiently large length scales in the x direction.

Note that the solution for h for a three-dimensional rivulet given by (2.21) has the same x and t dependence as Huppert's [41] similarity solution representing unsteady two-dimensional (y-independent) flow of a thin viscous film down an inclined plane, in which h also varies according to $x^{1/2}$ and $t^{-1/2}$.

We non-dimensionalise according to

$$\begin{gathered} x = Xx^*, \qquad y = \left(\frac{4\mu\cos^2\alpha\,X^3}{9\rho g\sin^3\alpha\,T}\right)^{\frac{1}{4}} y^*, \qquad z = \left(\frac{\mu X}{\rho g\sin\alpha\,T}\right)^{\frac{1}{2}} z^*, \qquad t = Tt^*, \\ h = \left(\frac{\mu X}{\rho g\sin\alpha\,T}\right)^{\frac{1}{2}} h^*, \qquad h_\mathrm{m} = \left(\frac{\mu X}{\rho g\sin\alpha\,T}\right)^{\frac{1}{2}} h_\mathrm{m}^*, \qquad a = \left(\frac{4\mu\cos^2\alpha\,X^3}{9\rho g\sin^3\alpha\,T}\right)^{\frac{1}{4}} a^*, \\ Q = \frac{1}{3}\left(\frac{4\mu^3\cos^2\alpha\,X^9}{9\rho^3 g^3\sin^5\alpha\,T^7}\right)^{\frac{1}{4}} Q^*, \qquad A = \left(\frac{4\mu^3\cos^2\alpha\,X^5}{9\rho^3 g^3\sin^5\alpha\,T^3}\right)^{\frac{1}{4}} A^*, \end{gathered} \tag{2.31}$$

where X (>0) and T (>0) are length and time scales, respectively, which we may choose arbitrarily. For convenience we immediately drop the superscript stars on non-dimensional quantities. Then the solution (2.21) takes the simpler form

$$h = \left|\frac{x}{t}\right|^{\frac{1}{2}} H, \qquad y = \left|\frac{x^3}{t}\right|^{\frac{1}{4}} \eta, \tag{2.32}$$

with H satisfying (2.22)–(2.24); from (2.25) the middle height h_{m} and semi-width a are given by

$$h_{\mathrm{m}} = \left|\frac{x}{t}\right|^{\frac{1}{2}} H_0, \qquad a = \left|\frac{x^3}{t}\right|^{\frac{1}{4}} \eta_0, \tag{2.33}$$

and from (2.26) and (2.27) the cross-sectional area A and flux Q are given by

$$A = \left|\frac{x^5}{t^3}\right|^{\frac{1}{4}} I_1, \qquad Q = \left|\frac{x^9}{t^7}\right|^{\frac{1}{4}} I_3. \tag{2.34}$$

2.2 General Results

A closed-form solution of the ordinary differential equation (2.22) is not available, and so it must, in general, be solved numerically for H subject to the boundary conditions (2.23) and (2.24), where H_0 and η_0 are parameters to be determined.

As far as the differential equation (2.22) is concerned, any choice of a set of values of S_t, S_g and S_x leads to the same *mathematical* problem as the set $-S_t$, $-S_g$ and $-S_x$ (though the two sets of values lead to very different *physical* interpretations of the solutions, as we shall show). Therefore, there are four distinct cases to consider, namely Case 1, where $S_t = S_g = S_x$ (corresponding to either a sessile rivulet in $x > 0$ with $t > 0$, or a pendent rivulet in $x < 0$ with $t < 0$), Case 2, where $S_t = -S_g = S_x$ (corresponding to either a pendent rivulet in $x > 0$ with $t > 0$, or a sessile rivulet in $x < 0$ with $t < 0$), Case 3, where $S_t = S_g = -S_x$ (corresponding to either a sessile rivulet in $x < 0$ with $t > 0$, or a pendent rivulet in $x > 0$ with $t < 0$), and Case 4, where $S_t = -S_g = -S_x$ (corresponding to either pendent rivulet in $x < 0$ with $t > 0$, or a sessile rivulet in $x > 0$ with $t < 0$). In fact, as we shall show, of these four cases, only Case 2 leads to physically realisable rivulet solutions.

2.2.1 Behaviour near $\eta_0 = 0$

We find straightforwardly that H satisfies

$$H = H_0 + \frac{S_x H_0^2 - S_t}{2 S_g H_0^2} \eta^2 + O\left(\eta^4\right) \tag{2.35}$$

as $\eta \to 0$.

2.2.2 Behaviour near $\eta = \eta_0$

Near the contact line $\eta = \eta_0$, we find that H satisfies either

$$H \sim \left[-\frac{3S_t}{2S_g} \eta_0 \left(\eta_0 - \eta \right) \right]^{\frac{1}{3}}, \tag{2.36}$$

valid only when $S_t = -S_g$ (i.e. in Case 2 and Case 4), or

$$H \sim C \left(\eta_0 - \eta \right)^{\frac{1}{4}} - \frac{2S_t \eta_0}{5S_g C^2} \left(\eta_0 - \eta \right)^{\frac{1}{2}}, \tag{2.37}$$

where C is a positive constant. Note that both (2.36) and (2.37) have $H' \to \infty$ as $\eta \to \eta_0$, showing that the lubrication approximation always fails near the contact lines.

The zero-mass-flux condition in (2.24) requires that $C = 0$. Therefore Cases 1 and 3, in which (2.37) is the only possible behaviour near the contact line, are immediately eliminated, and so are not discussed subsequently. Determining C, and, in particular, determining the physical solutions from the condition $C = 0$, will be considered later; with this in mind it is useful to note here that integration of equation (2.22) from $\eta = 0$ to $\eta = \eta_0$ leads to

$$6 \int_0^{\eta_0} \left(S_t H - S_x H^3 \right) d\eta = \begin{cases} 0 & \text{for (2.36)}, \\ S_g C^4 & \text{for (2.37)}, \end{cases} \tag{2.38}$$

so that C in (2.37) satisfies

$$C = \left[6 S_g \int_0^{\eta_0} \left(S_t H - S_x H^3 \right) \, \mathrm{d}\eta \right]^{\frac{1}{4}} = \left[3 S_g \left(S_t I_1 - S_x I_3 \right) \right]^{\frac{1}{4}}. \tag{2.39}$$

2.2.3 Stationary points of H

From equation (2.22), at any stationary point of the free surface (where $H' = 0$), we have

$$H^2 H'' = S_g \left(H^2 S_x - S_t \right), \tag{2.40}$$

provided that $H \neq 0$. Since there are two contact lines $\eta = \pm\eta_0$, at which $H = 0$, the function H (≥ 0) must have at least one maximum in $|\eta| \leq \eta_0$.

In Case 2 ($S_t = -S_g = S_x$) equation (2.40) gives

$$H'' = \frac{1 - H^2}{H^2}, \tag{2.41}$$

so that any stationary point for which $H < 1$ is a minimum, and any stationary point for which $H > 1$ is a maximum. In principle, it is possible for H to have $2n - 1$ minima and $2n$ maxima when $H_0 < 1$, and $2n - 2$ minima and $2n - 1$ maxima when $H_0 > 1$ (where $n = 1, 2, 3, \ldots$). However, numerically it was found that only two types of solution occur (both with $n = 1$), namely a solution with one minimum at $\eta = 0$ and two symmetrically placed maxima when $H_0 < 1$ ("double-humped" profiles), and one with a single maximum at $\eta = 0$ when $H_0 > 1$ ("single-humped" profiles), both of which are consistent with equation (2.35).

In Case 4 ($S_t = -S_g = -S_x$) equation (2.40) gives

$$H'' = \frac{H^2 + 1}{H^2} > 0, \tag{2.42}$$

showing that any stationary point of H is a minimum; thus there is no solution H with a maximum, and so Case 4 is immediately eliminated.

With Cases 1, 3 and 4 now eliminated, the only case that could possibly lead to physically relevant solutions for H is Case 2, and so it is this case that we now discuss in detail.

2.3 Case 2: $S_t = -S_g = S_x$

In this case, equation (2.22) becomes

$$\frac{1}{2}\eta H' - H = -\left(H^3 H'\right)' + \frac{1}{2}\eta\left(H^3\right)' - H^3, \tag{2.43}$$

which was solved numerically for H subject to (2.23) for a given value of H_0 by means of a shooting technique, the value of η_0 being determined as the point where $H = 0$. As a check, some of the computations were also performed by means of a finite-difference method, with Newton iteration to solve the resulting nonlinear

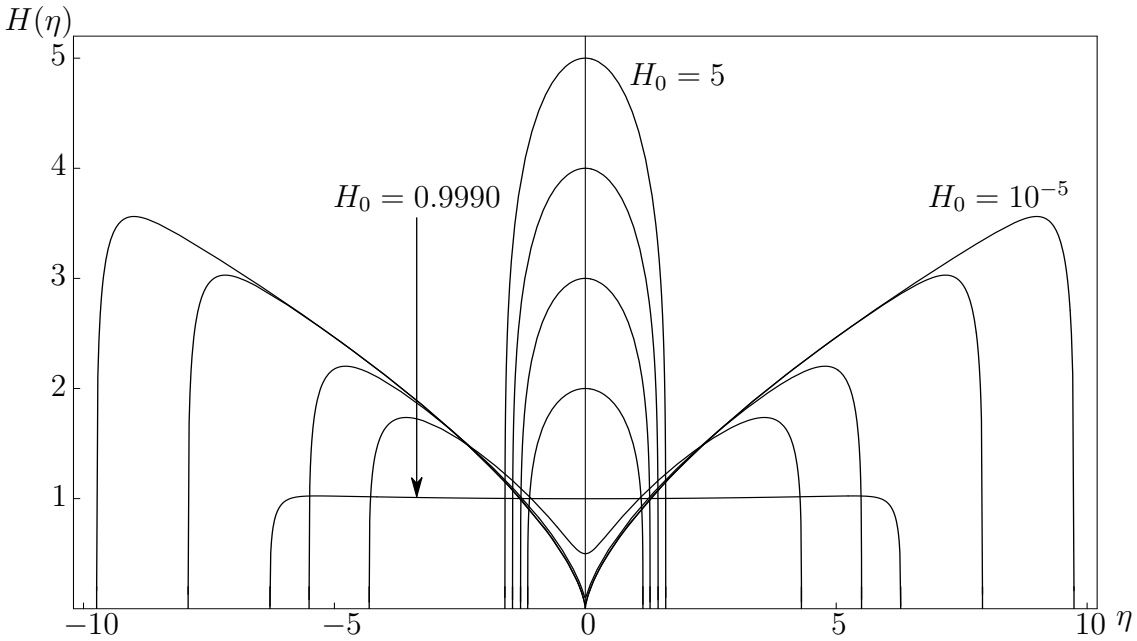

Figure 2.2: Numerically calculated profiles $H = H(\eta)$ for $H_0 = 10^{-5}$, 10^{-3}, 10^{-1}, 0.5, 0.9990, 2, 3, 4 and 5.

algebraic equations; the solutions obtained in this way were found to be in good agreement with those obtained by the shooting method. It was found that there is a solution for all $H_0 > 0$ except in a small "window" near $H_0 = 1$; specifically, no solutions were found in the interval $H_{01} < H_0 < H_{02}$, where H_{01} and H_{02} were determined numerically to be $H_{01} \simeq 0.9995$ and $H_{02} \simeq 1.1059$. (Here and subsequently, quantities obtained numerically are given to four decimal places, in general.) The forms of the behaviour of H as $H_0 \to 0^+$ and as $H_0 \to \infty$ were obtained by asymptotic analysis which will be described subsequently.

Figure 2.2 shows profiles H for a range of values of H_0. Consistent with the discussion in section 2.2.3, it was found that in the case $H_0 \geq H_{02}$ (> 1) the profiles are single-humped, whereas in the case $H_0 \leq H_{01}$ (< 1) they are double-humped (albeit for H_0 near H_{01} the curvature of the free surface near the middle of the rivulet is small, and so the humps are rather flat, as shown in Figure 2.2 in the case $H_0 = 0.9990$).

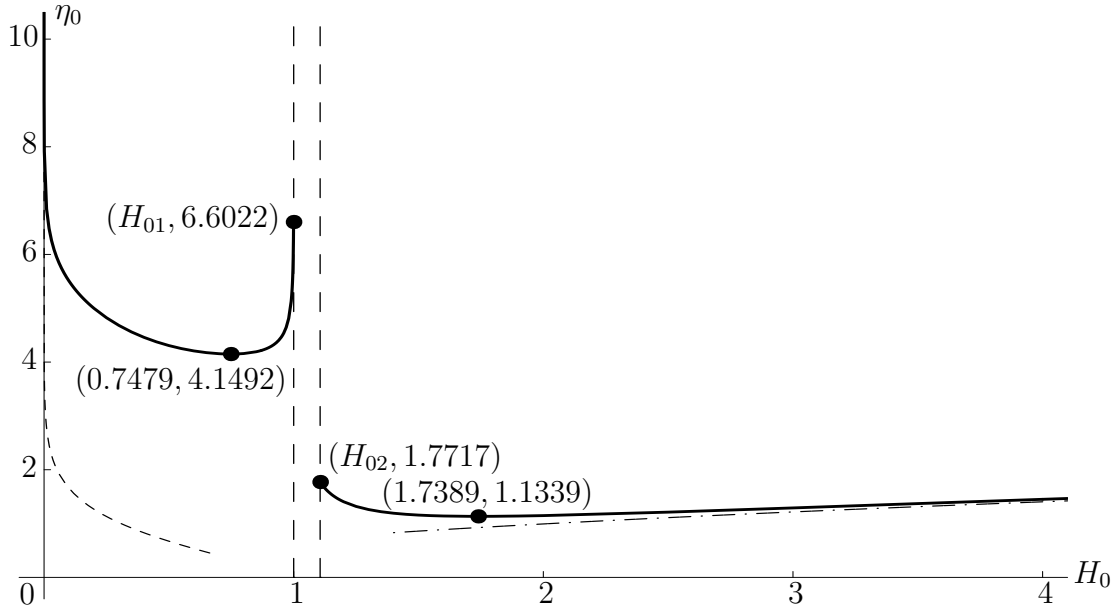

Figure 2.3: Plot of η_0 as a function of H_0 (full curve), together with the leading order asymptotic solution solutions in the limit $H_0 \to 0^+$ (dashed curve) and in the limit $H_0 \to \infty$ (dashed-dotted curve); here $H_{01} \simeq 0.9995$ and $H_{02} \simeq 1.1059$.

Figure 2.3 shows η_0 as a function of H_0 calculated numerically from (2.43) and (2.23), and clearly illustrates that there is a solution for all $H_0 > 0$ except in the narrow window $H_{01} < H_0 < H_{02}$, in which there is no solution. Clearly, the relation between H_0 and η_0 is not monotonic. For any given value of H_0 outside the interval $H_{01} < H_0 < H_{02}$, there is a corresponding unique value of η_0. However, for any given value of η_0 there can be zero, one, two or three solutions, depending on the value of η_0. Specifically, for $0 < H_0 < H_{01}$ there is no solution for $\eta_0 < 4.1492$, one solution for $\eta_0 = 4.1492$ as well as for $\eta_0 > 6.6022$, and two for $4.1492 < \eta_0 \leq 6.6022$, whereas for $H_0 > H_{02}$ there is no solution for $\eta_0 < 1.1339$, one for $\eta_0 = 1.1339$ as well as for $\eta_0 > 1.7717$, and two for $1.1339 < \eta_0 \leq 1.7717$.

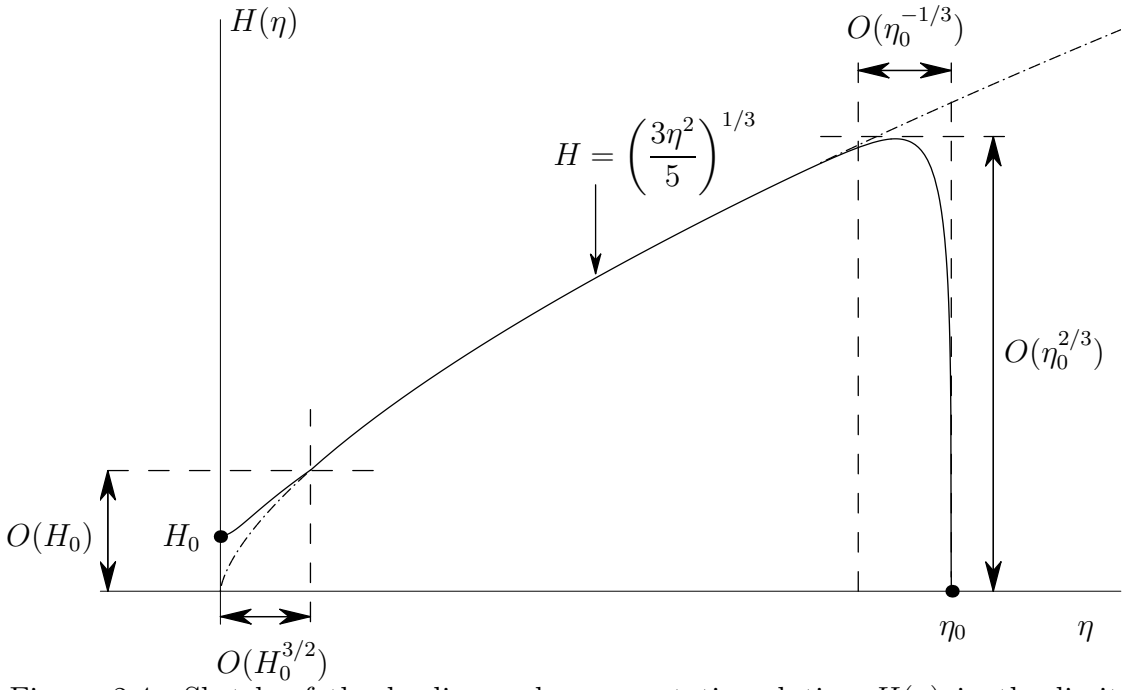

Figure 2.4: Sketch of the leading order asymptotic solution $H(\eta)$ in the limit $H_0 \to 0^+$, showing the outer solution $H = (3\eta^2/5)^{1/3}$ and the inner solutions near $\eta = 0$ and $\eta = \eta_0 \to \infty$. The dashed-dotted curve shows the outer solution drawn from $\eta = 0$ to $\eta > \eta_0$.

2.3.1 Behaviour in the limit $H_0 \to 0^+$

In this subsection we analyse the asymptotic behaviour of the solution H of equation (2.43) subject to (2.23) and (2.24) in the singular limit $H_0 \to 0^+$.

As sketched in Figure 2.4, the solution comprises an outer solution valid away from $\eta = 0$ and $\eta = \eta_0$, a boundary layer of width $O(H_0^{3/2})$ near $\eta = 0$ in which $H = O(H_0)$, and a boundary layer near the contact line $\eta = \eta_0$ of width $O(\eta_0^{-1/3})$ in which $H = O(\eta_0^{2/3})$, with $\eta_0 \to \infty$ as $H_0 \to 0^+$.

The leading order outer solution is $H = (3\eta^2/5)^{1/3}$. In fact, this form of H is a solution to the unapproximated differential equation (2.43), but it does not satisfy the boundary conditions (2.23) and (2.24).

In the boundary layer near $\eta = 0$ we scale variables according to

$$H = H_0 \hat{H}(\hat{\eta}), \quad \eta = H_0^{\frac{3}{2}} \hat{\eta}, \tag{2.44}$$

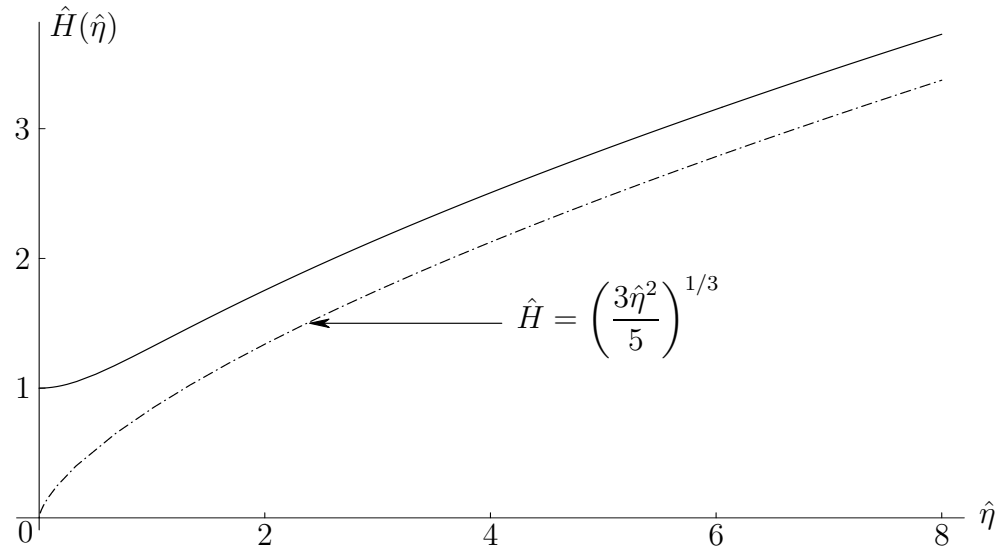

Figure 2.5: Plot of the leading order inner solution near $\eta = 0$ (full curve) and the leading order outer solution (dashed-dotted curve) in the limit $H_0 \to 0^+$.

and so in this region equation (2.43) gives

$$\frac{1}{2}\hat{\eta}\hat{H}' - \hat{H} + \left(\hat{H}^3\hat{H}'\right)' = 0 \tag{2.45}$$

at leading order, which is readily solved numerically subject to the boundary conditions

$$\hat{H}(0) = 1, \qquad \hat{H}'(0) = 0. \tag{2.46}$$

Figure 2.5 shows a plot of the leading order inner solution near $\eta = 0$, together with the inner limit of the (rescaled) leading order outer solution $\hat{H} = (3\hat{\eta}^2/5)^{1/3}$ (represented by a dashed-dotted curve) as $\hat{\eta} \to \infty$.

In the boundary layer near $\eta = \eta_0$ we scale variables according to

$$H = \left(\frac{3\eta_0^2}{5}\right)^{\frac{1}{3}} \tilde{H}(\tilde{\eta}), \qquad \eta = \eta_0 - \eta_0^{-\frac{1}{3}}\tilde{\eta}, \tag{2.47}$$

and so in this region equation (2.43) gives

$$6\left(\tilde{H}^3\tilde{H}'\right)' + 45^{\frac{1}{3}}\left(\tilde{H}^3\right)' = 0 \tag{2.48}$$

at leading order, which may be solved subject to $\tilde{H}(0) = 0$ and $\tilde{H} \to 1$ as $\tilde{\eta} \to \infty$,

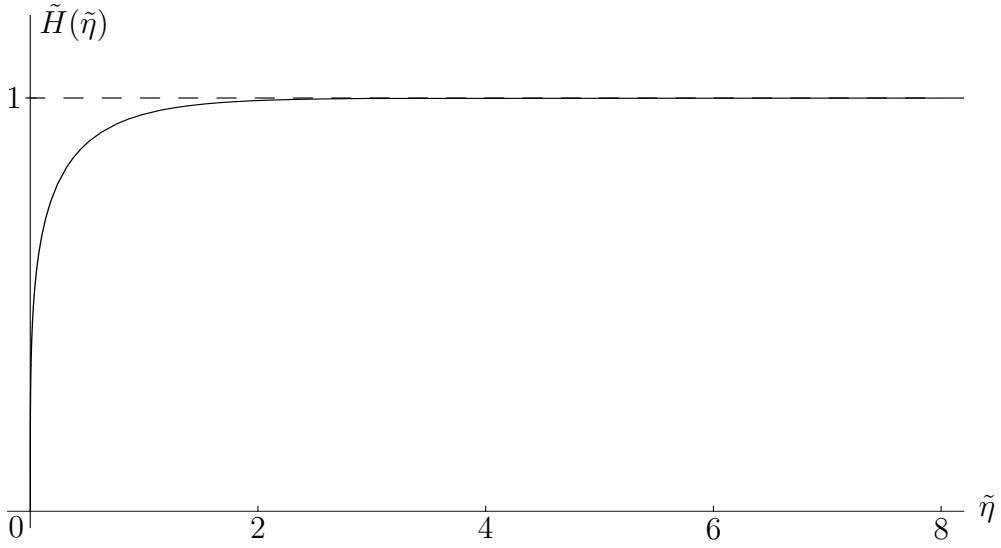

Figure 2.6: Plot of the leading order inner solution near $\eta = \eta_0$ (full curve) approaching a constant value of 1 (dashed line) in the limit $H_0 \to 0^+$.

yielding the implicit solution

$$-\tilde{H} + \frac{1}{6}\log\frac{1+\tilde{H}+\tilde{H}^2}{(1-\tilde{H})^2} + \frac{1}{\sqrt{3}}\tan^{-1}\left(\frac{\sqrt{3}\tilde{H}}{\tilde{H}+2}\right) = \frac{1}{2}\left(\frac{5}{3}\right)^{\frac{1}{3}}\tilde{\eta}. \tag{2.49}$$

Figure 2.6 is a plot of this leading order inner solution near $\eta = \eta_0$, which clearly shows that $\tilde{H}$ is a monotonically increasing function of $\tilde{\eta}$.

To complete the solution we must determine η_0, and to do this we must consider the first order outer solution, and so we write

$$H = \left(\frac{3\eta^2}{5}\right)^{\frac{1}{3}} + h, \tag{2.50}$$

where $h \ll (3\eta^2/5)^{1/3}$, and hence h satisfies

$$6\eta^2 h'' + 29\eta h' + 2h - 45^{\frac{1}{3}}\eta^{\frac{4}{3}}(3\eta h' - 2h) = 0. \tag{2.51}$$

In particular, the inner limit as $\eta \to 0$ of the outer solution (2.50) takes the from

$$\hat{H} = \left(\frac{3\hat{\eta}^2}{5}\right)^{\frac{1}{3}} + \hat{h}(\hat{\eta}), \tag{2.52}$$

with $\hat{h}$ satisfying

$$6\hat{\eta}^2\hat{h}'' + 29\hat{\eta}\hat{h}' + 2\hat{h} = 0, \tag{2.53}$$

which may be solved exactly to give

$$\hat{h} = \hat{A}\hat{\eta}^{m_1} + \hat{B}\hat{\eta}^{m_2}, \tag{2.54}$$

where $\hat{A}$ and $\hat{B}$ are (unknown) constants, and the exponents m_1 and m_2 are given by

$$m_1 = \frac{-23 + \sqrt{481}}{12} \simeq -0.0890, \qquad m_2 = \frac{-23 - \sqrt{481}}{12} \simeq -3.7443. \tag{2.55}$$

As $\hat{\eta} \to \infty$ we thus have

$$h \sim H_0 \hat{A} \left(\frac{\eta}{H_0^{3/2}} \right)^{m_1} = \hat{A} H_0^{m^*} \eta^{m_1}, \tag{2.56}$$

where $m^* = 1 - 3m_1/2 \simeq 1.1335$, and the constant $\hat{A}$ is determined numerically by solving the inner equation (2.45) for $\hat{H}$ subject to (2.46), and evaluating

$$\hat{A} = \lim_{\hat{\eta} \to \infty} \frac{1}{\hat{\eta}^{m_1}} \left(\hat{H}(\hat{\eta}) - \left(\frac{3\hat{\eta}^2}{5} \right)^{1/3} \right) \simeq 0.4212. \tag{2.57}$$

Motivated by (2.56) we write the solution h of (2.51) as

$$h = A(\eta) H_0^{m^*} \eta^{m_1} \tag{2.58}$$

with $A(\eta) \to \hat{A}$ as $\eta \to 0$; hence $A = A(\eta)$ satisfies

$$6\eta^2 A'' + (12m_1 + 29)\eta A' - 45^{\frac{1}{3}} \eta^{\frac{4}{3}} (3\eta A' - 2m^* A) = 0, \tag{2.59}$$

and we seek a solution as a function of $X = D\eta^{4/3}$, for some constant D. With the choice $D = (3^5 5)^{1/3}/8 \simeq 1.3338$, equation (2.59) reduces to

$$XA'' + (b - X) A' - aA = 0, \tag{2.60}$$

where

$$a = -\frac{m^*}{2} \simeq -0.5668, \qquad b = \frac{12m_1 + 31}{8} \simeq 3.7415. \tag{2.61}$$

The general solution of (2.60) is

$$A = A_1 M(a, b, X) + A_2 U(a, b, X), \tag{2.62}$$

where A_1 and A_2 are arbitrary constants, and $M(a,b,X)$ and $U(a,b,X)$ are Kummer functions (Abramowitz and Stegun [3]), and so the general solution of (2.51) is

$$h = \left[A_1 M(a,b,X) + A_2 U(a,b,X)\right] H_0^{m^*} \eta^{m_1}. \tag{2.63}$$

We can obtain the values of A_1 and A_2 by matching the outer limit of the inner solution, given in (2.56), with the inner limit of the outer solution (2.63) as $\eta \to 0^+$ (i.e. as $X \to 0^+$), in which $M \to 1$ and $U \to -\infty$, leading to $A_1 = \hat{A}$ and $A_2 = 0$, and therefore

$$h = \hat{A} M\left(a,b,D\eta^{\frac{4}{3}}\right) H_0^{m^*} \eta^{m_1}. \tag{2.64}$$

This outer solution breaks down near $\eta = \eta_0$, since $h \to \infty$ there, and so at leading order the value of η_0 is given by setting H to zero at $\eta = \eta_0$ in (2.50), that is,

$$\left(\frac{3\eta_0^2}{5}\right)^{\frac{1}{3}} + \hat{A} M\left(a,b,D\eta_0^{\frac{4}{3}}\right) H_0^{m^*} \eta_0^{m_1} = 0. \tag{2.65}$$

Since

$$M(a,b,X) = \frac{\Gamma(b)}{\Gamma(a)} e^X X^{a-b}\left[1 + O\left(\frac{1}{X}\right)\right] \tag{2.66}$$

as $X \to \infty$, at leading order equation (2.65) yields

$$\left(\frac{3\eta_0^2}{5}\right)^{\frac{1}{3}} + \frac{\hat{A}\Gamma(b)}{\Gamma(a)} e^X X^{a-b} H_0^{m^*} \eta_0^{m_1} = 0. \tag{2.67}$$

Recalling that $X = D\eta^{4/3}$ we write $X_0 = D\eta_0^{4/3}$ to obtain

$$X_0^{-\frac{39}{8}} e^{X_0} - Y = 0, \tag{2.68}$$

where

$$Y = -\left(\frac{3}{5}\right)^{\frac{1}{3}} \frac{\Gamma(a) D^a}{\Gamma(b)\hat{A} H_0^{m^*}} \quad (>0). \tag{2.69}$$

Equation (2.68) may be solved to give

$$X_0 = -\frac{39}{8} \mathrm{W}\left(-\frac{8}{39 Y^{\frac{8}{39}}}\right), \tag{2.70}$$

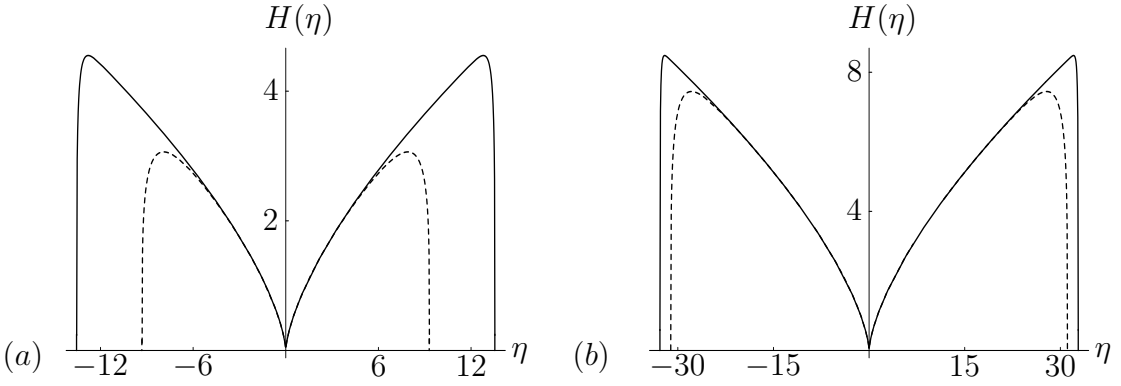

Figure 2.7: Profiles of H obtained numerically (full curves) and from the leading order asymptotic solution in the limit $H_0 \to 0^+$ (dashed curves) for (a) $H_0 = 10^{-10}$ and (b) $H_0 = 10^{-50}$.

where W is Lambert's W function (Abramowitz and Stegun [3]). Then in the limit $H_0 \to 0^+$ (i.e. $Y \to \infty$), with $\mathrm{W}(z) \sim \log(-z) \to -\infty$ as $z \to 0^-$, we obtain

$$X_0 = D\eta_0^{\frac{4}{3}} \sim \frac{39}{8} \log\left(\frac{39Y^{\frac{8}{39}}}{8}\right), \tag{2.71}$$

so that the leading order asymptotic solution for η_0 is given by

$$\begin{aligned} \eta_0 \sim \left(-\frac{m^*}{D}\log H_0\right)^{\frac{3}{4}} &= \left(-\frac{\left(31-\sqrt{481}\right)}{(3^5 5)^{\frac{1}{3}}}\log H_0\right)^{\frac{3}{4}} \\ &\simeq (-K\log H_0)^{\frac{3}{4}} \to \infty \quad \text{as} \quad H_0 \to 0^+, \end{aligned} \tag{2.72}$$

where $K = (31-\sqrt{481})(3^5 5)^{-1/3} \simeq 0.8498$.

Figure 2.7 shows a comparison between profiles H computed numerically and the leading order asymptotic solution as $H_0 \to 0^+$ in the cases $H_0 = 10^{-10}$ and $H_0 = 10^{-50}$, demonstrating that, because η_0 in (2.72) grows only extremely slowly as $H_0 \to 0^+$, extremely small values of H_0 are needed for the leading order asymptotic solution to be in reasonable agreement with the exact numerical result. Figure 2.3 also includes the leading order asymptotic solution as $H_0 \to 0^+$ as a dashed curve; again the agreement is good only for extremely small values of H_0.

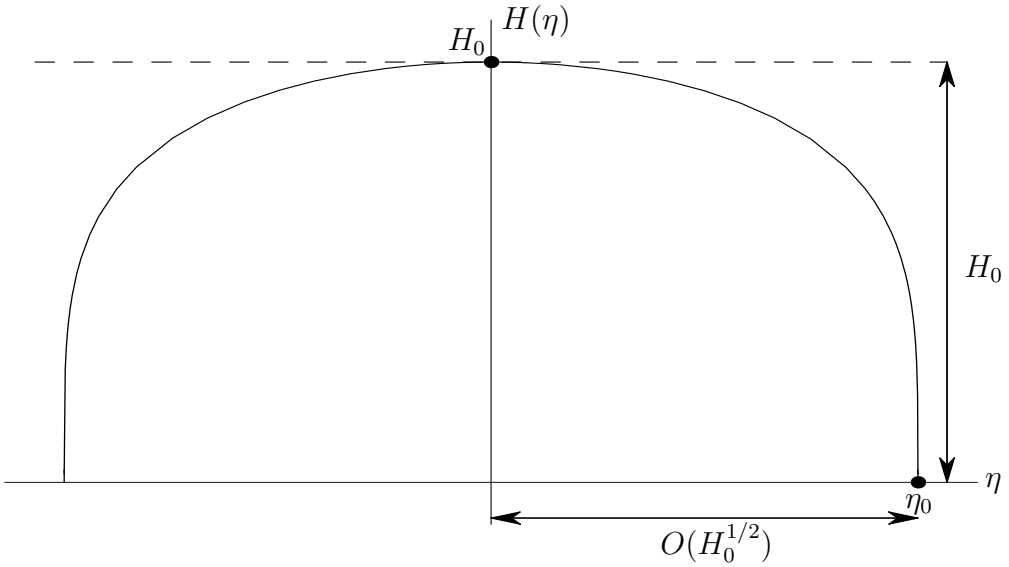

Figure 2.8: Sketch of the leading order asymptotic solution $H(\eta)$ in the limit $H_0 \to \infty$.

2.3.2 Behaviour in the limit $H_0 \to \infty$

In the limit $H_0 \to \infty$, it is found that $H = O(H_0)$ and $\eta_0 = O(H_0^{1/2})$, and so we write

$$H = H_0 \bar{H}(\bar{\eta}), \qquad \eta = H_0^{\frac{1}{2}} \bar{\eta}, \qquad \eta_0 = H_0^{\frac{1}{2}} \bar{\eta}_0. \tag{2.73}$$

At leading order equation (2.43) reduces to

$$\left(\bar{H}^3 \bar{H}'\right)' - \frac{1}{2}\bar{\eta}\left(\bar{H}^3\right)' + \bar{H}^3 = 0, \tag{2.74}$$

which is readily solved numerically subject to the boundary conditions

$$\bar{H}(0) = 1, \qquad \bar{H}'(0) = 0 \tag{2.75}$$

to yield $\bar{\eta}_0 \simeq 0.7021$. Figure 2.8 shows a sketch of this asymptotic solution, and Figure 2.9 shows a comparison between profiles H computed numerically and the leading order asymptotic solution as $H_0 \to \infty$ in the cases $H_0 = 3$ and $H_0 = 10$, demonstrating that this asymptotic solution is in good agreement with the exact numerical solution even for values of H_0 as small as 10. Figure 2.3 also includes the leading order asymptotic solution as $H_0 \to \infty$ as a dashed-dotted curve; again

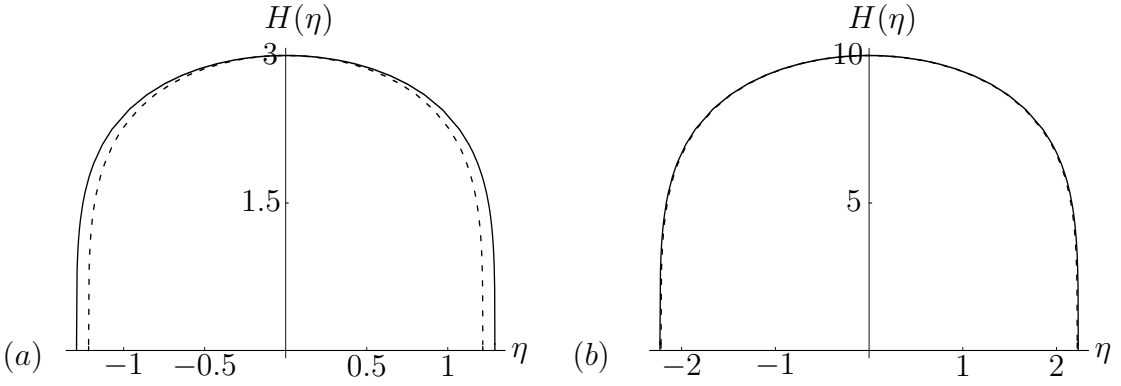

Figure 2.9: Profiles of H obtained numerically (full curves) and from the leading order asymptotic solution in the limit $H_0 \to \infty$ (dashed curves) for (a) $H_0 = 3$ and (b) $H_0 = 10$; in part (b) the two curves are virtually indistinguishable.

the agreement with the exact numerical solution is good even for relatively small values of H_0.

Figures 2.10 and 2.11 show three-dimensional plots of the pendent rivulets ($S_t = -S_g = S_x = 1$) predicted by the similarity solution (2.32) in the cases $H_0 = 0.8$ and $H_0 = 2$, respectively, at times $t = 1$, 10 and 100, and illustrate that the rivulets become wider and thicker as they flow down the plane, and that they become narrower and thinner (while maintaining their cross-sectional shapes) as time elapses. As shown in the insets, for $H_0 = 0.8$ (or generally $H_0 < H_{01}$) the cross-sectional profile is double-humped, and for $H_0 = 2$ (or generally $H_0 > H_{02}$) it is single-humped.

Figure 2.12 shows plots of I_1 and I_3 defined in (2.28) as functions of H_0. Using the asymptotic solutions described above we find that

$$\begin{aligned} I_1 &\sim 2\left(\frac{3}{5}\right)^{\frac{4}{3}} (-K\log H_0)^{\frac{5}{4}} \simeq 0.8258\,(-\log H_0)^{\frac{5}{4}} \to \infty, \\ I_3 &\sim \frac{2}{5}\,(-K\log H_0)^{\frac{9}{4}} \simeq 0.2773\,(-\log H_0)^{\frac{9}{4}} \to \infty \end{aligned} \tag{2.76}$$

in the limit $H_0 \to 0^+$, and

$$\begin{aligned} I_1 &\sim k_1 H_0^{\frac{3}{2}} \simeq 1.2298 H_0^{\frac{3}{2}} \to \infty, \\ I_3 &\sim k_3 H_0^{\frac{7}{2}} \simeq 1.0137 H_0^{\frac{7}{2}} \to \infty \end{aligned} \tag{2.77}$$

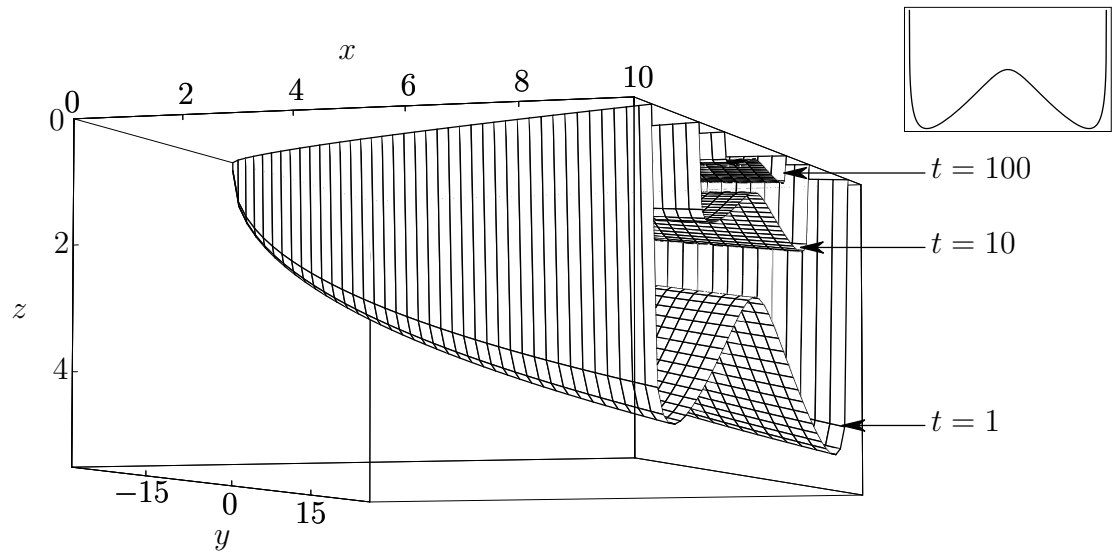

Figure 2.10: Three-dimensional plot of the free surface $z = h$ of a pendent rivulet predicted by the similarity solution (2.32) with H satisfying (2.43) for $H_0 = 0.8$ at times $t = 1$, 10 and 100. The inset shows the cross-sectional profile.

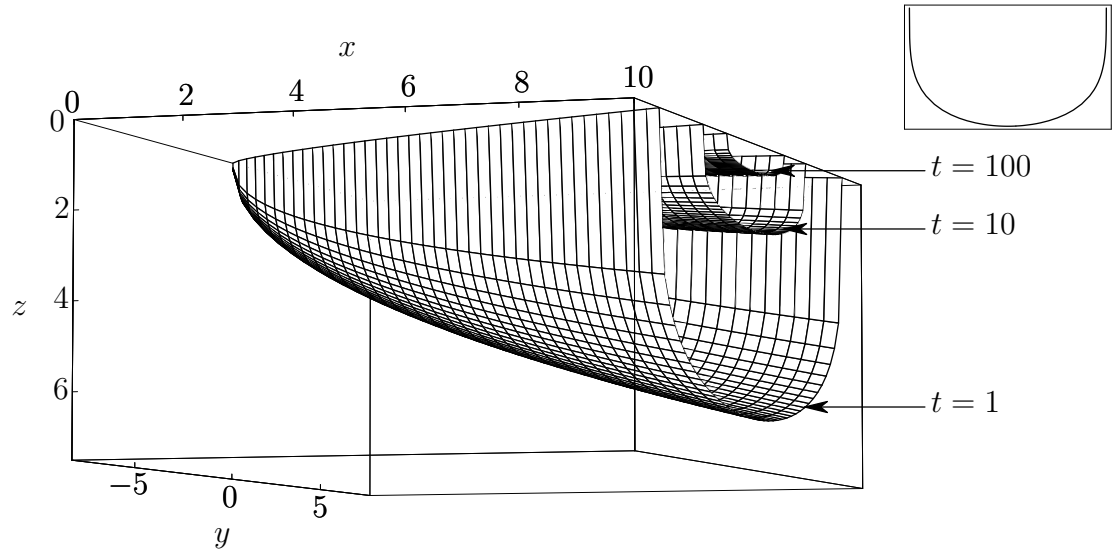

Figure 2.11: As in Figure 2.10 but for $H_0 = 2$.

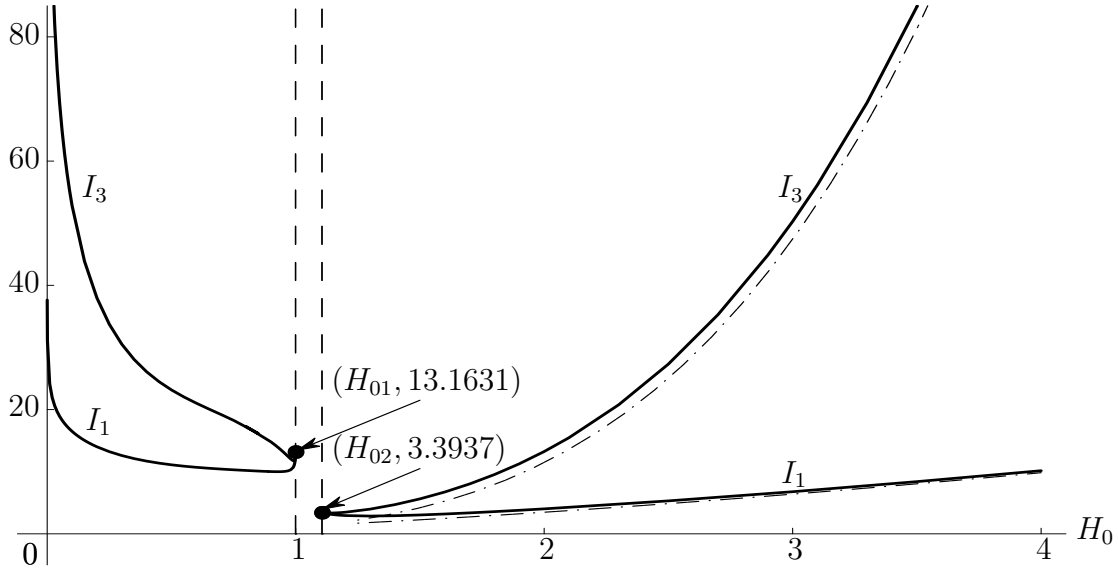

Figure 2.12: Plot of I_1 and I_3 defined in (2.28) as functions of H_0 (full curves), together with the leading order asymptotic solutions (2.77) in the limit $H_0 \to \infty$ (dashed-dotted curves); here $H_{01} \simeq 0.9995$ and $H_{02} \simeq 1.1059$.

in the limit $H_0 \to \infty$, where the constants k_n are defined by

$$k_n = 2 \int_0^{\bar{\eta}_0} \bar{H}^n \, \mathrm{d}\bar{\eta}; \tag{2.78}$$

the asymptotic forms (2.77) are included (represented by dashed-dotted curves) in Figure 2.12.

Thus far we have obtained a one-parameter family of solutions of (2.22), (2.23) and $(2.24)_1$, parameterised by H_0, and with η_0 determined in terms of H_0. However, this does not fully answer the problem of determining all physically realisable solutions of (2.16) of the form (2.18); to do this we must also impose condition $(2.24)_2$, or equivalently the condition $C = 0$. It was found that determining the coefficient C in (2.37) from the behaviour of the numerical solution H near $\eta = \eta_0$ is rather sensitive (presumably because of the infinite slope there); a more robust (and simpler) way of calculating C is to use (2.39), and Figure 2.13 shows a plot of C as a function of H_0, calculated this way. It is found that

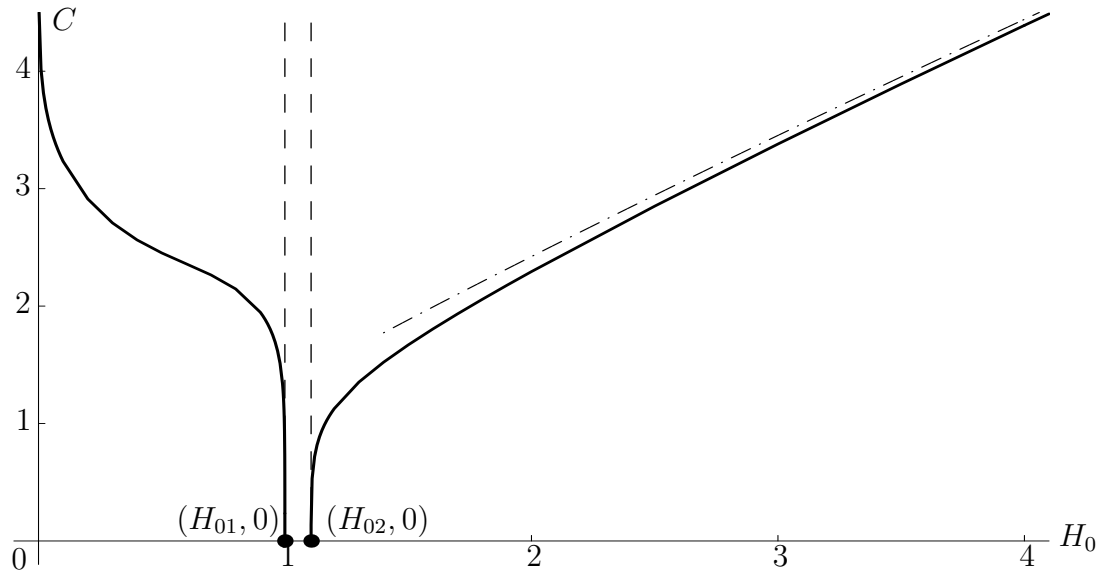

Figure 2.13: Plot of C given by (2.39) as a function of H_0 (full curve), together with the leading order asymptotic solution (2.80) in the limit $H_0 \to \infty$ (dashed-dotted curve); here $H_{01} \simeq 0.9995$ and $H_{02} \simeq 1.1059$.

$$C \sim \left(\frac{6}{5}\right)^{\frac{1}{4}} (-K \log H_0)^{\frac{9}{16}} \simeq 0.9551\,(-\log H_0)^{\frac{9}{16}} \to \infty \tag{2.79}$$

in the limit $H_0 \to 0^+$, and

$$C \sim \left(6k_3 H_0^{\frac{7}{2}}\right)^{\frac{1}{4}} \simeq 1.3205 H_0^{\frac{7}{8}} \to \infty \tag{2.80}$$

in the limit $H_0 \to \infty$; the asymptotic form (2.80) is included (as a dashed-dotted curve) in Figure 2.13. Figure 2.13 shows that $C = 0$ at $H_0 = H_{01}$ and $H_0 = H_{02}$, and that C is non-zero for all other values of H_0. We thus arrive at our main result, namely that there are precisely two physically realisable solutions of the type sought, that these occur only for Case 2, and that they correspond to the values $H_0 = H_{01} \simeq 0.9995$ and $H_0 = H_{02} \simeq 1.1059$ of the scaled middle height H_0; the corresponding values of η_0 are $\eta_0 \simeq 6.6022$ and $\eta_0 \simeq 1.7717$, respectively. Note, incidentally, that the relationship (2.39) shows that $I_1 = I_3$ for both of these solutions, in agreement with Figure 2.12.

Each solution represents both sessile and pendent rivulets; Figures 2.14 and

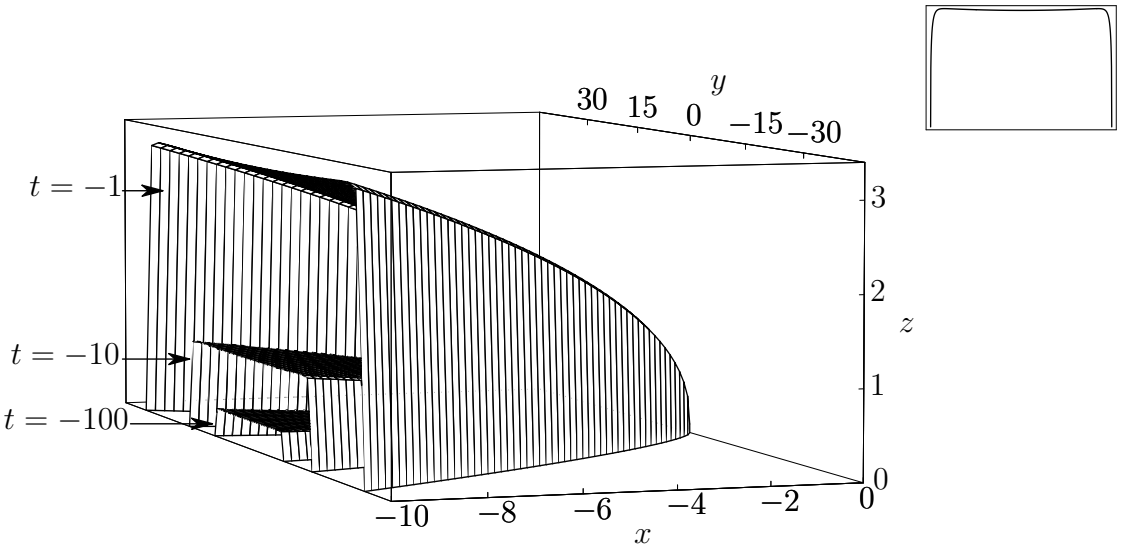

Figure 2.14: Three-dimensional plot of the free surface $z = h$ of a sessile rivulet predicted by the similarity solution (2.32) with H satisfying (2.43) for $H_0 = H_{01}$ at times $t = -100$, -10 and -1 in Case 2 with $S_t = -1$, $S_g = 1$ and $S_x = -1$.

2.15 show three-dimensional plots of the sessile rivulets ($S_t = -S_g = S_x = -1$) for $H_0 = H_{01}$ and $H_0 = H_{02}$, respectively, at times $t = -100$, -10 and -1. Note that, although the profile in Figure 2.14 is double-humped, the curvature near the middle of the rivulet is small (since H_{01} is very close to 1), and hence the double-hump is barely discernible in Figure 2.14.

2.4 The Special Case $H_0 = 0$

The behaviour in the case $H_0 = 0$ requires special consideration, different from the general case $H_0 > 0$.

Near $\eta = 0$, we find that H satisfies either

$$H \sim \left(-\frac{3S_t}{5S_g}\eta^2\right)^{\frac{1}{3}}, \tag{2.81}$$

valid only when $S_t = -S_g$ (i.e. in Case 2 and Case 4), or

$$H \sim \; H_2\eta^2 + \frac{(7H_2S_g + S_x)\,H_2^3}{S_t}\eta^6, \tag{2.82}$$

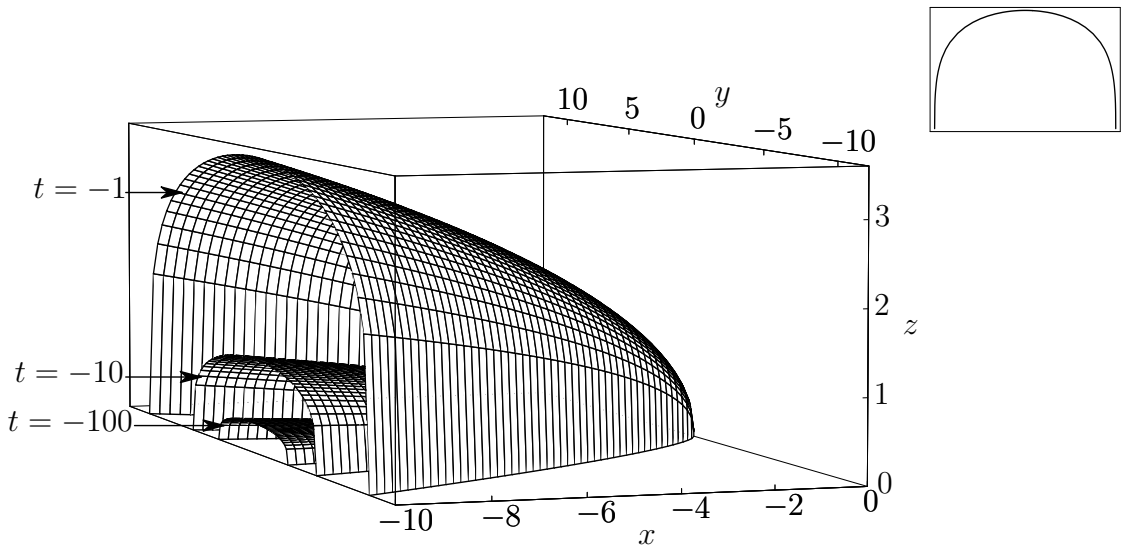

Figure 2.15: As in Figure 2.14 but for $H_0 = H_{02}$.

or

$$H \sim \mathcal{H}\eta^{\frac{1}{4}} - \frac{14S_t}{45\mathcal{H}^2 S_g}\eta^{\frac{3}{2}}, \tag{2.83}$$

the latter two valid in all cases, where H_2 and $\mathcal{H}$ are positive constants. Note that the asymptotic forms (2.81) and (2.83) are not smooth at $\eta = 0$, and the condition $H'(0) = 0$ must be abandoned in these cases. Near the contact line $\eta = \eta_0$, equations (2.36) and (2.37) again hold.

We may again eliminate Cases 1, 3 and 4 from consideration, using the same arguments as in the case $H_0 \neq 0$ in sections 2.2.2 and 2.2.3. We therefore now consider Case 2 only.

Equation (2.43) was solved numerically (again via a shooting technique) subject to boundary conditions obtained from equations (2.81)–(2.83) in turn. The numerical computation cannot be started from $\eta = 0$, so instead it was started from a position $\eta = \delta$, where δ (> 0) is small; the computation was then repeated with smaller values of δ (as small as $\delta = 10^{-20}$ in some cases) until the solution converged to within a given tolerance. For example, for (2.83) the approximated

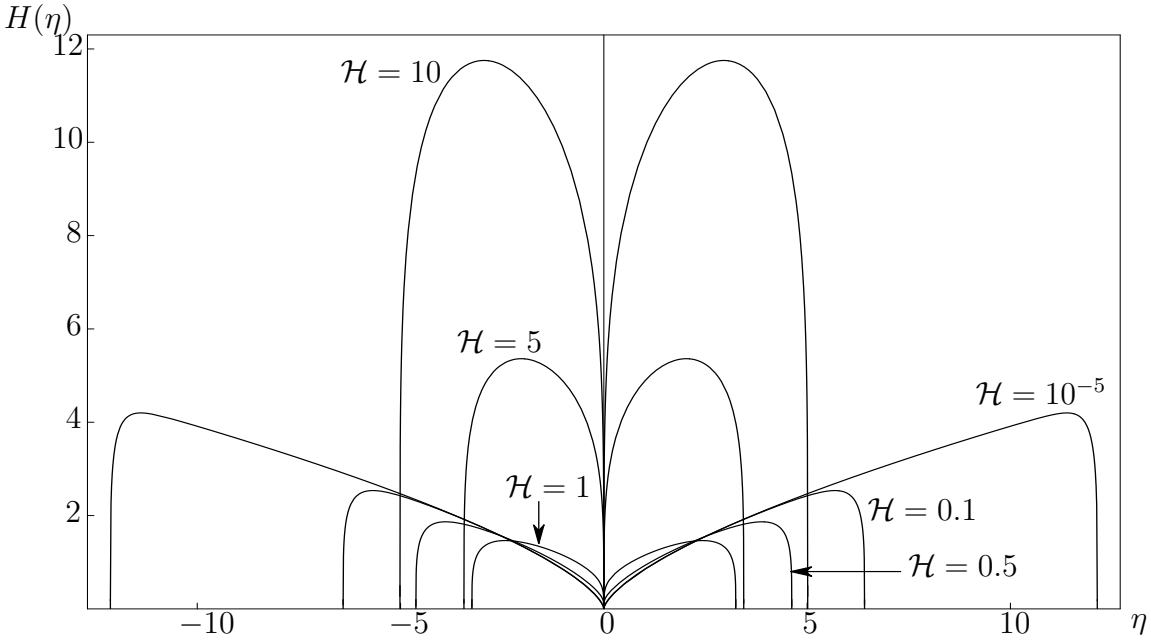

Figure 2.16: Numerically calculated profiles $H = H(\eta)$ in the case $H_0 = 0$ for a range of values of $\mathcal{H}$.

boundary conditions are

$$H(\delta) = \mathcal{H}\delta^{\frac{1}{4}} + \frac{14}{45\mathcal{H}^2}\delta^{\frac{3}{2}}, \quad H'(\delta) = \frac{1}{4}\mathcal{H}\delta^{-\frac{3}{4}} + \frac{7}{15\mathcal{H}^2}\delta^{\frac{1}{2}}, \tag{2.84}$$

and similarly for (2.81) and (2.82). The computation was considered successful if a contact-line position $\eta = \eta_0$ where $H = 0$ was achieved, but was abandoned if it became clear that H was never going to become zero. Using this method, we could not find any solution in the cases satisfying (2.81) or (2.82).

However, solutions of (2.43) subject to (2.83) were found for all values of $\mathcal{H} > 0$; Figure 2.16 shows cross-sectional profiles $H(\eta)$ for a range of values of $\mathcal{H}$, and Figure 2.17 shows η_0 as a function of $\mathcal{H}$ for this family of solutions.

In the limit $\mathcal{H} \to \infty$, we write

$$H = \mathcal{H}^{\frac{8}{7}}\bar{H}(\bar{\eta}), \quad \eta = \mathcal{H}^{\frac{4}{7}}\bar{\eta}, \quad \eta_0 = \mathcal{H}^{\frac{4}{7}}\bar{\eta}_0, \tag{2.85}$$

for some $\bar{\eta}_0$. Then at leading order, equation (2.43) again reduces to (2.74), which is readily solved numerically subject to the boundary conditions $\bar{H}\left(\bar{\delta}\right) = \bar{\delta}^{\frac{1}{4}}$ and

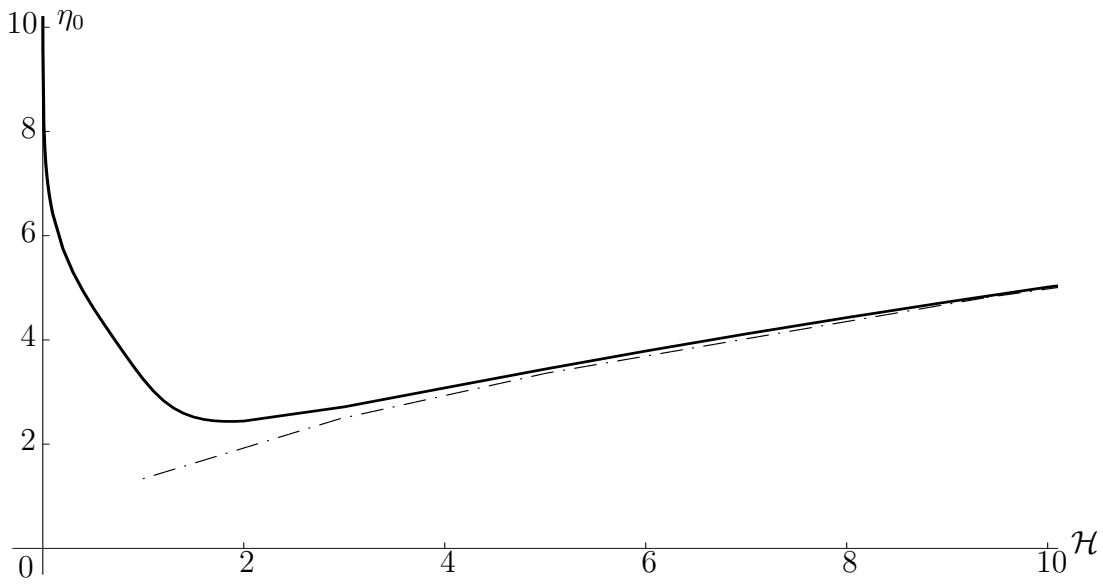

Figure 2.17: Plot of η_0 as a function of $\mathcal{H}$ (full curve) in the case $H_0 = 0$, together with the leading order asymptotic solution in the limit $\mathcal{H} \to \infty$ (dashed-dotted curve).

$\bar{H}'\left(\bar{\delta}\right) = \frac{1}{4}\bar{\delta}^{-\frac{3}{4}}$, where $\bar{\delta} = \mathcal{H}^{-4/7}\delta$, from which we find that $\bar{\eta}_0 \simeq 1.3384$. The asymptotic form (2.85) of η_0 as $\mathcal{H} \to \infty$ is included (as a dashed-dotted curve) in Figure 2.17.

Integrating equation (2.43) from $\eta = 0$ to $\eta = \eta_0$ subject to (2.37) at $\eta = \eta_0$ and (2.83) at $\eta = 0$, we find that (2.39) no longer holds, and that C is now given by

$$C = \left[6\int_0^{\eta_0}\left(H^3 - H\right)\,\mathrm{d}\eta - \mathcal{H}^4\right]^{\frac{1}{4}} = (3I_3 - 3I_1 - \mathcal{H}^4)^{\frac{1}{4}}. \tag{2.86}$$

In particular, it is found that

$$C \sim \mathcal{H}\left(6\int_0^{\bar{\eta}_0}\bar{H}^3\mathrm{d}\bar{\eta} - 1\right)^{\frac{1}{4}} \simeq 1.2493\mathcal{H} \to \infty \tag{2.87}$$

in the limit $\mathcal{H} \to \infty$. Figure 2.18 shows C as a function of $\mathcal{H}$ from (2.86), together with the leading order asymptotic solution (2.87) as $\mathcal{H} \to \infty$ (shown as a dashed-dotted curve). Clearly C is nonzero for all the values of $\mathcal{H}$ shown; we may therefore conclude that there are no physically realisable solutions in the special case $H_0 = 0$.

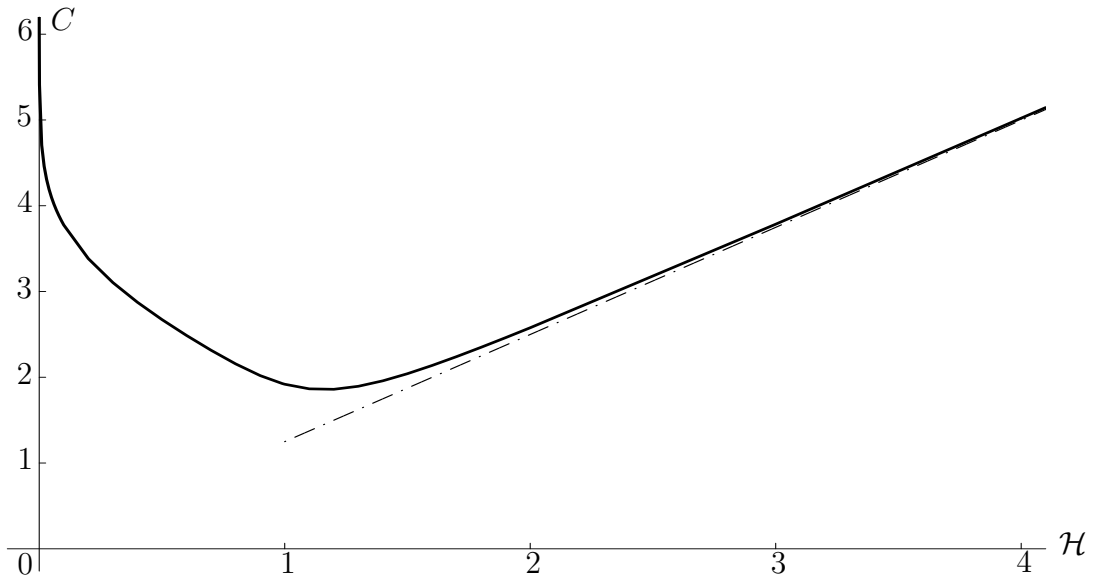

Figure 2.18: Plot of C given by (2.86) as a function of $\mathcal{H}$ (full curve) in the case $H_0 = 0$, together with the leading order asymptotic solution (2.87) in the limit $\mathcal{H} \to \infty$ (dashed-dotted curve).

2.5 Unsteady Flow around a Slender Dry Patch

We use the same approach as discussed previously for rivulet to investigate the possibility of obtaining similarity solutions of type (2.18) for unsteady gravity-driven flow of an infinitely wide thin film around a symmetric slender dry patch $|y| < a(x,t)$ on an inclined plane, the fluid film being of finite depth far from the dry patch. The free surface profile is again governed by (2.16), and with (2.18) it is found that equation (2.19) must again hold, and so with the choice (2.20) the solution takes the form (2.21), where $H(\eta)$ again satisfies the ordinary differential equation (2.22). We have four cases to consider, namely Cases 1–4 as defined in Section 2.2 for the rivulet problem.

We seek a solution H satisfying $H \to H_\infty$ as $\eta \to \infty$, where H_∞ is a positive constant. Then equation (2.22) gives $S_t H_\infty = S_x H_\infty^3$, which requires both that $S_t = S_x$ and that $H_\infty = 1$. Therefore equation (2.22) becomes

$$S_t \left[\frac{1}{2} \eta \left(H - H^3 \right)' - \left(H - H^3 \right) \right] = S_g \left[H^3 H' \right]', \tag{2.88}$$

and the appropriate far field conditions are

$$H \to 1, \qquad H' \to 0 \qquad \text{as} \qquad \eta \to \infty; \tag{2.89}$$

also the (unknown) position of the contact line where $H = 0$ is again denoted $\eta = \eta_0$ (and the fluid region now corresponds to $|\eta| \geq \eta_0$).

It is found that H satisfies $H = 1 + F$ (with $|F| \ll 1$) as $\eta \to \infty$, where $F = F(\eta)$ satisfies

$$S_g F'' + S_t \eta F' - 2S_t F = 0 \tag{2.90}$$

and $F \to 0$ as $\eta \to \infty$; hence if $S_t = S_g$ then

$$F \propto \left(1 + \eta^2\right) \operatorname{erfc}\left(\frac{1}{\sqrt{2}}\eta\right) - \frac{\sqrt{2}}{\sqrt{\pi}}\eta \exp\left(-\frac{1}{2}\eta^2\right), \tag{2.91}$$

so that

$$F \propto \eta^{-3} \exp\left(-\frac{1}{2}\eta^2\right) \quad \text{as} \quad \eta \to \infty, \tag{2.92}$$

while if $S_t \neq S_g$ then no solution is possible. Therefore for a dry patch solution of this type it is necessary that $S_t = S_g = S_x$ (i.e. only Case 1 is possible), and then the transverse profile of the dry patch approaches its uniform value of unity monotonically as $\eta \to \infty$. Moreover, from equation (2.88) with $S_t = S_g$, at any stationary point of the free surface, we have

$$H'' = \frac{H^2 - 1}{H^2}, \tag{2.93}$$

showing that any stationary point with $H < 1$ ($H > 1$) would be a maximum (minimum), and we conclude that H must increase monotonically from $H = 0$ at $\eta = \eta_0$ to $H = 1$ as $\eta \to \infty$, with $0 \leq H < 1$.

Near the contact line $\eta = \eta_0{}^+$, behaviour (2.36) (now valid only when $S_t = S_g$) still holds for a dry patch, whereas (2.37) is replaced by

$$H \sim C\left(\eta - \eta_0\right)^{\frac{1}{4}} + \frac{2S_t\eta_0}{5S_gC^2}\left(\eta - \eta_0\right)^{\frac{1}{2}}, \tag{2.94}$$

where C is a positive constant. However, as before, the zero-mass-flux condition $\bar{v} = 0$ at the contact lines requires $C = 0$, and so (2.94) is eliminated. Then

integrating equation (2.88) with $S_t = S_g$ from $\eta = \eta_0$ to $\eta = \infty$ leads to

$$\int_{\eta_0}^{\infty} \left(H - H^3\right) d\eta = 0, \tag{2.95}$$

which is impossible for monotonic H satisfying $0 \leq H < 1$. Hence, we conclude that there are no dry-patch solutions of the type (2.18) with finite depth far from the dry patch.

2.6 Discussion

We have obtained similarity solutions describing the unsteady gravity-driven flow of a thin slender rivulet of Newtonian fluid down an inclined plane. The velocity and pressure are given by (2.10)–(2.12) in terms of the free surface profile h, which in turn is given by (2.21), where $H(\eta)$ satisfies (2.22)–(2.24), in which H_0 and η_0 are parameters that are determined as part of the solution. There were four cases to consider (labelled Cases 1, 2, 3 and 4), but we quickly showed that there are no solutions in Cases 1, 3 and 4, leaving just Case 2, for which either $S_t = -S_g = S_x = 1$, corresponding to pendent rivulets in $x > 0$ with $t > 0$, or $S_t = -S_g = S_x = -1$, corresponding to sessile rivulets in $x < 0$ with $t < 0$.

Numerical and asymptotic considerations led to the conclusion that for each of these there are just two physically realisable solutions, one for $H_0 = H_{01} \simeq 0.9995$ and one for $H_0 = H_{02} \simeq 1.1059$. The rivulet has a double-humped cross-sectional profile in the case $H_0 = H_{01}$, and a single-humped profile in the case $H_0 = H_{02}$. Each rivulet has a nose that remains stationary at O at all times. At any time t (> 0) a pendent rivulet widens with increasing x (> 0) according to $x^{3/4}$ and thickens according to $x^{1/2}$, and at any station x (> 0) it narrows according to $t^{-1/4}$ and thins according to $t^{-1/2}$. Meanwhile, for a sessile rivulet, at any time t (< 0) it narrows with increasing x (< 0) according to $(-x)^{3/4}$ and thins according to $(-x)^{1/2}$, and at any station x (< 0) it widens according to $(-t)^{-1/4}$ and thickens according to $(-t)^{-1/2}$. Each solution exhibits a finite-time singularity, becoming infinite everywhere at $t = 0$.

It is interesting to note that Huppert's [41] analysis of two-dimensional unsteady flow of a thin film down an inclined plane may be recovered from (2.16) by setting $h_y \equiv 0$, so that $h = h(x,t)$. This leads to Huppert's similarity solution $h \propto x^{1/2}/t^{1/2}$ for $t > 0$, corresponding to (two-dimensional versions of) our Case 1 for a sessile rivulet in $x > 0$, and our Case 2 for a pendent rivulet in $x > 0$, thickening with increasing x but thinning with increasing t in both cases. Equation (2.16) with $h_y \equiv 0$ also has the similarity solution $h \propto (-x)^{1/2}/(-t)^{1/2}$ for $t < 0$, corresponding to (two-dimensional versions of) our Case 2 for a sessile rivulet in $x < 0$, and our Case 1 for a pendent rivulet in $x < 0$, thinning with increasing x but thickening with increasing t in both cases, and exhibiting a finite-time singularity at $t = 0$.

So far we have interpreted each of our solutions as representing an infinitely long rivulet, involving an infinite volume of fluid. In the spirit of Huppert's [41] analysis, we may alternatively interpret each solution as representing a rivulet of (prescribed) finite volume, by truncating it at some finite length $L = L(t)$, so that it occupies $0 \leq |x| \leq L$. The volume of fluid in such a rivulet, denoted by V, is given by

$$V = S_x \int_0^{S_x L(t)} \int_{-a}^{a} \int_0^h \mathrm{d}z\,\mathrm{d}y\,\mathrm{d}x = S_x \int_0^{S_x L(t)} A\,\mathrm{d}x = \left(\frac{4^5 \mu^3 \cos^2\alpha\, L^9}{9^5 \rho^3 g^3 \sin^5\alpha\, |t|^3} \right)^{\frac{1}{4}} I_1, \tag{2.96}$$

and so the length L of the rivulet at time t is given by

$$L = \left(\frac{9^5 \rho^3 g^3 \sin^5\alpha\, V^4}{4^5 \mu^3 \cos^2\alpha\, I_1^4} \right)^{\frac{1}{9}} |t|^{\frac{1}{3}}. \tag{2.97}$$

Figures 2.19 and 2.20 show three-dimensional plots of sessile rivulets of finite volume for $H_0 = H_{01}$ and $H_0 = H_{02}$, respectively, at different times. Equation (2.97) and the corresponding expressions for a and h_m at $x = L$ obtained from (2.25) involve the same scales as in Lister's [52] solution for the large-time behaviour of a rivulet emitted from a point source on an inclined plane, in the case when V increases in proportion to some power of t (see the second entry of his Table 1).

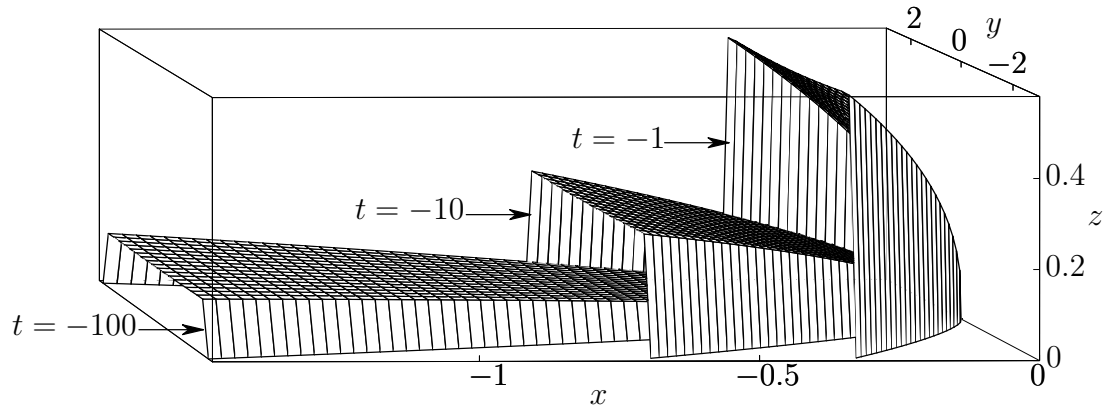

Figure 2.19: Three-dimensional plot of a sessile rivulet with finite (constant) volume for $H_0 = H_{01}$ at times $t = -100$, -10 and -1.

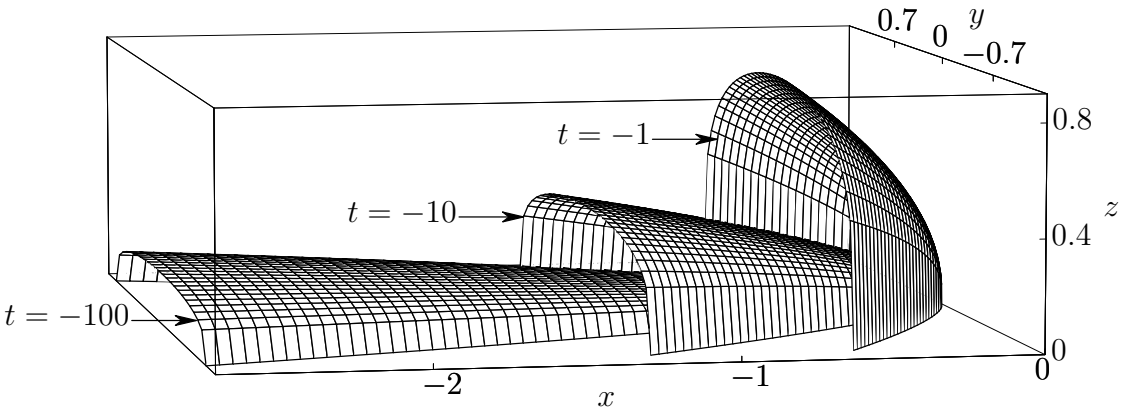

Figure 2.20: As in Figure 2.19 but for $H_0 = H_{02}$.

Lastly, it is worth commenting that although unsteady similarity solutions of (2.16) of the form (2.21) may at first sight seem feasible for the rather different physical context of gravity-driven flow of a thin film of fluid around a slender dry patch on an inclined plane (analogous to the steady similarity solutions obtained by Wilson et al. [109]), the analysis given in Section 2.5 shows that there are, in fact, no such dry-patch solutions.

Chapter 3

Unsteady Numerical Computations of Thin-Film Flows

In Chapter 2, we obtained the similarity solution (2.21) for unsteady gravity-driven flow of a thin and slender rivulet in the case $S_t = -S_g = S_x$. Physically, the case $S_t = -S_g = S_x = 1$ corresponds to a pendent rivulet in $x > 0$ with $t > 0$, whereas the case $S_t = -S_g = S_x = -1$ corresponds to a sessile rivulet in $x < 0$ with $t < 0$. We showed that there are two values of H_0 for physically realisable solutions, namely $H_0 = H_{01} \simeq 0.9995$ and $H_0 = H_{02} \simeq 1.1059$.

We are interested in determining the stability of these two solutions. Grundy and McLaughlin [32] studied the stability of Pattle's [75] two-dimensional and axisymmetric unsteady similarity solutions of the nonlinear diffusion equation (1.30) (described in Chapter 1). For both of these similarity solutions, they constructed an asymptotic solution in the limit $t \to \infty$, with the appropriate similarity solution as the leading term. Pattle's [75] similarity solutions have an infinite slope at the contact line and this leads to singular terms in the expansion. Grundy and McLaughlin [32] overcame this difficulty by using a "strained coordinate" transformation. In this transformation, a new independent variable (the strained coordinate) is introduced to provide a new expansion in which the singularity is removed. Grundy and McLaughlin [32] showed that the large-time perturbations

in Pattle's [75] similarity solutions decay in time, and concluded that both the two-dimensional and the axisymmetric solutions are linearly stable at large time to two-dimensional and axisymmetric perturbations, respectively. Mathunjwa and Hogg [56] extended the analysis of Grundy and McLaughlin [32] to consider the stability of Pattle's [75] axisymmetric similarity solution subject to asymmetric perturbations. They encountered a similar difficulty to Grundy and McLaughlin [32], and to overcome this problem, they transformed the dependent variable so that the slope at the contact line becomes finite. Mathunjwa and Hogg [56] found that the similarity solution is linearly stable to both axisymmetric and asymmetric perturbations. Mathunjwa and Hogg [56] also showed that an axisymmetric perturbation decays faster than an asymmetric perturbation of equal amplitude, which implies that the flow with an axisymmetric perturbation approaches the similarity solution faster than the flow with an asymmetric perturbation.

However, for our solution obtained in Chapter 2, even a restricted stability analysis of this kind is likely to be a formidable task since our solutions are fully three-dimensional. Instead, in this chapter we take a more pragmatic approach by investigating the stability of the similarity solutions numerically using the finite element package COMSOL Multiphysics. Specifically, this chapter reports on computations of various thin-film flows and, in particular, a numerical study of the stability of the similarity solution (2.21) obtained in Chapter 2.

3.1 A Brief Introduction to COMSOL

COMSOL Multiphysics (formerly known simply as FEMLAB) is a commercial finite element analysis code, used for modelling and simulation of various physical systems and engineering applications, such as acoustics, diffusion, fluid mechanics, structural mechanics and electromagnetics. Basically, it uses the finite element method to solve systems of coupled partial differential equations (PDEs). There are three types of formulation provided within COMSOL to solve a system of

PDEs, namely a "coefficient form" (for linear or almost linear PDEs), a "general form" (for nonlinear PDEs) and a "weak form" (using a weak formulation of the PDEs). In the present computations, we used the general form formulation.

In COMSOL, the general form of a time-dependent PDE for a single unknown variable $u = u(\mathbf{x}, t)$, where t denotes time and $\mathbf{x}$ denotes spatial position in a prescribed domain Ω, is given by

$$e_a \frac{\partial^2 u}{\partial t^2} + d_a \frac{\partial u}{\partial t} + \nabla \cdot \Gamma = F \quad \text{in} \quad \Omega, \tag{3.1}$$

where e_a is called the "mass coefficient", d_a is called the "damping coefficient", Γ is called the "flux vector" and F is a scalar. The quantities e_a, d_a, Γ and F can be functions of $\mathbf{x}$, t, u and its space and time derivatives. Equation (3.1) is solved subject to either the general Neumann boundary condition

$$-\mathbf{n} \cdot \Gamma = G + \left(\frac{\partial R}{\partial u} \right)^T \kappa \quad \text{on} \quad \partial\Omega, \tag{3.2}$$

or the Dirichlet boundary condition

$$R = 0 \quad \text{on} \quad \partial\Omega, \tag{3.3}$$

where $\mathbf{n}$ is the outward unit normal to the boundary $\partial\Omega$ of Ω, both G and R are scalars which can be functions of $\mathbf{x}$, t, u and its space and time derivatives, the superscript T denotes transpose, and κ is a Lagrange multiplier[1] associated with the Neumann boundary condition.

In COMSOL, there are two alternative methods to solve unsteady problems, namely, a "backward differential formula" (BDF) method and a "generalized-α" method, where α is a parameter in the algorithm. The BDF method is used for a wide range of problems, whereas the generalized-α method was initially derived to solve structural dynamics problems, and is often used for wave-equation type

[1]Within COMSOL, if $R \neq 0$ then (3.2) simply gives the value of κ (which is not of interest to us) and in effect only (3.3) is imposed, whereas if $R \equiv 0$ then (3.3) gives no information and only (3.2) is imposed (for which κ has now disappeared).

problems. There are several choices of linear system solver, categorised into direct solvers and iterative solvers. Direct solvers, such as UMFPACK and SPOOLES, are commonly used for one-dimensional problems, two-dimensional problems, and also for three-dimensional problems with few degrees of freedom. They are generally stable and reliable, but the downside of this type of solver is that they require considerable memory, especially for three-dimensional problems. Iterative solvers, such as GMRES and FGMRES, are more efficient in solving three-dimensional problems. However, iterative solvers are generally less stable (so that convergence of the solution is not guaranteed) and require considerable computational time. Further information on COMSOL Multiphysics can be found in [2]. In the present computations, we used a BDF method with a GMRES linear system solver.

COMSOL can also be linked to MATLAB for the purpose of preprocessing data and postprocessing solutions. In this chapter we will use both COMSOL and MATLAB packages for the numerical computation of various thin-film flow problems.

3.2 Validation of the Numerical Procedure

The main purpose of this section is to validate the accuracy and reliability of the numerical procedure that we will use for the stability study of our similarity solution (2.21). In order to validate our numerical procedure we seek to recover previously known similarity solutions as the long time behaviour of unsteady numerical computations for appropriate thin-film flows on an inclined plane and on a horizontal plane with and without injection of fluid. Specifically, we seek to recover the similarity solutions of Smith [92], Duffy and Moffatt [24], Smith [93] and Huppert [42] described in Chapter 1. In doing this, we also obtained new numerical results, notably in recovering the steady similarity solution of Duffy and Moffatt [24] from an unsteady numerical computation.

In all our computations, we used a Cartesian coordinate system (x,y,z) with

x and y denoting longitudinal and transverse coordinates, respectively, and z denoting the normal to the plane. The free surface profile $z = h(x, y, t)$ satisfies the partial differential equation (derived in Chapter 2)

$$3\mu h_t = \nabla \cdot \left[h^3 \nabla \left(\rho g \cos\alpha h - \sigma \nabla^2 h\right)\right] - \rho g \sin\alpha \left[h^3\right]_x . \tag{3.4}$$

We wish to solve a variety of unsteady thin-film problems described by (3.4) by neglecting some of the terms appropriately. Therefore, in the general PDE given by (3.1), h is the variable u, Γ depends on the governing equation that we want to solve, and F depends on the injection of fluid (where $F = 0$ correspond to no injection of fluid), and we set $e_a = 0$ and $d_a = 1$.

The numerical problems were solved on the rectangular domain Ω with $X_1 \leq x \leq X_2$, $|y| \leq Y$, where X_1, X_2 and Y were chosen to be sufficiently large that the (nominal) contact lines of the film remained well away from the domain boundaries $\partial\Omega$ during the computations. The domain was discretized initially using triangular mesh elements and the mesh was refined appropriately to increase the accuracy of the solution. In each mesh refinement, each element is divided into four smaller triangular elements. However, the resulting calculations then require more computational time and therefore the number of mesh elements was chosen appropriately in order that a balance was achieved between accuracy of the solution and computational effort required.

We applied the boundary conditions $h_x = 0$ and $h_y = 0$ at the boundaries of the domain Ω, and the initial condition $h(x, y, 0) = h_p$, where h_p is the uniform thickness of a thin precursor layer covering the domain at $t = 0$, included in order to alleviate any singularities at any moving contact lines that may be present. We found that the precursor layer was needed in certain computations, especially when the domain had a very refined mesh (a large number of mesh elements) or when the computation was run for larger times. These boundary and initial conditions were used in all computations in this section, unless mentioned otherwise.

3.2.1 Steady similarity solutions

In this subsection we describe numerical solutions of unsteady thin-film flows on an inclined plane computed using COMSOL that approach the steady similarity solutions obtained by Smith [92] in the case of weak surface-tension effects and Duffy and Moffatt [24] in the case of strong surface-tension effects at large times and length scales.

(a) Smith [92]

As described in Chapter 1, Smith [92] obtained the unique steady similarity solution (1.24) describing a slender non-uniform rivulet driven by gravity on an inclined plane. This similarity solution was validated numerically by Schwartz and Michaelides [89] using a finite difference method. Specifically, Schwartz and Michaelides [89] studied the unsteady problem of a thin film of fluid being supplied by continuous injection at a constant rate through a circular hole of radius R_0 centred at $(0, 0, 0)$ on a plane inclined at an angle α to the horizontal. The governing equation of the thin-film problem solved by Schwartz and Michaelides [89] is given by (3.4) with the surface-tension term neglected but with the addition of an appropriate source term, which yields

$$3\mu h_t = \rho g \cos\alpha \left[\left(h^3 h_y\right)_y + \left(h^3 h_x\right)_x \right] - \rho g \sin\alpha \left(h^3\right)_x + w, \tag{3.5}$$

where $w = w(r)$ is the prescribed (parabolic) injection velocity normal to the plane given by

$$w = \begin{cases} \dfrac{6\mu\Gamma_0}{\pi R_0^2}\left(1 - \dfrac{r^2}{R_0^2}\right) & \text{for} \quad r < R_0, \\ 0 & \text{for} \quad r \geq R_0, \end{cases} \tag{3.6}$$

where

$$\Gamma_0 = \int_0^{2\pi} \int_0^{R_0} w\, r \, \mathrm{d}r \, \mathrm{d}\theta \tag{3.7}$$

is the constant rate of volumetric injection, and $r = \sqrt{x^2 + y^2}$ is the radial distance measured from the centre of the hole.

Equation (3.5) may be non-dimensionalised using R_0 as a characteristic length scale and $T = 3\mu/\rho g R_0$ as a characteristic time scale to yield

$$h_t = \cos\alpha \left[\left(h^3 h_y\right)_y + \left(h^3 h_x\right)_x \right] - \sin\alpha \left(h^3\right)_x + \bar{w}, \tag{3.8}$$

where $\bar{w}$ is the non-dimensional injection velocity given by

$$\bar{w} = \begin{cases} \dfrac{2\chi}{\pi}\left(1 - r^2\right) & \text{for} \quad r < 1, \\ 0 & \text{for} \quad r \geq 1, \end{cases} \tag{3.9}$$

and $\chi = 3\mu\Gamma_0/\rho g R_0^4$ is a non-dimensional measure of the rate of volumetric injection. Based on the experimental results of Hallworth et al. [33], Schwartz and Michaelides [89] chose the parameter values so that $\chi = 0.844$ and (for a sessile rivulet) $\alpha = 15°$. Their computations were performed using central differences in space, and were advanced in time using a marching scheme. The evolution of the flow was calculated from the start of the flow at $t = 0$ (at which time the plane was unwetted) until $t = 1200$. Schwartz and Michaelides [89] found that at sufficiently large t their numerical results are in a good agreement with the similarity solution obtained by Smith [92] except near the source and near the leading edge.

We also solved equation (3.8) numerically using the same values of χ and α. For the computational domain in COMSOL, X_1, X_2 and Y were taken to be -10, 110 and 20, respectively, and the domain was discretized uniformly with approximately 79000 triangular mesh elements. The precursor layer was taken to have thickness $h_p = 10^{-5}$ so that there was a good compromise between numerical accuracy and computational effort, and the computation was run from $t = 0$ until $t = 1200$.

Figures 3.1(a) and (b) show the cross-sectional profiles at $y = 0$ as functions of x and the cross-sectional profiles at $x = 15.2$ as functions of y, respectively, obtained numerically (represented by full curves), together with the similarity solution (1.24) obtained by Smith [92] (represented by dashed curves) at times $t = 200$, 400, 600, 800, 1000 and 1200. These figures show good agreement between the numerical results and the steady similarity solution for large t except near the

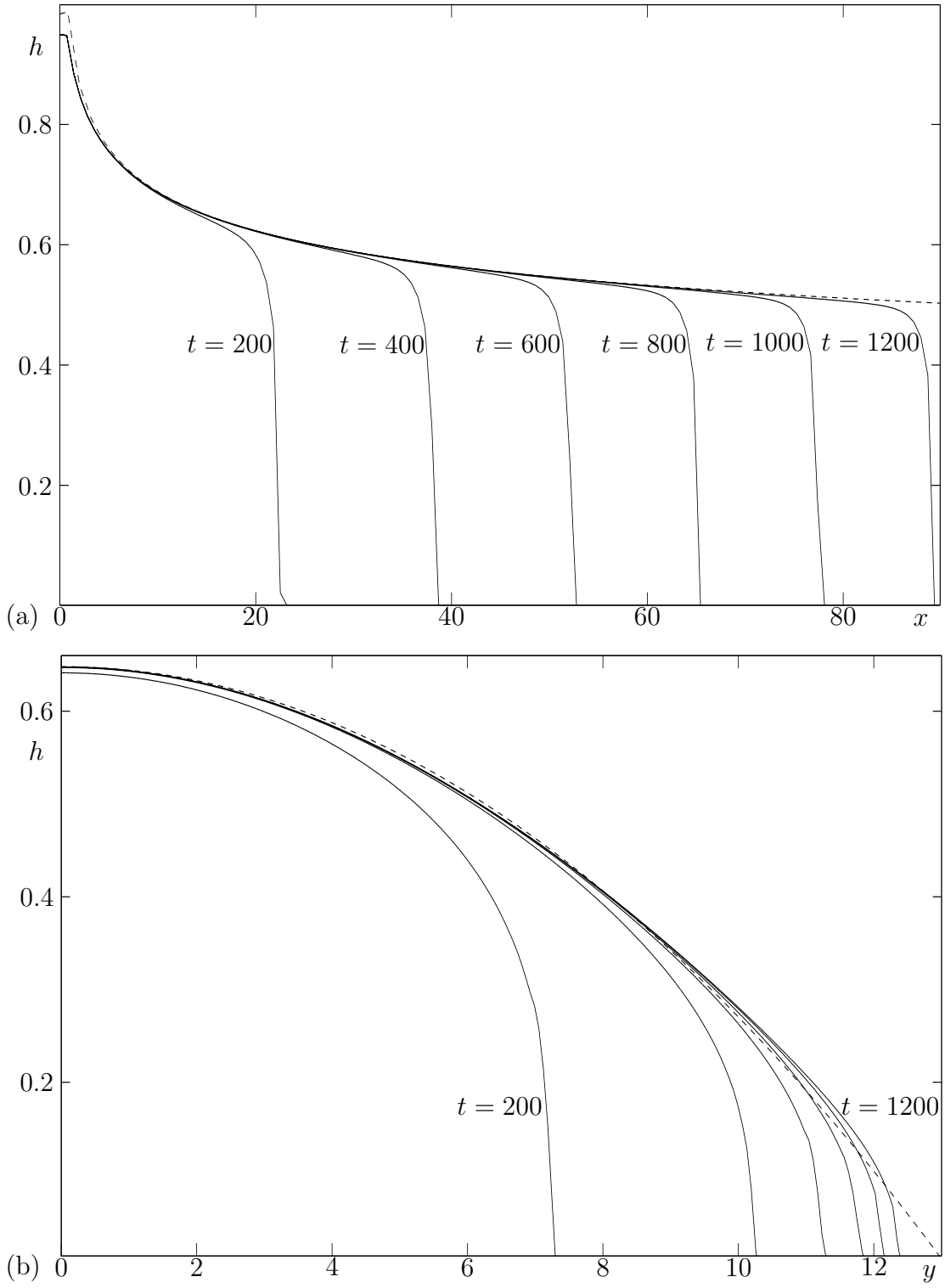

Figure 3.1: Plots of the cross-sectional profiles of a sessile rivulet (a) at $y = 0$ as functions of x, and (b) at $x = 15.2$ as functions of y (full curves), together with Smith's [92] similarity solution (1.24) (dashed curves) at times $t = 200$, 400, 600, 800, 1000 and 1200.

source (shown in Figure 3.1(a)) and near the leading edge (shown in Figure 3.1(b)). Our numerical results thus confirm the results obtained by Schwartz and Michaelides [89] and the validity of Smith's [92] similarity solution.

(b) Duffy and Moffatt [24]

As we have just described, Schwartz and Michaelides [89] validated the steady similarity solution of Smith [92] for a slender gravity-driven rivulet with weak surface-tension effects, but to our knowledge no-one has previously performed the corresponding validation for the steady similarity solution obtained by Duffy and Moffatt [24] for a slender gravity-driven rivulet on an inclined plane with strong surface-tension effects.

To do this we used the same approach as that described above for Smith's [92] solution. In this case, the partial differential equation for h is given by (3.4) with the first gravity term on the right neglected but with the addition of an appropriate source term, which yields

$$3\mu h_t = -\sigma\left[\left(h^3 h_{yyy}\right)_y + \left(h^3 h_{xxx}\right)_x\right] - \rho g \sin\alpha \left(h^3\right)_x + w, \tag{3.10}$$

where w is the prescribed injection velocity normal to the plane again given by (3.6). Equation (3.10) is non-dimensionalised in the same way as before to give

$$h_t = -A\left[\left(h^3 h_{yyy}\right)_y + \left(h^3 h_{xxx}\right)_x\right] - \sin\alpha \left(h^3\right)_x + \bar{w}, \tag{3.11}$$

where $\bar{w}$ the non-dimensional injection velocity again given by (3.9) and $A = \sigma/\rho g R_0^2$ is an inverse Bond number denoting a non-dimensional measure of surface-tension effects. We used the same values of χ and α as before, and in the absence of any corresponding experimental results, we chose $A = 1$ for simplicity. For the computational domain, X_1, X_2 and Y were taken to be -10, 160 and 10, respectively, and the domain was discretised uniformly with approximately 24000 triangular elements. The precursor layer was taken to have thickness $h_p = 10^{-2}$ and the computation was run from $t = 0$ until $t = 1000$.

Figures 3.2(a) and (b) show the cross-sectional profiles at $y = 0$ as functions of x and the cross-sectional profiles at $x = 20$ as functions of y, respectively, obtained numerically (represented by full curves), together with the similarity solution (1.27) obtained by Duffy and Moffatt [24] (represented by dashed curves) at times $t = 200$, 400, 600, 800 and 1000. Duffy and Moffatt's [24] similarity solution (1.27) involves a free parameter G_0; we chose the value of G_0 randomly at first and adjusted it manually to improve the agreement with the numerical solution. We found that there is a good agreement between numerical and similarity solutions for the cross-sectional profiles at $x = 20$ when $G_0 = 0.08$. However, for the cross-sectional profiles at $y = 0$, the numerical solution and similarity solution agree only to a certain extent. In Figure 3.2(a) the numerical solutions show the occurrence of a capillary ridge near the front of the film which is typical in flows with significant surface-tension effects but is not captured in Duffy and Moffatt's [24] similarity solution. Figures 3.3(a) and (b) show three-dimensional plot and contour plot of free surface profile h satisfying (3.11) at time $t = 1000$.

3.2.2 Unsteady similarity solutions

Thus far we have considered thin-film flows which recover known steady similarity solutions, but the same approach can be applied to unsteady similarity solutions. Similarity solutions for axisymmetric gravity-driven spreading of a sessile thin drop on a horizontal plane with negligible surface-tension effects were obtained by Smith [93] (for the case when the volume of fluid is constant) and by Huppert [42] (for the case when the volume of fluid is constant or changes with some power of t). The governing equation for h is given by

$$3\mu h_t = \frac{\rho g}{r}\left(r h^3 h_r\right)_r , \tag{3.12}$$

where r is the radial coordinate measured from the centre of the drop. We non-dimensionalised equation (3.12) in the same way as before to yield

$$h_t = \frac{1}{r}\left(r h^3 h_r\right)_r . \tag{3.13}$$

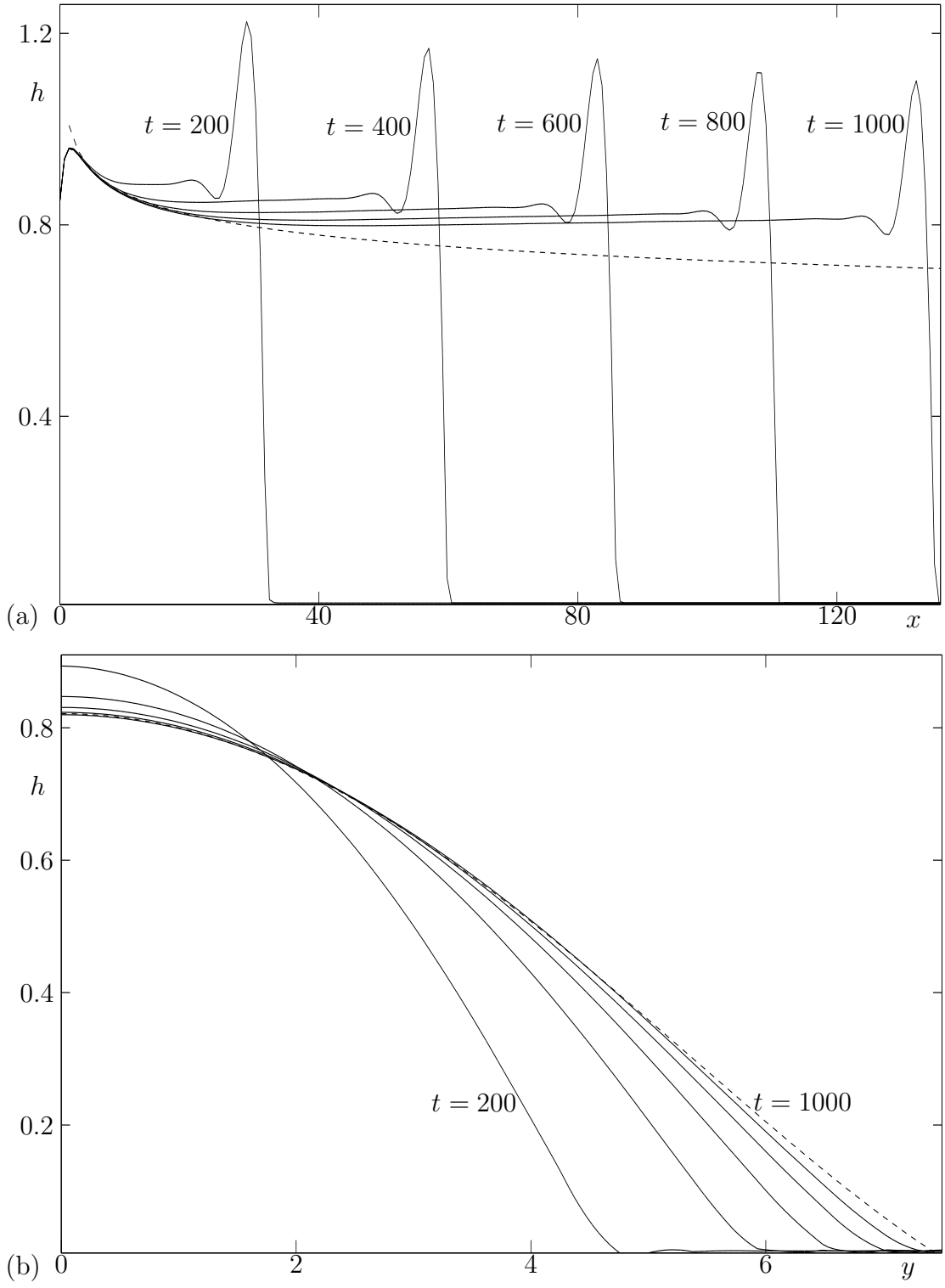

Figure 3.2: Plots of the cross-sectional profiles of a sessile rivulet (a) at $y = 0$ as functions of x, and (b) at $x = 20$ as functions of y (full curves), together with Duffy and Moffatt's [24] similarity solution (1.27) (dashed curves) in the case $G_0 = 0.08$, at times $t = 200$, 400, 600, 800 and 1000.

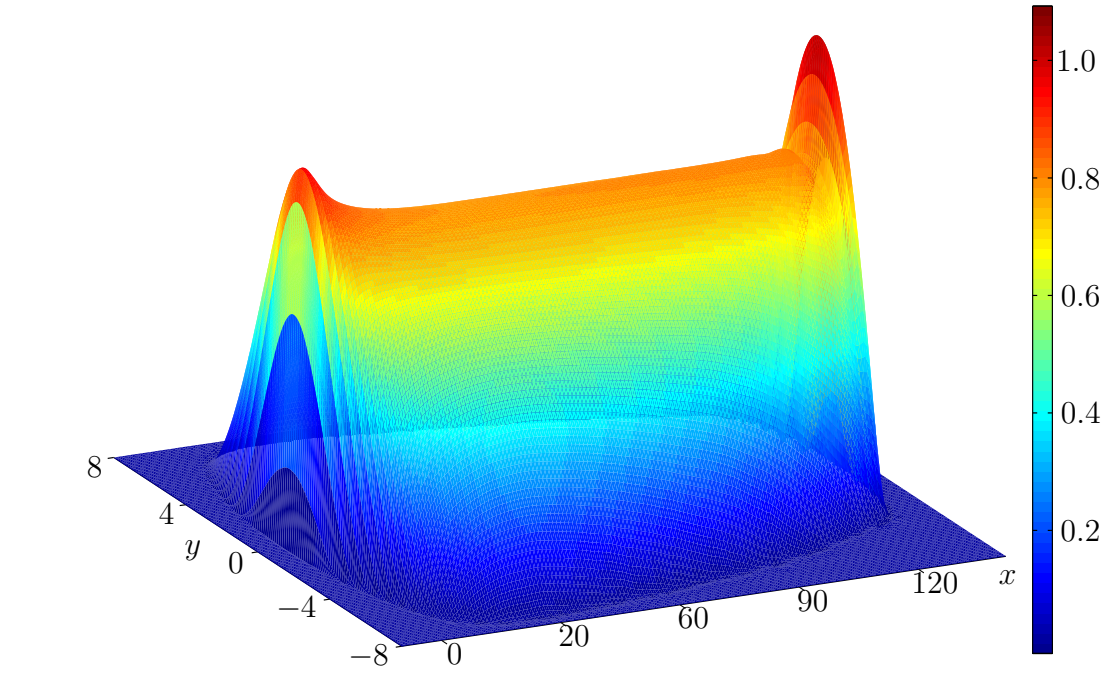

(a)

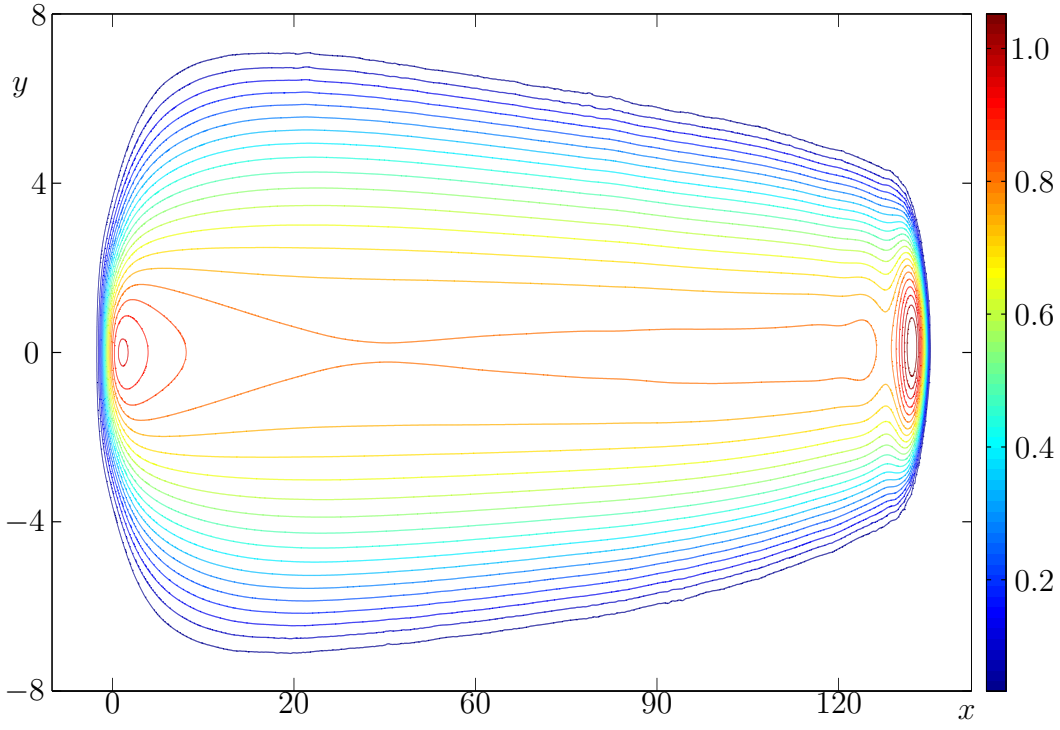

(b)

Figure 3.3: (a) Three-dimensional plot and (b) contour plot of the numerical solution for free surface profile h satisfying (3.11) at time $t = 1000$.

(a) Smith [93]

Axisymmetric spreading of a drop of constant volume on a horizontal plane was considered by Smith [93], who found a similarity solution to (3.12) which is given by

$$h(r,t) = \left(\frac{9\mu}{16\rho g}\right)^{\frac{1}{3}} t^{-\frac{1}{4}} \left[\left(\frac{1024V^3\rho g}{243\pi^3\mu}\right)^{\frac{1}{4}} - r^2 t^{-\frac{1}{4}}\right]^{\frac{1}{3}}, \tag{3.14}$$

where

$$V = \int_{-\infty}^{\infty}\int_{-\infty}^{\infty} h \,\mathrm{d}y\,\mathrm{d}x \tag{3.15}$$

is the constant volume of the drop. To solve this problem numerically using COMSOL, we write (3.13) in Cartesian coordinates (x, y, z) to give

$$h_t = \left[\left(h^3 h_x\right)_x + \left(h^3 h_y\right)_y\right]. \tag{3.16}$$

We used a square domain with $Y = 2$ (so that $X_1 = -2$ and $X_2 = 2$), and the domain was discretised uniformly with approximately 9400 triangular mesh elements. The initial shape of the film was chosen to be a paraboloid, so that the initial condition is given by

$$h(x,y,0) = \begin{cases} 1 - r^2 & \text{for} \quad r < 1, \\ 0 & \text{for} \quad r \geq 1, \end{cases} \tag{3.17}$$

where $r = \sqrt{x^2 + y^2}$ is the radial distance measured from the centre of the paraboloid. We found that for this problem, the computation can be run (within a specified time) without the precursor layer and therefore h_p was not required here. The computation was run from $t = 0$ until $t = 50$.

Figure 3.4 shows a comparison between the cross-sectional profiles obtained numerically (represented by full curves) and the profiles from the similarity solution obtained by Smith [93] (represented by dashed curves) at times $t = 0, 1$, 10, 20, 30, 40 and 50. Initially (at $t = 1$), the numerical solutions predict that the height at the middle of the drop is lower and the width of the drop is larger than those predicted from the similarity solution. However, the numerical solution and the

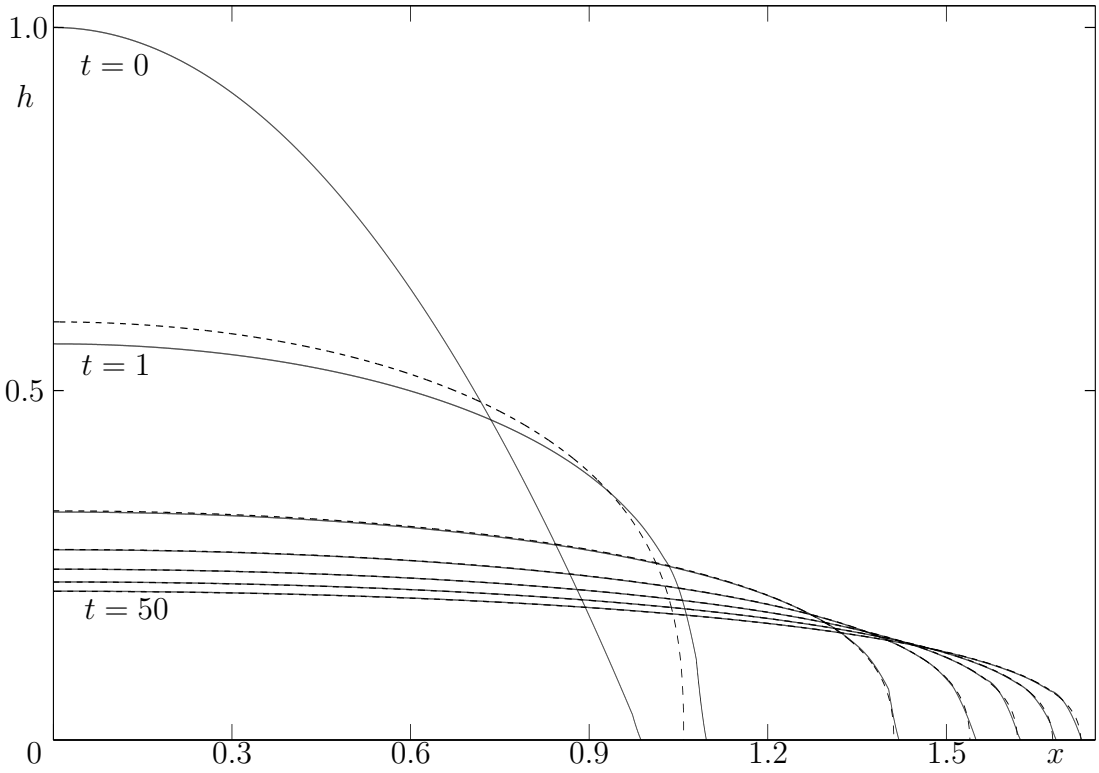

Figure 3.4: Plot of the cross-sectional profiles of an axisymmetric spreading sessile thin film in the case when the volume of fluid is constant (full curves), together with Smith's [93] similarity solution (3.14) (dashed curves) at times $t = 0$ (only for the numerical solution), 1, 10, 20, 30, 40 and 50.

similarity solution are in good agreement at large times (specifically from about $t = 10$).

(b) Huppert [42]

Axisymmetric spreading of a drop on a horizontal plane governed by equation (3.12) was also considered by Huppert [42]. He recovered the similarity solution of Smith [93] for the case when the volume of the drop is constant and extended his study to the case when the volume of the drop changes according to a prescribed power of t. In the latter case he obtained a similarity solution in the

form

$$h(r,t) = \xi_N^{\frac{2}{3}} \left(\frac{3\mu Q}{\rho g}\right)^{\frac{1}{4}} t^{\frac{\gamma-1}{4}} \varphi\left(\frac{\xi}{\xi_N}\right), \qquad \xi = \left(\frac{3\mu}{\rho g Q^3}\right)^{\frac{1}{8}} r t^{-\frac{3\gamma+1}{8}}, \tag{3.18}$$

where

$$V = Qt^\gamma = 2\pi \int_0^{r_N} r h(r,t)\,\mathrm{d}r, \tag{3.19}$$

in which Q and γ are prescribed constants, and

$$\xi_N = \left(2\pi \int_0^1 z\varphi(z)\mathrm{d}z\right)^{-\frac{3}{8}} \tag{3.20}$$

is the value of ξ at front of the drop given by

$$r = r_N = \left(\frac{\rho g Q^3}{3\mu}\right)^{\frac{1}{8}} \xi_N t^{\frac{3\gamma+1}{8}}, \tag{3.21}$$

with $\varphi = \varphi(z)$ satisfying the ordinary differential equation

$$\left(z\varphi^3\varphi'\right)' + \frac{1}{8}\left(3\gamma+1\right) z^2\varphi' - \frac{1}{4}\left(\gamma-1\right) z\varphi = 0, \tag{3.22}$$

where $z = \xi/\xi_N$ (so that $z = 1$ at the front of the drop). Note that solutions of (3.22) are singular at the origin $r = 0$ for $\gamma \neq 0$ due to the fact that the fluid is being introduced there. The case when the volume of the drop is constant considered by Smith [93] corresponds to $\gamma = 0$ and the case when the flux of fluid into the drop is constant corresponds to $\gamma = 1$.

In the case $\gamma = 1$ the similarity solution can be obtained by solving (3.22) numerically subject to the boundary conditions

$$\varphi(1-\delta) = \left(\frac{3}{2}\right)^{\frac{1}{3}} \left(\delta^{\frac{1}{3}} - \frac{\delta^{\frac{4}{3}}}{12}\right), \qquad \varphi'(1-\delta) = \left(\frac{3}{2}\right)^{\frac{1}{3}} \left(-\frac{1}{3\delta^{\frac{2}{3}}} + \frac{\delta^{\frac{1}{3}}}{9}\right), \tag{3.23}$$

where δ (> 0) is a small offset from the contact line $z = 1$ and is introduced because the numerical computation cannot be started exactly at the contact line $z = 1$ due to the singularity there. Thus the computation was started from a position $z = 1 - \delta$, and was then repeated with smaller values of δ (as small as $\delta = 10^{-10}$) until the solution converged to within a given tolerance.

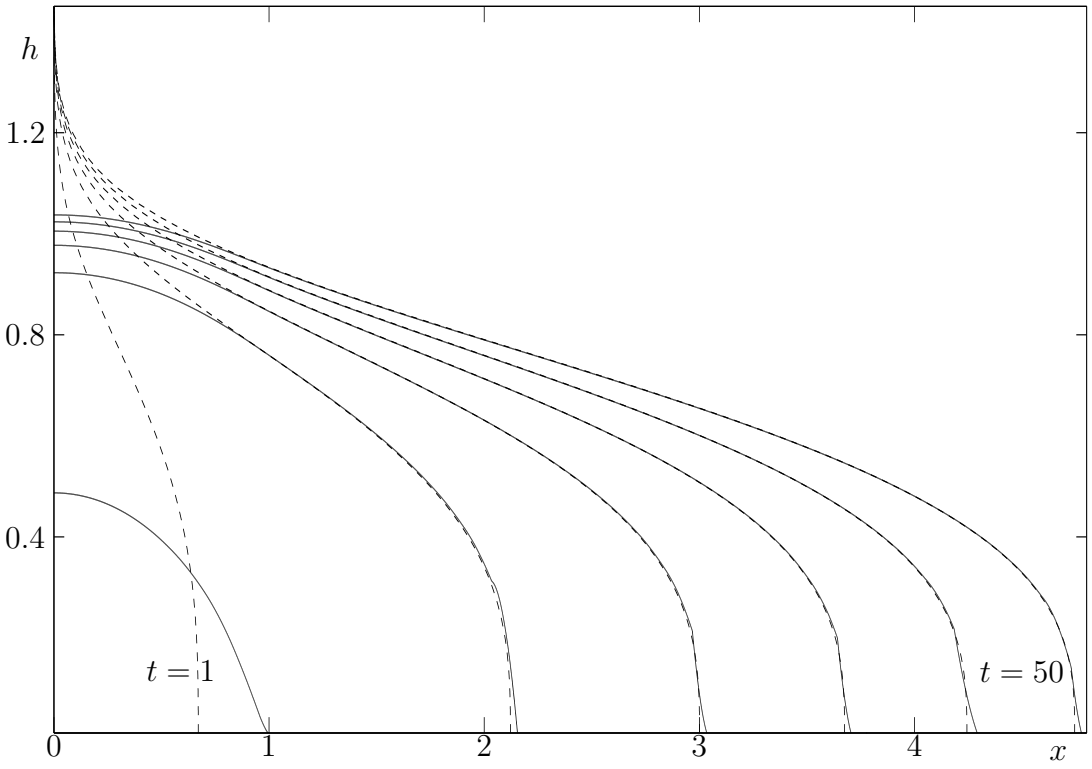

Figure 3.5: Plot of the cross-sectional profiles of an axisymmetric spreading sessile thin film when the flux of fluid is constant (full curves), together with Huppert's [42] similarity solution (3.18) calculated by solving (3.22) numerically (dashed curves) at times $t = 1$, 10, 20, 30, 40 and 50.

We already solved the case $\gamma = 0$ and we now consider the case $\gamma = 1$. Again, we used the same approach as that described previously. The non-dimensional governing equation for h is given by (3.16) with the addition of an appropriate source term, namely

$$h_t = \left(h^3 h_y\right)_y + \left(h^3 h_x\right)_x + \bar{w}, \tag{3.24}$$

where $\bar{w}$ is the non-dimensional injection velocity again given by (3.9) and $\Gamma_0 = Q$ is the constant rate of volumetric injection (3.7). For definiteness we used the same value of χ as before and the problem was solved in a square computational domain with $Y = 5$ (so that $X_1 = -5$ and $X_2 = 5$), and the domain was discretised uniformly with approximately 9400 triangular mesh elements. Again, we found

that the precursor layer was not required here, and the computation was run from $t = 0$ until $t = 50$.

Figure 3.5 shows a comparison between the cross-sectional profiles obtained numerically (represented by full curves) and the profiles from the similarity solution (3.18) obtained by Huppert [42] calculated by solving (3.22) numerically (represented by dashed curves) at times $t = 1$, 10, 20, 30, 40 and 50. As before, numerical solutions predict that the height at the middle of the drop is lower and the width of the drop is larger than those predicted from the similarity solution. However, the two solutions are in close agreement except near $x = 0$ (where the similarity solution exhibits a singularity) at large times.

3.3 Numerical Investigation of the Stability of the Similarity Solutions in Chapter 2

We now arrive at the main purpose of this chapter, namely, a numerical investigation of the stability of the two similarity solutions (2.21) obtained in Chapter 2 for $H_0 = H_{01}$ and $H_0 = H_{02}$, in the case of a sessile rivulet and in the case of a pendent rivulet. To do this we solve the partial differential equation (3.4) (with the surface-tension effects neglected by setting $\sigma = 0$). First, we re-scale (3.4) according to (2.31) so that it becomes

$$h_t = \frac{1}{2} S_g \left[\left(h^3 h_y \right)_y + \lambda \left(h^3 h_x \right)_x \right] - \frac{1}{3} \left(h^3 \right)_x , \tag{3.25}$$

where again $S_g = 1$ corresponds to a sessile rivulet and $S_g = -1$ corresponds to a pendent rivulet, and the new parameter λ, given by

$$\lambda = \frac{2|\cos\alpha|}{3} \left(\frac{\mu}{\rho g \sin^3 \alpha X T} \right)^{\frac{1}{2}} , \tag{3.26}$$

is a measure of slenderness of the rivulet (the smaller the value of λ, the more slender the rivulet is). Note that choosing $\lambda = 0$ corresponds to the non-dimensional version of the partial differential equation (2.16) for a slender rivulet studied in

Chapter 2. In the present computations, we chose λ to be small ($\lambda \ll 1$); specifically, we chose $\lambda = 0.1$. Since $\lambda \neq 0$, perfect agreement cannot be expected between the numerical solutions and the similarity solutions (2.21), but we would like to examine the extent of agreement between these two solutions as time elapses.

3.3.1 Stability of a sessile rivulet ($S_g = 1$)

In the case of a sessile rivulet in $x \leq 0$ with $t < 0$, the similarity solution blows up at $t = 0$ and becomes infinite everywhere. Thus, for the computational domain, X_2 was taken to be 0 and X_1 (< 0) was chosen to be sufficiently far from X_2; also Y was chosen to be sufficiently large that the contact lines of the rivulets remained well away from the domain boundaries $y = \pm Y$ during the evolution.

Using the same numerical procedure as in Section 3.2, we solved equation (3.25). As the initial condition for h we imposed the similarity solution at some chosen time $t = t_0$. As the boundary condition at $x = X_2 = 0$ we imposed simply $h = 0$, thereby preventing the nose of the rivulet from advancing down the plane. At $x = X_1$ (< 0) we imposed a boundary condition in the form of the similarity solution with a small-amplitude perturbation superposed, so that

$$h(X_1, y, t) = h_{\text{ss}}(X_1, y, t)\,[1 + f(y, t)]\,, \tag{3.27}$$

where $h_{\text{ss}}(x, y, t)$ denotes the similarity solution given in (2.21), and $f(y, t)$ (with $|f(y, t)| \ll 1$) denotes the perturbation. In all the rivulets described subsequently f was taken to be sinusoidal in the y direction, either continuously or over a short time interval only; specifically we chose three different types of perturbation at the boundary $x = X_1$, namely

$$f(y, t) = \epsilon \cos\left(\frac{n\pi y}{2a}\right), \tag{3.28}$$

$$f(y, t) = \epsilon \sin\left(\frac{n\pi y}{a}\right), \tag{3.29}$$

and

$$f(y, t) = \begin{cases} \epsilon \cos\left(\dfrac{\pi y}{2a}\right) & \text{for} \quad t \leq t_1, \\ 0 & \text{for} \quad t > t_1, \end{cases} \tag{3.30}$$

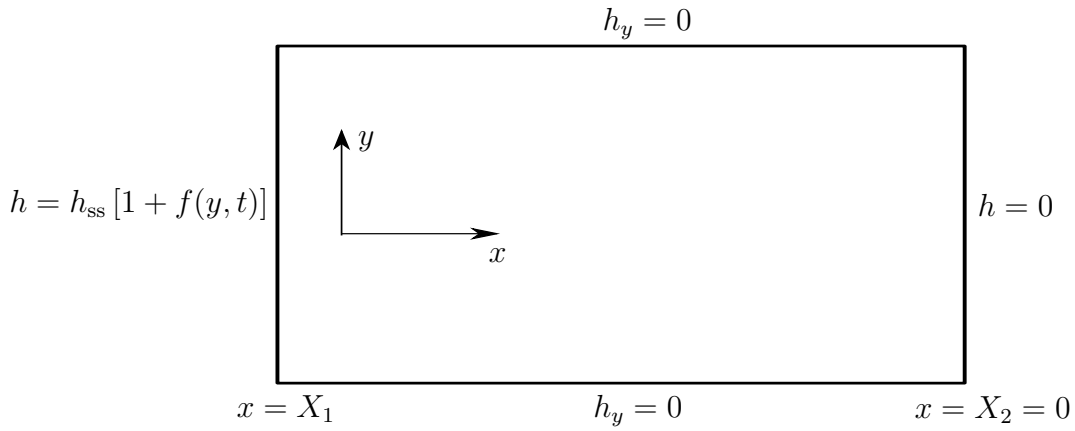

Figure 3.6: Sketch of the computational domain with the prescribed boundary conditions in the case of a sessile rivulet.

where $a = a(x,t)$ is the non-dimensional semi-width of the rivulet given by $(2.33)_2$, and ϵ, n and $t_0 < t_1 < 0$ may be chosen appropriately. At $y = \pm Y$ we imposed the boundary condition $h_y = 0$. These boundary conditions are represented in the sketch of the computational domain shown in Figure 3.6.

For the computations we chose $x = X_1 = -30$ and $t = t_0 = -1$. The computations were run from $t_0 = -1$ until they failed at times between $t = -0.1$ and $t = 0$ (consistent with the fact that the similarity solutions become singular everywhere at $t = 0$). Firstly, we ran the computation without any perturbation at $x = X_1$ (so that $f(y,t) \equiv 0$) with $\lambda = 0.1$. Then, the computations were run with the three different types of perturbation at $x = X_1$ given by equations (3.28), (3.29) and (3.30). This procedure was carried out for both similarity solutions, i.e. for $H_0 = H_{01}$ and $H_0 = H_{02}$.

Similarity solution with $H_0 = H_{01}$

For $H_0 = H_{01} \simeq 0.9995$, Y was taken to be 200, with approximately 180000 mesh elements in the computational domain. We first ran the computation without any perturbation at $x = X_1$. Figures 3.7(a) and (b) show the cross-sectional profiles of an unperturbed rivulet at $x = -20$ and $y = 0$, respectively, at various

times, obtained from the numerical solution of equation (3.25) with $\lambda = 0.1$ (full curves) and the similarity solution (2.21) (dashed curves) for the case $H_0 = H_{01}$. In particular, Figure 3.7 shows that the numerical solutions are in satisfactory agreement with the similarity solutions. The middle height and the width of the numerical solutions are slightly larger than the similarity solutions as time elapses from $t = -1$ to $t = -0.1$. However, as shown in Figure 3.7(a) the maximum height near the leading edge obtained from the numerical solutions is slightly lower than the similarity solutions, since the rivulet tends to spread (its width becoming larger) because $\lambda \neq 0$.

We then imposed the perturbations (3.28) with $\epsilon = 0.01$ and $n = 5$, (3.29) with $\epsilon = 0.05$ and $n = 4$, and (3.30) with $\epsilon = 0.05$ for a short time interval $-1 \leq t \leq -0.9$ at the boundary $x = X_1$. Figures 3.8 and 3.9 show examples of the evolution of perturbed rivulets with continuous perturbations of the form (3.28) and (3.29), respectively, at various times, for $H_0 = H_{01}$. Figures 3.8 and 3.9 show that the rather large perturbation seen in Figures 3.8(a) and 3.9(a) does not grow with x. Figures 3.10(a) and (b) show examples of the evolution of a perturbed rivulet with a perturbation of the form (3.30) for a short time interval $-1 \leq t \leq -0.9$, at various times for $H_0 = H_{01}$. Figure 3.10(b) shows that the perturbation (the smooth "bump" on the free surface) is convected with the flow without growing.

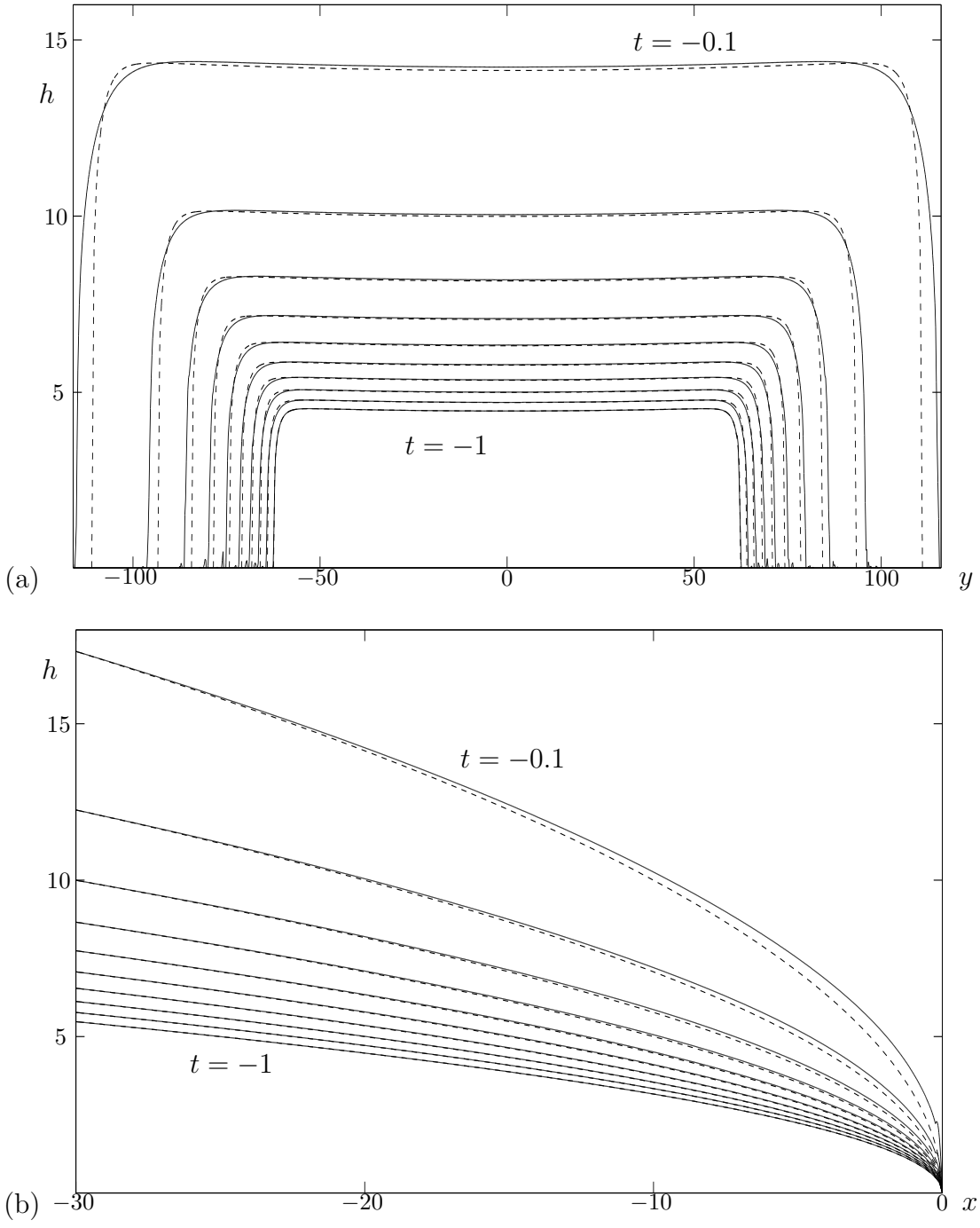

Figure 3.7: Plots of the cross-sectional profiles at (a) $x = -20$ and (b) $y = 0$, at times $t = -1, -0.9, -0.8, \ldots, -0.1$, of an unperturbed rivulet obtained from the numerical solutions of equation (3.25) with $\lambda = 0.1$ (full curves) and the similarity solution (2.21) (dashed curves) for $H_0 = H_{01}$ in the case $X_1 = -30$.

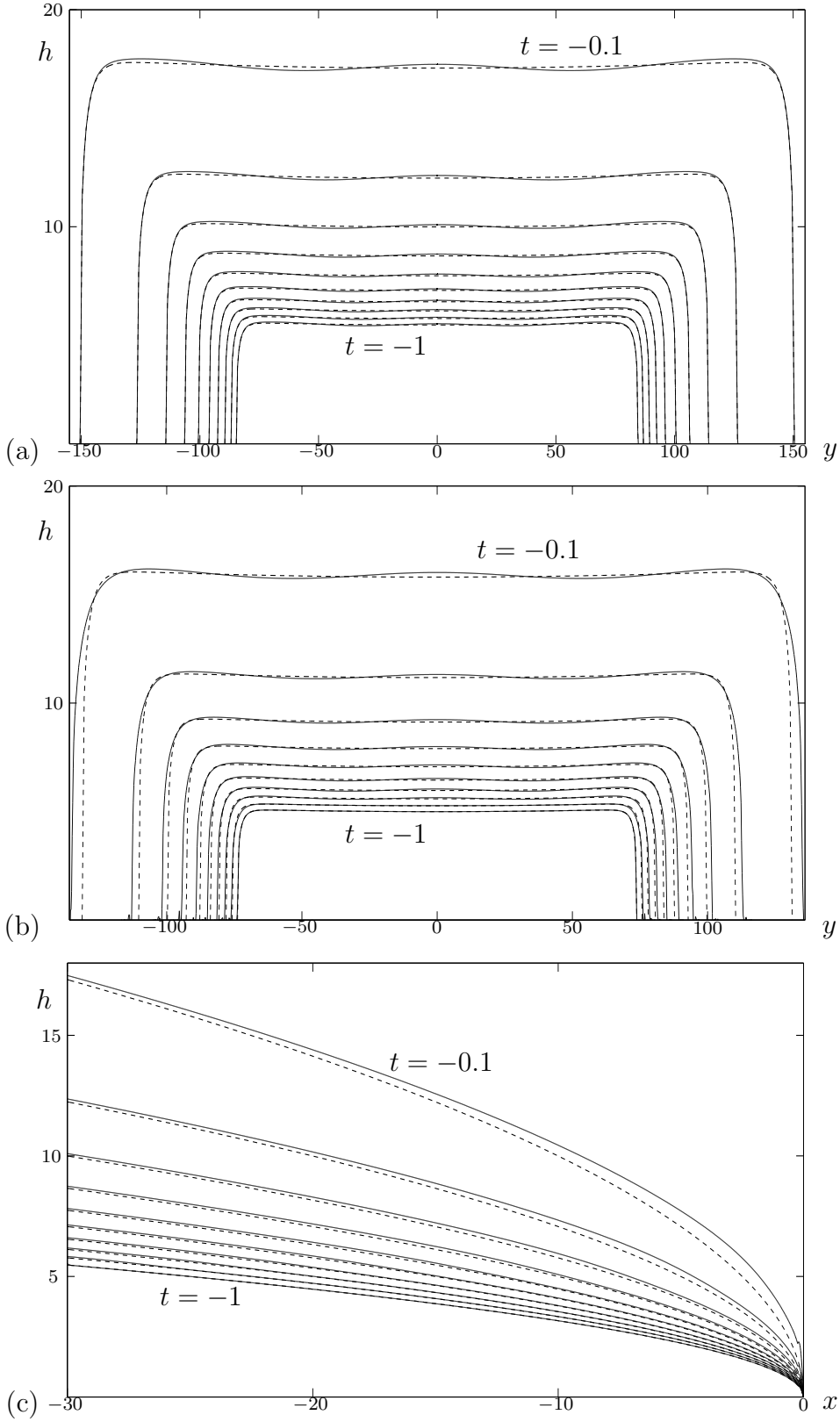

Figure 3.8: Plots of the cross-sectional profiles at (a) $x = -30$, (b) $x = -25$ and (c) $y = 0$, at times $t = -1, -0.9, -0.8, \ldots, -0.1$, of a rivulet perturbed according to (3.28) with $\epsilon = 0.05$ and $n = 5$, in the case $X_1 = -30$ for $H_0 = H_{01}$.

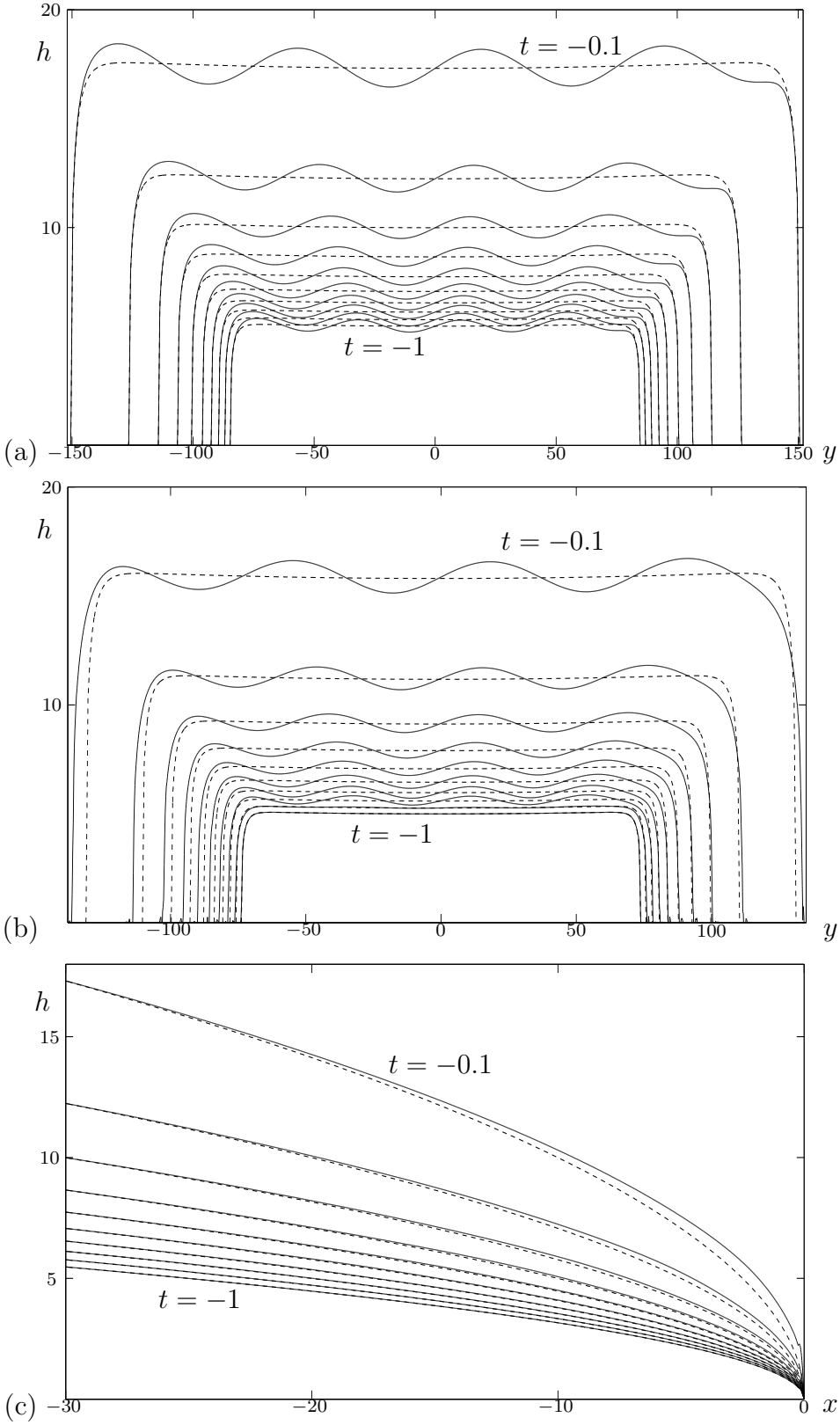

Figure 3.9: Plots of the cross-sectional profiles at (a) $x = -30$, (b) $x = -25$ and (c) $y = 0$, at times $t = -1, -0.9, -0.8, \ldots, -0.1$, of a rivulet perturbed according to (3.29) with $\epsilon = 0.05$ and $n = 4$, in the case $X_1 = -30$ for $H_0 = H_{01}$.

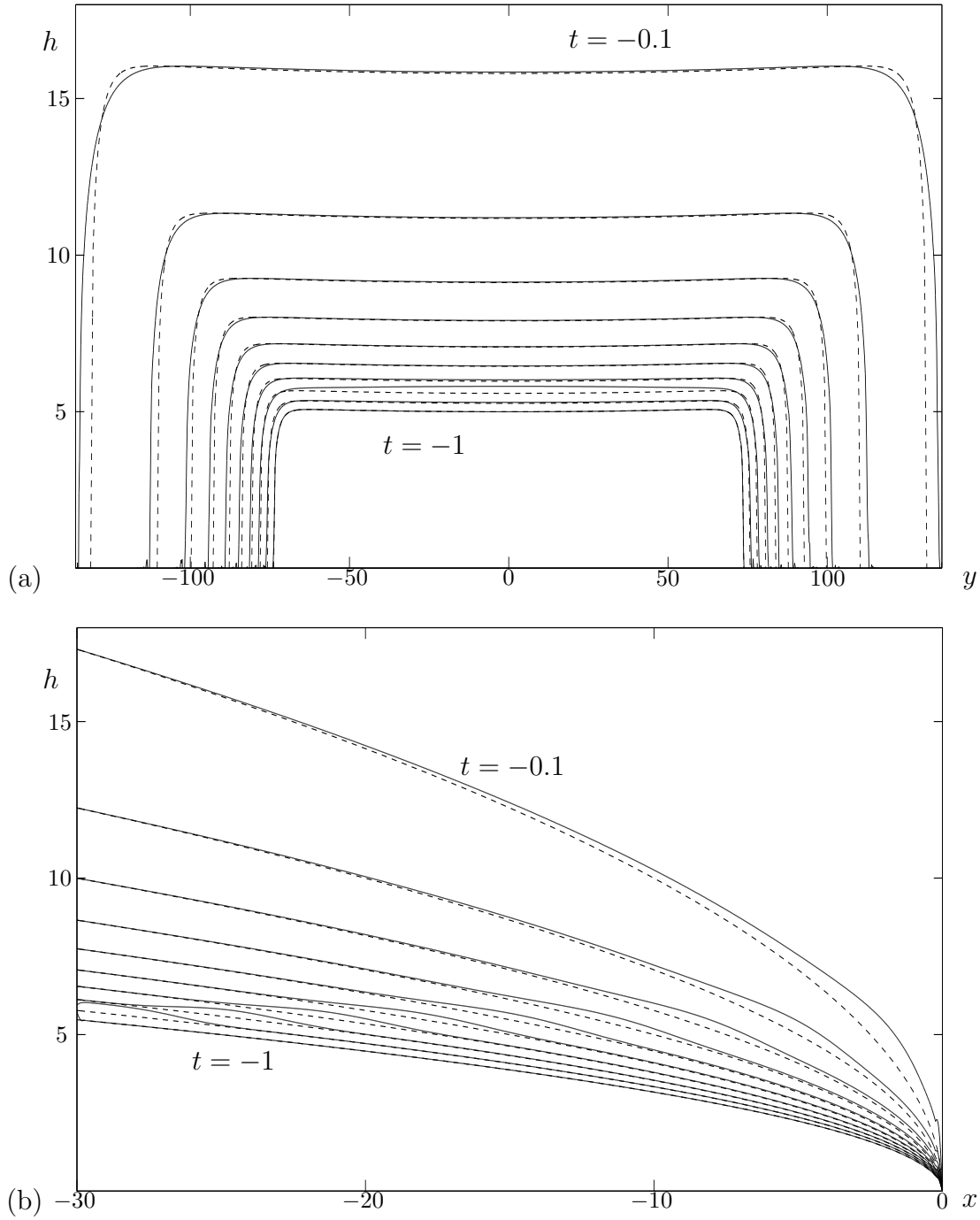

Figure 3.10: Plots of the cross-sectional profiles at (a) $x = -25$ and (b) $y = 0$, at times $t = -1, -0.9, -0.8, \ldots, -0.1$, of a rivulet perturbed according to (3.30) with $\epsilon = 0.05$ for $-1 \leq t \leq -0.9$, in the case $X_1 = -30$ for $H_0 = H_{01}$.

Similarity solution with $H_0 = H_{02}$

For $H_0 = H_{02} \simeq 1.1059$, Y was taken to be 50, with approximately 42000 triangular mesh elements in the computational domain. Figures 3.11(a) and (b) show the cross-sectional profiles of an unperturbed rivulet at $x = -20$ and $y = 0$, respectively, at various times, obtained from the numerical solution of equation (3.25) with $\lambda = 0.1$ (full curves) and the similarity solution (2.21) (dashed curves) for $H_0 = H_{02}$. As before, Figure 3.11 shows that the numerical solutions are in satisfactory agreement with the similarity solutions, the middle height and the width of the numerical solution being slightly larger than the similarity solution as time elapses from $t = -1$ to $t = -0.1$.

We then imposed the perturbations (3.28) with $n = 5$, (3.29) with $n = 3$, and (3.30) for a short time interval $-1 \leq t \leq -0.9$ at the boundary $x = X_1$ with $\epsilon = 0.05$ in each case. Figures 3.12 and 3.13 show examples of the evolution of perturbed rivulets with continuous perturbations of the form (3.28) and (3.29), respectively, at various times for $H_0 = H_{02}$. Again, Figures 3.12 and 3.13 show that the rather large perturbation seen in Figures 3.12(a) and 3.13(a) does not grow with x. Figures 3.14(a) and (b) show examples of the evolution of a perturbed rivulet with a perturbation of the form (3.30) for a short time interval $-1 \leq t \leq -0.95$, at various times, for $H_0 = H_{02}$. Again, these figures demonstrate how the perturbation is convected with the flow without growing.

All of the perturbations applied to the rivulets appear not to grow. Thus, we may conclude from these results that the similarity solutions with both $H_0 = H_{01}$ and $H_0 = H_{02}$ in the case of a sessile rivulet are stable to perturbations of the type investigated.

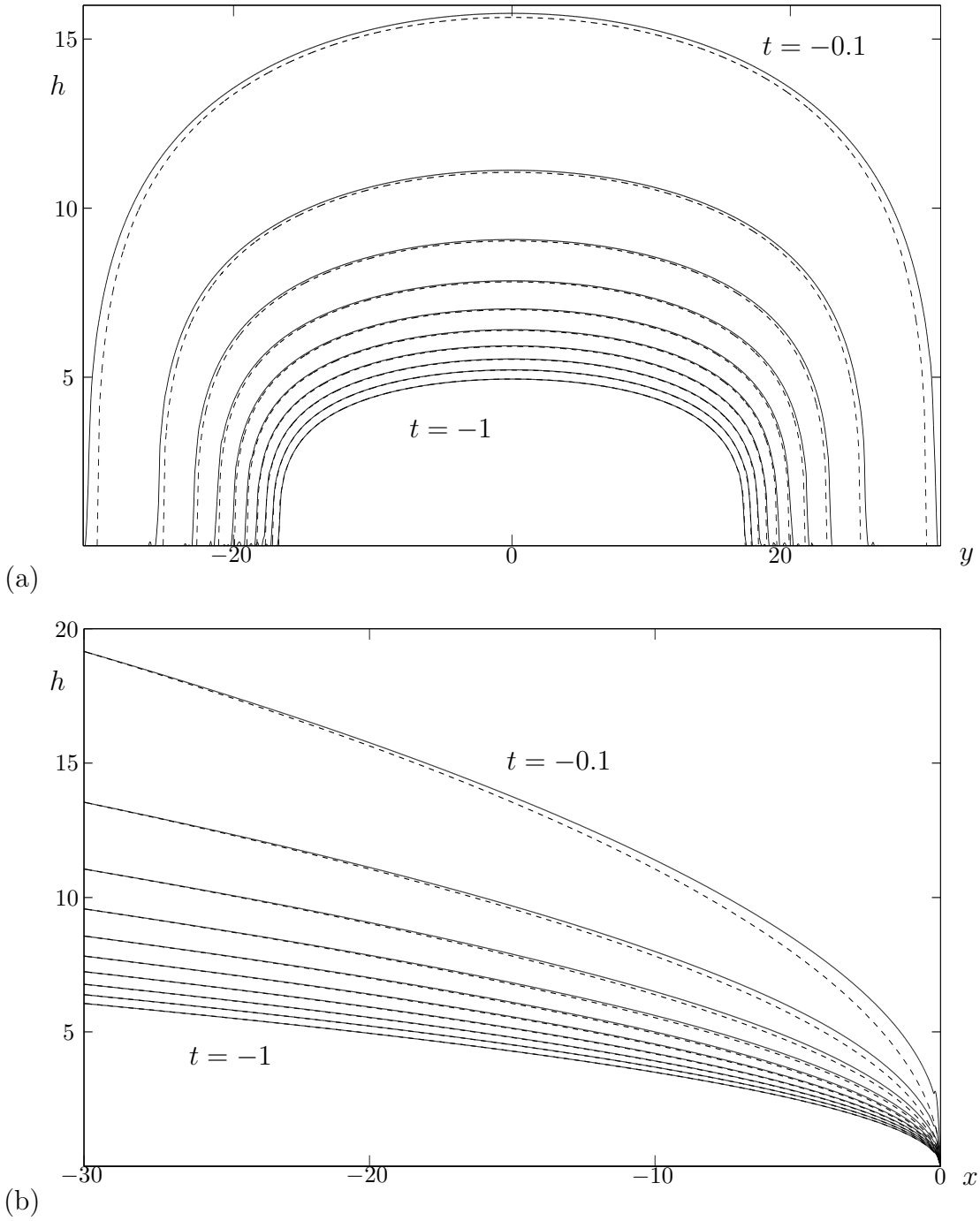

Figure 3.11: Plots of the cross-sectional profiles at (a) $x = -20$ and (b) $y = 0$, at times $t = -1, -0.9, -0.8, \ldots, -0.1$, of an unperturbed rivulet obtained from the numerical solutions of equation (3.25) with $\lambda = 0.1$ (full curves) and the similarity solution (2.21) (dashed curves) for $H_0 = H_{02}$ in the case $X_1 = -30$.

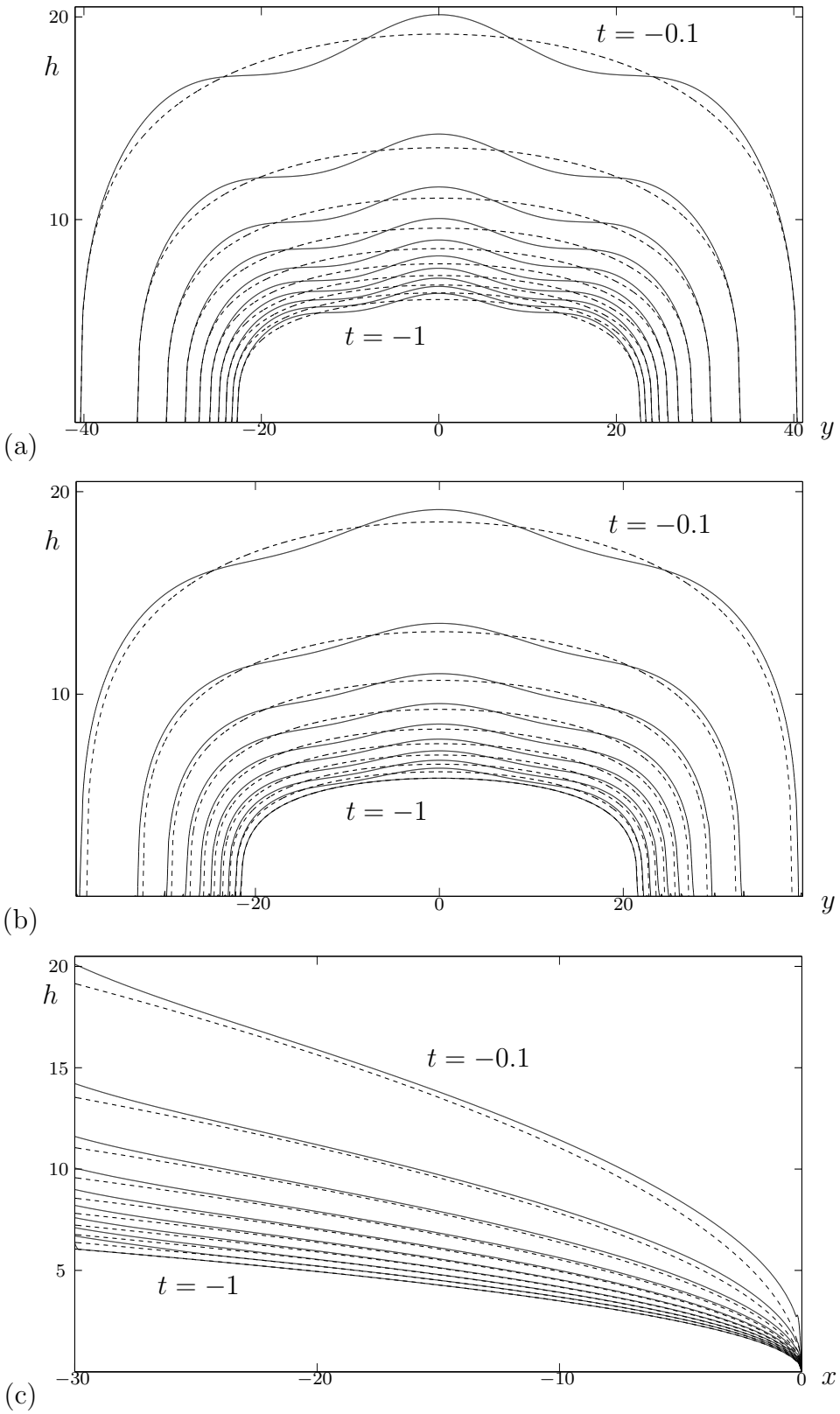

Figure 3.12: Plots of the cross-sectional profiles at (a) $x = -30$, (b) $x = -28$ and (c) $y = 0$, at times $t = -1, -0.9, -0.8, \ldots, -0.1$, of a rivulet perturbed according to (3.28) with $\epsilon = 0.01$ and $n = 5$, in the case $X_1 = -30$ for $H_0 = H_{02}$.

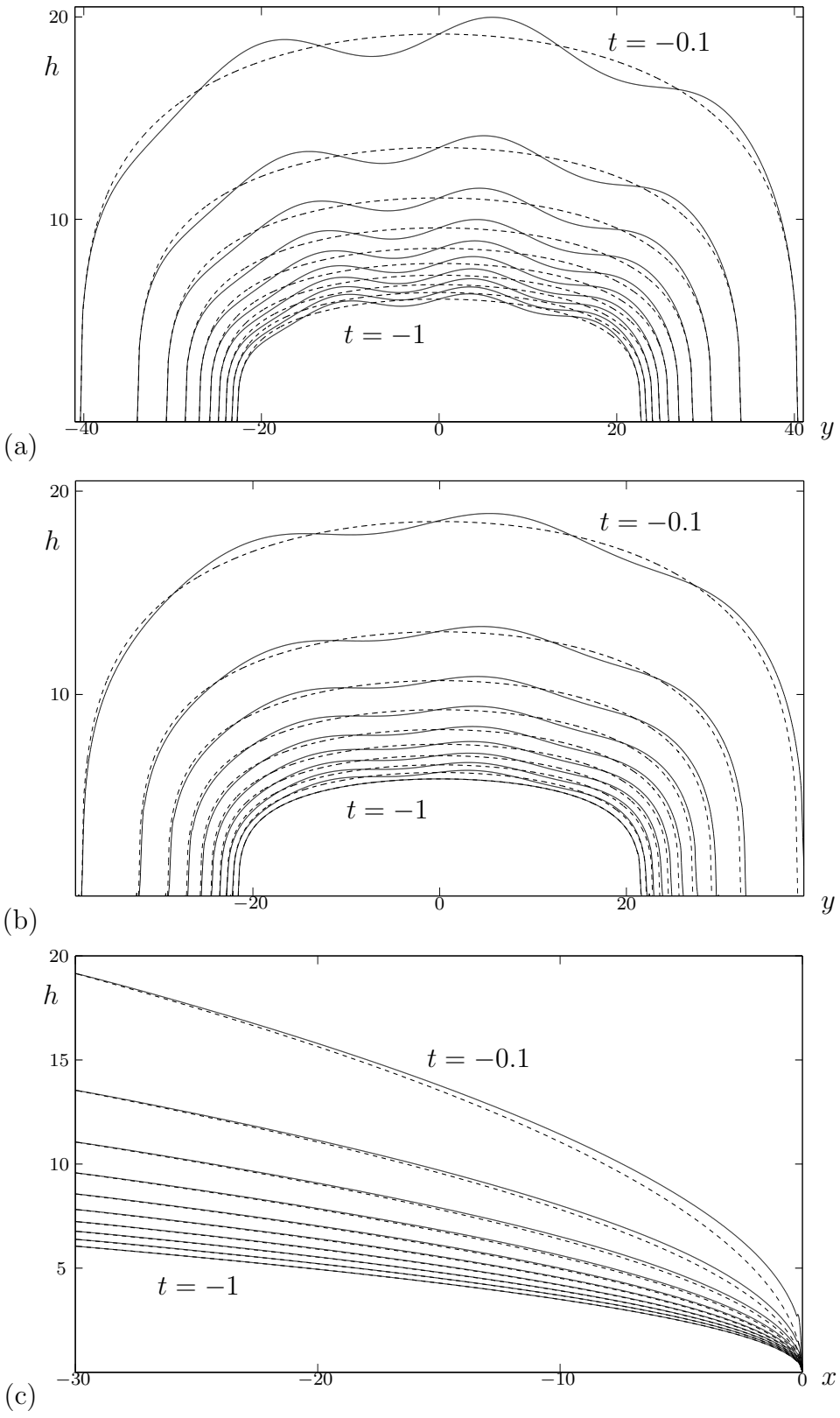

Figure 3.13: Plots of the cross-sectional profiles at (a) $x = -30$, (b) $x = -28$ and (c) $y = 0$, at times $t = -1, -0.9, -0.8, \ldots, -0.1$, of a rivulet perturbed according to (3.29) with $\epsilon = 0.05$ and $n = 3$, in the case $X_1 = -30$ for $H_0 = H_{02}$.

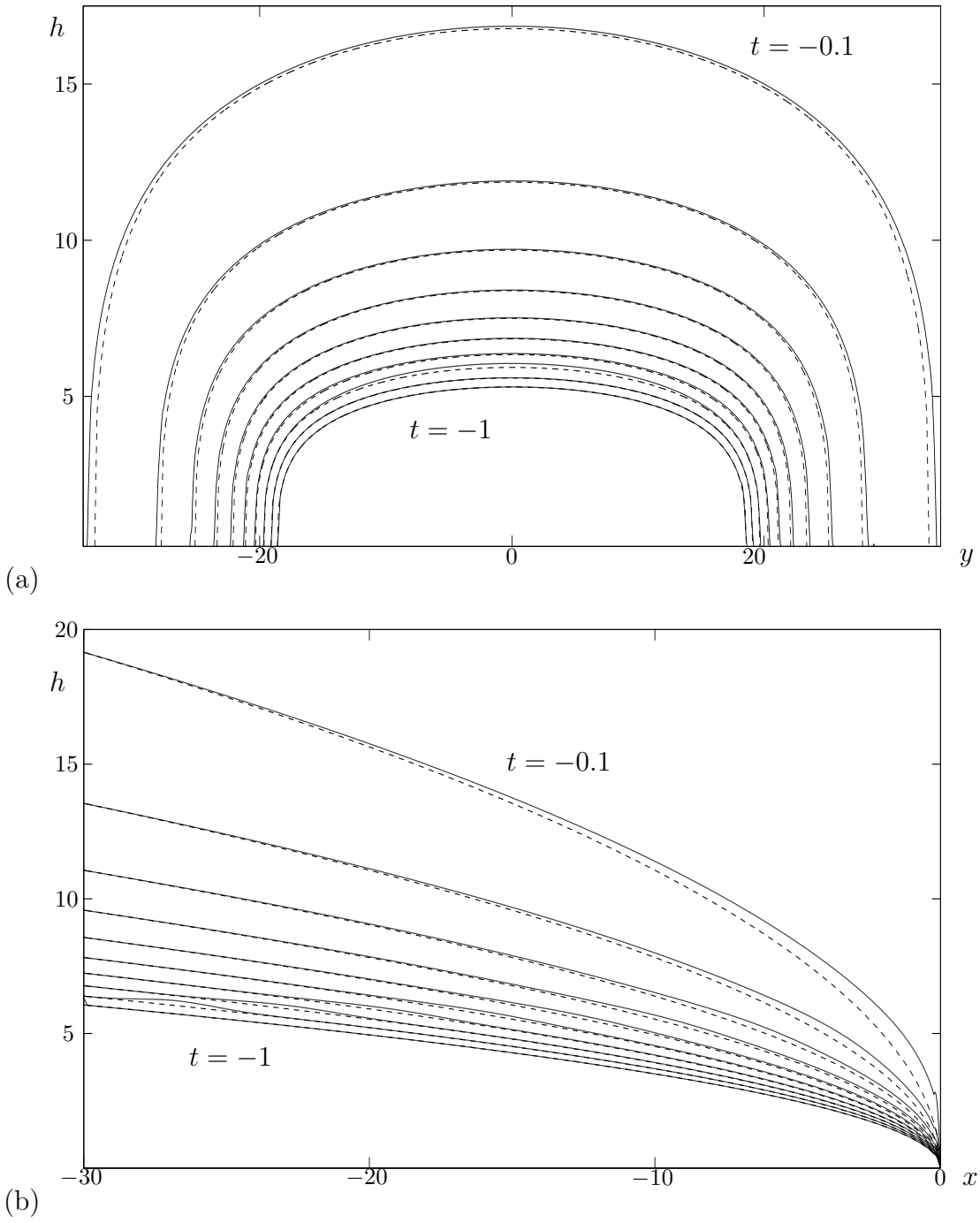

Figure 3.14: Plots of the cross-sectional profiles at (a) $x = -23$ and (b) $y = 0$, at times $t = -1, -0.9, -0.8, \ldots, -0.1$, of a rivulet perturbed according to (3.30) with $\epsilon = 0.05$ for $-1 \leq t \leq -0.95$, in the case $X_1 = -30$ for $H_0 = H_{02}$.

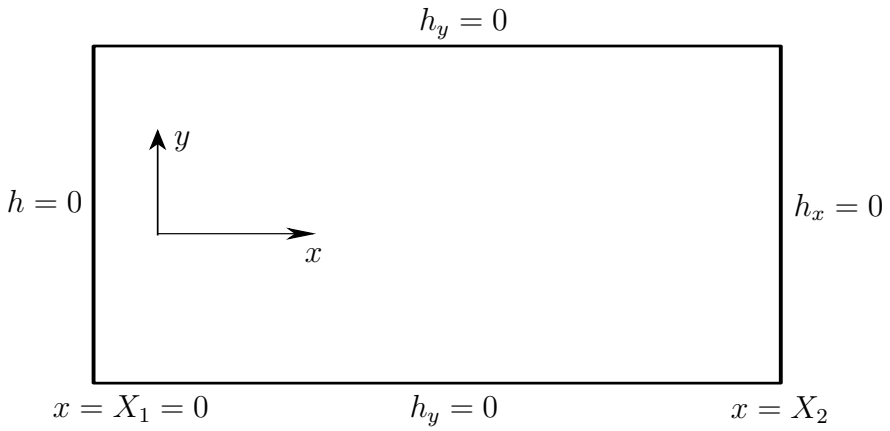

Figure 3.15: Sketch of the computational domain with the prescribed boundary conditions in the case of a pendent rivulet.

3.3.2 Stability of a pendent rivulet ($S_g = -1$)

An analogous procedure was used to consider the stability of a pendent rivulet in $x \geq 0$ with $t > 0$, for both $H_0 = H_{01}$ and $H_0 = H_{02}$. In this case X_1 was taken to be 0 and X_2 was chosen to be sufficiently far from X_1; also Y was chosen to be sufficiently large that the contact lines of the rivul ets remained well away from the domain boundaries $y = \pm Y$ during the evolution.

As the initial condition for h we imposed the similarity solution at some chosen time $t = t_0$. As the boundary condition at $x = X_1 = 0$ we imposed simply $h = 0$. At $x = X_2$ (> 0) we imposed $h_x = 0$ to allow flux to escape at this boundary. At $y = \pm Y$ we imposed simply $h_y = 0$. The boundary conditions discussed above are represented in the sketch of the computational domain shown in Figure 3.15. For the computations we chose $x = X_2 = 30$ and $t = t_0 = 1$, and the computations were run with $\lambda = 0.1$.

However, unlike in the case of a sessile rivulet described previously, the numerical computations for a pendent rivulet ran for only a very small time, and failed to produce any reliable results for either $H_0 = H_{01}$ or $H_0 = H_{02}$ even without any perturbation being applied at the boundary. Several attempts were made to

resolve this problem, such as changing the numerical method, the boundary conditions at $x = X_1$ and $x = X_2$, values of tolerances, number of mesh elements and time steps, and including a precursor layer as an initial condition, but all to no avail. Using COMSOL, we then computed solutions to one-dimensional linear "forwards-diffusion" and "backwards-diffusion" problems, for which the governing equations are given by

$$h_t = Sh_{xx}, \tag{3.31}$$

where $S = 1$ corresponds to a forwards-diffusion equation, and $S = -1$ corresponds to a backwards-diffusion equation, subject to the boundary conditions

$$h(0,t) = 1, \qquad h(1,t) = 0, \tag{3.32}$$

and the initial condition

$$h(x,0) = 0. \tag{3.33}$$

We found that for the forwards-diffusion problem, the computation produced a reliable result; however, for the backwards-diffusion problem, which is highly unstable, the computational process failed in the same manner as in our problem. Thus we may speculate that for our equation (3.25) with $S_g = -1$, which is a nonlinear backwards-diffusion equation, the similarity solutions for both $H_0 = H_{01}$ and $H_0 = H_{02}$ in the case of a pendent rivulet are unstable.

Chapter 4

Unsteady Gravity-Driven Rivulets of a Non-Newtonian Power-Law Fluid

In this chapter we generalise our approach in Chapter 2 to consider unsteady gravity-driven flow of thin slender non-uniform rivulets of a non-Newtonian power-law fluid on an inclined plane.

4.1 Problem Formulation

Consider the unsteady flow of a thin slender rivulet of a non-Newtonian power-law fluid with constant density ρ and variable viscosity $\mu = \mu_0 \gamma^{N-1}$, where μ_0 is a constant, γ is the local shear rate and $N > 0$ is the power-law index, down a planar substrate inclined at an angle α $(0 < \alpha < \pi)$ to the horizontal subject to gravitational acceleration g when surface-tension effects are negligible. As described previously in Chapter 1, when $0 < N < 1$ the fluid is shear thinning, when $N > 1$ it is shear thickening, and when $N = 1$ the special case of a Newtonian fluid with constant viscosity μ_0 is recovered.

We adopt the same Cartesian coordinates $Oxyz$ as in Chapter 2 and denote

the free surface profile of the rivulet by $z = h(x, y, t)$. We restrict our attention to flows that are symmetric about $y = 0$ with (unknown) semi-width $a = a(x, t)$, so that $h = 0$ at the contact lines $y = \pm a$. The geometry of the problem is again given by Figure 2.1.

With the usual lubrication approximation the velocity (u, v, w) and pressure p of the fluid satisfy the governing equations

$$u_x + v_y + w_z = 0, \tag{4.1}$$

$$(\mu u_z)_z + \rho g \sin\alpha = 0, \tag{4.2}$$

$$(\mu v_z)_z - p_y = 0, \tag{4.3}$$

$$-p_z - \rho g \cos\alpha = 0. \tag{4.4}$$

Since the rivulet is taken to be thin and slender, and since we will be considering only problems in which u_z is always non-negative, the shear rate is given by $\gamma = u_z$ approximately (see Appendix A), and therefore the viscosity μ in (4.2) and (4.3) is given by $\mu = \mu_0 u_z^{N-1}$. Equations (4.1)–(4.4) are to be integrated subject to the boundary conditions of no slip and no penetration (2.5) on the substrate $z = 0$, and balances of normal and tangential stress on the free surface:

$$p = p_{\mathrm{a}}, \quad \mu u_z = \mu v_z = 0 \quad \text{on} \quad z = h, \tag{4.5}$$

where p_{a} denotes atmospheric pressure, together with the kinematic condition (2.7) on the free surface and the zero-mass-flux condition (2.9) at the contact lines $y = \pm a$.

Integrating equations (4.2)–(4.4) subject to boundary conditions (2.5) and (4.5) yields

$$p = p_{\mathrm{a}} + \rho g \cos\alpha\,(h - z)\,, \tag{4.6}$$

$$u = \frac{N}{N+1}\left(\frac{\rho g \sin\alpha}{\mu_0}\right)^{\frac{1}{N}}\left[h^{\frac{N+1}{N}} - (h-z)^{\frac{N+1}{N}}\right], \tag{4.7}$$

$$v = -\frac{N}{N+1}p_y\left(\frac{(\rho g \sin\alpha)^{1-N}}{\mu_0}\right)^{\frac{1}{N}}\left[h^{\frac{N+1}{N}} - (h-z)^{\frac{N+1}{N}}\right], \tag{4.8}$$

and substituting (4.7) and (4.8) into (2.8) gives

$$\bar{u} = \frac{N}{2N+1}\left(\frac{\rho g \sin\alpha}{\mu_0}\right)^{\frac{1}{N}} h^{\frac{2N+1}{N}}, \quad \bar{v} = -\frac{Np_y}{2N+1}\left(\frac{(\rho g \sin\alpha)^{1-N}}{\mu_0}\right)^{\frac{1}{N}} h^{\frac{2N+1}{N}}. \tag{4.9}$$

The kinematic condition (2.7) then yields the governing partial differential equation for h, namely

$$\frac{2N+1}{N}\mu_0\left(\frac{\rho g \sin\alpha}{\mu_0}\right)^{\frac{N-1}{N}} h_t = \rho g \cos\alpha \left[h^{\frac{2N+1}{N}} h_y\right]_y - \rho g \sin\alpha \left[h^{\frac{2N+1}{N}}\right]_x. \tag{4.10}$$

Once this is solved for h, the complete solution for p, u and v is given by (4.6)–(4.8). Note that in the special case $N = 1$, equation (4.10) reduces to (2.16) studied in Chapter 2. From (4.9) we have $\bar{u} = 0$ at $y = \pm a$, so that the zero-mass-flux condition (2.9) reduces to $\bar{v} = 0$ at $y = \pm a$; thus we have the contact-line conditions

$$h = 0 \quad \text{at} \quad y = \pm a, \qquad h^{\frac{2N+1}{N}} h_y \to 0 \quad \text{as} \quad y \to \pm a. \tag{4.11}$$

We shall be concerned with unsteady similarity solutions of (4.10) of the form

$$h = h_0 \left|\frac{x}{t}\right|^{\frac{N}{N+1}} H(\eta), \qquad y = y_0 \left(\frac{|x|^{2N+1}}{|t|^N}\right)^{\frac{1}{2(N+1)}} \eta, \tag{4.12}$$

where H (≥ 0) and η are defined to be dimensionless, and h_0 and y_0 are positive constants, which, without loss of generality, we may write as

$$h_0 = \left(\frac{\mu_0}{\rho g \sin\alpha}\right)^{\frac{1}{N+1}}, \qquad y_0 = \left(\frac{N+1}{2N+1}\right)^{\frac{1}{2}} \left(\frac{\mu_0 |\cos\alpha|^{N+1}}{\rho g \sin^{N+2}\alpha}\right)^{\frac{1}{2(N+1)}}. \tag{4.13}$$

Hence (4.10) reduces to the ordinary differential equation

$$S_t\left[\frac{1}{2}\eta H' - H\right] = S_g\left[H^{\frac{2N+1}{N}} H'\right]' + S_x\left[\frac{1}{2}\eta (H^{\frac{2N+1}{N}})' - H^{\frac{2N+1}{N}}\right] \tag{4.14}$$

for H, generalising equation (2.22), where a dash denotes differentiation with respect to η. As in Chapter 2, we again introduced the notation $S_t = \text{sgn}(t) = \pm 1$, $S_g = \text{sgn}(\cos\alpha) = \pm 1$ and $S_x = \text{sgn}(x) = \pm 1$.

For a symmetric rivulet, appropriate boundary and symmetry conditions are given by (2.23). The (unknown) position of the contact line is denoted by $\eta = \eta_0$, so that with (4.11) we have

$$H = 0 \quad \text{at} \quad \eta = \eta_0, \qquad H^{\frac{2N+1}{N}} H' \to 0 \quad \text{as} \quad \eta \to \eta_0. \tag{4.15}$$

The middle height of the rivulet, $h_{\mathrm{m}} = h(x, 0, t)$, and the semi-width of the rivulet vary with x and t according to

$$h_{\mathrm{m}} = h_0 \left|\frac{x}{t}\right|^{\frac{N}{N+1}} H_0, \qquad a = y_0 \left(\frac{|x|^{2N+1}}{|t|^N}\right)^{\frac{1}{2(N+1)}} \eta_0, \tag{4.16}$$

predicting that at any time t the rivulet widens or narrows according to $|x|^{(2N+1)/2(N+1)}$ and thickens or thins according to $|x|^{N/(N+1)}$ as it flows down the plane; moreover, at any station x, it widens or narrows according to $|t|^{-N/2(N+1)}$ and thickens or thins according to $|t|^{-N/(N+1)}$.

The volume flux of fluid across any section x = constant, denoted by Q, is given by

$$Q = 2\int_0^a \bar{u}\,\mathrm{d}y = \frac{N(N+1)^{\frac{1}{2}}}{(2N+1)^{\frac{3}{2}}} \left(\frac{\mu_0^3 |\cos\alpha|^{N+1} |x|^{3(2N+1)}}{\rho^3 g^3 \sin^{N+4}\alpha\, |t|^{5N+2}}\right)^{\frac{1}{2(N+1)}} I, \tag{4.17}$$

and the cross-sectional area of the rivulet at any station x, denoted by A, is given by

$$A = 2\int_0^a h\,\mathrm{d}y = \left(\frac{N+1}{2N+1}\right)^{\frac{1}{2}} \left(\frac{\mu_0^3 |\cos\alpha|^{N+1} |x|^{4N+1}}{\rho^3 g^3 \sin^{N+4}\alpha\, |t|^{3N}}\right)^{\frac{1}{2(N+1)}} J, \tag{4.18}$$

where the constants I and J are defined by

$$I = 2\int_0^{\eta_0} H^{\frac{2N+1}{N}}\,\mathrm{d}\eta, \qquad J = 2\int_0^{\eta_0} H\,\mathrm{d}\eta. \tag{4.19}$$

Conditions for the rivulet to be thin and slender are that the length scales in the x, y and z directions (namely $|x|$, a and h_{m}, respectively) satisfy $h_{\mathrm{m}} \ll a \ll |x|$, which in turn requires that

$$\frac{|x||t|^N \rho g |\cos\alpha|^{N+1}}{\mu_0 \sin^N \alpha} \gg 1, \qquad \frac{|x||t|^N \rho g \sin^{N+2}\alpha}{\mu_0 |\cos\alpha|^{N+1}} \gg 1, \tag{4.20}$$

showing that $|x||t|^N$ must be sufficiently large (and that α cannot be close to 0, $\pi/2$ or π).

For simplicity in plotting results, we now re-scale according to

$$x = Xx^*, \qquad y = y_0\left(\frac{X^{2N+1}}{T^N}\right)^{\frac{1}{2(N+1)}} y^*, \qquad z = h_0\left(\frac{X}{T}\right)^{\frac{N}{N+1}} z^*, \qquad t = Tt^*,$$
$$h = h_0\left(\frac{X}{T}\right)^{\frac{N}{N+1}} h^*, \qquad h_{\rm m} = h_0\left(\frac{X}{T}\right)^{\frac{N}{N+1}} h_{\rm m}^*, \qquad a = y_0\left(\frac{X^{2N+1}}{T^N}\right)^{\frac{1}{2(N+1)}} a^*,$$
$$Q = \frac{N(N+1)^{\frac{1}{2}}}{(2N+1)^{\frac{3}{2}}}\left(\frac{\mu_0^3|\cos\alpha|^{N+1}X^{3(2N+1)}}{\rho^3 g^3 \sin^{N+4}\alpha\, T^{5N+2}}\right)^{\frac{1}{2(N+1)}} Q^*,$$
$$A = \left(\frac{N+1}{2N+1}\right)^{\frac{1}{2}}\left(\frac{\mu_0^3|\cos\alpha|^{N+1}X^{4N+1}}{\rho^3 g^3 \sin^{N+4}\alpha\, T^{3N}}\right)^{\frac{1}{2(N+1)}} A^*, \tag{4.21}$$

where X (>0) and T (>0) are length and time scales, respectively, which we may choose arbitrarily. Then, with superscript stars dropped immediately for clarity, the solution (4.12) takes the slightly simpler form

$$h = \left|\frac{x}{t}\right|^{\frac{N}{N+1}} H(\eta), \qquad y = \left(\frac{|x|^{2N+1}}{|t|^N}\right)^{\frac{1}{2(N+1)}} \eta, \tag{4.22}$$

with H satisfying (4.14)–(4.15); from (4.16) the middle height $h_{\rm m}$ and semi-width a are given by

$$h_{\rm m} = \left|\frac{x}{t}\right|^{\frac{N}{N+1}} H_0, \qquad a = \left(\frac{|x|^{2N+1}}{|t|^N}\right)^{\frac{1}{2(N+1)}} \eta_0, \tag{4.23}$$

and from (4.17) and (4.18) the flux Q and cross-sectional area A become

$$Q = \left(\frac{|x|^{3(2N+1)}}{|t|^{5N+2}}\right)^{\frac{1}{2(N+1)}} I, \qquad A = \left(\frac{|x|^{4N+1}}{|t|^{3N}}\right)^{\frac{1}{2(N+1)}} J. \tag{4.24}$$

4.2 Results

A closed-form solution of the ordinary differential equation (4.14) is not available, and so it must, in general, be solved numerically for H subject to the boundary conditions (2.23) and (4.15), where H_0 and η_0 are parameters to be determined.

As far as the differential equation (4.14) is concerned, any choice of a set of values of S_t, S_g and S_x leads to the same mathematical problem as the set $-S_t$, $-S_g$ and $-S_x$ (though the two sets of values lead to different physical interpretations of the solutions). Therefore there are four distinct cases to consider; however, we shall show below that by using the same arguments as in Chapter 2, only the case $S_t = -S_g = S_x$ can lead to physically realisable solutions.

Near $\eta = 0$ we find straightforwardly that H satisfies

$$H = H_0 + \frac{S_x H_0^{\frac{N+1}{N}} - S_t}{2S_g H_0^{\frac{N+1}{N}}}\eta^2 + O\left(\eta^4\right) \tag{4.25}$$

as $\eta \to 0$, and near the contact line $\eta = \eta_0$ we find that H satisfies either

$$H \sim \left[-\frac{(2N+1)S_t\eta_0}{2NS_g}(\eta_0 - \eta)\right]^{\frac{N}{2N+1}}, \tag{4.26}$$

valid only when $S_t = -S_g$, or

$$H \sim C(\eta_0 - \eta)^{\frac{N}{3N+1}} - \frac{(3N+1)S_t\eta_0}{2\,(4N+1)\,C^{\frac{N+1}{N}}S_g}(\eta_0 - \eta)^{\frac{2N}{3N+1}} \tag{4.27}$$

as $\eta \to \eta_0$, where C is a positive constant.[1] However, the zero-mass-flux condition in (4.15) requires that $C = 0$, and so cases where $S_t = S_g$, in which (4.27) is the only possible behaviour near the contact line, are immediately eliminated. Determining the physical solutions from the condition $C = 0$ will be discussed shortly.

In cases where $S_t = -S_g$, at any stationary points of the free surface (where $H' = 0$) equation (4.14) gives

$$H'' = H^{-\frac{N+1}{N}} - S_x S_t, \tag{4.28}$$

[1]Note that both (4.26) and (4.27) have $H' \to \infty$ as $\eta \to \eta_0$, showing that the lubrication approximation again fails near the contact lines.

provided that $H \neq 0$. Since the rivulet has two contact lines, at $\eta = \pm\eta_0$, the function H (≥ 0) must have at least one maximum in $|\eta| \leq \eta_0$. In the case where $S_t = -S_g = -S_x$, equation (4.28) shows that any stationary point of H is a minimum, so there can be no solution for H with a maximum, and therefore this case is eliminated. In the case where $S_t = -S_g = S_x$, equation (4.28) shows that any stationary point for which $H < 1$ ($H > 1$) is a minimum (maximum); later, we will show from the numerically determined profiles H that there are in fact only two types of solution in this case, one with a minimum at $\eta = 0$ and two symmetrically placed maxima when $H_0 < 1$ (double-humped profiles), and one with a single maximum at $\eta = 0$ when $H_0 > 1$ (single-humped profiles).

With all other cases eliminated, the only case that could lead to physically realisable solutions is the one where $S_t = -S_g = S_x$, corresponding to a converging sessile rivulet in $x < 0$ with $t < 0$, or a diverging pendent rivulet in $x > 0$ with $t > 0$. In this case, equation (4.14) becomes

$$\frac{N}{3N+1}\left(H^{\frac{3N+1}{N}}\right)'' = \frac{1}{2}\eta\left(H^{\frac{2N+1}{N}} - H\right)' - \left(H^{\frac{2N+1}{N}} - H\right), \qquad (4.29)$$

which was solved numerically by means of a shooting method subject to (2.23) to find η_0 for a given value of H_0 (> 0). Again, as a check, some of the computations were also performed by means of a finite-difference method, with Newton iteration to solve the resulting nonlinear algebraic equations; the solutions obtained in this way were found to be in good agreement with those obtained by the shooting method.

Figure 4.1 shows η_0 as a function of H_0 for several values of N. For each value of N there is a solution for every H_0 except in a narrow window $H_{01} < H_0 < H_{02}$, where $H_{01} = H_{01}(N) < 1$ and $H_{02} = H_{02}(N) > 1$, in which there is no solution. This window is larger for larger values of N, with H_{01} and H_{02} taking correspondingly smaller and larger values, respectively. For example, for $N = 1/20$, we found that $H_{01} \simeq 0.9999$ and $H_{02} \simeq 1.0178$, whereas for $N = 20$, we found that $H_{01} \simeq 0.9993$ and $H_{02} \simeq 1.1409$; furthermore, in the Newtonian case

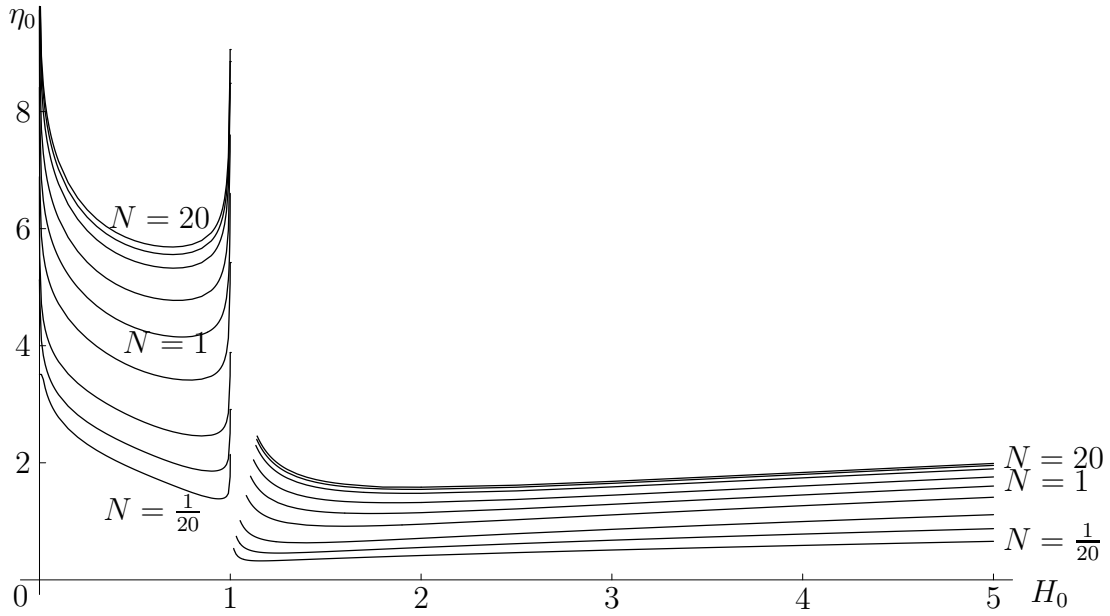

Figure 4.1: Plot of η_0 as a function of H_0 for $N = 1/20$, $1/10$, $1/5$, $1/2$, 1, 2, 5, 10 and 20.

($N = 1$), $H_{01} \simeq 0.9995$ and $H_{02} \simeq 1.1059$, in agreement with the values given in Chapter 2.

In order to choose the physically realisable solutions from this family of solutions, we impose the condition (4.15), or equivalently the condition $C = 0$. As discussed in Chapter 2, a simple way to determine C accurately is by integrating equation (4.14) from $\eta = 0$ to $\eta = \eta_0$ and using (2.23) and (4.15) to obtain

$$\frac{3\,(3N+1)}{2N}\int_0^{\eta_0}\left(H^{\frac{2N+1}{N}} - H\right)\,\mathrm{d}\eta = \begin{cases} 0 & \text{for (4.26)}, \\ C^{\frac{3N+1}{N}} & \text{for (4.27)}, \end{cases} \tag{4.30}$$

so that the coefficient C in (4.27) is given by

$$C = \left[\frac{3\,(3N+1)}{2N}\int_0^{\eta_0}\left(H^{\frac{2N+1}{N}} - H\right)\,\mathrm{d}\eta\right]^{\frac{N}{3N+1}} = \left[\frac{3(3N+1)}{4N}\,(I-J)\right]^{\frac{N}{3N+1}}, \tag{4.31}$$

which we use to find C from the numerical solution for H obtained with a given value of H_0. Also these values of C were checked against those obtained from the behaviour of the numerical solution near $\eta = \eta_0$, according to (4.27).

Figure 4.2 shows a plot of C calculated from (4.31) as a function of H_0 for the values of N used in Figure 4.1. From this plot, we see that for each value of N there are precisely two values of H_0 for which $C = 0$, namely $H_0 = H_{01}$ and $H_0 = H_{02}$. Thus we arrive at our main result: there are precisely two physically realisable solutions of the type sought for an unsteady rivulet, these solutions corresponding to the two values $H_0 = H_{01}$ (with associated $\eta_0 = \eta_{01}$) and $H_0 = H_{02}$ (with associated $\eta_0 = \eta_{02}$).

Equation (4.31) shows that I and J satisfy $I = J$ for both $H_0 = H_{01}$ and $H_0 = H_{02}$, and Figure 4.3 shows plots of I $(= J)$ as a function of N.

Figures 4.4 and 4.5 show numerically calculated profiles $H = H(\eta)$ of the two physically realisable solutions with $H_0 = H_{01}$ and $H_0 = H_{02}$, respectively, for a range of values of N. These two sets of solutions have different types of profiles, namely a (barely discernible) double-humped profile for $H_0 = H_{01}$ and a single-humped profile for $H_0 = H_{02}$, consistent with the earlier discussion of stationary points.

Figure 4.6 shows a plot of H_{01} and H_{02} as functions of N; the inset shows an enlargement of the H_{01} curve, as the details are hard to distinguish at this scale. Figure 4.7 shows a plot of η_{01} and η_{02} as functions of N; we see that $\eta_{01} > \eta_{02}$ for all N.

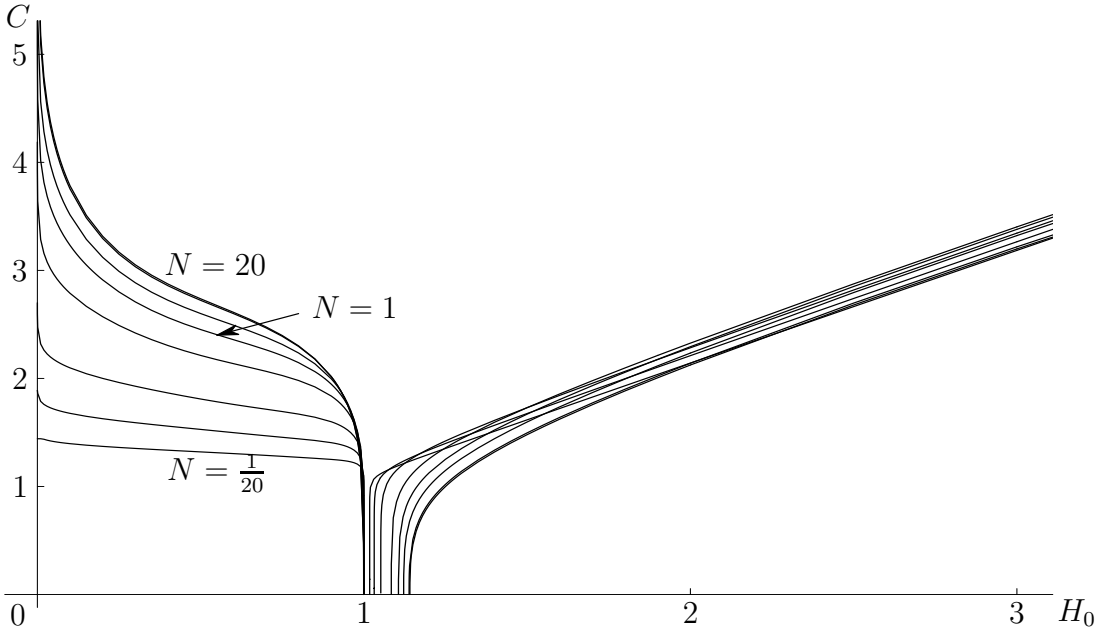

Figure 4.2: Plot of C in (4.31) as a function of H_0 for $N = 1/20$, $1/10$, $1/5$, $1/2$, 1, 2, 5, 10 and 20.

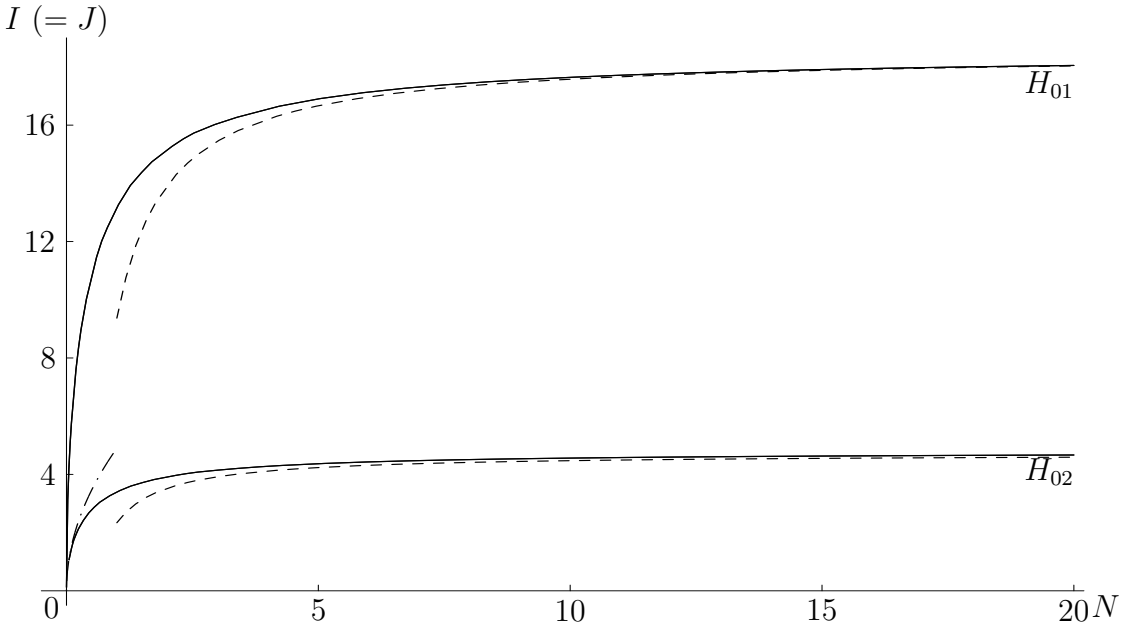

Figure 4.3: Plot of I $(= J)$ given by (4.19) as a function of N for $H_0 = H_{01}$ and $H_0 = H_{02}$, together with the asymptotic solutions (4.38) in the limit $N \to 0^+$ (represented by a dashed-dotted curve) and (4.46) in the limit $N \to \infty$ (represented by dashed curves).

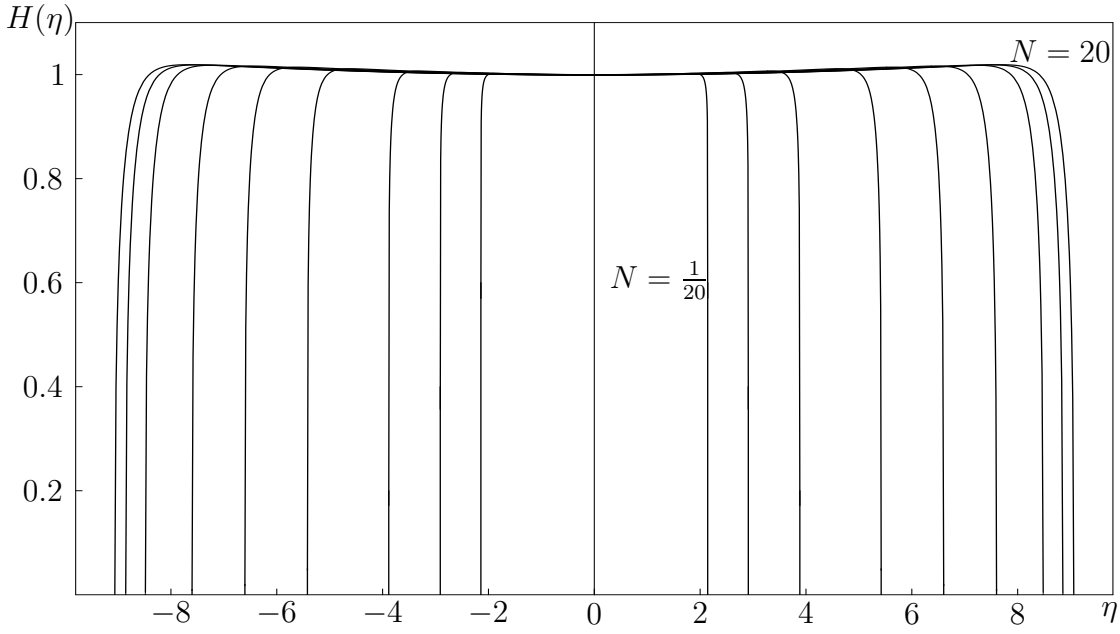

Figure 4.4: Numerically calculated profiles $H = H(\eta)$ for the case $H_0 = H_{01}$, for $N = 1/20$, $1/10$, $1/5$, $1/2$, 1, 2, 5, 10 and 20.

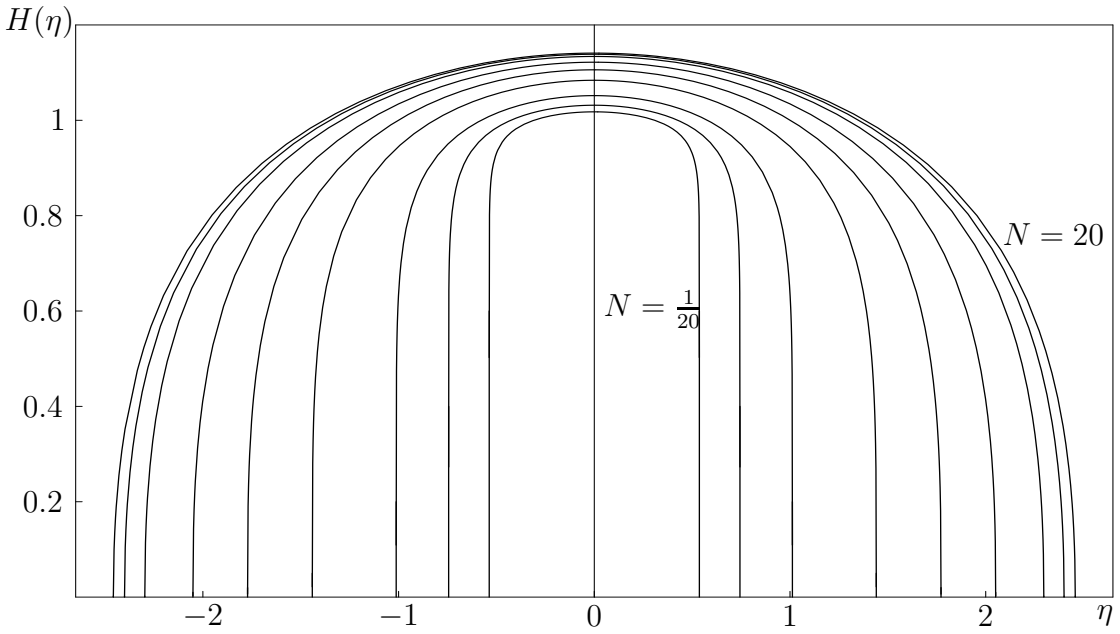

Figure 4.5: As in Figure 4.4, but for the case $H_0 = H_{02}$.

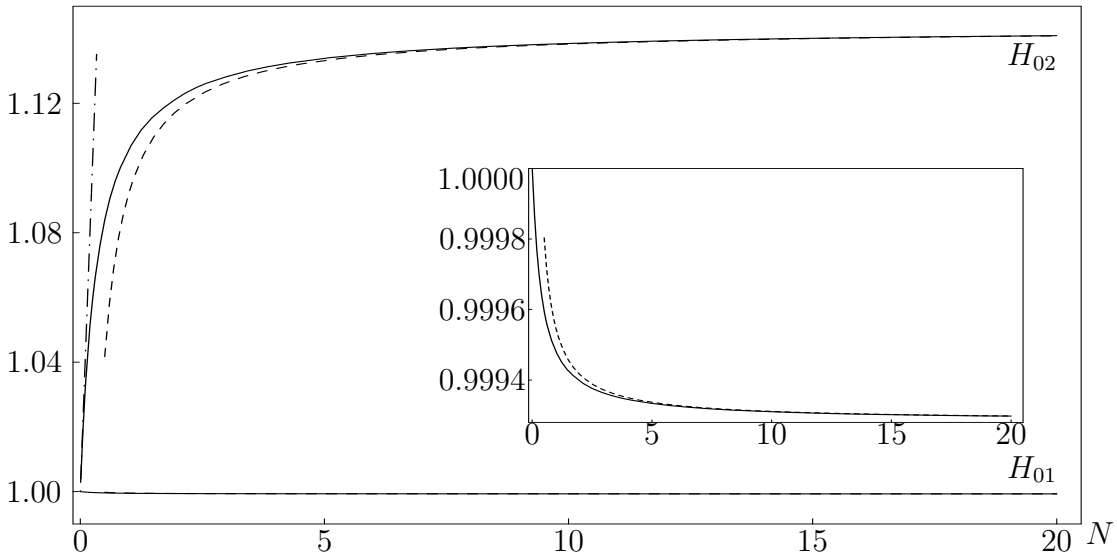

Figure 4.6: Plots of H_{01} and H_{02} as functions of N, together with the asymptotic solutions $(4.37)_2$ in the limit $N \to 0^+$ (represented by a dashed-dotted curve) and $(4.39)_2$ in the limit $N \to \infty$ (represented by dashed curves). The results for H_{01} are difficult to distinguish at this scale, and so the inset shows an enlargement of the H_{01} curve.

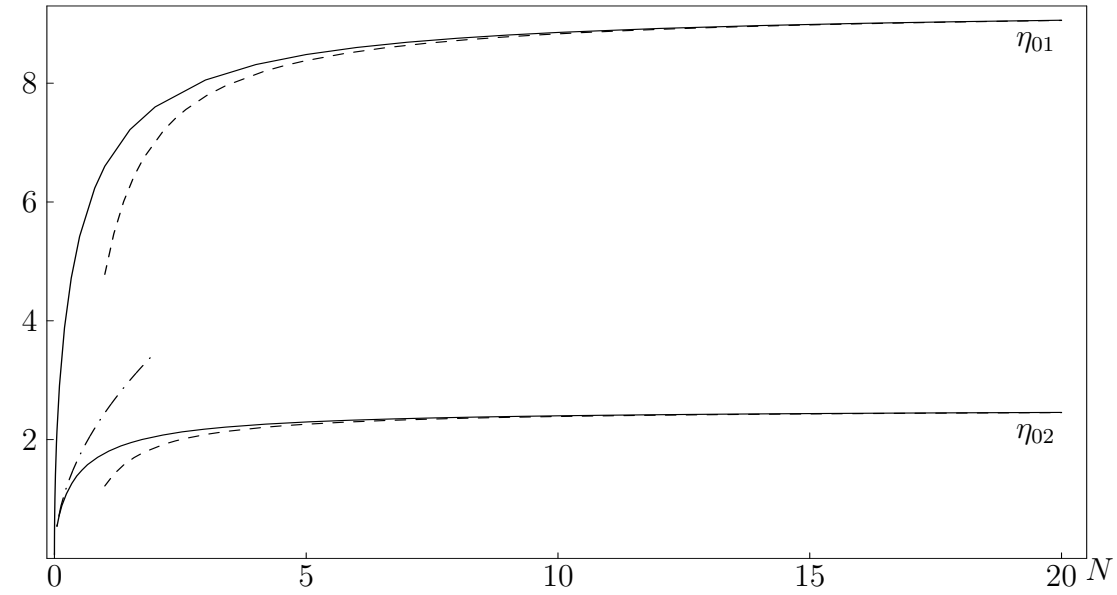

Figure 4.7: Plots of η_{01} and η_{02} as functions of N, together with the asymptotic solutions $(4.37)_3$ in the limit $N \to 0^+$ (represented by a dashed-dotted curve) and $(4.39)_3$ in the limit $N \to \infty$ (represented by dashed curves).

4.2.1 Asymptotic solution in the limit $N \to 0^+$

In this subsection we shall discuss the behaviour of the solution for H in the limit of a strongly shear-thinning fluid, $N \to 0^+$.

For the case in which $H_0 = H_{02}$ and N is small, our numerical solutions suggest that $\eta_0 \sim \sqrt{N}$ and that $H = 1 + O(N)$ and $H^{\frac{2N+1}{N}} = O(1)$ except very close to the contact line $\eta = \eta_0$. Therefore in the limit $N \to 0^+$ we re-scale H and η according to

$$H = 1 + N\hat{h}(\hat{\eta}), \quad \eta = \sqrt{N}\hat{\eta}, \quad \eta_{02} = \sqrt{N}\hat{\eta}_{02}. \tag{4.32}$$

With the result $\lim_{N\to 0}(1 + N\hat{h})^{1/N} = e^{\hat{h}} = O(1)$, equation (4.29) then yields

$$\left(e^{\hat{h}}\right)'' - \frac{1}{2}\hat{\eta}\left(e^{\hat{h}}\right)' + e^{\hat{h}} = 1 \tag{4.33}$$

at leading order in N, whose solution subject to the boundary condition $\hat{h}'(0) = 0$ is

$$\hat{h} = \log\left(e^{\hat{h}_0} + \frac{1 - e^{\hat{h}_0}}{2}\hat{\eta}^2\right), \tag{4.34}$$

where $\hat{h}_0 = \hat{h}(0) = (H_{02} - 1)/N$ (> 0) is the (unknown) value of $\hat{h}$ at $\hat{\eta} = 0$. The solution (4.34) is valid provided that $e^{\hat{h}_0} + \frac{1}{2}(1 - e^{\hat{h}_0})\hat{\eta}^2 > 0$, which requires $\hat{\eta} < \hat{\eta}_{02}$, where

$$\hat{\eta}_{02} = \left(\frac{2e^{\hat{h}_0}}{e^{\hat{h}_0} - 1}\right)^{\frac{1}{2}}, \tag{4.35}$$

and we note that $\hat{h} = 0$ at $\hat{\eta} = \sqrt{2}$, and that $\hat{\eta}_{02} > \sqrt{2}$.

To determine $\hat{h}_0$ we use equation (4.31) with $C = 0$ (that is, $I = J$), leading to $\hat{h}_0 = \log(3/2)$. Then equations (4.34) and (4.35) become

$$\hat{h} = \log\left(\frac{6 - \hat{\eta}^2}{4}\right), \qquad \hat{\eta}_{02} = \sqrt{6}, \tag{4.36}$$

and hence to first order we have

$$H \sim 1 + N\log\left[\frac{3}{2}\left(1 - \frac{\eta^2}{\eta_{02}^2}\right)\right], \quad H_{02} \sim 1 + N\log\frac{3}{2}, \quad \eta_{02} \sim \sqrt{6N}, \tag{4.37}$$

in the limit $N \to 0^+$. Lastly the integrals I and J in (4.19) satisfy

$$I \sim 2\int_0^{\sqrt{N}\hat{\eta}_{02}} \frac{6N - \eta^2}{4N}\,\mathrm{d}\eta = 2\sqrt{6N}, \quad J \sim 2\sqrt{N}\hat{\eta}_{02} = 2\sqrt{6N} \tag{4.38}$$

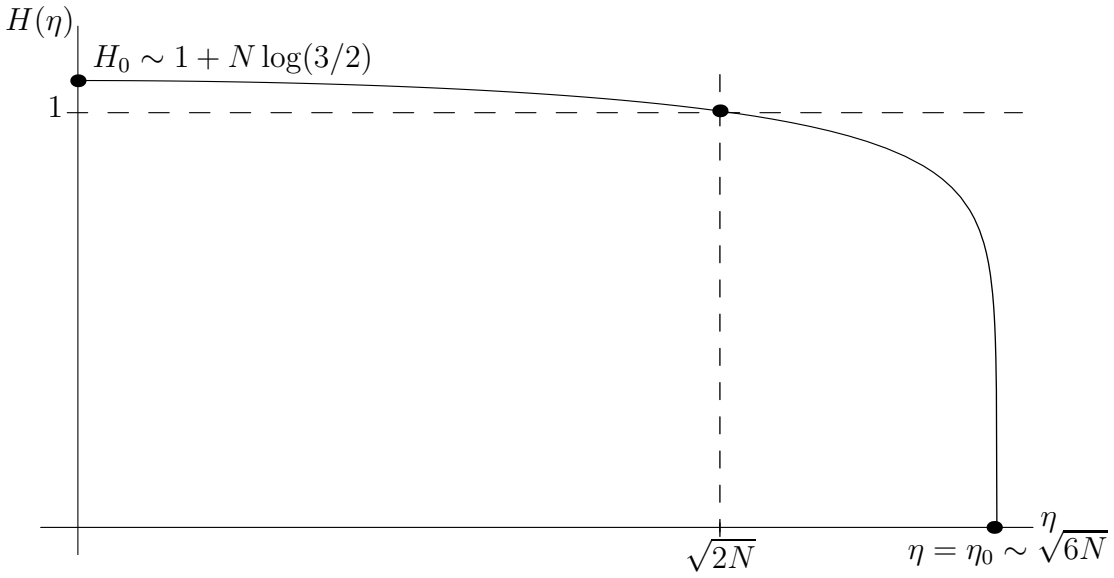

Figure 4.8: Sketch of the asymptotic solution (4.37) for H to $O(N)$ in the limit $N \to 0^+$ for $H_0 = H_{02}$.

in the limit $N \to 0^+$; there is a boundary layer in the solution for H near $\eta = \eta_0$, but it does not contribute to these integrals to this order.

A sketch of the asymptotic solution for H given in (4.37) is shown in Figure 4.8, and Figure 4.9 shows a comparison between profiles H computed numerically (represented by full curves) and the asymptotic solution (4.37) in the limit $N \to 0^+$ (represented by dashed curves) in the cases $N = 1/2$ and $N = 1/20$; the asymptotic solution is in good agreement with the exact numerical solution away from the contact line.

The asymptotic forms of H_{02} and η_{02} in the limit $N \to 0^+$ given in (4.37) are included in Figures 4.6 and 4.7 as dashed-dotted curves, and similarly the asymptotic forms for I $(= J)$ are included in Figure 4.3 as a dashed-dotted curve.

Numerical calculations indicate that the behaviour of the solution for H in the case $H_0 = H_{01}$ in the limit $N \to 0^+$ is somewhat similar to (4.37) but with multiplicative factors and terms in $\log N$ which we have not been able to determine with certainty.

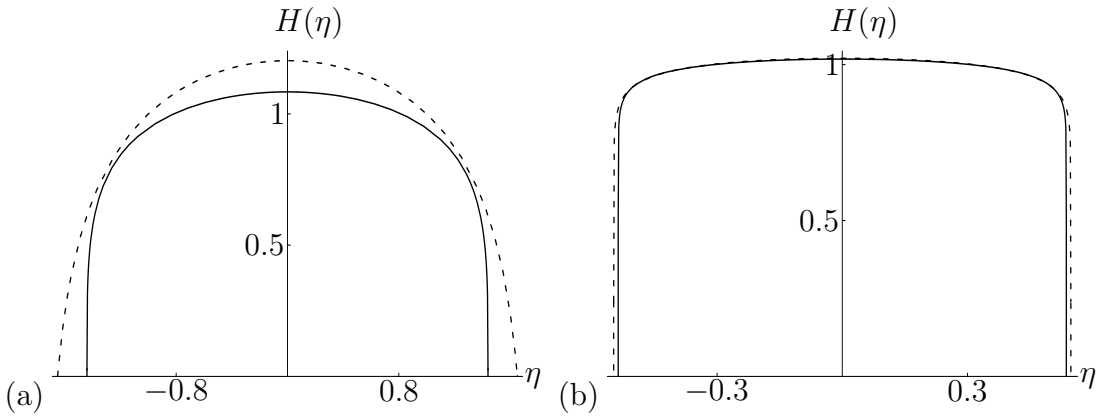

Figure 4.9: Profiles H for the case $H_0 = H_{02}$ obtained numerically (full curves) and from the asymptotic solution to $O(N)$ in the limit $N \to 0^+$ given by (4.37) (dashed curves) for (a) $N = 1/2$ and (b) $N = 1/20$.

4.2.2 Asymptotic solution in the limit $N \to \infty$

In the limit of a strongly shear-thickening fluid, $N \to \infty$, the solutions for both $H_0 = H_{01}$ and $H_0 = H_{02}$ may be expressed as regular expansions in powers of $1/N$ about the solutions for $1/N = 0$, and so we write

$$\begin{aligned} H(\eta) &= \bar{H}_0 + \frac{1}{N}\bar{H}_1 + O\left(\frac{1}{N^2}\right), \\ H_{0k} &= \bar{H}_{00} + \frac{1}{N}\bar{H}_{01} + O\left(\frac{1}{N^2}\right), \\ \eta_{0k} &= \bar{\eta}_{00} + \frac{1}{N}\bar{\eta}_{01} + O\left(\frac{1}{N^2}\right) \end{aligned} \tag{4.39}$$

for $k = 1$ and 2. Then equation (4.29) gives

$$\frac{1}{2}\eta\bar{H}_0' - \bar{H}_0 = -\left(\bar{H}_0^2\bar{H}_0'\right)' + \frac{1}{2}\eta(\bar{H}_0^2)' - \bar{H}_0^2 \tag{4.40}$$

at leading order in $1/N$, and

$$\begin{aligned} \left(\bar{H}_0^2\bar{H}_1\right)'' + \frac{1}{2}\eta\left[\left(1-2\bar{H}_0\right)\bar{H}_1\right]' - \left(1-2\bar{H}_0\right)\bar{H}_1 &= \left(\frac{1}{2}\eta\bar{H}_0' - \bar{H}_0\right)\log\bar{H}_0 \\ &- \bar{H}_0\bar{H}_0'\left(\bar{H}_0' - \frac{1}{2}\eta\right) \end{aligned} \tag{4.41}$$

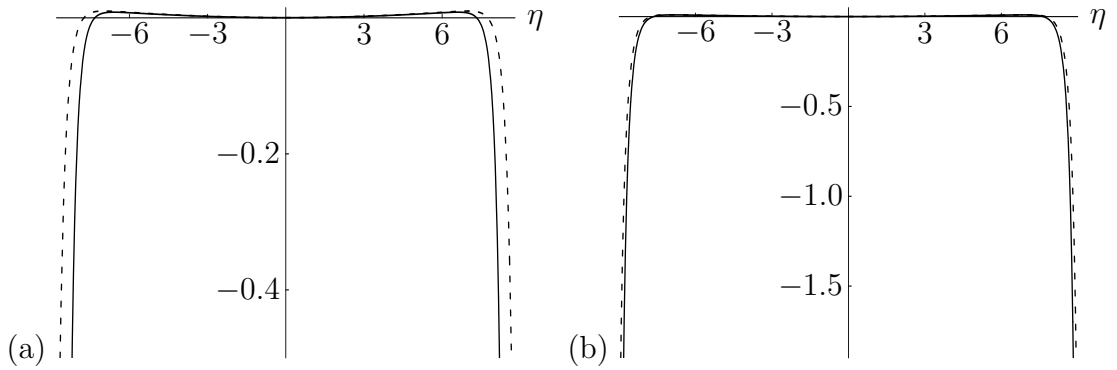

Figure 4.10: Asymptotic solution in the limit $N \to \infty$ for the case $H_0 = H_{01}$: comparison between $\bar{H}_1$ (dashed curves) and $N(H - \bar{H}_0)$ (full curves) for (a) $N = 5$ and (b) $N = 20$.

at first order. Equations (4.40) and (4.41) were solved numerically subject to the boundary conditions

$$\bar{H}_0(0) = \bar{H}_{00}, \quad \bar{H}_0'(0) = 0, \quad \bar{H}_1(0) = \bar{H}_{01}, \quad \bar{H}_1'(0) = 0, \tag{4.42}$$

where the constants $\bar{H}_{00}$ and $\bar{H}_{01}$ are chosen so that conditions obtained from (4.31) with $C = 0$, namely

$$\int_0^{\bar{\eta}_{00}} (\bar{H}_0^2 - \bar{H}_0)\, \mathrm{d}\eta = 0 \tag{4.43}$$

and

$$\int_0^{\bar{\eta}_{00}} \left[\bar{H}_1 \left(1 - 2\bar{H}_0\right) - \bar{H}_0^2 \log \bar{H}_0\right] \mathrm{d}\eta = 0, \tag{4.44}$$

are satisfied. For $H_0 = H_{01}$, we find that $\bar{H}_{00} \simeq 0.9993$, $\bar{\eta}_{00} \simeq 9.2811$ and $\bar{H}_{01} \simeq 0.0002592$; for $H_0 = H_{02}$, we find that $\bar{H}_{00} \simeq 1.1434$, $\bar{\eta}_{00} \simeq 2.5190$ and $\bar{H}_{01} \simeq -0.05084$. Figure 4.10 shows comparisons between $\bar{H}_1$ and $N(H - \bar{H}_0)$ for $N = 5$ and $N = 20$, respectively, for $H_0 = H_{01}$, and Figure 4.11 shows the corresponding results for $H_0 = H_{02}$; the asymptotic solutions are in good agreement with the exact numerical solutions for both $H_0 = H_{01}$ and $H_0 = H_{02}$. The corresponding asymptotic forms of H_{01}, H_{02}, η_{01} and η_{02} in the limit $N \to \infty$ are included in Figures 4.6 and 4.7 as dashed curves. Also using these asymptotic solutions we

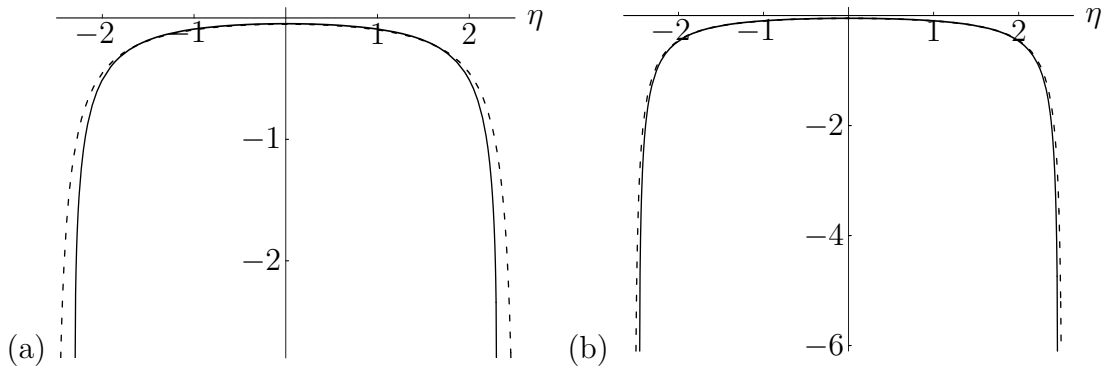

Figure 4.11: As in Figure 4.10, but for the case $H_0 = H_{02}$.

find that

$$I \sim 2\int_0^{\bar{\eta}_{00}} \left[\bar{H}_0^2 + \frac{1}{N}\left(\bar{H}_0^2 \log \bar{H}_0 + 2\bar{H}_0\bar{H}_1\right)\right] \mathrm{d}\eta, \quad J \sim 2\int_0^{\bar{\eta}_{00}} \left(\bar{H}_0 + \frac{1}{N}\bar{H}_1\right) \mathrm{d}\eta \tag{4.45}$$

in the limit $N \to \infty$, so that

$$I = J \sim a + \frac{1}{N}b, \tag{4.46}$$

where $a \simeq 18.4903$ and $b \simeq -9.1214$ for $H_0 = H_{01}$, and $a \simeq 4.7804$ and $b \simeq -2.3697$ for $H_0 = H_{02}$; these asymptotic solutions for I $(= J)$ in the limit $N \to \infty$ are included in Figure 4.3 as dashed curves.

4.3 Discussion

We have obtained unsteady similarity solutions for gravity-driven flow of a thin slender rivulet of a power-law fluid down an inclined plane. We found that there are physically realisable solutions only in the case $S_t = -S_g = S_x$, and then there are two distinct solutions for each value of the power-law index N, namely one for which $H_0 = H_{01}$, with a double-humped cross-sectional profile, and one for which $H_0 = H_{02}$, with a single-humped cross-sectional profile.

Physically, the case $S_t = -S_g = S_x = 1$ corresponds to pendent rivulets in $x > 0$ with $t > 0$, whereas the case $S_t = -S_g = S_x = -1$ corresponds to sessile

rivulets in $x < 0$ with $t < 0$. However, results of a numerical study of the stability of corresponding similarity solutions for a Newtonian fluid in Chapter 3 suggest that the sessile case is stable but that the pendent case is unstable. Presumably the same is true in the non-Newtonian case, that is, only the sessile case $S_t = -S_g = S_x = -1$ is likely to be stable. Figure 4.12 shows three-dimensional plots of the free surface $z = h$ in the cases $H_0 = H_{01}$ and $H_0 = H_{02}$ for $N = 5$, at times $t = -100$, -10 and -1, for the sessile case $S_t = -S_g = S_x = -1$; the insets show the cross-sectional profiles.

Each solution predicts that at time t, the rivulet (in $x < 0$) narrows according to $(-x)^{(2N+1)/2(N+1)}$ and thins according to $(-x)^{N/(N+1)}$ as it flows down the plane, the nose of the rivulet remaining stationary at O at all time. At any station x, the rivulet widens according to $(-t)^{N/2(N+1)}$ and thickens according to $(-t)^{N/(N+1)}$, for $t < 0$; at $t = 0$, both solutions exhibit a finite-time singularity, becoming infinite everywhere at that instant.

So far we have interpreted each of our solutions as representing an infinitely long rivulet, involving an infinite volume of fluid. As described previously in Chapter 2, we may alternatively interpret each solution as representing a rivulet of (prescribed) finite volume, by truncating it at some finite length $L = L(t)$, so that it occupies $-L \leq x \leq 0$. The volume of fluid in such a rivulet, denoted by V, is given by

$$V = \int_{-L}^{0} \int_{-a}^{a} h \, \mathrm{d}y \, \mathrm{d}x = \frac{2}{3} \left(\frac{N+1}{2N+1} \right)^{\frac{3}{2}} \left(\frac{\mu_0^3 |\cos\alpha|^{N+1} L^{3(2N+1)}}{\rho^3 g^3 \sin^{N+4}\alpha |t|^{3N}} \right)^{\frac{1}{2(N+1)}} I; \quad (4.47)$$

thus the length L of the rivulet at time t is given by

$$L = \left[\left(\frac{2N+1}{N+1} \right)^{N+1} \left(\frac{9V^2 \sin\alpha}{4I^2 |\cos\alpha|} \right)^{\frac{N+1}{3}} \frac{\rho g \sin\alpha}{\mu_0} \right]^{\frac{1}{2N+1}} |t|^{\frac{N}{2N+1}}, \quad (4.48)$$

generalising equations (2.96) and (2.97), respectively.

Lastly, we also used the approach described for the rivulet to investigate whether there are corresponding similarity solutions for the rather different physical context of unsteady gravity-driven flow of an infinitely wide thin film of a

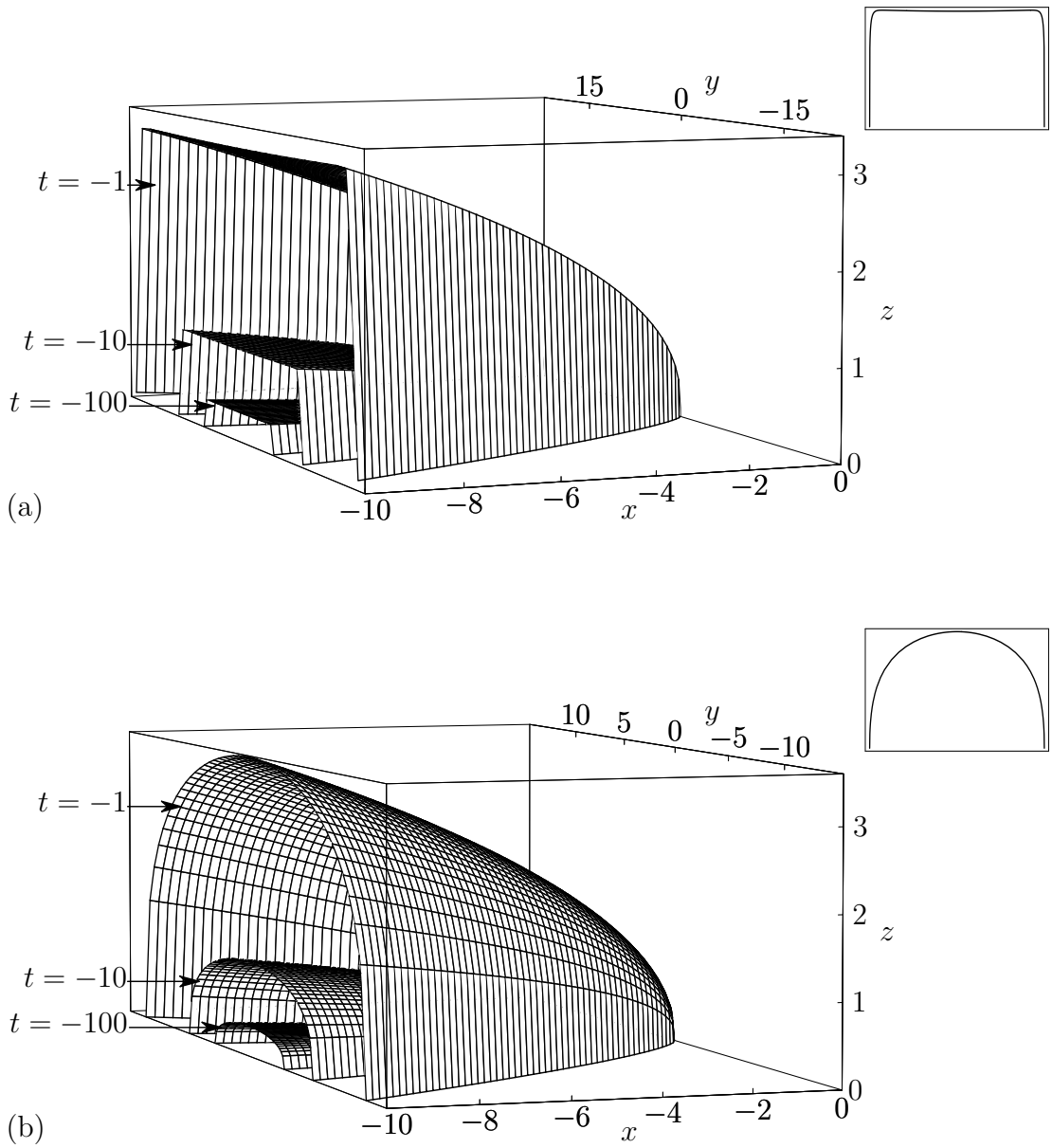

Figure 4.12: Three-dimensional plots of the free surfaces h of the sessile rivulets for the cases (a) $H_0 = H_{01}$ and (b) $H_0 = H_{02}$ with $N = 5$, at times $t = -100$, -10 and -1. The insets show the cross-sectional profiles.

power-law fluid around a symmetric slender dry patch $|y| < a(x,t)$ on an inclined plane (so that the fluid occupies $|y| \geq a(x,t)$, and its free surface $z = h$ again satisfies (4.11)). In that case the governing equation (4.10) again holds, and if we seek a similarity solution of the form (4.12) then $H(\eta)$ again satisfies the ordinary differential equation (4.14). We now look for a solution H satisfying $H \to H_\infty$ as $\eta \to \infty$, where H_∞ is a positive constant; then equation (4.14) immediately gives $S_t H_\infty = S_x H_\infty^{\frac{2N+1}{N}}$, which requires both that $S_t = S_x$ and that $H_\infty = 1$, so that the appropriate far-field conditions for (4.14) are $H \to 1$ and $H' \to 0$ as $\eta \to \infty$. Moreover, H must again satisfy the contact-line conditions (4.15), where η_0 again denotes the position of the contact line.

Consideration of the far-field behaviour of H shows that only the case $S_t = S_g = S_x$ could possibly lead to physical solutions. From equation (4.14) with $S_t = S_g = S_x$, at any stationary point of the free surface we have $H'' = 1 - H^{-\frac{N+1}{N}}$, showing that any stationary point with $H < 1$ ($H > 1$) would be a maximum (minimum); we conclude that H must therefore increase monotonically from $H = 0$ at $\eta = \eta_0$ to $H \to 1$ as $\eta \to \infty$, with $0 \leq H < 1$.

Near the contact line $\eta = \eta_0$, behaviour (4.26) still holds for a dry patch but now with $S_t = S_g$, whereas behaviour (4.27) is replaced by

$$H \sim \; C(\eta - \eta_0)^{\frac{N}{3N+1}} - \frac{(3N+1)\eta_0}{2\,(4N+1)\,C^{\frac{N+1}{N}}}(\eta - \eta_0)^{\frac{2N}{3N+1}}, \tag{4.49}$$

where C is a positive constant; however, as in the earlier analysis of rivulet flow, the contact-line conditions then require that $C = 0$, so that (4.49) is eliminated, and only (4.26) need be considered. Then integrating equation (4.14) from $\eta = \eta_0$ to $\eta = \infty$ gives

$$\int_{\eta_0}^{\infty} \left(H - H^{\frac{2N+1}{N}} \right) \mathrm{d}\eta = 0, \tag{4.50}$$

which is impossible for monotonic H satisfying $0 \leq H < 1$. Therefore, using the same kind of argument as in Chapter 2, we conclude that there are no dry-patch solutions of the type sought.

Chapter 5

Unsteady Shear-Stress-Driven Flows of Newtonian and Non-Newtonian Power-Law Fluids

In this chapter we extend our analysis in Chapter 2 and 4 to investigate unsteady shear-stress-driven flows for both Newtonian and non-Newtonian power-law fluids on an inclined plane.

5.1 Problem Formulation

Consider again unsteady flow of a thin film of a non-Newtonian power-law fluid with constant density ρ and variable viscosity $\mu = \mu_0 \gamma^{N-1}$, where μ_0 is a constant, γ is the local shear rate and N (> 0) is the power-law index, on a planar substrate inclined at an angle α ($0 \leq \alpha \leq \pi$) to the horizontal, but this time the flow is driven by a constant shear stress τ (> 0) at its free surface directed down the plane. As before, surface-tension effects are neglected. We shall be concerned with both unsteady rivulets of a power-law fluid and unsteady dry patches in a

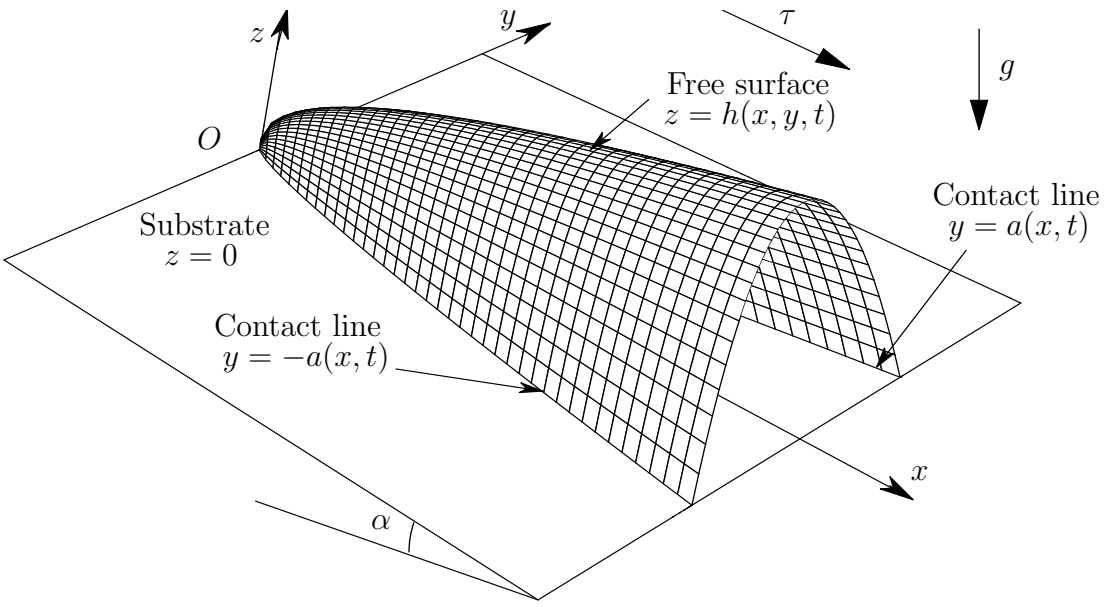

Figure 5.1: Sketch of the geometry of the rivulet problem.

film of such a fluid.

We adopt Cartesian coordinates (x, y, z) as in Chapter 2 and we denote the free surface profile of the film by $z = h(x, y, t)$. Again, we restrict attention to flows that are symmetric about $y = 0$. We denote the (unknown) semi-width of the rivulet or dry patch by $a = a(x, t)$, so that $h = 0$ at the contact lines $y = \pm a$; for a rivulet the fluid occupies $|y| \leq a$, whereas for a dry patch the fluid occupies $|y| \geq a$. Figures 5.1 and 5.2 show the geometries of the rivulet and dry-patch problems, respectively.

With the usual lubrication approximation the velocity (u, v, w), pressure p and film thickness h satisfy the governing equations

$$u_x + v_y + w_z = 0, \tag{5.1}$$

$$(\mu u_z)_z - p_x + \rho g \sin\alpha = 0, \tag{5.2}$$

$$(\mu v_z)_z - p_y = 0, \tag{5.3}$$

$$-p_z - \rho g \cos\alpha = 0, \tag{5.4}$$

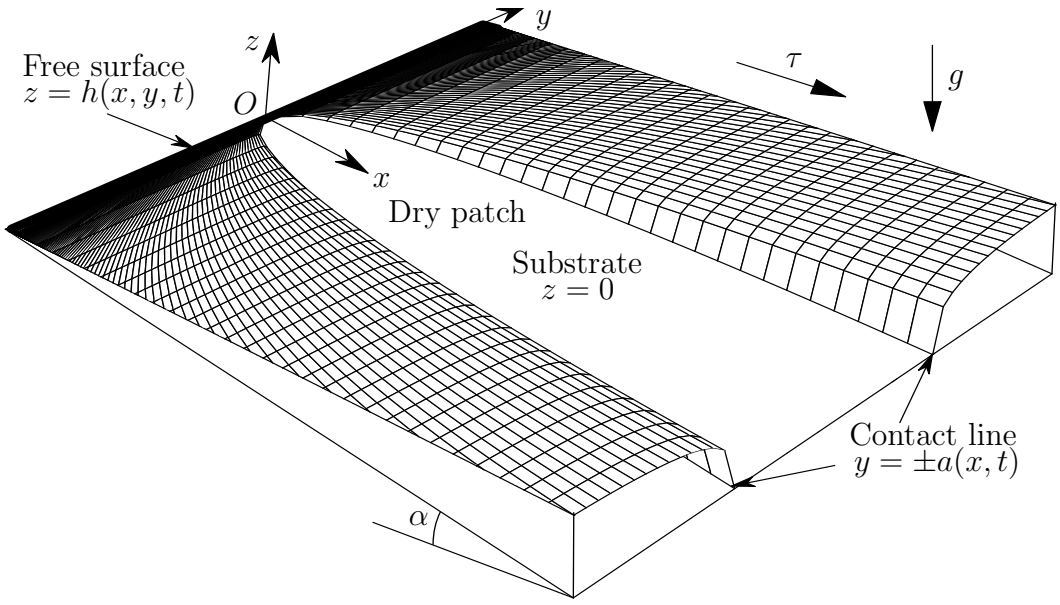

Figure 5.2: Sketch of the geometry of the dry-patch problem.

where g denotes gravitational acceleration. We consider the case in which the rivulet or dry patch is slender and the draining down the plane caused by gravity is negligible in comparison with the flow down the plane driven by the surface shear stress τ, so that the terms p_x and $\rho g \sin\alpha$ in (5.2) may be neglected (see later in Section 5.3). Equations (5.1)–(5.4) are to be integrated subject to the boundary conditions of no slip and no penetration (2.5) on the substrate $z = 0$, balances of normal and tangential stress on the free surface $z = h$:

$$p = p_{\mathrm{a}}, \quad \mu u_z = \tau, \quad \mu v_z = 0, \tag{5.5}$$

where p_{a} denotes atmospheric pressure, together with the kinematic condition (2.7) on $z = h$ and zero-mass-flux condition (2.9) at the contact lines $y = \pm a(x, t)$.

Since the rivulet and dry patch are slender, and since we will be considering only problems in which u_z is always non-negative, the shear rate is again given by $\gamma = u_z$ approximately (see Appendix A), and so the viscosity μ in (5.2), (5.3) and (5.5) is again given by $\mu = \mu_0 u_z^{N-1}$. Therefore integrating equation (5.2) once

subject to $(5.5)_2$ on $z = h$ gives

$$\gamma = \left(\frac{\tau}{\mu_0}\right)^{\frac{1}{N}} = \text{constant}, \qquad \mu = \mu_0 u_z^{N-1} = \mu_0 \left(\frac{\tau}{\mu_0}\right)^{\frac{N-1}{N}} = \text{constant}. \tag{5.6}$$

Integrating equations (5.2)–(5.4) subject to (2.5) on $z = 0$ and (5.5) on $z = h$ yields

$$p = p_{\mathrm{a}} + \rho g \cos\alpha \,(h - z)\,, \tag{5.7}$$

$$u = \left(\frac{\tau}{\mu_0}\right)^{\frac{1}{N}} z, \tag{5.8}$$

$$v = -\frac{p_y}{2\mu}\left(2hz - z^2\right). \tag{5.9}$$

Substituting (5.8) and (5.9) into (2.8) gives

$$\bar{u} = \frac{1}{2}\left(\frac{\tau}{\mu_0}\right)^{\frac{1}{N}} h^2, \quad \bar{v} = -\frac{p_y}{3\mu} h^3, \tag{5.10}$$

and then the kinematic condition (2.7) yields the governing partial differential equation for h, namely

$$3\mu h_t = \rho g \cos\alpha \left[h^3 h_y\right]_y - \frac{3\tau}{2}\left[h^2\right]_x, \tag{5.11}$$

which, we note, is independent of N. From (5.10) we have $\bar{u} = 0$ at $y = \pm a$, so that the zero-mass-flux condition (2.9) at the contact lines reduces to $\bar{v} = 0$ at $y = \pm a$; thus again we have the contact-line conditions

$$h = 0 \quad \text{at} \quad y = \pm a, \qquad h^3 h_y \to 0 \quad \text{as} \quad y \to \pm a. \tag{5.12}$$

5.2 A Similarity Solution

Equation (5.11) has an unsteady similarity solution of the form

$$h = \left(\frac{\mu_0}{\tau}\right)^{\frac{1}{N}} \left|\frac{x}{t}\right| H(\eta), \qquad \eta = \left(\frac{3}{\rho g |\cos\alpha|}\right)^{\frac{1}{2}} \left(\frac{\tau^{N+2}}{\mu_0^2}\right)^{\frac{1}{2N}} \frac{|t|}{|x|^{\frac{3}{2}}} y, \tag{5.13}$$

where the function $H = H(\eta)$ (≥ 0) and the independent variable η are dimensionless. Hence (5.11) reduces to the ordinary differential equation

$$S_t\left(\eta H' - H\right) = S_g\left(H^3 H'\right)' + S_x\left(\frac{3}{4}\eta (H^2)' - H^2\right) \tag{5.14}$$

for H, where a dash denotes differentiation with respect to η, and the notation $S_t = \mathrm{sgn}(t) = \pm 1$, $S_g = \mathrm{sgn}(\cos\alpha) = \pm 1$ and $S_x = \mathrm{sgn}(x) = \pm 1$ are used. We note that, like (5.11), equation (5.14) is also independent of N.

We now investigate solutions of the type (5.13) representing a rivulet in Section 5.3 and a dry patch in Section 5.4.

5.3 A Rivulet

For a symmetric rivulet, appropriate boundary and symmetry conditions on H are again given by (2.23) and the (unknown) position where $H = 0$ is denoted by $\eta = \eta_0$, so that with (5.12) we have

$$H = 0 \quad \text{at} \quad \eta = \eta_0, \qquad H^3 H' \to 0 \quad \text{as} \quad \eta \to \eta_0. \tag{5.15}$$

From (5.13) the middle thickness of the rivulet, $h_\mathrm{m} = h(x, 0, t)$, and the semi-width of the rivulet vary with x and t according to

$$h_\mathrm{m} = \left(\frac{\mu_0}{\tau}\right)^{\frac{1}{N}} \left|\frac{x}{t}\right| H_0, \qquad a = \left(\frac{\rho g |\cos\alpha|}{3}\right)^{\frac{1}{2}} \left(\frac{\mu_0^2}{\tau^{N+2}}\right)^{\frac{1}{2N}} \frac{|x|^{\frac{3}{2}}}{|t|} \eta_0, \tag{5.16}$$

predicting that at any time t the rivulet widens or narrows according to $|x|^{3/2}$ and thickens or thins according to $|x|$, and that at any station x the rivulet widens or narrows according to $|t|^{-1}$ and thickens or thins according to $|t|^{-1}$, independent of the power-law index N. Again, the rivulet has a nose that remains stationary at the origin O for all time.

Conditions for the rivulet to be thin and slender are that the length scales in the x, y and z directions (namely $|x|$, a and h_m, respectively) satisfy $h_\mathrm{m} \ll a \ll |x|$, which in turn requires that

$$\frac{|\rho g \cos\alpha\, x|}{\tau} \gg 1, \qquad \frac{\tau^{\frac{N+2}{2N}} |t|}{|\rho g \cos\alpha\, x|^{\frac{1}{2}} \mu_0^{\frac{1}{N}}} \gg 1, \tag{5.17}$$

showing that α cannot be close to $\pi/2$, and that $|x|$ and $|t|$ must be sufficiently large (and, in particular, that $|t| \gg (\mu_0/\tau)^{1/N}$). Moreover, the condition that the

gravity-driven draining is negligible in comparison with the flow driven by τ is that $\rho g \sin\alpha\, h_{\rm m} \ll \tau$, leading to

$$\frac{\tau^{\frac{N+1}{N}}|t|}{\rho g \sin\alpha\, |x| \mu_0^{\frac{1}{N}}} \gg 1. \tag{5.18}$$

The cross-sectional area of the rivulet at any station x, denoted by A, is given by

$$A = 2\int_0^a h\,\mathrm{d}y = \left(\frac{\rho g|\cos\alpha|}{3}\right)^{\frac{1}{2}} \left(\frac{\mu_0^4}{\tau^{N+4}}\right)^{\frac{1}{2N}} \frac{|x|^{\frac{5}{2}}}{t^2} I_1, \tag{5.19}$$

and the total volume flux of fluid across any section $x =$ constant, denoted by Q, is given by

$$Q = 2\int_0^a \bar{u}\,\mathrm{d}y = \left(\frac{\tau}{\mu_0}\right)^{\frac{1}{N}} \int_0^a h^2\,\mathrm{d}y = \frac{1}{2}\left(\frac{\rho g|\cos\alpha|}{3}\right)^{\frac{1}{2}} \left(\frac{\mu_0^4}{\tau^{N+4}}\right)^{\frac{1}{2N}} \frac{|x|^{\frac{7}{2}}}{|t|^3} I_2, \tag{5.20}$$

where I_n is defined as

$$I_n = 2\int_0^{\eta_0} H^n\,\mathrm{d}\eta. \tag{5.21}$$

The area of a finite length L_0 of the wetted part of the inclined plane in $0 \le |x| \le L_0$ (that is, the "footprint" of that part of the rivulet), denoted by A_0, is given by

$$A_0 = 2\int_0^{L_0} a\,\mathrm{d}x = \frac{4}{5}\left(\frac{\rho g|\cos\alpha|}{3}\right)^{\frac{1}{2}} \left(\frac{\mu_0^2}{\tau^{N+2}}\right)^{\frac{1}{2N}} \frac{\eta_0 L_0^{\frac{5}{2}}}{|t|}. \tag{5.22}$$

For simplicity in plotting the results, we now re-scale according to

$$\begin{gathered} x = Xx^*, \quad y = \left(\frac{\rho g|\cos\alpha|}{3}\right)^{\frac{1}{2}} \left(\frac{\mu_0^2}{\tau^{N+2}}\right)^{\frac{1}{2N}} \frac{X^{\frac{3}{2}}}{T} y^*, \quad t = Tt^*, \quad h = \left(\frac{\mu_0}{\tau}\right)^{\frac{1}{N}} \frac{X}{T} h^*, \\ A = \left(\frac{\rho g|\cos\alpha|}{3}\right)^{\frac{1}{2}} \left(\frac{\mu_0^4}{\tau^{N+4}}\right)^{\frac{1}{2N}} \frac{X^{\frac{5}{2}}}{T^2} A^*, \quad Q = \frac{1}{2}\left(\frac{\rho g|\cos\alpha|}{3}\right)^{\frac{1}{2}} \left(\frac{\mu_0^4}{\tau^{N+4}}\right)^{\frac{1}{2N}} \frac{X^{\frac{7}{2}}}{T^3} Q^*, \\ A_0 = \frac{4}{5}\left(\frac{\rho g|\cos\alpha|}{3}\right)^{\frac{1}{2}} \left(\frac{\mu_0^2}{\tau^{N+2}}\right)^{\frac{1}{2N}} \frac{L_0^{\frac{5}{2}}}{T}, \end{gathered} \tag{5.23}$$

where X (> 0) and T (> 0) are length and time scales, respectively, which we may choose arbitrarily. Then, with superscript stars dropped immediately for clarity, the solution (5.13) takes the simpler form

$$h = \left|\frac{x}{t}\right| H, \qquad \eta = \frac{|t|}{|x|^{\frac{3}{2}}} y, \tag{5.24}$$

with H satisfying (5.14), (2.23) and (5.15); from (5.16) the middle thickness h_{m} and semi-width a are given by

$$h_{\mathrm{m}} = \left|\frac{x}{t}\right| H_0, \qquad a = \frac{|x|^{\frac{3}{2}}}{|t|}\eta_0, \tag{5.25}$$

and from (5.19), (5.20) and (5.22), the cross-sectional area A, flux Q and wetted area A_0 become

$$A = \frac{|x|^{\frac{5}{2}}}{|t|^2} I_1, \qquad Q = \frac{|x|^{\frac{7}{2}}}{|t|^3} I_2, \qquad A_0 = \frac{\eta_0}{|t|}. \tag{5.26}$$

In the differential equation (5.14) there are again four distinct cases to consider, namely $S_t = S_g = S_x$, $S_t = -S_g = S_x$, $S_t = S_g = -S_x$ and $S_t = -S_g = -S_x$. As discussed in previous chapters, each of these cases has two different physical interpretations but the two cases will have exactly the same mathematical solution. In fact, we shall show shortly, by using the same arguments as before, only the case $S_t = -S_g = S_x$ can lead to physically realisable solutions.

Near $\eta = 0$, we find straightforwardly that H satisfies

$$H = H_0 + \frac{S_x H_0 - S_t}{2 S_g H_0^2}\eta^2 + O\left(\eta^4\right) \tag{5.27}$$

as $\eta \to 0$ when $H_0 \neq 0$, and near the contact line $\eta = \eta_0$, we find that H satisfies either

$$H \sim \left[-\frac{3 S_t \eta_0}{S_g}(\eta_0 - \eta)\right]^{\frac{1}{3}} \tag{5.28}$$

provided that $S_g = -S_t$, or

$$H \sim C(\eta_0 - \eta)^{\frac{1}{4}} - \frac{4 S_t \eta_0}{5 S_g C^2}(\eta_0 - \eta)^{\frac{1}{2}} \tag{5.29}$$

as $\eta \to \eta_0$, where C is a positive constant[1]. However, with (5.29) the zero-mass-flux condition $(5.15)_2$ would require that $C = 0$; therefore the two cases with $S_t = S_g$, in which (5.29) is the only possible behaviour near the contact line, are immediately eliminated.

[1]Note that both (5.28) and (5.29) have $H' \to \infty$ as $\eta \to \eta_0$, showing that the lubrication approximation again fails near the contact lines.

Since the rivulet has two contact lines, at $\eta = \pm\eta_0$, the function H (≥ 0) must have at least one maximum in $|\eta| \leq \eta_0$. From equation (5.14), at any stationary point of the free surface (where $H' = 0$) for the cases with $S_t = -S_g$ we have

$$H^2 H'' = 1 - S_t S_x H, \tag{5.30}$$

provided that $H \neq 0$. In the case $S_t = -S_g = -S_x$, equation (5.30) shows immediately that any stationary point of H is a minimum, so there can be no solution for H with a maximum, and therefore this case is eliminated.

With all other cases eliminated, the only case that could lead to physically realisable solutions is $S_t = -S_g = S_x$. In this case, equation (5.14) becomes

$$\left(H^3 H'\right)' - \frac{3}{4}\eta (H^2)' + \eta H' + H^2 - H = 0. \tag{5.31}$$

Again a closed-form solution of the ordinary differential equation (5.31) is not available, and so it must, in general, be solved numerically. Using the same procedure as in Chapters 2 and 4, we did this in two stages, first by using a shooting method to solve (5.31) subject to (2.23) to determine the value of η_0 in $(5.15)_1$ for a given value of H_0, and then by using the condition $C = 0$ to select the physically realisable solutions from this family of solutions; H_0 and η_0 are thus determined as part of the solution. Figure 5.3 shows the results for η_0 as a function of H_0 obtained by the shooting method. This function has four branches, labelled as branches 1, 2, 3 and 4 in Figure 5.3; branch 1 extends from $H_0 \simeq 0.0000$ to $H_0 \simeq 0.9250$, branch 2 from $H_0 \simeq 0.9250$ to $H_0 \simeq 1.0000$, branch 3 from $H_0 \simeq 1.0000$ to $H_0 \simeq 1.2708$, and branch 4 from $H_0 \simeq 1.2708$ to large values of H_0, there being asymptotes to the function at $H_0 \simeq 0.9250$, $H_0 \simeq 1.0000$ and $H_0 \simeq 1.2708$. There is a solution η_0 for every value of H_0 except at the asymptotes, at which there is no solution. Figure 5.4 shows numerically calculated cross-sectional profiles H for a range of values of H_0 on the different branches. Equation (5.30) shows that any stationary point for which $H < 1$ is a minimum, and any stationary point for which $H > 1$ is a maximum. Solutions on branches 1 and 2 are double-humped, with a minimum

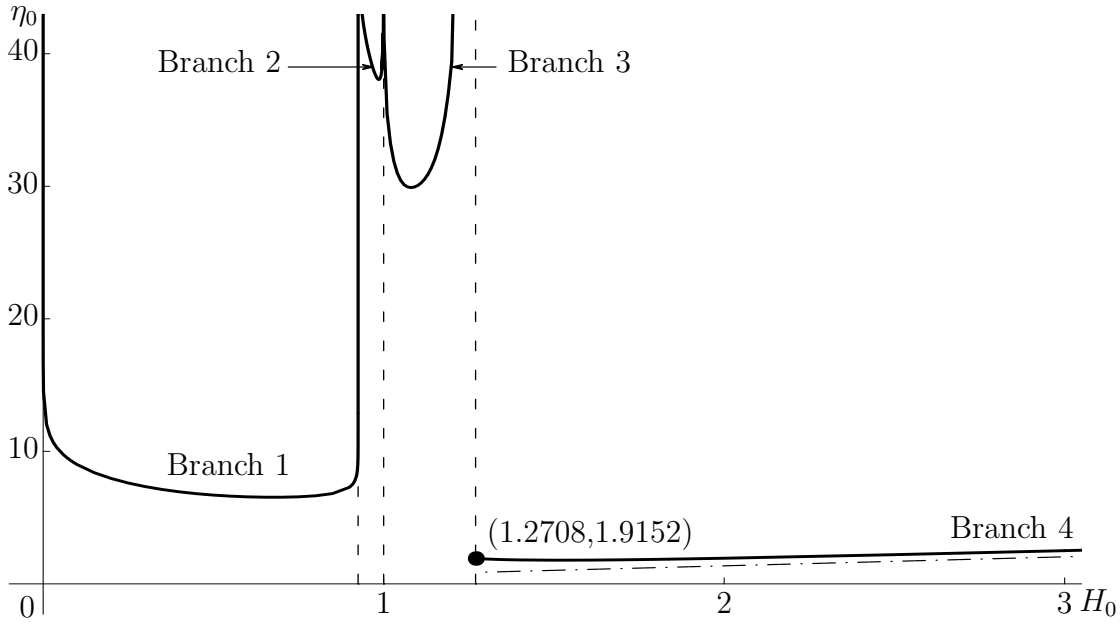

Figure 5.3: Plot of η_0 as a function of H_0, obtained by solving (5.31) numerically subject to (2.23). The dashed-dotted curve is the leading-order asymptotic solution in the limit $H_0 \to \infty$.

at $\eta = 0$ and two equal maxima symmetrically placed about $\eta = 0$, and solutions on branch 3 are triple-humped, with a maximum at $\eta = 0$, and two equal maxima and two equal minima symmetrically placed about $\eta = 0$; solutions on branch 4 are single-humped, with a single maximum at $\eta = 0$.

As discussed previously in Chapter 2, we can understand the large-H_0 limit shown in Figure 5.3 by analysing the behaviour of H and η_0 in the limit $H_0 \to \infty$. From the numerically calculated solutions, it is found that $H = O(H_0)$ and $\eta_0 = O(H_0)$, and so we write

$$H = H_0 \bar{H}(\bar{\eta}), \qquad \eta = H_0 \bar{\eta}, \qquad \eta_0 = H_0 \bar{\eta}_0; \tag{5.32}$$

then at leading order equation (5.31) reduces to

$$\left(\bar{H}^3 \bar{H}'\right)' - \frac{3}{4}\bar{\eta}\left(\bar{H}^2\right)' + \bar{H}^2 = 0, \tag{5.33}$$

which is readily solved numerically subject to the boundary conditions

$$\bar{H}(0) = 1, \qquad \bar{H}'(0) = 0, \tag{5.34}$$

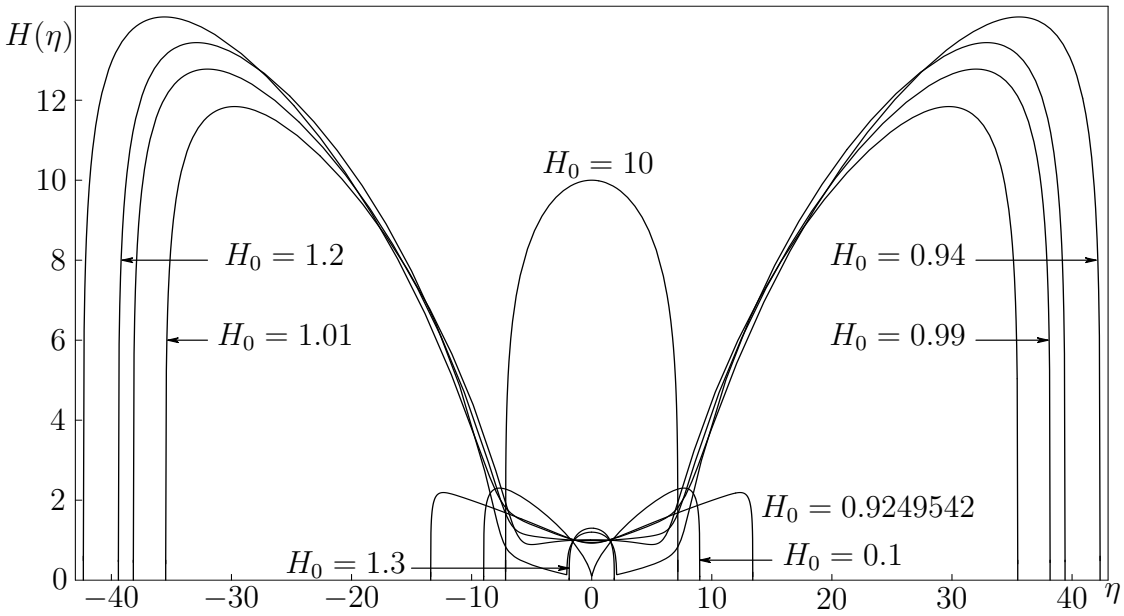

Figure 5.4: Numerically calculated cross-sectional rivulet profiles $H = H(\eta)$ for $H_0 = 0.1$ and 0.9249542 (branch 1), 0.94 and 0.99 (branch 2), 1.01 and 1.2 (branch 3), and 1.3 and 10 (branch 4).

to yield $\bar{\eta}_0 \simeq 0.6801$. Figure 5.5 shows comparisons between profiles H for $H_0 = 3$ and $H_0 = 10$ computed numerically (full curves) and from the leading order asymptotic solution in the limit $H_0 \to \infty$ (dashed curves), demonstrating good agreement between the two for sufficiently large H_0. Also Figure 5.3 includes (as a dashed-dotted curve) the leading order asymptotic solution for η_0 as a function of H_0 in the limit $H_0 \to \infty$.

Next we choose the physically realisable solutions from the family of solutions shown in Figure 5.3. In order to do this, we again impose condition (5.15), or equivalently the condition $C = 0$ in (5.29). We determine C by integrating equation (5.31) from $\eta = 0$ to $\eta = \eta_0$, which leads to

$$\int_0^{\eta_0} 7H^2 - 8H \, \mathrm{d}\eta = \begin{cases} 0 & \text{for (5.28)}, \\ C^4 & \text{for (5.29)}, \end{cases} \tag{5.35}$$

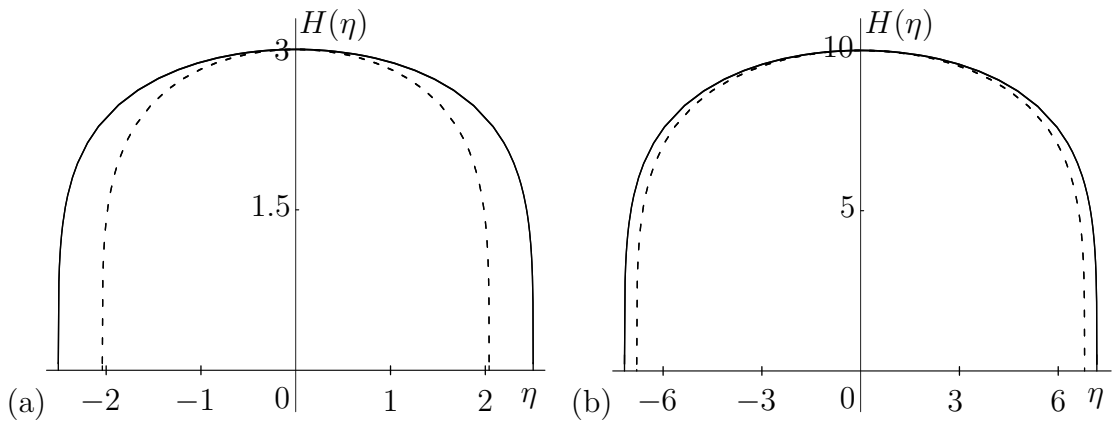

Figure 5.5: Cross-sectional rivulet profiles $H = H(\eta)$ obtained by solving (5.31) numerically subject to (2.23) (full curves) and from the leading order asymptotic solution in the limit $H_0 \to \infty$ (dashed curves) for (a) $H_0 = 3$ and (b) $H_0 = 10$.

so that C in (5.29) is given by

$$C = \left[\int_0^{\eta_0} 7H^2 - 8H \, \mathrm{d}\eta\right]^{\frac{1}{4}} = \left[\frac{1}{2}\left(7I_2 - 8I_1\right)\right]^{\frac{1}{4}}, \tag{5.36}$$

which is evaluated with the numerical solution for $H(\eta)$. Also these values of C were checked against values that we obtained from (5.29) using the numerical solution near $\eta = \eta_0$. Figure 5.6 shows a plot of C calculated from (5.36) as a function of H_0. From this plot we see that there is only one value of H_0 for which $C = 0$, namely $H_0 \simeq 1.2708$, for which the corresponding value of η_0 is $\eta_0 \simeq 1.9152$. Thus our main conclusion is that there is a unique physically realisable solution of the type sought for an unsteady rivulet. This solution has a single-humped cross-sectional profile; the associated values of I_1 and I_2 in the expressions (5.19) and (5.20) for the cross-sectional area A and flux Q are given by equation (5.21) as $I_1 \simeq 4.2495$ and $I_2 \simeq 4.8565$, consistent with the fact that $8I_1 = 7I_2$ in the case $C = 0$.

As mentioned previously, although the cases where $S_t = -S_g = S_x = 1$ and $S_t = -S_g = S_x = -1$ have the same mathematical solution, the two cases have different physical interpretations, the former representing a pendent rivulet and the latter a sessile rivulet. However, numerical results of a stability study of

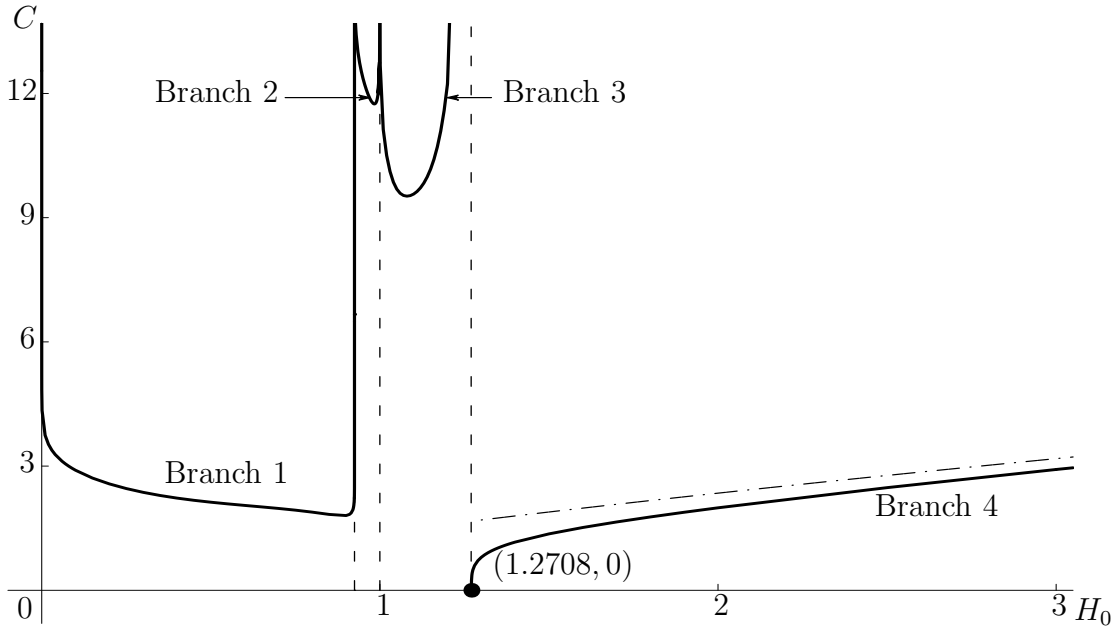

Figure 5.6: Plot of C calculated from equation (5.36) as a function of H_0. The dashed-dotted curve is the leading-order asymptotic solution in the limit $H_0 \to \infty$.

corresponding similarity solutions for a gravity-driven flow of a Newtonian fluid in Chapter 3 suggest that the sessile case is stable but that the pendent case is unstable, indicating that we may also tentatively eliminate the possibility of a pendent rivulet for the present problem. Figure 5.7 shows a three-dimensional plot of the free surface $z = h$ of the sessile rivulet predicted by the similarity solution (5.24) for the physical solution $H_0 \simeq 1.2708$, $\eta_0 \simeq 1.9152$, at times $t = -3$, -2 and -1; the inset shows the (single-humped) cross-sectional profile of the solution. In particular, Figure 5.7 illustrates that the sessile rivulet becomes narrower and thinner with $|x|$ as it flows down the plane, but becomes wider and thicker as time elapses (from $t \to -\infty$ to $t = 0$), eventually exhibiting a finite-time singularity, becoming infinite everywhere at $t = 0$.

As before, we may alternatively interpret the solution (5.13) as representing a rivulet of (prescribed) finite volume, by truncating it at some finite length $L = L(t)$, so that in the sessile case it occupies $-L \leq x \leq 0$. The volume of fluid in

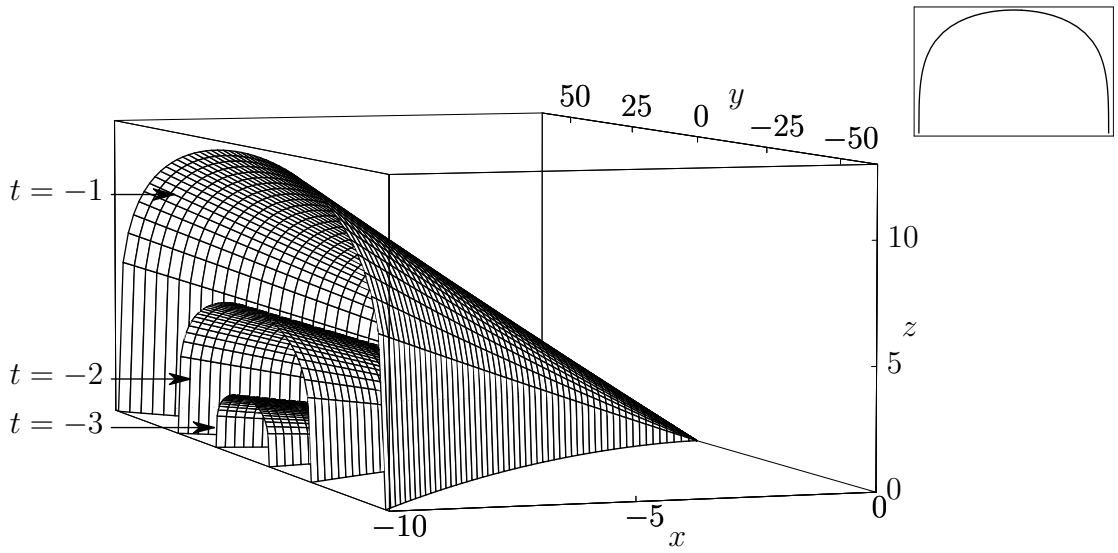

Figure 5.7: Three-dimensional plot of the free surface $z = h$ of the sessile rivulet predicted by the present similarity solution (5.24) with H satisfying (5.31) subject to (2.23) and (5.15), for which $H_0 \simeq 1.2708$ and $\eta_0 \simeq 1.9152$, at times $t = -3$, -2 and -1. The inset shows the cross-sectional profile.

such a rivulet, denoted by V, is given (in dimensional terms) by

$$V = \int_{-L(t)}^{0} \int_{-a}^{a} h \, \mathrm{d}y \, \mathrm{d}x = \frac{2I_1}{7t^2} \left(\frac{\mu_0^4}{\tau^{N+4}} \right)^{\frac{1}{2N}} \left(\frac{\rho g |\cos\alpha| \, L^7}{3} \right)^{\frac{1}{2}}, \tag{5.37}$$

and so the length L of the rivulet at time t is given by

$$L = \left(\frac{147 V^2 \tau^{\frac{N+4}{N}}}{4 \mu_0^{\frac{4}{N}} \rho g |\cos\alpha| I_1^2} \right)^{\frac{1}{7}} t^{\frac{4}{7}}, \tag{5.38}$$

decreasing with t according to $t^{4/7}$.

5.4 A Dry Patch

The approach discussed in Section 5.3 may also be used to investigate unsteady shear-stress-driven flow of an infinitely wide thin film of non-Newtonian power-law fluid around a symmetric slender dry patch on an inclined plane. In that case the governing equation (5.11) again holds, but now the fluid occupies $|y| \geq a$, where $a = a(x)$ denotes the semi-width of the dry patch, the region $|y| < a$ of the inclined plane being dry. Seeking a similarity solution of the form (5.13) we find that $H(\eta)$ again satisfies the ordinary differential equation (5.14), now valid in $|\eta| \geq \eta_0$, where $\eta = \eta_0$ again denotes the (unknown) position of the contact line where $H = 0$ (and the fluid region now corresponds to $|\eta| \geq \eta_0$). The similarity solution predicts that at any time t the dry patch (whose semi-width a is as in (5.16)) widens or narrows according to $|x|^{3/2}$ and the film thickens or thins according to $|x|$, and that at any station x the dry patch widens or narrows like $|t|^{-1}$ and the film thickens or thins like $|t|^{-1}$, independent of the power-law index N. Conditions for the dry patch to be thin and slender and for the gravity-driven draining to be negligible in comparison with the flow driven by τ are again given by (5.17) and (5.18), respectively.

We look for solutions H satisfying $H \to H_\infty$ as $\eta \to \infty$, where H_∞ is a positive constant representing the depth of the film far from the dry patch; then equation (5.14) immediately gives $S_t H_\infty = S_x H_\infty^2$, which requires both that $S_t = S_x$ and that $H_\infty = 1$. Therefore appropriate far-field conditions are

$$H \to 1, \quad H' \to 0 \quad \text{as} \quad \eta \to \infty \tag{5.39}$$

(so that the dimensional film thickness satisfies $h \to (\mu_0/\tau)^{1/N}|x/t|$ as $y \to \pm\infty$, showing that the film becomes uniform in y far from the dry patch, but varies with x and t). From equation (5.39) H satisfies $H \sim 1 + F$ with $F \to 0$ as $\eta \to \infty$, and so by (5.14) with $S_t = S_x$ we find that $F = F(\eta)$ satisfies

$$S_g F'' + S_t \left(\frac{\eta}{2} F' - F \right) = 0 \tag{5.40}$$

at leading order as $\eta \to \infty$. If $S_t = S_g$ then (5.40) has general solution

$$F = c_1 \left(1 + \frac{\eta^2}{2}\right) + c_2 \exp\left(-\frac{\eta^2}{4}\right) \mathrm{H}_{-3}\left(\frac{\eta}{2}\right), \tag{5.41}$$

where c_1 and c_2 are constants and H_{-3} denotes a Hermite function of degree -3 (see [1]); then equation (5.39) requires that $c_1 = 0$, and therefore

$$H \sim 1 + c_2 \eta^{-3} \exp\left(-\frac{\eta^2}{4}\right) \quad \text{as} \quad \eta \to \infty, \tag{5.42}$$

showing that H approaches its far-field value 1 monotonically as $\eta \to \infty$. On the other hand if $S_t = -S_g$ then no solution of (5.40) satisfying $F \to 0$ as $\eta \to \infty$ is possible; therefore only the case $S_t = S_g = S_x$ could possibly lead to a physically realisable dry-patch solution of the type sought.

The free-surface profile H must again satisfy the contact-line conditions in (5.15). Near the contact line $\eta = \eta_0$, the asymptotic behaviour of solutions of (5.14) given in (5.28) also holds for a dry patch (now with $S_t = S_g$ and $\eta \geq \eta_0$), but (5.29) is replaced by

$$H \sim C(\eta - \eta_0)^{\frac{1}{4}} + \frac{4S_t\eta_0}{5S_gC^2}(\eta - \eta_0)^{\frac{1}{2}} \tag{5.43}$$

as $\eta \to \eta_0^+$, where C again denotes a positive constant. However, (5.15) again requires that $C = 0$, implying again that only the case $S_t = S_g = S_x$ could lead to a physically realisable solution, in which case equation (5.14) becomes

$$\left(H^3H'\right)' + \frac{3}{4}\eta(H^2)' - \eta H' - H^2 + H = 0. \tag{5.44}$$

From equation (5.44), at any stationary point of the free surface we have

$$H'' = \frac{H - 1}{H^2}, \tag{5.45}$$

showing that any stationary point with $H < 1$ ($H > 1$) would be a maximum (minimum); we conclude that H must increase monotonically from $H = 0$ at $\eta = \eta_0$ to $H = 1$ as $\eta \to \infty$, with $0 \leq H < 1$.

As in the corresponding analysis for a rivulet described previously, we solved the ordinary differential equation (5.44) numerically by means of a shooting method.

For a dry patch we may shoot either from some far-field position $\eta = \eta_\infty \gg 1$ (using approximate boundary conditions obtained from (5.42)) until the solution achieves a contact line at some position $\eta = \eta_0$, or from a chosen position $\eta = \eta_0$ to see whether the solution settles down to a constant value $H = 1$ as η becomes large; we chose to use the latter method. The numerical computation cannot be started exactly at the contact line $\eta = \eta_0$ (because of the singularity there), so instead it was started from a position $\eta = \eta_0 + \delta$, where δ (> 0) is small; thus in practice we solved equation (5.44) subject to approximated boundary conditions obtained from (5.28), namely

$$H(\eta_0 + \delta) \sim (3\eta_0\delta)^{\frac{1}{3}}, \qquad H'(\eta_0 + \delta) \sim \left(\frac{\eta_0}{9\delta^2}\right)^{\frac{1}{3}}. \tag{5.46}$$

This procedure was then repeated with different values of η_0. In this way we arrived at our main conclusion, namely that there is only one physically realisable dry-patch solution of the type sought, and that for this solution $\eta_0 \simeq 0.9573$.

As in the rivulet case, it may again be anticipated that the sessile solution will be stable whereas the pendent solution will be unstable. Figure 5.8 shows a three-dimensional plot of the solution (re-scaled as in (5.23) and (5.24)) for a sessile film ($S_t = S_g = S_x = +1$) at the instant $t = 1$; the inset shows the cross-sectional profile of the solution. In particular, Figure 5.8 illustrates the widening of the dry patch and the thickening of the film with x; also we note that, as for the rivulet, the dry patch has a nose that remains stationary at O for all time.

The film is of infinite lateral extent, and its cross-sectional area (at constant x) is infinite, as is the volume flux of fluid down the inclined plane. However, the difference between the cross-sectional area of a film of thickness $(\mu_0/\tau)^{1/N}|x/t|$ (uniform in y) and that of a film containing a dry patch with the same thickness far from the patch, denoted $\triangle A$, is finite and is given (in dimensional terms) by

$$\triangle A = \left(\frac{4\rho g|\cos\alpha|}{3}\right)^{\frac{1}{2}} \left(\frac{\mu_0^4}{\tau^{N+4}}\right)^{\frac{1}{2N}} \frac{|x|^{\frac{5}{2}}}{|t|^2}(\eta_0 + J_1), \tag{5.47}$$

and similarly the difference in volume flux in the two films, denoted $\triangle Q$, is finite

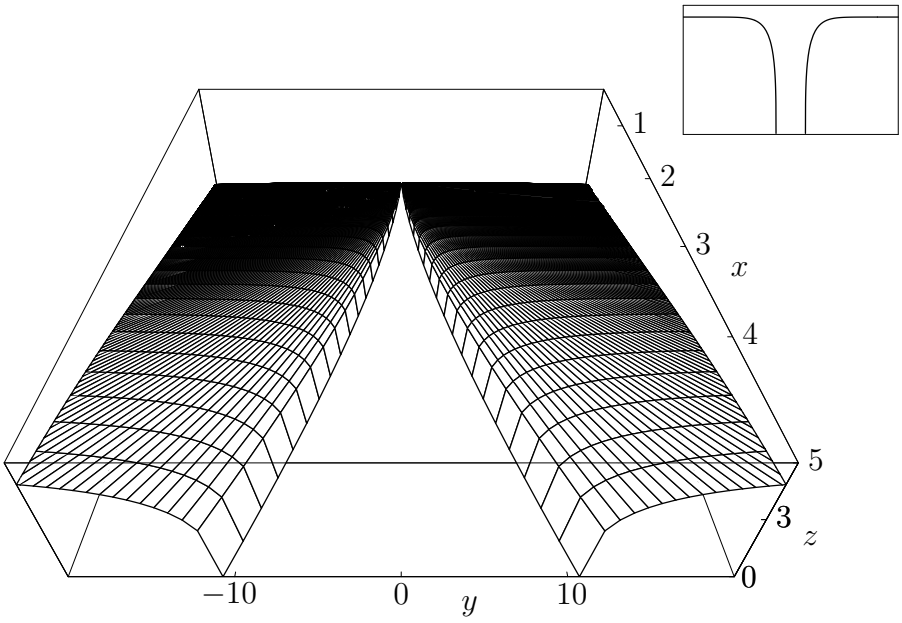

Figure 5.8: Three-dimensional plot of the free surface $z = h$ of the sessile dry patch predicted by the present similarity solution (5.24) with H satisfying (5.44) subject to (5.15) and (5.39), for which $\eta_0 \simeq 0.9573$, at time $t = 1$. The inset shows the cross-sectional profile.

and is given by

$$\triangle Q = \left(\frac{\rho g|\cos\alpha|}{3}\right)^{\frac{1}{2}} \left(\frac{\mu_0^4}{\tau^{N+4}}\right)^{\frac{1}{2N}} \frac{|x|^{\frac{7}{2}}}{|t|^3}(\eta_0 + J_2), \tag{5.48}$$

where we have defined the constants J_n by

$$J_n = \int_{\eta_0}^{\infty} 1 - H^n \,\mathrm{d}\eta, \tag{5.49}$$

so that $J_1 \simeq 0.2382$ and $J_2 \simeq 0.4090$. (Integration of (5.44) from $\eta = \eta_0$ to $\eta = \infty$ leads to $7J_2 - 8J_1 = \eta_0$, numerical confirmation of which provides a check on the accuracy of the numerical solution.) Also the area A_0 of a finite length L_0 of the dry part of the inclined plane in $0 < |x| < L_0$ is again given by (5.22).

5.5 Discussion

We have obtained similarity solutions of the form (5.13) representing unsteady flow of a thin slender rivulet of a non-Newtonian power-law fluid and unsteady flow of a thin film of such a fluid around a slender dry patch on an inclined plane, the flow in each case being driven by a constant longitudinal shear stress applied at the free surface. There were four cases to consider for each problem, but we showed that the only cases that could lead to physically realisable solutions are $S_t = -S_g = S_x$ for a rivulet and $S_t = S_g = S_x$ for a dry patch. In the case of a rivulet we found that there is only one physically realisable solution, with a single-humped cross-sectional profile of thickness $H_0 \simeq 1.2708$ and semi-width $\eta_0 \simeq 1.9152$, and in the case of a dry patch there is again only one physically realisable solution, of semi-width $\eta_0 \simeq 0.9573$, independent of the power-law index N. Although N also does not appear in the partial differential equation (5.11) for h, nor in the powers of x and t in the similarity solution (5.13), nor in ordinary differential equation (5.14) for H, it nevertheless affects the nature of the solutions; this may be illustrated by a comparison of the rivulet solution for a power-law fluid with $N \neq 1$ with that for a Newtonian fluid (for which $N = 1$) of the same density ρ, on the same incline α, subject to the same driving surface shear stress τ, as follows. With a superposed hat used to denote quantities for the Newtonian fluid, at a given position x and time t we have

$$\frac{h_{\rm m}}{\hat{h}_{\rm m}} = \frac{a}{\hat{a}} = \frac{A_0}{\hat{A}_0} = \frac{\mu}{\hat{\mu}}, \qquad \frac{A}{\hat{A}} = \frac{Q}{\hat{Q}} = \left(\frac{\mu}{\hat{\mu}}\right)^2, \tag{5.50}$$

where $\mu = \mu_0(\tau/\mu_0)^{(N-1)/N}$ again denotes the viscosity of the power-law fluid in this flow. Thus for a shear-thinning fluid ($N < 1$), if, for given values of μ_0 and $\hat{\mu}$, τ satisfies $\tau < \tau_{\rm c}$, where $\tau_{\rm c}$ is defined by $\tau_{\rm c} = (\hat{\mu}^N/\mu_0)^{1/(N-1)}$, then $\mu > \hat{\mu}$, so that the quantities in (5.50) are greater than 1, whereas if $\tau > \tau_{\rm c}$ then $\mu < \hat{\mu}$, so that the quantities in (5.50) are less than 1. Therefore a rivulet of a shear-thinning fluid subject to a weak shear stress ($\tau < \tau_{\rm c}$) will be wider and thicker than a corresponding rivulet of a Newtonian fluid, whereas such a

rivulet subject to a strong shear stress ($\tau > \tau_c$) will be narrower and thinner than a corresponding rivulet of a Newtonian fluid; a converse statement holds for a rivulet of a shear-thickening fluid. On the other hand, if, for given values of τ and $\hat{\mu}$, μ_0 satisfies $\mu_0 > \mu_{0c}$ ($\mu_0 < \mu_{0c}$), where μ_{0c} is defined by $\mu_{0c} = \hat{\mu}^N/\tau^{N-1}$, then a rivulet of a power-law fluid will be wider and thicker (narrower and thinner) than a corresponding rivulet of a Newtonian fluid, independent of whether the power-law fluid is shear thinning or shear thickening. Analogous statements hold for flow around a dry patch.

Both the rivulet and dry patch have a nose that remains stationary at O for all time. The solution for a sessile rivulet again exhibits a finite-time singularity, becoming infinite everywhere at time $t = 0$.

Finally, it is worth mentioning that there are significant differences between shear-stress-driven flow studied herein and gravity-driven flow studied in Chapter 2 and 4. In gravity-driven rivulet flow there are two physically realisable solutions (one with a double-humped cross-sectional profile and the other with a single-humped cross-sectional profile), whereas in shear-stress-driven flow there is only one physically realisable solution (whose cross-sectional profile is single-humped). Furthermore, there are no dry-patch similarity solutions of the type sought in gravity-driven flow, whereas there is a dry-patch solution in the present shear-stress-driven problem.

Chapter 6

Travelling-Wave Similarity Solutions for Flows around Slender Dry Patches

In this chapter we consider a completely different kind of similarity solution, namely a travelling-wave solution. We investigate unsteady flows of thin films of a Newtonian fluid around slender dry patches moving with constant velocity on an inclined plane driven either by gravity or a constant surface shear stress.

6.1 Problem Formulation

Consider a thin film of Newtonian fluid with constant density ρ and constant viscosity μ on a planar substrate inclined at an angle α ($0 < \alpha < \pi$) to the horizontal, subject to gravitational acceleration g and a prescribed constant shear stress τ on its free surface (acting up or down the slope), and with the substrate moving parallel to itself at constant speed U_0 up or down the slope. We shall be concerned with unsteady flow of such a film around a dry patch on the substrate, as sketched in Figure 6.1.

The same Cartesian coordinates $Oxyz$ as in previous chapters are adopted,

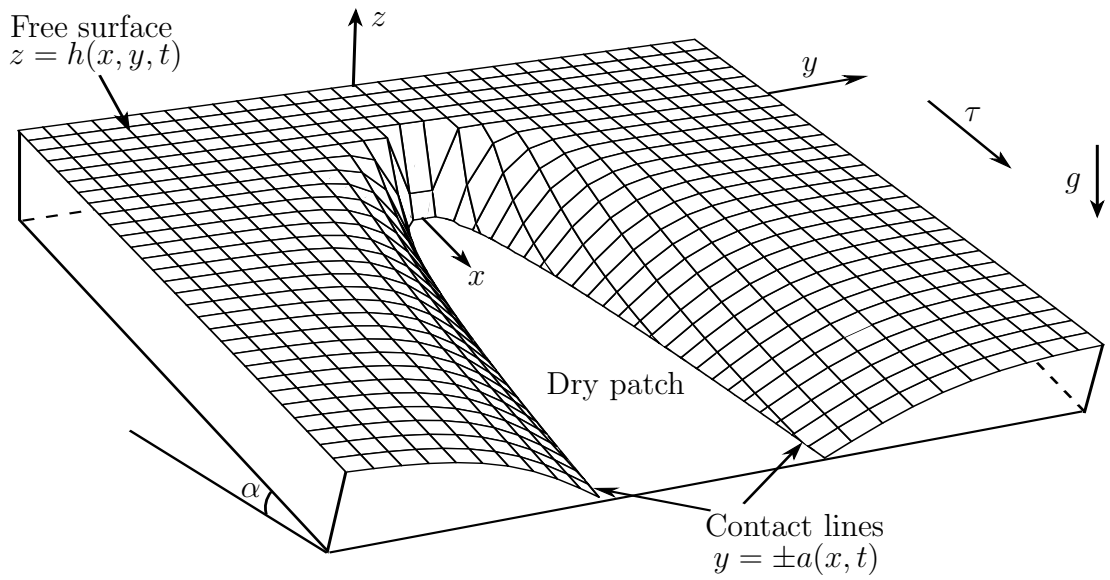

Figure 6.1: Sketch of the geometry of the problem: a moving dry patch in a thin film.

and the free surface profile of the film is denoted by $z = h(x, y, t)$. The substrate velocity is $U_0\mathbf{i}$, with $U_0 > 0$ ($U_0 < 0$) if the substrate is moving downwards (upwards); also $\tau > 0$ ($\tau < 0$) if the prescribed surface shear stress acts down (up) the substrate.

Again, we take the dry patch to be slender (varying much more slowly in the longitudinal (x) direction than in the transverse (y) direction), and we neglect surface-tension effects. Then with the familiar lubrication approximation, the velocity (u, v, w), pressure p and thickness h satisfy the governing equations

$$u_x + v_y + w_z = 0, \tag{6.1}$$

$$\mu u_{zz} + \rho g \sin\alpha = 0, \tag{6.2}$$

$$-p_y + \mu v_{zz} = 0, \tag{6.3}$$

$$-p_z - \rho g \cos\alpha = 0, \tag{6.4}$$

subject to the boundary conditions of no slip and no penetration on the substrate

$z = 0$:

$$u = U_0, \quad v = w = 0, \tag{6.5}$$

balances of normal and tangential stresses on the free surface $z = h$:

$$p = p_{\mathrm{a}}, \quad \mu u_z = \tau, \quad v_z = 0 \tag{6.6}$$

where p_{a} denotes atmospheric pressure, and the kinematic condition (2.7) on $z = h$.

Integrating (6.2)–(6.4) subject to (6.5) and (6.6) yields

$$p = p_{\mathrm{a}} + \rho g \cos\alpha \, (h - z) \,, \tag{6.7}$$

$$u = \frac{\rho g \sin\alpha}{2\mu} \, (2h - z) \, z + \frac{\tau}{\mu} z + U_0, \tag{6.8}$$

$$v = -\frac{\rho g \cos\alpha}{2\mu} h_y \, (2h - z) \, z. \tag{6.9}$$

Substituting (6.8) and (6.9) into (2.8) gives

$$\bar{u} = \frac{\rho g \sin\alpha}{3\mu} h^3 + \frac{\tau}{2\mu} h^2 + U_0 h, \quad \bar{v} = -\frac{\rho g \cos\alpha}{3\mu} h^3 h_y, \tag{6.10}$$

and hence the kinematic condition (2.7) yields the governing partial differential equation for h:

$$h_t = \frac{\rho g \cos\alpha}{3\mu} \left(h^3 h_y\right)_y - \frac{\rho g \sin\alpha}{3\mu} \left(h^3\right)_x - \frac{\tau}{2\mu} \left(h^2\right)_x - U_0 h_x. \tag{6.11}$$

Once h is determined from (6.11) the solution for p, u and v in (6.7)–(6.9) is known.

In the case of a film of constant uniform thickness h_∞ the solution takes the form $p = p_\infty = p_\infty(z)$, $u = u_\infty = u_\infty(z)$ and $v = v_\infty = 0$, where

$$p_\infty = p_{\mathrm{a}} + \rho g \cos\alpha \, (h_\infty - z) \,, \quad u_\infty = \frac{\rho g \sin\alpha}{2\mu} \, (2h_\infty - z) \, z + \frac{\tau}{\mu} z + U_0, \tag{6.12}$$

representing steady unidirectional flow up or down the substrate, with depth-averaged velocity $U\mathbf{i}$, where

$$U = \frac{\rho g \sin\alpha}{3\mu} h_\infty^2 + \frac{\tau}{2\mu} h_\infty + U_0, \tag{6.13}$$

which may be positive, negative or zero. We are concerned with unsteady flow around a dry patch in a film of thickness h_∞ at infinity (that is, in a film that would be of uniform thickness h_∞ if the dry patch were absent). We shall restrict attention to dry patches that are symmetric about $y = 0$ (so that h is even in y) with (unknown) semi-width $a = a(x,t)$, so that the fluid occupies $|y| \geq a$, and $h = 0$ at the contact lines $y = \pm a$. From (6.10) we have $\bar{u} = 0$ at $y = \pm a$, so that the zero-mass-flux condition (2.9) at the contact lines reduces to $\bar{v} = 0$ at $y = \pm a$, and therefore again we have the contact-line conditions

$$h = 0 \quad \text{at} \quad y = \pm a, \qquad h^3 h_y \to 0 \quad \text{as} \quad y \to \pm a. \tag{6.14}$$

6.1.1 A similarity solution

We seek an unsteady travelling-wave similarity solution of (6.11) in the form

$$\left.\begin{array}{ll} h = h_\infty F(\eta), \quad \eta = \dfrac{y}{[\ell(x-ct)]^n} & \text{if } \ell(x-ct) \geq 0, \\ h = h_\infty & \text{if } \ell(x-ct) < 0, \end{array}\right\} \tag{6.15}$$

where $c\mathbf{i}$ (with c positive, negative or zero) is the velocity of the dry patch up or down the substrate, the constant ℓ is to be specified, and the exponent n and the dimensionless function $F = F(\eta)$ (≥ 0) of the dimensionless similarity variable η are to be determined. The dry patch lies in the region where $\ell(x-ct) \geq 0$, and the fluid in the region where $\ell(x-ct) < 0$ (ahead of or behind the dry patch) is of uniform thickness h_∞; at $x = ct$ the thickness h and its derivative h_y are continuous (so that u, v and p are continuous there), except at the singular point $x = ct$, $y = 0$, at which the free surface is normal to the substrate, occupying $0 \leq z \leq h_\infty$. With $(6.15)_1$ the terms in (6.11) balance provided that $n = 1/2$ (so that ℓ has physical dimensions of length), and then (6.11) reduces to an ordinary differential equation for $F(\eta)$, namely

$$4\rho g \cos\alpha h_\infty^3 \left(F^3 F'\right)' + \ell\eta \left[2\rho g \sin\alpha h_\infty^2 F^3 + 3\tau h_\infty F^2 - 6\mu(c - U_0)F\right]' = 0, \tag{6.16}$$

where a dash denotes differentiation with respect to η.

We denote the (unknown) position where $F = 0$ by $\eta = \eta_0$ (corresponding to the contact-line position $y = a$), so that the fluid lies in $|\eta| \geq \eta_0$, and

$$a = \sqrt{\ell\,(x - ct)}\,\eta_0, \quad \frac{y}{a} = \frac{\eta}{\eta_0}, \tag{6.17}$$

showing that the dry patch has a parabolic shape. From (6.14) we have

$$F = 0 \quad \text{at} \quad \eta = \eta_0, \qquad F^3 F' \to 0 \quad \text{as} \quad \eta \to \eta_0; \tag{6.18}$$

in addition, F must satisfy the far-field condition

$$F \to 1 \quad \text{as} \quad \eta \to \infty. \tag{6.19}$$

6.1.2 Behaviour near $\eta = \eta_0$

Near the contact line $\eta = \eta_0$ we find from (6.16) that F satisfies

$$F \sim \left[\frac{9\eta_0\mu\ell(c - U_0)(\eta - \eta_0)}{2\rho g \cos\alpha h_\infty^3}\right]^{\frac{1}{3}} \tag{6.20}$$

as $\eta \to \eta_0^+$, which can be valid only if

$$\ell \cos\alpha(c - U_0) > 0. \tag{6.21}$$

Also (6.20) shows that the fluid film has infinite slope at the contact line $\eta = \eta_0$, and so the lubrication approximation fails there.

6.1.3 Behaviour in the limit $\eta \to \infty$

In the limit $\eta \to \infty$ we write $F = 1 + f$ with $|f| \ll 1$ in (6.16), in which case $f = f(\eta)$ satisfies

$$f'' + K\eta f' = 0, \tag{6.22}$$

where we have defined the constant K by

$$K = \frac{3\mu\ell}{2\rho g \cos\alpha h_\infty^3}\left(\frac{\rho g \sin\alpha h_\infty^2}{\mu} + \frac{\tau h_\infty}{\mu} + U_0 - c\right). \tag{6.23}$$

The solution of (6.22) satisfying $f \to 0$ as $\eta \to \infty$ has the far-field behaviour

$$f \propto \frac{1}{\eta} \exp\left(-\frac{K\eta^2}{2}\right) \tag{6.24}$$

as $\eta \to \infty$, provided that $K > 0$; equation (6.24) shows that the transverse profile of the fluid film approaches the uniform far-field value in (6.19) monotonically.

6.1.4 Physical forms of the solutions

The condition $K > 0$ together with condition (6.21) shows that a dry patch is possible only if

$$\ell \cos\alpha h_\infty \tau_0 > \mu\ell \cos\alpha\,(c - U_0) > 0, \tag{6.25}$$

where we have defined $\tau_0 = \rho g \sin\alpha h_\infty + \tau$ (so that τ_0, which may be positive, negative or zero, represents the shear stress $\mu \mathrm{d}u_\infty/\mathrm{d}z$ at $z = 0$ acting on the substrate due to the flow (6.12) of a film of uniform thickness h_∞). Thus in the sessile case ($\cos\alpha > 0$) if $\tau_0 > 0$ then $\ell > 0$ and $c > U_0$, so that the dry patch occupies $x \geq ct$, moves *downwards* relative to the substrate, and has semi-width $a = \sqrt{\ell(x - ct)}\,\eta_0$, widening with increasing x, the fluid in $x < ct$ being of uniform thickness h_∞, whereas if $\tau_0 < 0$ then $\ell < 0$ and $c < U_0$, so that the dry patch occupies $x \leq ct$, moves *upwards* relative to the substrate, and has semi-width $a = \sqrt{|\ell|(ct - x)}\,\eta_0$, narrowing with increasing x, the fluid in $x > ct$ being of uniform thickness h_∞; analogous remarks apply to the pendent case ($\cos\alpha < 0$). The forms of the dry patch in these various cases are sketched in Figure 6.2, in which (a) and (b) show sessile cases, and (c) and (d) show pendent cases; in (a) and (c) the dry patch is moving downwards, and in (b) and (d) it is moving upwards.

Other things being equal, at any given instant t the free-surface profile in a sessile or pendent case on a substrate inclined at an angle α is the mirror image in the plane $x = ct$ of the free-surface profile in a pendent or sessile case on a substrate inclined at an angle $\pi - \alpha$.

The limit $\tau_0 \to 0$ corresponds to $c \to U_0$, that is, to a dry patch that is stationary relative to the substrate; in this case the local behaviour (6.20) no

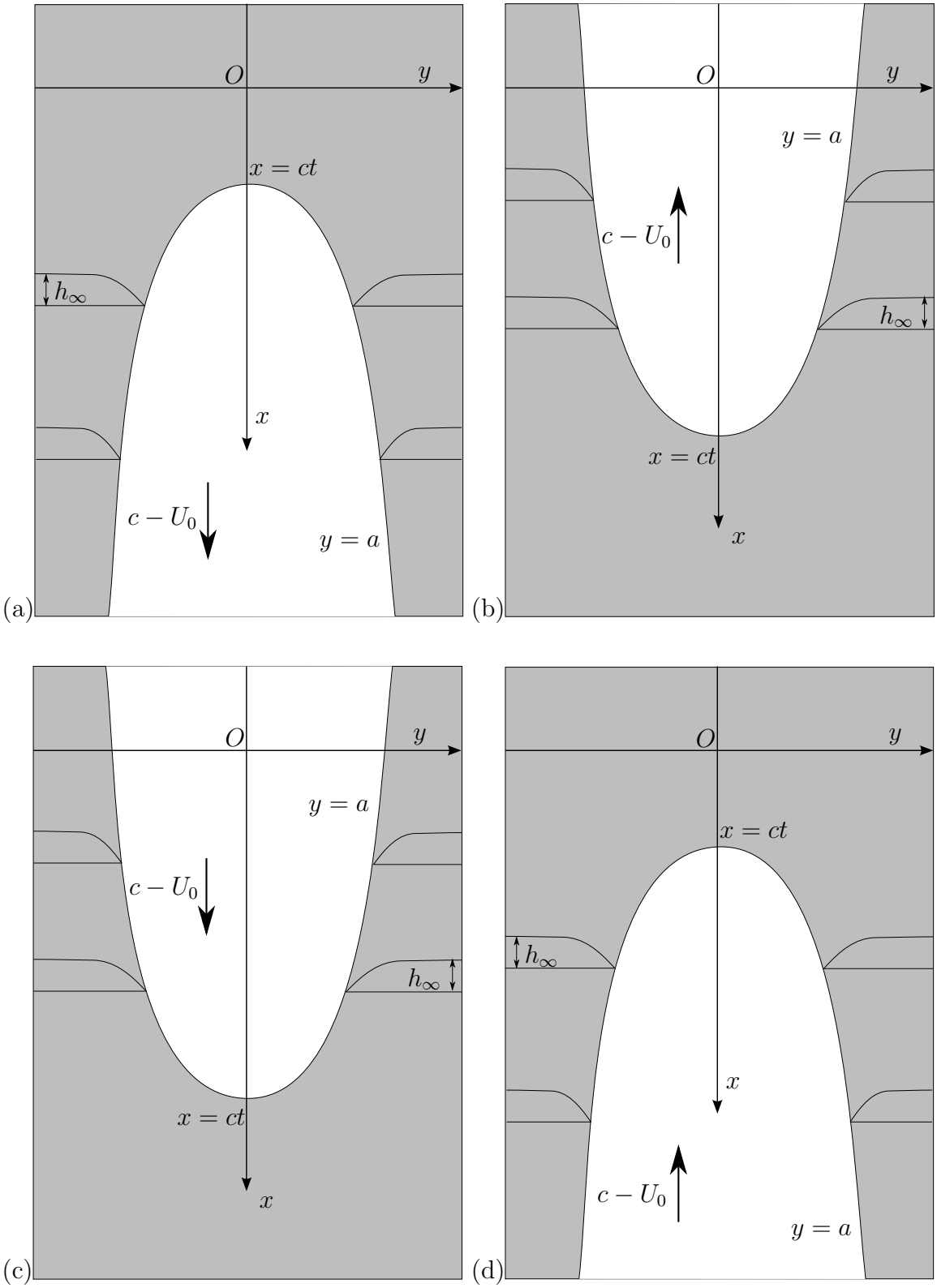

Figure 6.2: Sketch of the possible forms of the moving dry patch: (a) and (b) show sessile cases, and (c) and (d) show pendent cases; in (a) and (c) the dry patch is moving downwards, and in (b) and (d) it is moving upwards.

longer holds, and it is found that there can be a physically realisable solution only if $\ell \cos\alpha > 0$, $\tau < 0$ and $\tau_0 > 0$, and then (6.20) is replaced by

$$F \sim \left[-\frac{3\eta_0 \ell \tau (\eta - \eta_0)}{2\rho g \cos\alpha h_\infty^2} \right]^{\frac{1}{2}}. \tag{6.26}$$

The motion of the substrate with constant velocity $U_0\mathbf{i}$ corresponds to a "shift" in the value of c by an amount U_0 in (6.16); thus a particular solution (6.15) representing an unsteady flow with a dry patch moving with velocity $c\mathbf{i}$ on a substrate moving with velocity $U_0\mathbf{i}$ also provides a solution for a *steady* flow (with a stationary dry patch) on a substrate moving with velocity $(U_0 - c)\mathbf{i}$ provided simply that $x - ct$ is replaced with x in η.

6.1.5 Cross-sectional area and volume flux

The film is of infinite lateral extent, and its cross-sectional area (at constant x) is infinite, as is the volume flux of fluid down the substrate. However, the difference between the cross-sectional area of the part of the film of uniform thickness h_∞ in the region where $\ell(x - ct) < 0$ and that of the part of the film in the region where $\ell(x - ct) \geq 0$ containing the dry patch, denoted $\triangle A$, is finite and is given by

$$\triangle A = \lim_{y_\infty \to \infty} 2 \left(h_\infty y_\infty - \int_a^{y_\infty} h \, \mathrm{d}y \right) = 2h_\infty \sqrt{\ell(x - ct)}\, q_{\text{area}} \tag{6.27}$$

for $\ell(x - ct) \geq 0$, where the constant q_{area} is defined by

$$q_{\text{area}} = \eta_0 + \int_{\eta_0}^{\infty} (1 - F) \, \mathrm{d}\eta. \tag{6.28}$$

Similarly the difference in volume flux in the two parts of the film, denoted $\triangle Q$, is finite and is given by

$$\triangle Q = \lim_{y_\infty \to \infty} 2 \left(U h_\infty y_\infty - \int_a^{y_\infty} \bar{u} \, \mathrm{d}y \right), \tag{6.29}$$

that is,

$$\begin{aligned} \triangle Q \;\; = \;\; & 2h_\infty \sqrt{\ell(x - ct)} \left[U\eta_0 + \int_{\eta_0}^{\infty} \frac{\rho g \sin\alpha h_\infty^2}{3\mu} (1 - F^3) \, \mathrm{d}\eta \right. \\ & \left. + \int_{\eta_0}^{\infty} \left(\frac{\tau h_\infty}{2\mu} (1 - F^2) + U_0 (1 - F) \right) \mathrm{d}\eta \right] \end{aligned} \tag{6.30}$$

for $\ell(x-ct) \geq 0$; however, an integration of (6.16) by parts and use of (6.18), (6.24), (6.27) and (6.28) shows that (6.30) reduces to simply

$$\triangle Q = c \triangle A = 2h_\infty \sqrt{\ell(x-ct)}\, c q_{\text{area}}. \tag{6.31}$$

Of particular interest are the cases of flow on a stationary substrate ($U_0 \equiv 0$) driven by gravity with no surface shear ($\tau \equiv 0$), and flow on a stationary substrate ($U_0 \equiv 0$) driven by surface shear with the down-slope component of gravity neglected (equivalent to setting $g \sin\alpha \equiv 0$); these two cases are now considered in more detail separately, in Section 6.2 and Section 6.3, respectively.

6.2 Gravity-Driven Flow

For purely gravity-driven flow on a stationary substrate (so that $\tau \equiv 0$ and $U_0 \equiv 0$) equation (6.16) reduces to

$$\left(F^3 F'\right)' + \frac{\ell \tan\alpha}{2h_\infty} \eta \left(F^3 - \frac{c}{U} F\right)' = 0, \tag{6.32}$$

where, from (6.13), $U = \rho g \sin\alpha h_\infty^2 / 3\mu$ (> 0) is the depth-averaged speed of the flow (6.12) in this case. Conditions (6.25) for the similarity solution to be valid reduce to

$$\ell \cos\alpha > 0, \quad 0 < c < 3U, \tag{6.33}$$

and without loss of generality we now write ℓ in the form

$$\ell = 2h_\infty \cot\alpha. \tag{6.34}$$

The result $c > 0$ shows that the dry patch moves *down* the substrate, not up, and the result $\ell \cos\alpha > 0$ means that in the sessile case ($\cos\alpha > 0$, so that $\ell > 0$) the dry patch occupies $x \geq ct$, with semi-width $a = \sqrt{\ell(x-ct)}\, \eta_0$ (widening with increasing x), whereas in the pendent case ($\cos\alpha < 0$, so that $\ell < 0$) it occupies $x \leq ct$, with semi-width $a = \sqrt{|\ell|(ct-x)}\, \eta_0$ (narrowing with increasing x), as

sketched in parts (a) and (c) of Figure 6.2. Also since now $U \neq 0$ we may write (6.31) in the form

$$\triangle Q = c\,\triangle A = 2Uh_\infty\sqrt{\ell(x-ct)}\,q_{\text{flux}}, \quad q_{\text{flux}} = \frac{c}{U}q_{\text{area}}. \tag{6.35}$$

We non-dimensionalise and re-scale variables according to

$$x = Xx^*, \quad y = \sqrt{|\ell|X}y^*, \quad z = h_\infty z^*, \quad t = \frac{X}{U}t^*, \quad h = h_\infty h^*, \quad a = \sqrt{|\ell|X}a^*,$$
$$c = Uc^*, \quad \triangle A = h_\infty\sqrt{|\ell|X}\triangle A^*, \quad \triangle Q = Uh_\infty\sqrt{|\ell|X}\triangle Q^*, \tag{6.36}$$

where X ($\gg h_\infty$) is a length scale in the x direction, which we may choose arbitrarily. Then with stars dropped for clarity, equation (6.33) requires that $0 < c < 3$, and the solution (6.15) takes the slightly simpler form

$$h = F(\eta), \quad y = \sqrt{S_g\,(x-ct)}\eta, \quad a = \sqrt{S_g\,(x-ct)}\eta_0, \quad \frac{y}{a} = \frac{\eta}{\eta_0} \tag{6.37}$$

(where we have defined $S_g = \text{sgn}(\cos\alpha)$), with F satisfying

$$\left(F^3F'\right)' + \eta\left(F^3 - cF\right)' = 0, \tag{6.38}$$

to be integrated subject to (6.18) and (6.19). Also from (6.27) and (6.35) we have

$$\triangle A = 2\sqrt{S_g\,(x-ct)}\,q_{\text{area}}, \quad \triangle Q = 2\sqrt{S_g\,(x-ct)}\,q_{\text{flux}}, \quad q_{\text{flux}} = cq_{\text{area}}, \tag{6.39}$$

with q_{area} given by (6.28).

Conditions for the dry patch to be thin and slender are that the length scales in the x, y and z directions, namely X, $\sqrt{|\ell|X}$ and h_∞, satisfy $h_\infty \ll \sqrt{|\ell|X} \ll X$, so that

$$X \gg h_\infty|\tan\alpha|, \quad X \gg h_\infty|\cot\alpha|, \tag{6.40}$$

respectively, showing that X must be much larger than h_∞ and that α cannot be close to 0, $\pi/2$ or π.

Near the contact line $\eta = \eta_0$ we have from (6.20)

$$F \sim [3c\eta_0(\eta - \eta_0)]^{\frac{1}{3}} \tag{6.41}$$

in the limit $\eta \to \eta_0^+$. Also from (6.24) we have

$$F - 1 \propto \frac{1}{\eta} \exp\left(-\frac{3-c}{2}\eta^2\right) \tag{6.42}$$

in the limit $\eta \to \infty$.

6.2.1 Numerical solution for $F(\eta)$

Since a closed-form solution of (6.38) is not available, we solved it numerically for F. Again, we did this using a shooting method, by shooting from a chosen value of the contact-line position $\eta = \eta_0$, with a chosen value of c. The solution F was monitored to see if it satisfied (6.19) to within a prescribed tolerance; if not then the value of c was changed and the calculation repeated until a solution satisfying (6.19) was found. In fact, the numerical computation cannot be started at $\eta = \eta_0$ (because of the singular slope there, given by (6.41)), so instead it was started from a position $\eta = \eta_0 + \delta$, where δ (> 0) is small; thus we solved (6.38) subject to the approximated boundary conditions

$$F(\eta_0 + \delta) = (3c\eta_0\delta)^{\frac{1}{3}}, \quad F'(\eta_0 + \delta) = \left(\frac{c\eta_0}{9\delta^2}\right)^{\frac{1}{3}}, \tag{6.43}$$

obtained from (6.41).

Figure 6.3 shows a plot of c as a function of η_0 obtained in this way, and Figure 6.4 shows examples of cross-sectional profiles $F(\eta)$ for various values of η_0. As Figure 6.3 shows, c is a single-valued function of η_0, but behaves non-monotonically; specifically, c decreases from its value $c = c_0 \simeq 1.8507$ when $\eta = 0$ to a (local) minimum value $c = c_{\min} \simeq 1.8501$ when $\eta_0 \simeq 0.0040$, then increases to a (global) maximum value $c = c_{\max} \simeq 1.8674$ when $\eta_0 \simeq 0.0450$, and thereafter decreases monotonically towards the value $c = 1$ as $\eta_0 \to \infty$. Thus the speed of the dry patch satisfies $1 < c \leq c_{\max}$ for any value of η_0, more restrictive than the necessary condition $0 < c < 3$ found earlier. Moreover, for a given value of c there is one corresponding value of η_0 if either $c = c_{\max}$ or $1 < c < c_{\min}$, two if either $c_0 < c < c_{\max}$ or $c = c_{\min}$, three if $c_{\min} < c \leq c_0$, and none if either $c > c_{\max}$ or $c \leq 1$; thus there can be zero, one, two or three different dry patches that travel

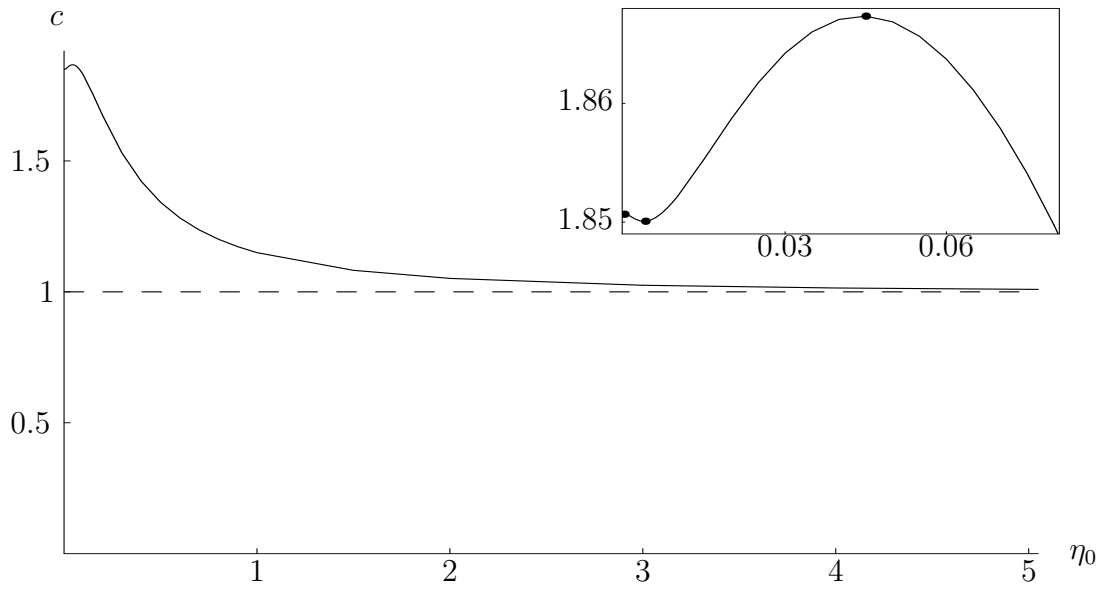

Figure 6.3: Plot of c as a function of η_0 for gravity-driven flow, together with the asymptotic value $c = c_\infty = 1$ in the limit $\eta_0 \to \infty$ (shown as a dashed line). The inset shows an enlargement of the behaviour near $\eta_0 = 0$; the point $c = c_0 \simeq 1.8507$ at $\eta_0 = 0$ is shown as a dot, as are the minimum $c = c_{\min} \simeq 1.8501$ at $\eta_0 \simeq 0.0040$ and the maximum $c = c_{\max} \simeq 1.8674$ at $\eta_0 \simeq 0.0450$.

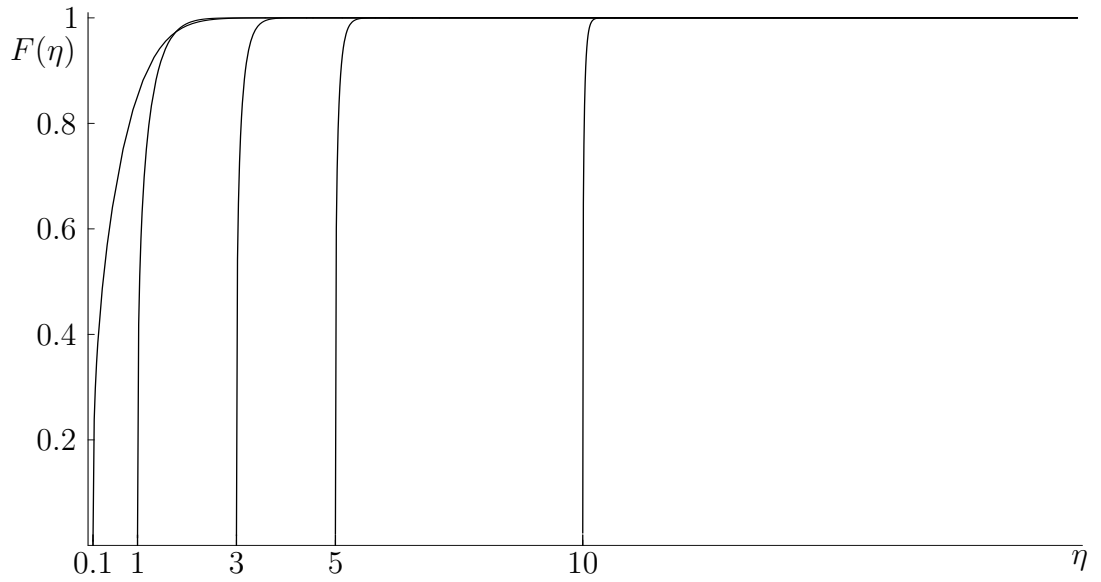

Figure 6.4: Cross-sectional profiles $F(\eta)$ for gravity-driven flow for several values of η_0.

at a given speed c.

Figure 6.4 shows that the cross-sectional profiles F increase monotonically with η, from $F = 0$ at $\eta = \eta_0$ to $F = 1$ as $\eta \to \infty$ (which means that, as expected, $\triangle A > 0$ and $\triangle Q > 0$). Figure 6.5 shows three-dimensional plots of the free-surface profiles h in a sessile case with $\eta_0 = 1$ at times $t = 0$, 1 and 3.

In the similarity solution (6.15) the value of η_0 is not determined as part of the solution, so that (6.15) represents a family of possible solutions. It is of interest to investigate the solutions in the asymptotic limits $\eta_0 \to 0$ and $\eta_0 \to \infty$, and, in particular, to compare them with numerical solutions.

6.2.2 Asymptotic solution in the limit $\eta_0 \to 0$

In the limit of a narrow dry patch, $\eta_0 \to 0$, we write

$$\eta = \eta_0 + \hat{\eta}, \quad F = \hat{F}(\hat{\eta}), \quad c = c_0; \tag{6.44}$$

then at leading order equation (6.38) gives

$$\left(\hat{F}^3\hat{F}'\right)' + \hat{\eta}\left(\hat{F}^3 - c_0\hat{F}\right)' = 0, \tag{6.45}$$

and the boundary conditions (6.18) and (6.19) give

$$\hat{F} = 0 \quad \text{at} \quad \hat{\eta} = 0, \qquad \hat{F}^3\hat{F}' \to 0 \quad \text{as} \quad \hat{\eta} \to 0, \qquad \hat{F} \to 1 \quad \text{as} \quad \hat{\eta} \to \infty. \tag{6.46}$$

At leading order in the limit $\hat{\eta} \to 0$ the solution of (6.45) and (6.46) for $\hat{F}$ has the asymptotic form

$$\hat{F} \sim \left(\frac{3}{5}c_0\hat{\eta}^2\right)^{\frac{1}{3}}. \tag{6.47}$$

We solved (6.45) for $\hat{F}$ numerically using a shooting method similar to that described above, subject to approximated boundary conditions obtained from (6.47), namely

$$\hat{F}(\delta) = \left(\frac{3}{5}c_0\delta^2\right)^{\frac{1}{3}}, \quad \hat{F}'(\delta) = \frac{2}{3}\left(\frac{3c_0}{5\delta}\right)^{\frac{1}{3}}, \tag{6.48}$$

where $0 < \delta \ll 1$. From this numerical solution it was found that $c_0 \simeq 1.8507$, confirming the value obtained earlier.

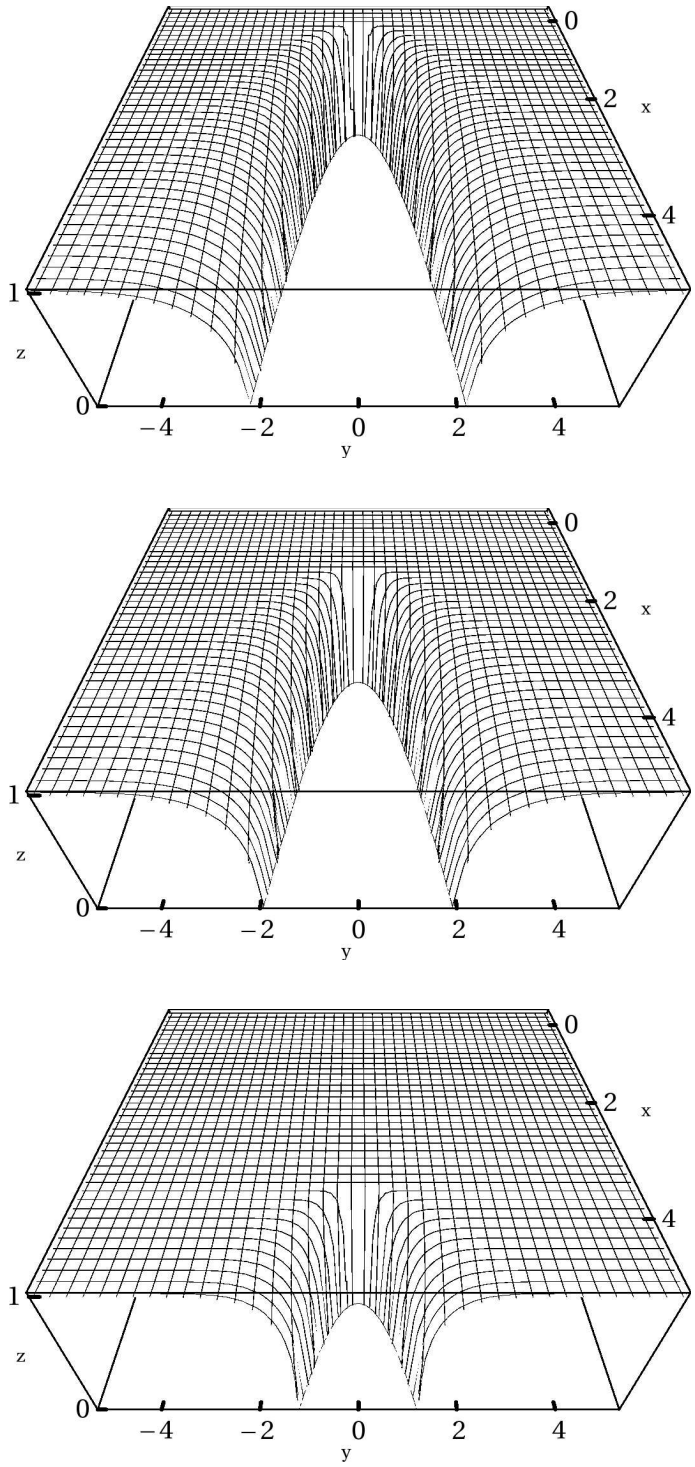

Figure 6.5: Three-dimensional plots of the free-surface profiles h for gravity-driven flow in a sessile case with $\eta_0 = 1$ at times $t = 0$, 1 and 3.

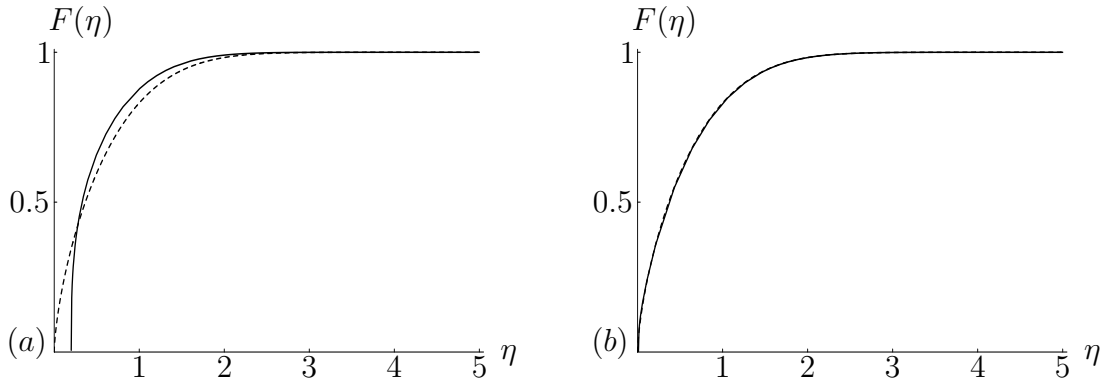

Figure 6.6: Numerical solutions of (6.38) for gravity-driven flow in the cases (a) $\eta_0 = 0.2$ and (b) $\eta_0 = 10^{-2}$, together with numerical solutions of the leading-order equation (6.45) in the limit $\eta_0 \to 0$ (shown as a dashed line).

Figure 6.6 shows a comparison between the numerical solution for F of equation (6.38) and the leading-order asymptotic solution for $\hat{F}$ in the cases $\eta_0 = 0.2$ and $\eta_0 = 10^{-2}$; clearly the agreement is good for small enough η_0.

Using the asymptotic solution we find that q_{area} in (6.28) and q_{flux} ($= cq_{\text{area}}$), in terms of which the "area difference" $\triangle A$ and the "flux difference" $\triangle Q$ are given by (6.39), satisfy

$$q_{\text{area}} \to \int_0^\infty \left(1 - \hat{F}\right) \mathrm{d}\hat{\eta} \simeq 0.5267, \quad q_{\text{flux}} \to c_0 q_{\text{area}} \simeq 0.9748 \tag{6.49}$$

in the limit $\eta_0 \to 0$.

6.2.3 Asymptotic solution in the limit $\eta_0 \to \infty$

In the limit of a wide dry patch, $\eta_0 \to \infty$, we write

$$\eta = \eta_0 + \frac{\tilde{\eta}}{\eta_0}, \quad F = \tilde{F}(\tilde{\eta}), \quad c = c_\infty; \tag{6.50}$$

then at leading order equation (6.38) reduces to

$$\left(\tilde{F}^3 \tilde{F}'\right)' + \left(\tilde{F}^3 - c_\infty \tilde{F}\right)' = 0, \tag{6.51}$$

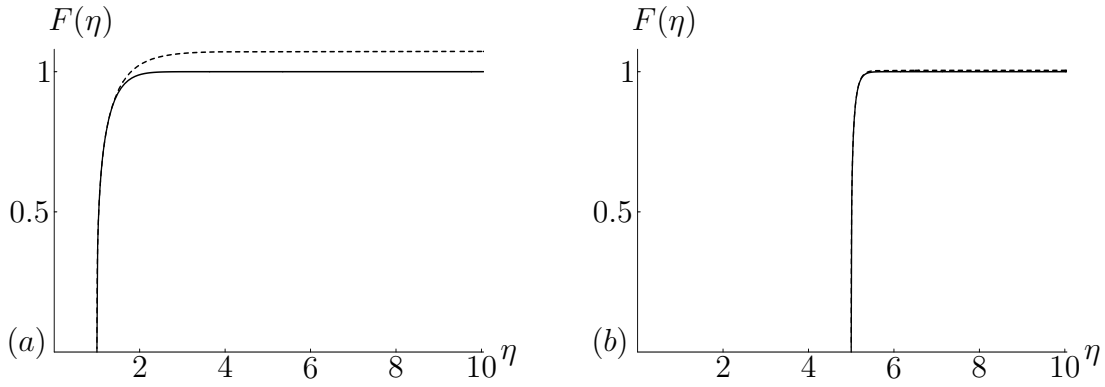

Figure 6.7: Numerical solutions of (6.38) for gravity-driven flow in the cases (a) $\eta_0 = 1$ and (b) $\eta_0 = 5$, together with the leading-order asymptotic solution (6.53) in the limit $\eta_0 \to \infty$ (shown as a dashed line).

which is readily solved subject to the boundary conditions

$$\tilde{F} = 0 \quad \text{at} \quad \tilde{\eta} = 0, \qquad \tilde{F}^3 \tilde{F}' \to 0 \quad \text{as} \quad \tilde{\eta} \to 0, \qquad \tilde{F} \to 1 \quad \text{as} \quad \tilde{\eta} \to \infty \tag{6.52}$$

to give the implicit solution

$$\tilde{\eta} = \frac{1}{2} \log \left(\frac{1 + \tilde{F}}{1 - \tilde{F}} \right) - \tilde{F}, \quad c_\infty = 1. \tag{6.53}$$

Figure 6.7 shows a comparison between the numerical solution for F of equation (6.38) and the leading-order asymptotic solution for $\tilde{F}$ in (6.53) in the cases $\eta_0 = 1$ and $\eta_0 = 5$; the agreement is good for large enough η_0. The asymptotic value $c = c_\infty = 1$ is included in Figure 6.3 as a dashed line.

Using the asymptotic solution we find that q_{area} in (6.28) and q_{flux} ($= cq_{\text{area}}$) satisfy

$$q_{\text{area}} \sim q_{\text{flux}} \sim \eta_0 \tag{6.54}$$

in the limit $\eta_0 \to \infty$.

Figure 6.8 shows plots of q_{area} and q_{flux} as functions of η_0, together with the asymptotic values (6.49) in the limit $\eta_0 \to 0$ and the asymptotic form (6.54) in the limit $\eta_0 \to \infty$; each of them decreases from its value at $\eta_0 = 0$ to a minimum value, and then increases monotonically to ∞ as $\eta_0 \to \infty$ according to (6.54).

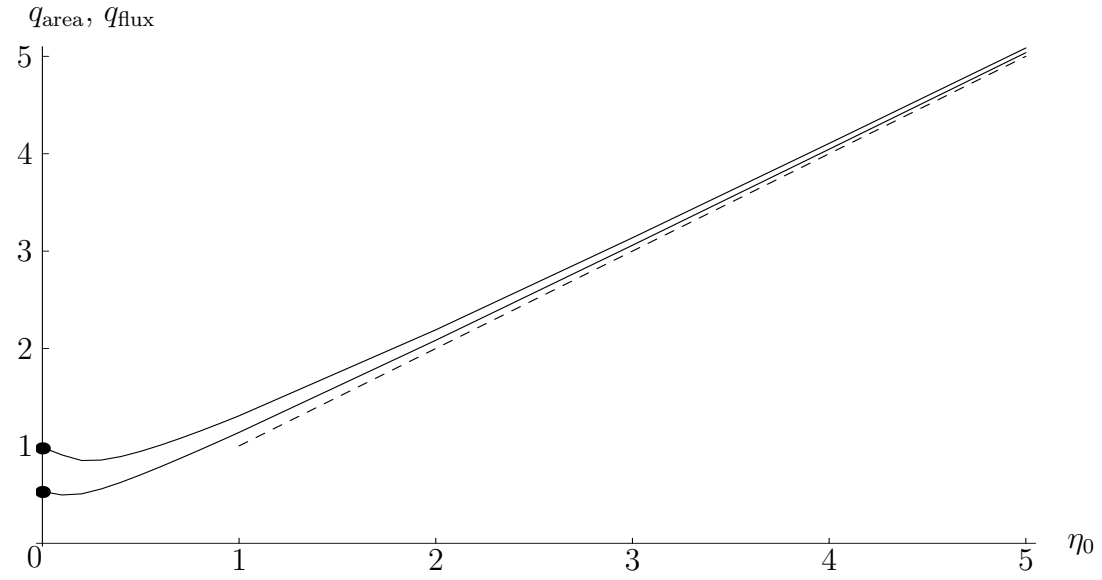

Figure 6.8: Plot of q_{area} in (6.28) (lower curve) and q_{flux} ($= cq_{\text{area}}$) (upper curve) as functions of η_0 for gravity-driven flow, together with the asymptotic values (6.49) in the limit $\eta_0 \to 0$ (shown as dots) and the asymptotic form (6.54) in the limit $\eta_0 \to \infty$ (shown as a dashed line).

6.3 Shear-Stress-Driven Flow

The analysis for purely shear-stress-driven flow on a stationary substrate (so that $g \sin\alpha \equiv 0$ and $U_0 \equiv 0$) proceeds very similarly to that for purely gravity-driven flow given in Section 6.2, and so the details need only be summarised here. Equation (6.16) reduces to

$$\left(F^3F'\right)' + \frac{3\tau\ell}{4\rho g\cos\alpha h_\infty^2}\eta\left(F^2 - \frac{c}{U}F\right)' = 0, \tag{6.55}$$

where, from (6.13), $U = \tau h_\infty/2\mu$ (> 0) is the depth-averaged speed of the flow (6.12) in this case, and without loss of generality we now take $\tau > 0$. Conditions (6.25) for the similarity solution to be valid reduce to

$$\ell\cos\alpha > 0, \quad 0 < c < 2U, \tag{6.56}$$

and without loss of generality we now write ℓ in the form

$$\ell = \frac{4\rho g\cos\alpha h_\infty^2}{3\tau}. \tag{6.57}$$

The result $c > 0$ shows that the dry patch moves in the direction of τ, and the implications of the result $\ell \cos\alpha > 0$ concerning the shape of the dry patch are the same as for the gravity-driven flow, as sketched in parts (a) and (c) of Figure 6.2. Also $\triangle A$ and $\triangle Q$ are again given by (6.35) with the appropriate form for U and with q_{area} again given by (6.28).

We non-dimensionalise and re-scale variables as in (6.36); then with stars dropped for clarity, equation (6.56) requires that $0 < c < 2$, and the solution (6.15) for h again takes the form (6.37), with F now satisfying

$$\left(F^3F'\right)' + \eta\left(F^2 - cF\right)' = 0, \tag{6.58}$$

to be integrated subject to (6.18) and (6.19). Also $\triangle A$ and $\triangle Q$ are again given by (6.39). The conditions $h_\infty \ll \sqrt{|\ell|X} \ll X$ for the dry patch to be thin and slender now require that

$$X \gg \frac{\tau}{\rho g|\cos\alpha|}, \quad X \gg \frac{\rho g|\cos\alpha|h_\infty^2}{\tau}, \tag{6.59}$$

respectively, showing that X must be sufficiently large and that α cannot be close to $\pi/2$.

Near the contact line $\eta = \eta_0$ the behaviour of F is again given by (6.41) in the limit $\eta \to \eta_0^+$, but from (6.24) we now have

$$F - 1 \propto \frac{1}{\eta}\exp\left(-\frac{2-c}{2}\eta^2\right) \tag{6.60}$$

in the limit $\eta \to \infty$.

6.3.1 Numerical solution for $F(\eta)$

We solved (6.58) numerically for F subject to (6.43), using the same procedure as in Section 6.2. Figure 6.9 shows a plot of c as a function of η_0, and Figure 6.10 shows examples of cross-sectional profiles $F(\eta)$ for various values of η_0. As these figures show, the behaviour of the solution in this case is qualitatively similar to

that in the case of gravity-driven flow; in particular, the cross-sectional profiles F again increase monotonically with η.

It is found that $c = c_0 \simeq 1.5424$ when $\eta = 0$, and that c has a (local) minimum value $c = c_{\min} \simeq 1.5421$ when $\eta_0 \simeq 0.0040$ and (global) maximum value $c = c_{\max} \simeq 1.5503$ when $\eta_0 \simeq 0.0470$, and again satisfies $1 < c \leq c_{\max}$ for any value of η_0; also there can again be up to three different dry patches that travel at a given speed c in this interval.

Figure 6.11 shows three-dimensional plots of the free-surface profiles h in a sessile case with $\eta_0 = 1$ at times $t = 0$, 1 and 3; these are qualitatively similar to those in Figure 6.5.

6.3.2 Asymptotic solution in the limit $\eta_0 \to 0$

In the limit of a narrow dry patch, $\eta_0 \to 0$, we again write η, F and c in the form (6.44); then at leading order equation (6.58) gives

$$\left(\hat{F}^3\hat{F}'\right)' + \hat{\eta}\left(\hat{F}^2 - c_0\hat{F}\right)' = 0, \tag{6.61}$$

with $\hat{F}$ satisfying (6.46).

At leading order in the limit $\hat{\eta} \to 0$ the solution of (6.61) and (6.46) for $\hat{F}$ has the asymptotic form (6.47), and we solved (6.61) for $\hat{F}$ numerically using the method described above, subject to the approximated boundary conditions (6.48) obtained from (6.47). From this numerical solution it was found that $c_0 \simeq 1.5424$, confirming the value obtained earlier. Figure 6.12 shows a comparison between the numerical solution for F of equation (6.58) and the leading-order asymptotic solution for $\hat{F}$ in the cases $\eta_0 = 0.2$ and $\eta_0 = 10^{-2}$; again the agreement is good for small enough η_0.

Using the asymptotic solution we find that q_{area} in (6.28) and q_{flux} ($= cq_{\text{area}}$) satisfy

$$q_{\text{area}} \to \int_0^\infty \left(1 - \hat{F}\right) \mathrm{d}\hat{\eta} \simeq 0.7418, \quad q_{\text{flux}} \to c_0 q_{\text{area}} \simeq 1.1441 \tag{6.62}$$

in the limit $\eta_0 \to 0$.

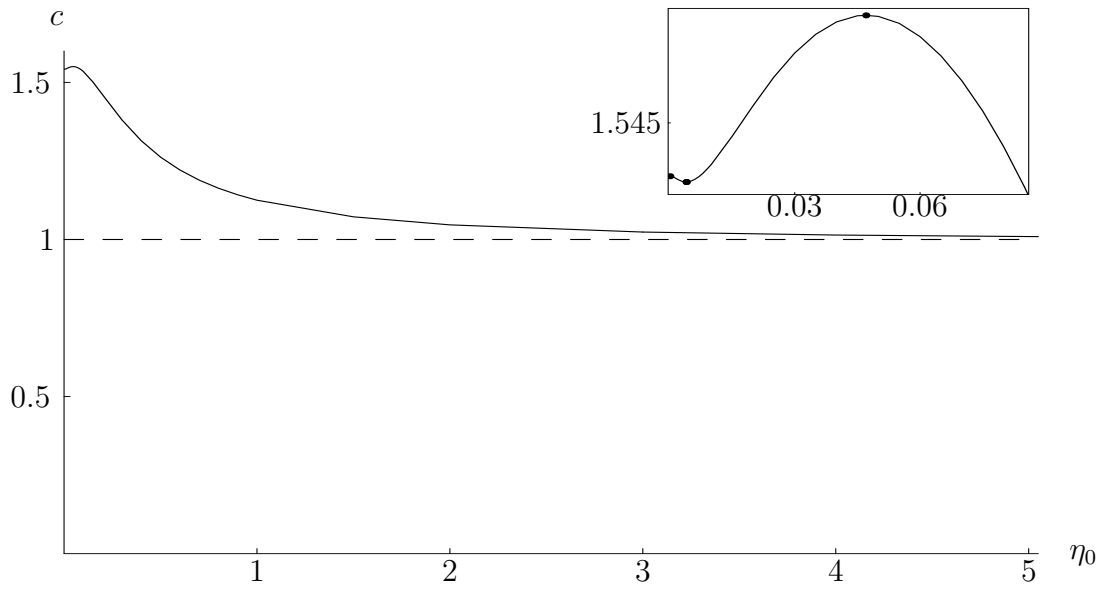

Figure 6.9: Plot of c as a function of η_0 for shear-stress-driven flow, together with the asymptotic value $c = c_\infty = 1$ in the limit $\eta_0 \to \infty$ (shown as a dashed line). The inset shows an enlargement of the behaviour near $\eta_0 = 0$; the point $c = c_0 \simeq 1.5424$ at $\eta_0 = 0$ is shown as a dot, as are the minimum $c = c_{\min} \simeq 1.5421$ at $\eta_0 \simeq 0.0040$ and the maximum $c = c_{\max} \simeq 1.5503$ at $\eta_0 \simeq 0.0470$.

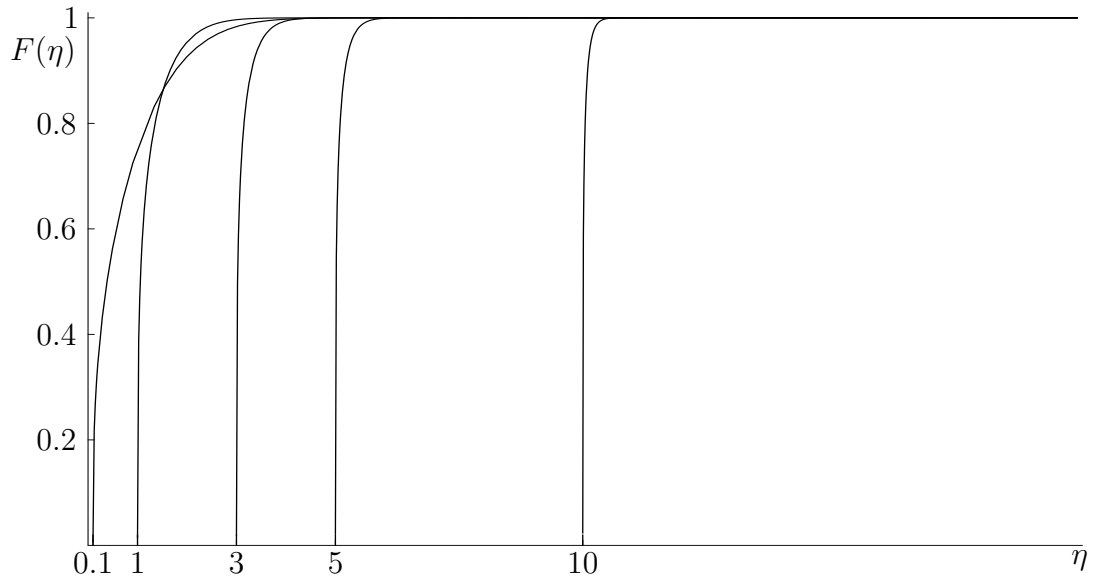

Figure 6.10: Cross-sectional profiles $F(\eta)$ for shear-stress-driven flow for several values of η_0.

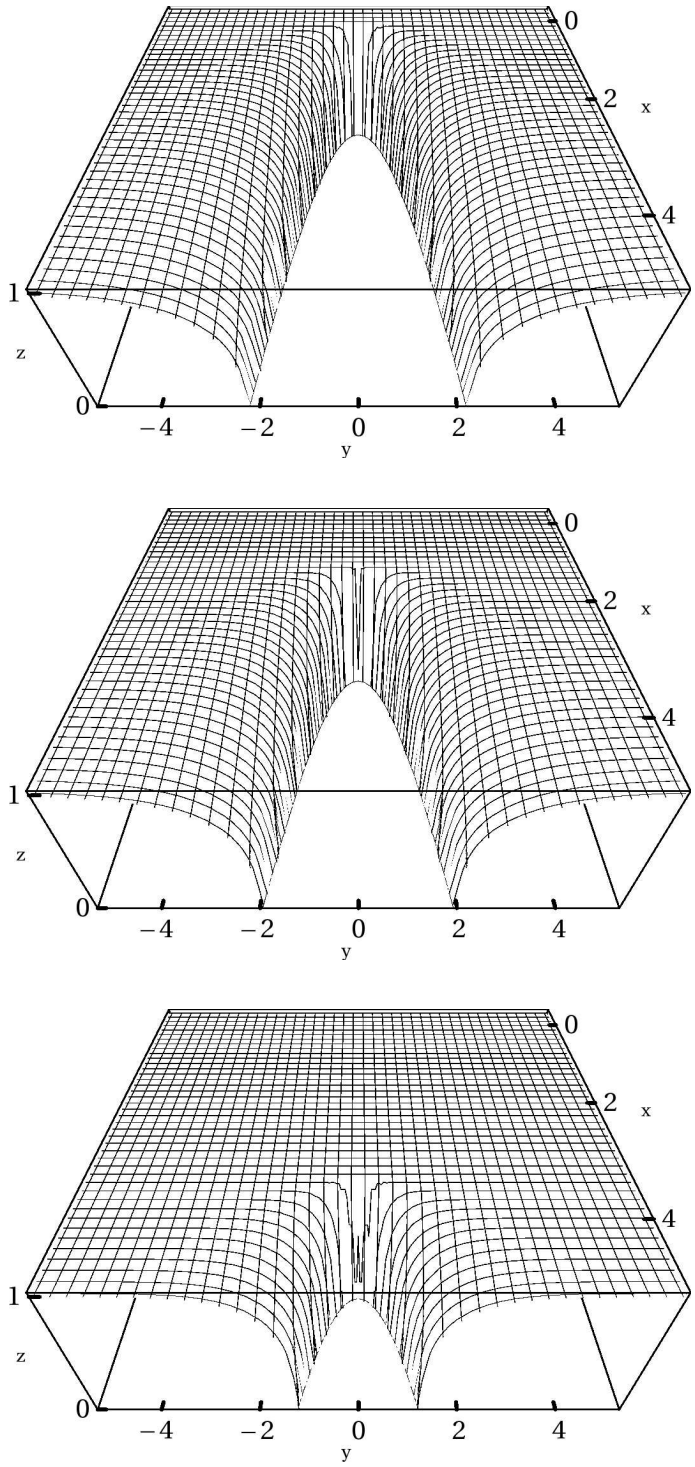

Figure 6.11: Three-dimensional plots of the free-surface profiles h for shear-stress-driven flow in a sessile case with $\eta_0 = 1$ at times $t = 0$, 1 and 3.

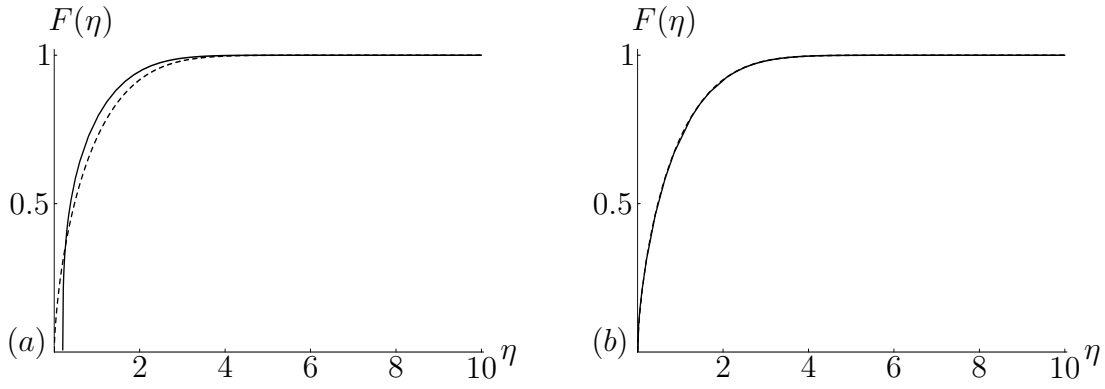

Figure 6.12: Numerical solutions of (6.58) for shear-stress-driven flow in the cases (a) $\eta_0 = 0.2$ and (b) $\eta_0 = 10^{-2}$, together with numerical solutions of the leading-order equation (6.61) in the limit $no \to 0$ (shown as a dashed line).

6.3.3 Asymptotic solution in the limit $\eta_0 \to \infty$

In the limit of a wide dry patch, $\eta_0 \to \infty$, we again write η, F and c in the form (6.50); then at leading order equation (6.58) reduces to

$$\left(\tilde{F}^3\tilde{F}'\right)' + \left(\tilde{F}^2 - c_\infty\tilde{F}\right)' = 0, \tag{6.63}$$

which is readily solved subject to the boundary conditions (6.52) to give the implicit solution

$$\tilde{\eta} = -\tilde{F} - \frac{\tilde{F}^2}{2} - \log\left(1-\tilde{F}\right), \quad c_\infty = 1. \tag{6.64}$$

Figure 6.13 shows a comparison between the numerical solution for F of equation (6.58) and the leading-order asymptotic solution for $\tilde{F}$ in (6.64) in the cases $\eta_0 = 1$ and $\eta_0 = 5$; again the agreement is good for large enough η_0. The asymptotic value $c = c_\infty = 1$ is included in Figure 6.9 as a dashed line. Using the asymptotic solution we find that q_{area} and q_{flux} again satisfy (6.54) in the limit $\eta_0 \to \infty$.

Figure 6.14 shows plots of q_{area} and q_{flux} as functions of η_0, together with the asymptotic values (6.62) in the limit $\eta_0 \to 0$ and the asymptotic form (6.54) in the limit $\eta_0 \to \infty$; the behaviour is qualitatively similar to that in Figure 6.8.

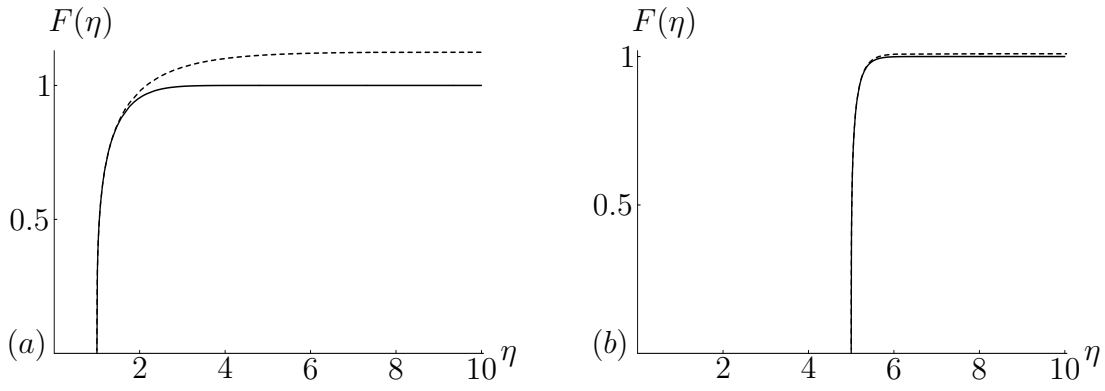

Figure 6.13: Numerical solutions of (6.58) for shear-stress-driven flow in the cases (a) $\eta_0 = 1$ and (a) $\eta_0 = 5$, together with the leading-order asymptotic solution (6.64) in the limit $\eta_0 \to \infty$ (shown as a dashed line).

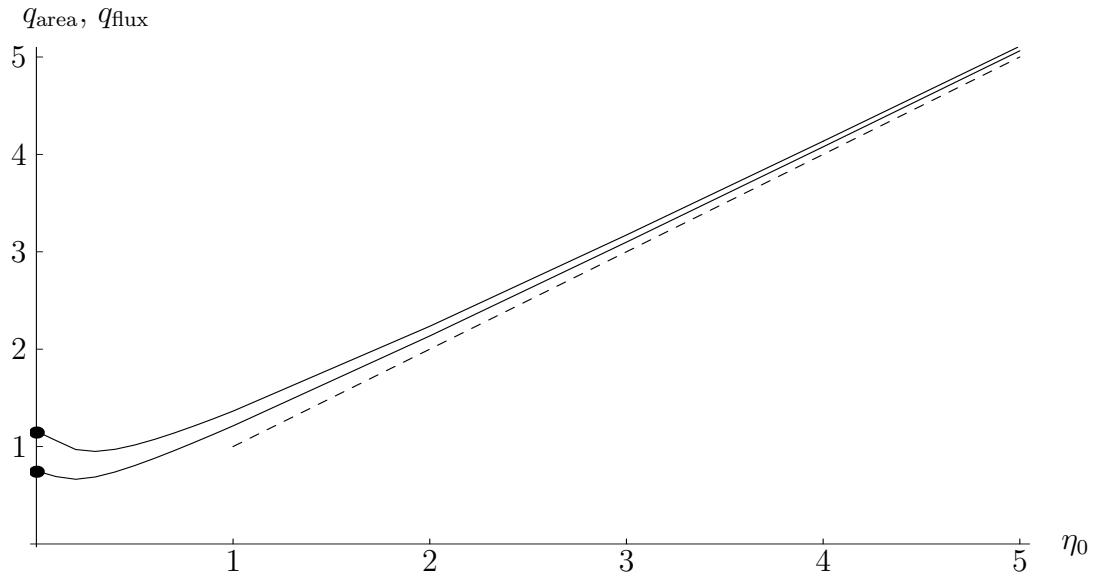

Figure 6.14: Plot of q_{area} in (6.28) (lower curve) and q_{flux} ($= cq_{\text{area}}$) (upper curve) as functions of η_0 for shear-stress-driven flow, together with the asymptotic values (6.62) in the limit $\eta_0 \to 0$ (shown as dots) and the asymptotic form (6.54) in the limit $\eta_0 \to \infty$ (shown as a dashed line).

6.4 Discussion

We have obtained unsteady travelling-wave similarity solutions of the form (6.15) for an infinitely wide thin film of Newtonian fluid of nominal uniform thickness h_∞ flowing around a symmetric slender dry patch moving at constant velocity $c\mathbf{i}$ on an inclined planar substrate, the flow being driven by gravity, a constant shear stress at the free surface, and/or steady motion of the substrate parallel to itself. The dry patch has a parabolic shape, which may be concave up or concave down the substrate, as indicated in Figure 6.2. If $\tau_0 > 0$ (corresponding to a surface shear stress τ that either acts downwards or acts upwards but is sufficiently weak) then the dry patch moves down the substrate, whereas if $\tau_0 < 0$ (corresponding to a sufficiently strong surface shear stress τ that acts upwards) then the dry patch moves up the substrate. Numerical solutions in the particular cases of purely gravity-driven flow and purely shear-stress-driven flow were found to be qualitatively similar; in both cases the film thickness increases monotonically away from the dry patch.

The parameter η_0 is not determined as part of the solution, so that (6.15) represents a one-parameter family of solutions; some additional criterion would be required to determine η_0.

The solutions obtained are valid for any value of h_∞, showing that for these solutions there is no critical thickness or critical flux below which a dry patch persists but above which it is "swept away" by the bulk flow.

Finally, it is worth noting that since there is no non-trivial solution near $\eta = 0$ satisfying $F'(0) = 0$, we may conclude that the corresponding rivulet solutions are not possible for this case.

Chapter 7

Conclusions and Further Work

7.1 Conclusions

In this thesis we obtained unsteady three-dimensional similarity solutions for a variety of flows of thin slender non-uniform rivulets and flows of thin films around slender dry patches on an inclined plane using the lubrication approximation. Specifically, we investigated the flows of Newtonian and non-Newtonian power-law fluids driven by either gravity or a constant shear stress at the free surface directed down the plane, and found two very different types of similarity solutions.

In Chapter 2 we derived a similarity solution describing the unsteady flow of gravity-driven rivulet of a Newtonian fluid. The similarity solution predicts that at any time t the rivulet widens or narrows according to $|x|^{3/4}$ and thickens or thins according to $|x|^{1/2}$, and at any station x it widens or narrows according to $|t|^{-1/4}$ and thickens or thins according to $|t|^{-1/2}$. Initially, we had four cases to consider, depending on the signs of S_t, S_g and S_x. However, we found that only the case with $S_t = -S_g = S_x = \pm 1$ leads to a physically realisable solution. The case $S_t = -S_g = S_x = 1$ corresponds to a pendent rivulet in $x > 0$ with $t > 0$, and the case $S_t = -S_g = S_x = -1$ corresponds to a sessile rivulet in $x < 0$ with $t < 0$. To solve the ordinary differential equation governing the similarity solution, we first used numerical and asymptotic methods to obtain a one-parameter family of

solutions parameterised by the (appropriately scaled) middle height H_0; then by imposing the condition of zero mass flux at the contact line, we showed that, of this family of solutions, only two are physically realisable, one with $H_0 = H_{01} \simeq 0.9995$ (having a double-humped cross-sectional profile) and one with $H_0 = H_{02} \simeq 1.1059$ (having a single-humped cross-sectional profile).

In Chapter 3 using the finite element package COMSOL we performed numerical investigations of the stability of the two similarity solutions corresponding to $H_0 = H_{01}$ and $H_0 = H_{02}$ for sessile and pendent rivulets by imposing three types of perturbations as boundary conditions. The numerical solutions showed that for a sessile rivulet the perturbations do not grow, whereas for a pendent rivulet our numerical computations failed at a small time (showing the same failure as occurs in numerical computation of a linear backwards-diffusion problem), which led us to the conclusion that the sessile rivulet is stable, whereas the pendent rivulet is unstable. In validating our numerical procedure, we solved a variety of problems concerning unsteady gravity-driven flow on an inclined plane and on a horizontal plane. The numerical solutions obtained were found to approach known similarity solutions at sufficiently large times and length scales. In particular, we obtained new numerical results for gravity-driven flow of a rivulet with strong surface-tension effects that verify the similarity solutions obtained by Duffy and Moffatt [24].

In Chapter 4 we generalised our approach in Chapter 2 to consider unsteady flow of a gravity-driven sessile rivulet of a power-law fluid (of index N). We obtained two physically realisable solutions with different middle heights $H_0 = H_{01}$ (< 1) and $H_0 = H_{02}$ (> 1) for each value of N; these solutions predict that at time t, the rivulet (in $x < 0$) narrows according to $(-x)^{(2N+1)/2(N+1)}$ and thins according to $(-x)^{N/(N+1)}$ as it flows down the plane, and at any station x, the rivulet widens according to $(-t)^{N/2(N+1)}$ and thickens according to $(-t)^{N/(N+1)}$. As the value of N is increased, H_{01} decreases whereas H_{02} increases. We also presented asymptotic solutions in the strongly shear-thinning limit $N \to 0$ and in

the strongly shear-thickening limit $N \to \infty$.

In Chapter 5 we extended our studies in Chapters 2 and 4 to investigate unsteady surface-shear-stress-driven flow for both Newtonian and power-law fluids. For this type of flow we obtained similarity solutions for both rivulet flow and flow around a dry patch (whereas in gravity-driven flow there is no corresponding solution for flow around a dry patch). The similarity solution predicts that at any time t the rivulet and dry patch widen or narrow according to $|x|^{3/2}$ and thicken or thin according to $|x|$, and that at any station x the rivulet and dry patch widen or narrow like $|t|^{-1}$ and the film thickens or thins like $|t|^{-1}$, independent of the power-law index N. Unlike in the case of gravity-driven flow, in this case, we found only one physically realisable solution, with $H_0 \simeq 1.2708$ (having a single-humped cross-sectional profile) for a rivulet in the case $S_t = -S_g = S_x$, and one physically realisable solution with scaled semi-width $\eta_0 \simeq 0.9573$ for a dry patch in the case $S_t = S_g = S_x$. For all the similarity solutions obtained in Chapter 2, 4 and 5, the nose of the rivulet remains stationary at O at all time; also at $t = 0$, the solution exhibits a finite-time singularity, becoming infinite everywhere at that instant.

Finally, in Chapter 6 we obtained a completely different kind of similarity solution, namely a travelling-wave solution for unsteady flow of a thin film of Newtonian fluid around a slender dry patch driven by either gravity or a constant surface shear stress. The similarity solution predicts that for both sessile ($S_g = 1$) and pendent ($S_g = -1$) cases the dry patch travels either up or down the plane at constant speed c, that it has a parabolic shape, its scaled semi-width η_0 varying like $(x-ct)^{1/2}$ and that the thickness of the fluid film increases monotonically away from the dry patch. We found that for any choice of η_0 there is a unique solution whose non-dimensional wave speed c takes values in a finite interval $1 < c \leq c_{max}$. However, for any choice of c, there can be zero, one, two or three different dry patches (of different width) that travel at the same speed. Solutions for a shear-stress-driven flow are qualitatively similar to those for gravity-driven flow. Unlike in previous chapters, there are no corresponding travelling-wave similarity

solutions for rivulets.

7.2 Further Work

Despite the progress that has been made, there are still many interesting open questions. Throughout the present work, we assumed that surface-tension effects were negligible for simplicity. Therefore, the most obvious extension of the current work is to consider unsteady three-dimensional similarity solutions in cases when surface-tension effects dominate the flow. As discussed previously in Chapter 1, a steady similarity solution for a flow of this type was already obtained by Duffy and Moffatt [24] for the case of a gravity-driven rivulet, but corresponding unsteady solutions have not been investigated.

In Chapter 2 we performed a numerical investigation of the stability of the similarity solutions for an unsteady gravity-driven rivulet using the finite element package COMSOL. It would be of interest to use the same numerical procedure to investigate the stability of the other similarity solutions for unsteady rivulets and dry patches for both Newtonian and power-law fluids obtained in Chapter 4, 5 and 6.

In addition, to further our understanding of the problems discussed here, it would be useful to conduct appropriate physical experiments. The question then arises as to how the flows described by the similarity solutions can be established in experiments. For instance, in the case of a gravity-driven sessile rivulet, it would be necessary to supply fluid far upstream and to arrange for the downstream nose of the rivulet to be fixed, so that the fluid piles up there with time, whereas in the case of a pendent rivulet, presumably an initial "lump" of fluid could simply be allowed to drain down the plane. In the case of shear-stress driven flow of sessile and pendent rivulets, it may be possible to use the same set up as in the case of gravity-driven rivulet, but with a jet of air blown along the free surface of the rivulets directed down the plane. In the case of shear-stress driven flow around a

dry patch, a jet of air could be blown at the fluid surface so that the dry patch will form.

Finally, in Chapter 6 we obtained a travelling-wave solution for an unsteady flow of a thin film of Newtonian fluid around a slender dry patch on an inclined plane driven by either gravity or a constant surface shear stress. It would be of considerable interest to examine the combined effects of both gravity and surface shear stress on the flow, and to compare the results with any available experimental data. It should also be possible to generalise the solution obtained in Chapter 6 to the case of a power-law fluid.

As discussed previously in Chapter 1, thin-film flows play a significant role in a variety of geophysical, biological and industrial contexts, and many open problems in this area continue to attract attention from theoreticians and experimentalist. While this thesis has provided some insights into problems concerning unsteady thin-film flows, in particular, for rivulets and dry patches, a wealth of other interesting and important problems remain to be tackled.

Appendix A

Derivation of the result $\gamma \simeq u_z$

In this Appendix we derive the result $\gamma \simeq u_z$, used in Chapters 4 and 5. From (1.17) the local shear rate γ is given by

$$\gamma = \left(2\,\mathrm{tr}(\mathbf{e}^2)\right)^{\frac{1}{2}}, \tag{A.1}$$

where the rate-of-deformation tensor $\mathbf{e}$ is

$$\mathbf{e} = \frac{1}{2}\left[(\nabla\mathbf{u}) + (\nabla\mathbf{u})^T\right]. \tag{A.2}$$

If we write $\mathbf{u} = (u(x,y,z,t), v(x,y,z,t), w(x,y,z,t))$ then

$$\mathbf{e} = \begin{pmatrix} u_x & \frac{1}{2}(u_y+v_x) & \frac{1}{2}(u_z+w_x) \\ \frac{1}{2}(v_x+u_y) & v_y & \frac{1}{2}(v_z+w_y) \\ \frac{1}{2}(w_x+u_z) & \frac{1}{2}(w_y+v_z) & w_z \end{pmatrix}, \tag{A.3}$$

and substituting (A.3) into (A.1) we obtain

$$\gamma = \left[2\,\mathrm{tr}\begin{pmatrix} u_x & \frac{1}{2}(u_y+v_x) & \frac{1}{2}(u_z+w_x) \\ \frac{1}{2}(v_x+u_y) & v_y & \frac{1}{2}(v_z+w_y) \\ \frac{1}{2}(w_x+u_z) & \frac{1}{2}(w_y+v_z) & w_z \end{pmatrix}^2\right]^{\frac{1}{2}}, \tag{A.4}$$

leading to the general result

$$\gamma = \left[2u_x^2 + 2v_y^2 + 2w_z^2 + (u_y+v_x)^2 + (u_z+w_x)^2 + (v_z+w_y)^2\right]^{\frac{1}{2}}. \tag{A.5}$$

For either a thin slender rivulet or a slender dry patch in a thin film we non-dimensionalise according to

$$\begin{aligned} x = L_x\, x^*, \qquad y = L_y\, y^*, \qquad z = L_z z^*, \\ u = U u^*, \qquad v = \epsilon U v^*, \qquad w = \epsilon\delta U w^*, \qquad \gamma = \frac{U}{L_z}\gamma^*, \end{aligned} \tag{A.6}$$

where L_x, L_y and L_z are characteristic length scales in the x, y and z directions, respectively, satisfying $L_z \ll L_y \ll L_x$, and δ and ϵ are aspect ratios defined by $\delta = \dfrac{L_z}{L_y} \ll 1$ and $\epsilon = \dfrac{L_y}{L_x} \ll 1$. Dropping the superscript stars for clarity we obtain

$$\begin{aligned} \gamma^2 \;=\; & u_z^2 + \epsilon^2 v_z^2 + \delta^2 u_y^2 + 2\epsilon^2\delta^2\left(u_x^2 + v_y^2 + w_z^2 + u_y v_x + v_z w_y + u_z w_x\right) \\ & + \epsilon^2\delta^4 w_y^2 + \epsilon^4\delta^2 v_x^2 + \epsilon^4\delta^4 w_x^2 \end{aligned} \tag{A.7}$$

from (A.5), showing that $\gamma^2 = u_z^2 + O(\epsilon^2, \delta^2)$ in the limit $\epsilon, \delta \to 0$, and hence that $\gamma \simeq |u_z|$. Therefore for flows with $u_z \geq 0$ considered in this thesis, the shear rate is given approximately by $\gamma \simeq u_z$.

Bibliography

[1] http://functions.wolfram.com/HypergeometricFunctions/HermiteHGeneral/. Accessed on January 2010.

[2] *COMSOL Multiphysics, Version 3.2*. COMSOL AB, Stockholm, Sweden, 2005.

[3] M. Abramowitz and I. A. Stegun. *Handbook of Mathematical Functions with Formulas, Graphs, and Mathematical Tables*. Dover Publication Inc., New York, 1970.

[4] R. P. Agarwal and D. O'Regan. Infinite interval problems arising in the model of a slender dry patch in a liquid film draining under gravity down an inclined plane. *Methods Appl. Anal.*, 10:363–376, 2003.

[5] R. F. Allen and C. M. Biggin. Longitudinal flow of a lenticular liquid filament down an inclined plane. *Phys. Fluids*, 17:287–291, 1974.

[6] N. J. Balmforth, A. S. Burbridge, R. V. Craster, J. Salzig, and A. Shen. Visco-plastic models of isothermal lava domes. *J. Fluid Mech.*, 403:37–65, 2000.

[7] S. G. Bankoff. Minimum thickness of a draining liquid film. *Int. J. Heat Mass Transfer*, 14:2143–2146, 1971.

[8] G. I. Barenblatt. On some unsteady fluids and gas motions in a porous medium. *Prikl. Mat. Mekh.*, 16:67–78, 1952 (in Russian).

[9] H. A. Barnes, J. F. Hutton, and K. Walters. *An Introduction to Rheology*. Elsevier Science Publishers, Amsterdam, 1989.

[10] M. Ben Amar, L. Cummings, and Y. Pomeau. Singular points of a moving contact line. *C. R. Acad. Sci., Ser IIb*, 329:277–282, 2001.

[11] M. Ben Amar, L. J. Cummings, and Y. Pomeau. Transition of a moving contact line from smooth to angular. *Phys. Fluids*, 15:2949–2960, 2003.

[12] M. Bentwich, D. Glasser, J. Kern, and D. Williams. Analysis of rectilinear rivulet flow. *AIChE J.*, 22:772–779, 1976.

[13] A. J. Bernoff and T. P. Witelski. Linear stability of source-type similarity solutions of the thin film equation. *Appl. Math. Lett.*, 15:599–606, 2002.

[14] S. I. Betelú and J. A. Diez. A two-dimensional similarity solution for capillary driven flows. *Physica D*, 126:136–140, 1999.

[15] S. I. Betelú and M. A. Fontelos. Capillarity driven spreading of power-law fluids. *Appl. Math. Lett.*, 16:1315–1320, 2003.

[16] S. I. Betelú and M. A. Fontelos. Capillarity driven spreading of circular drops of shear-thinning fluid. *Math. Comput. Modell.*, 40:729–734, 2004.

[17] R. J. Braun and A. D. Fitt. Modelling drainage of the precorneal tear film after a blink. *Math. Med. Bio.*, 20:1–28, 2003.

[18] R. P. Chhabra and J. F. Richardson. *Non-Newtonian Flow in the Process Industries: Fundamentals and Engineering Applications*. Butterworth-Heinemann, Oxford, 1999.

[19] M. Colburn, B. J. Choi, S. V. Sreenivasan, R. T. Bonnecaze, and C. G. Willson. Ramifications of lubrication theory on imprint litography. *Microelectron. Eng.*, 75:321–329, 2004.

[20] P. Colinet, H. Kaya, S. Rossomme, and B. Scheid. Some advances in lubrication-type theories. *Eur. Phys. J. Special Topics*, 146:377–389, 2007.

[21] P. Coussot and S. Proust. Slow, unconfined spreading of a mudflow. *J. Geophys. Res.*, 101:25217–25229, 1996.

[22] R. V. Craster and O. K. Matar. Dynamics and stability of thin liquid films. *Rev. Mod. Phys.*, 81:1131–1198, 2009.

[23] B. R. Duffy and H. K. Moffatt. Flow of a viscous trickle on a slowly varying incline. *Chem. Eng. J.*, 60:141–146, 1995.

[24] B. R. Duffy and H. K. Moffatt. A similarity solution for viscous source flow on a vertical plane. *Eur. J. Appl. Math.*, 8:37–47, 1997.

[25] I. Eames, M. A. Gilbertson, and M. Landeryou. The effect of an ambient flow on the spreading of a viscous gravity current. *J. Fluid Mech.*, 523:261–275, 2005.

[26] M. S. El-Genk and H. H. Saber. Minimum thickness of a flowing down liquid film on a vertical surface. *Int. J. Heat Mass Transfer*, 44:2809–2825, 2001.

[27] X. Fanton, A. M. Cazabat, and D. Quéré. Thickness and shape of films driven by a Marangoni flow. *Langmuir*, 12:5875–5880, 1996.

[28] J. Ferguson and Z. Kemblowski. *Applied Fluid Rheology.* Elsevier Science Publishers, London, 1991.

[29] E. Y. Gatapova and O. A. Kabov. Shear-driven flows of locally heated liquid films. *Int. J. Heat Mass Transfer*, 51:4797–4810, 2008.

[30] V. A. Gorodtsov. Spreading of a film of nonlinearly viscous liquid over a horizontal smooth solid surface. *J. Eng. Phys.*, 57:879–884, 1990.

[31] J. Gratton, F. Minotti, and S. M. Mahajan. Theory of creeping gravity currents of a non-Newtonian liquid. *Phys. Rev. E*, 60:6960–6967, 1999.

[32] R. E. Grundy and R. McLaughlin. Eigenvalues of the Barenblatt-Pattle similarity solution in nonlinear diffusion. *Proc. R. Soc. London, Ser. A*, 383:89–100, 1982.

[33] M. A. Hallworth, H. E. Huppert, and R. S. J. Sparks. A laboratory simulation of basaltic lava flows. *Mod. Geol.*, 11:93–107, 1987.

[34] B. J. Hamrock. *Fundamentals of Fluid Film Lubrication.* McGraw-Hill, New York, 1994.

[35] D. E. Hartley and W. Murgatroyd. Criteria for the break-up of thin liquid layers flowing isothermally over solid surfaces. *Int. J. Heat Mass Transfer*, 7:1003–1015, 1964.

[36] F. J. Higuera. Steady creeping flow down a slope. *Phys. Fluids*, 7:2918–2920, 1995.

[37] T. Hobler. Minimum surface wetting. *Chemia Stosowana*, 2B:145–159, 1964 (in Polish).

[38] D. Holland, S. K. Wilson, and B. R. Duffy. Similarity solutions for slender dry patches with thermocapillarity. *J. Eng. Math.*, 44:369–394, 2002.

[39] D. Holland, S. K. Wilson, and B. R. Duffy. Similarity solutions for slender rivulets with thermocapillarity. *Q. J. Mech. Appl. Math.*, 56:411–439, 2003.

[40] D. P. Hoult. Oil spreading on the sea. *Ann. Rev. Fluid Mech.*, 4:341–368, 1972.

[41] H. E. Huppert. Flow and instability of a viscous current down a slope. *Nature*, 300:427–429, 1982.

[42] H. E. Huppert. The propagation of two-dimensional and axisymmetric viscous gravity currents over a rigid horizontal surface. *J. Fluid Mech.*, 121:43–58, 1982.

[43] H. E. Huppert. The intrusion of fluid mechanics into geology. *J. Fluid Mech.*, 173:557–594, 1986.

[44] A. C. King and E. O. Tuck. Thin liquid layers supported by steady air-flow surface traction. *J. Fluid Mech.*, 251:709–718, 1993.

[45] A. C. King, E. O. Tuck, and J.-M. Vanden-Broeck. Air-blown waves on thin viscous sheets. *Phys. Fluids A*, 5:973–978, 1993.

[46] J. R. King. Approximate solutions to a nonlinear diffusion equation. *J. Eng. Math.*, 22:53–72, 1988.

[47] J. R. King. Two generalisations of the thin film equation. *Math. Comput. Modell.*, 34:737–756, 2001.

[48] Y. Y. Koh, Y. C. Lee, P. H. Gaskell, P. K. Jimack, and H. M. Thompson. Droplet migration: Quantitative comparisons with experiment. *Eur. Phys. J. Special Topics*, 166:117–120, 2009.

[49] N. Le Grand, A. Daerr, and L. Limat. Shape and motion of drops sliding down an inclined plane. *J. Fluid Mech.*, 541:293–315, 2005.

[50] R. Levy, M. Shearer, and T. P. Witelski. Gravity-driven thin liquid films with insoluble surfactant: smooth traveling waves. *Eur. J. Appl. Math.*, 18:679–708, 2007.

[51] L. Limat and H. A. Stone. Three-dimensional lubrication model of a contact line corner singularity. *Europhys. Lett.*, 65:365–371, 2004.

[52] J. R. Lister. Viscous flows down an inclined plane from point and line sources. *J. Fluid Mech.*, 242:631–653, 1992.

[53] P. G. López, M. J. Miksis, and S. G. Bankoff. Stability and evolution of a dry spot. *Phys. Fluids*, 13:1601–1614, 2001.

[54] P. S. Lykoudis and R. Roos. The fluid mechanics of the ureter from a lubrication theory point of view. *J. Fluid Mech.*, 43:661–674, 1970.

[55] V. Manukian and S. Schecter. Travelling waves for a thin liquid film with surfactant on an inclined plane. *Nonlinearity*, 22:85–122, 2009.

[56] J. S. Mathunjwa and A. J. Hogg. Self-similar gravity currents in porous media: linear stability of the Barenblatt-Pattle solution revisited. *Eur. J. Mech. B. Fluids*, 25:360–378, 2006.

[57] I. S. McKinley and S. K. Wilson. The linear stability of a ridge of fluid subject to a jet of air. *Phys. Fluids*, 13:872–883, 2001.

[58] I. S. McKinley and S. K. Wilson. The linear stability of a drop of fluid during spin coating or subject to a jet of air. *Phys. Fluids*, 14:133–142, 2002.

[59] I. S. McKinley, S. K. Wilson, and B. R. Duffy. Spin coating and air-jet blowing of thin viscous drops. *Phys. Fluids*, 11:30–47, 1999.

[60] J. Mikielewicz and J. R. Moszynski. Minimum thickness of a liquid film flowing vertically down a solid surface. *Int. J. Heat Mass Transfer*, 19:771–776, 1976.

[61] J. Mikielewicz and J. R. Moszynski. An improved analysis of breakdown of thin liquid films. *Arch. Mech.*, 30:489–500, 1978.

[62] J. A. Moriarty and L. W. Schwartz. Dynamic considerations in the closing and opening of holes in thin liquid films. *J. Colloid Interface Sci.*, 161:335–342, 1993.

[63] J. A. Moriarty, L. W. Schwartz, and E. O. Tuck. Unsteady spreading of thin liquid films with small surface tension. *Phys. Fluids A*, 3:733–742, 1991.

[64] L. W. Morland and I. R. Johnson. Steady motion of ice sheets. *J. Glaciol.*, 25:229–246, 1980.

[65] W. Murgatroyd. The role of shear and form forces in the stability of a dry patch in two-phase film flow. *Int. J. Heat Mass Transfer*, 8:297–301, 1965.

[66] T. G. Myers. Thin films with high surface tension. *SIAM Rev.*, 40:441–462, 1998.

[67] T. G. Myers. Application of non-Newtonian models to thin film flow. *Phys. Rev. E*, 72:066302–1–066302–11, 2005.

[68] T. G. Myers, J. P. F. Charpin, and S. J. Chapman. The flow and solidification of a thin fluid film on an arbitrary three-dimensional surface. *Phys. Fluids.*, 14:2788–2803, 2002.

[69] S. B. G. O'Brien and L. W. Schwartz. Theory and modelling of thin film flows. In *Encyclopedia of Surface and Colloid Sci.* Marcel Dekker, New York, 5283–5297, 2002.

[70] A. Oron, S. H. Davis, and S. G. Bankoff. Long-scale evolution of thin liquid films. *Rev. Mod. Phys.*, 69:931–980, 1997.

[71] A. A. Osiptsov. Three-dimensional isothermal lava flows over a non-axisymmetric conical surface. *Fluid Dyn.*, 41:198–210, 2006.

[72] H. Pascal. Gravity flow of a non-Newtonian fluid sheet on an inclined plane. *Int. J. Eng. Sci.*, 29:1307–1313, 1991.

[73] H. Pascal. Similarity solutions to some unsteady flows of non-Newtonian fluids of power law behaviour. *Int. J. Nonlinear Mech.*, 27:759–771, 1992.

[74] J. P. Pascal. A two-layer model for a non-Newtonian gravity current subjected to wind shear. *Acta Mech.*, 162:83–98, 2003.

[75] R. E. Pattle. Diffusion from an instantaneous point source with a concentration-dependent coefficient. *Q. J. Mech. Appl. Math.*, 12:407–409, 1959.

[76] D. G. Penn, M. L. de Bertodano, P. S. Lykoudis, and S. G. Beus. Dry patch stability of shear driven liquid films. *J. Fluids Eng.*, 123:857–862, 2001.

[77] C. A. Perazzo and J. Gratton. Thin film of non-Newtonian fluid on an incline. *Phys. Rev. E*, 67:016307–1–016307–6, 2003.

[78] C. A. Perazzo and J. Gratton. Steady and traveling flows of a power-law liquid over an incline. *J. Non-Newtonian Fluid Mech.*, 118:57–64, 2004.

[79] C. A. Perazzo and J. Gratton. Exact solutions for two-dimensional steady flows of a power-law liquid on an incline. *Phys. Fluids*, 17:013102–1–013102–8, 2005.

[80] G. J. Pert. A class of similar solutions of the non-linear diffusion equation. *J. Phys. A: Math. Gen.*, 10:583–593, 1977.

[81] T. Podgorski, J.-M. Flesselles, and L. Limat. Dry arches within flowing films. *Phys. Fluids*, 11:845–852, 1999.

[82] T. Podgorski, J.-M. Flesselles, and L. Limat. Corner, cusps, and pearls in running drops. *Phys. Rev. Lett.*, 87:036102–1–036102–4, 2001.

[83] T. Podgorski, J.-M. Flesselles, and L. Limat. Curvature of a dry patch boundary in a flowing film. *C. R. Acad. Sci., Ser IV*, 2:1361–1367, 2001.

[84] A. B. Ponter, G. A. Davies, T. K. Ross, and P. G. Thornley. The influence of mass transfer on liquid film breakdown. *Int. J. Heat Mass Transfer*, 10:349–359, 1967.

[85] E. Rio, A. Daerr, and L. Limat. Probing with a laser sheet the contact angle distribution along a contact line. *J. Colloid Interface Sci.*, 269:164–170, 2004.

[86] E. Rio and L. Limat. Wetting hysteresis of a dry patch left inside a flowing film. *Phys. Fluids*, 18:032102–1–032102–8, 2006.

[87] H. H. Saber and M. S. El-Genk. On the breakup of a thin liquid film subject to interfacial shear. *J. Fluid Mech.*, 500:113–133, 2004.

[88] L. W. Schwartz. On the asymptotic analysis of surface-stress-driven thin-layer flow. *J. Eng. Math.*, 39:171–188, 2001.

[89] L. W. Schwartz and E. E. Michaelides. Gravity flow of a viscous liquid down a slope with injection. *Phys. Fluids*, 31:2739–2741, 1988.

[90] L. W. Schwartz, D. Roux, and J. J. Cooper-White. On the shapes of droplets that are sliding on a vertical wall. *Physica D*, 209:236–244, 2005.

[91] J. Sébilleau, L. Lebon, and L. Limat. Stability of a dry patch in a viscous flowing film. *Eur. Phys. J. Special Topics*, 166:139–142, 2009.

[92] P. C. Smith. A similarity solution for slow viscous flow down an inclined plane. *J. Fluid Mech.*, 58:275–288, 1973.

[93] S. H. Smith. On initial value problems for the flow in a thin sheet of viscous liquid. *J. Appl. Math. Phys.*, 20:556–560, 1969.

[94] N. F. Smyth and J. M. Hill. High-order nonlinear diffusion. *IMA J. Appl. Math.*, 40:73–86, 1988.

[95] J. H. Snoeijer, N. Le Grand-Piteira, L. Limat, H. A. Stone, and J. Eggers. Cornered drops and rivulets. *Phys. Fluids*, 19:042104–1–042104–10, 2007.

[96] J. H. Snoeijer, E. Rio, N. Le Grand, and L. Limat. Self-similar flow and contact line geometry at the rear of cornered drops. *Phys. Fluids*, 17:072101–1–072101–12, 2005.

[97] H. A. Stone, L. Limat, S. K. Wilson, J.-M. Flesselles, and T. Podgorski. Corner singularity of a contact line moving on a solid substrate. *C. R. Physique*, 3:103–110, 2002.

[98] J. M. Sullivan, S. K. Wilson, and B. R. Duffy. A thin rivulet of perfectly wetting fluid subject to a longitudinal surface shear stress. *Q. J. Mech. Appl. Math.*, 61:25–61, 2008.

[99] A. Z. Szeri. *Fluid Film Lubrication: Theory and Design.* Cambridge University Press, Cambridge, 1998.

[100] D. Takagi and H. E. Huppert. The effect of confining boundaries on viscous gravity currents. *J. Fluid Mech.*, 577:495–505, 2007.

[101] D. Takagi and H. E. Huppert. Viscous gravity currents inside confining channels and fractures. *Phys. Fluids*, 20:023104–1–023104–8, 2008.

[102] R. I. Tanner. *Engineering Rheology (Rev. ed.).* Oxford University Press, 1988.

[103] G. I. Taylor and D. H. Michael. On making holes in a sheet of fluid. *J. Fluid Mech.*, 58:625–639, 1973.

[104] G. D. Towell and L. B. Rothfeld. Hydrodynamics of rivulet flow. *AIChE J.*, 12:972–980, 1966.

[105] S. D. R. Wilson. The stability of a dry patch on a wetted wall. *Int. J. Heat Mass Transfer*, 17:1607–1615, 1974.

[106] S. D. R. Wilson and S. L. Burgess. The steady, spreading flow of a rivulet of mud. *J. Non-Newtonian Fluid Mech.*, 79:77–85, 1998.

[107] S. K. Wilson and B. R. Duffy. An asymptotic analysis of small holes in thin fluid layers. *J. Eng. Math.*, 30:445–457, 1996.

[108] S. K. Wilson and B. R. Duffy. Unidirectional flow of a thin rivulet on a vertical substrate subject to a prescribed uniform shear stress at its free surface. *Phys. Fluids*, 17:108105–1–108105–4, 2005.

[109] S. K. Wilson, B. R. Duffy, and S. H. Davis. On a slender dry patch in a liquid film draining under gravity down an inclined plane. *Eur. J. Appl. Math.*, 12:233–252, 2001.

[110] S. K. Wilson, B. R. Duffy, and R. Hunt. A slender rivulet of a power-law fluid driven by either gravity or a constant shear stress at the free surface. *Q. J. Mech. Appl. Math.*, 55:385–408, 2002.

[111] T. P. Witelski. Similarity solutions of the lubrication equation. *Appl. Math. Lett.*, 10:107–113, 1997.

[112] Y. M. Yatim, B. R. Duffy, and S. K. Wilson. Similarity solutions for unsteady shear-stress-driven flow of a power-law fluid: slender rivulets and dry patches. Submitted to *J. Eng. Math.*

[113] Y. M. Yatim, B. R. Duffy, S. K. Wilson, and R. Hunt. Similarity solutions for unsteady gravity-driven slender rivulets. To appear in *Q. J. Mech. Appl. Math.*

[114] Y. M. Yatim, S. K. Wilson, and B. R. Duffy. Unsteady gravity-driven slender rivulets of a power-law fluid. *J. Non-Newtonian Fluid Mech.*, 165:1423–1430, 2010.

[115] Y. M. Yatim, S. K. Wilson, B. R. Duffy, and R. Hunt. Similarity solutions for unsteady rivulets. In *Progress in Industrial Mathematics at ECMI 2008.* Springer–Verlag, Berlin and Heidelberg, 617-622, 2010.

[116] Y. B. Zel'dovich and A. S. Kompaneets. On the theory of heat propagation for temperature-dependent thermal conductivity. In *Collection Commemorating the 70th Anniversary of A. F. Joffe.* Izdat. Akad. Nauk SSSR, Moscow, 61–71, 1950 (in Russian).